Precision Measurement of Neutrino Oscillation Parameters with KamLAND

by

Thomas Michael ODonnell

A dissertation submitted in partial satisfaction of the

requirements for the degree of

Doctor of Philosophy

in

Physics

in the

Graduate Division

of the

University of California, Berkeley

Committee in charge:

Professor Stuart J. Freedman, Chair

Professor Yury G. Kolomensky

Professor Chung-Pei Ma

Fall 2011

Precision Measurement of Neutrino Oscillation Parameters with KamLAND

Thomas Michael ODonnell

Abstract

Precision Measurement of Neutrino Oscillation Parameters with KamLAND

by

Thomas Michael ODonnell

Doctor of Philosophy in Physics

University of California, Berkeley

Professor Stuart J. Freedman, Chair

This dissertation describes a measurement of the neutrino oscillation parameters Δm^2_{21}, θ_{12} and constraints on θ_{13} based on a study of reactor antineutrinos at a baseline of $\sim 180\,\mathrm{km}$ with the KamLAND detector. The data presented here was collected between April 2002 and November 2009, and amounts to a total exposure of $2.64 \pm 0.07 \times 10^{32}$ proton-years. For this exposure we expect $2140 \pm 74(syst)$ antineutrino candidates from reactors, assuming standard model neutrino behavior, and $350 \pm 88(syst)$ candidates from background. The number observed is 1614. The ratio of background-subtracted candidates observed to expected is

$$\frac{N_{Obs} - N_{Bkg}}{N_{Exp}} = 0.59 \pm 0.02(stat) \pm 0.045(syst)$$

which confirms reactor neutrino disappearance at greater than 5σ significance. Interpreting this deficit as being due to neutrino oscillation, the best-fit oscillation parameters from a three-flavor analysis are $\Delta m^2_{21} = 7.60^{+0.20}_{-0.19} \times 10^{-5}\mathrm{eV}^2$, $\theta_{12} = 32.5 \pm 2.9$ degrees and $\sin^2\theta_{13} = 0.025^{+0.035}_{-0.035}$, the 95% confidence-level upper limit on $\sin^2\theta_{13}$ is $\sin^2\theta_{13} < 0.083$. Assuming CPT invariance, a combined analysis of KamLAND and solar neutrino data yields best-fit values: $\Delta m^2_{21} = 7.60^{+0.20}_{-0.20} \times 10^{-5}\mathrm{eV}^2$, $\theta_{12} = 33.5^{+1.0}_{-1.1}$ degrees, and $\sin^2\theta_{13} = 0.013 \pm 0.028$ or $\sin^2\theta_{13} < 0.06$ at the 95% confidence level.

To my family

An excellent plumber is infnitely more admirable than an incompetent philosopher. The society which scorns excellence in plumbing because plumbing is a humble duty and tolerates shoddiness in philosophy because it is an exalted activity will have neither good plumbing nor good philosophy. Neither its pipes nor its theories will hold water.

— John W. Gardner[1]

[1]John W. Gardner, Excellence, Can We Be Equal and Excellent Too? Harper, New York, 1961, p. 86.

Contents

List of Figures

List of Tables

Glossary of terms

ADC Analog-to-Digital Converter

AKat American KamLAND analysis toolkit, a library of software with tools for KamLAND data analysis developed by member of the US side of the collaboration. The Japanese side of the collaboration use an independently developed library of analysis software.

ATWD Analog Transient Waveform Digitizer — a key component of the KamLAND electronics.

BO Buffer Oil, refers to the volume of mineral oil that encapsulates the KamLAND liquid scintillator.

DAQ Data acquisition system

FOM Figure of merit

GEANT GEometry ANd Tracking, a software platform designed to simulate the passage of elementary particles through matter using Monte Carlo methods.

ID The inner detector of KamLAND

KamFEE KamLAND FrontEnd Electronics

KamLAND Kamioka Liquid Scintillation AntiNeutrino Detector

LBNL Lawrence Berkeley National Laboratory

LS Liquid scintillator, refers specifically to the cocktail of scintillator deployed in the KamLAND experiment

NSum The number of channels in the KamLAND PMT array that have a signal above thrshold, this variable is used for triggering the detector.

NSumMax The maximum value of NSum during an event.

OD The outer detector of KamLAND

PDC Prompt delayed coincidence — the coincident event structure associated with the antineutrino signal.

PDF Probability Density Function

PDG Particle Data Group

PMT Photo multiplier tube

PTF Peak time fitter — the name of the position reconstruction algorithm used by the US analysis group.

ROOT Data analysis package developed at CERN in the mid-1990s and

run A period of dating taking at KamLAND, typically 24 hours in duration.

SM Standard Model of particle physics

SRIM Stopping and Range of Ions in Matter — a collection of proprietary software packages which calculate features of ion transport in matter.

SSM Standard Solar Model

Acknowledgments

Acknowledgement is due to the entire KamLAND collaboration, past and present, for their hard work and I wish to thank them all for allowing me to participate in the experiment and for their contribution to its success.

Of course KamLAND would not be possible without the support of several funding bodies, namely the Grant-in-Aid for Specially Promoted Research under grant 16002002 of the Japanese Ministry of Education, Culture, Sports, Science and Technology; the World Premier International Research Center Initiative (WPI Initiative), MEXT, Japan; and the U.S. Department of Energy (DOE) under Grants DEFG03-00ER41138, DE-AC02-05CH11231, and DE-FG02- 01ER41166.

My research could not have been completed without computing resources of the National Energy Research Scientific Computing Center, which is supported by the Office of Science of the U.S. Department of Energy under Contract No. DE-AC02-05CH11231.

The reactor operation data were provided by courtesy of the following electric associations in Japan: Hokkaido, Tohoku, Tokyo, Hokuriku, Chubu, Kansai, Chugoku, Shikoku, and Kyushu Electric Power Companies, Japan Atomic Power Company, and Japan Atomic Energy Agency. Thanks to Dr. Glenn Horton-smith for supervising my access to this data and helping me with the tools.

I'd like to thank everyone who passed through the Weak Interactions group at Berkeley while I was here, they all contributed to various aspects of my education and experience. I owe many thanks to the group leader and my thesis adviser, Prof. Stuart Freedman, for supporting me for many years, for his patience and advice, and most of all for assembling a broad and capable group of people from which to learn. Many post-docs, scientists and engineers, most within the group but some outside it, guided me or made possible my day-to-day research, particularly I am very grateful to Drs. Brian Fujikawa, Patrick Decowski, Christian Lendvai, Richard Kadel, Bruce Berger, Fred Gray, Paul Vetter, Jesse Goldman, Lauren Hsu, Karsten Heeger, Jason Detwiler, Tom Banks and Joe Wallig. I need to thank my "big brother and sister", Drs. Dan Dwyer and Lindley Winslow who were the older graduate students in the Berkeley KamLAND group when I started and who helped me immensely from the beginning. Much of their work was the foundation for mine and I missed them terribly when they graduated and left Berkeley. More recently thanks to Drs. Laura Kogler, Thomas Bloxham, Ke Han, Guy Ron and Yuan Mei for being good and encouraging group mates.

During my dissertation work I had the to opportunity to mentor a couple of really outstanding undergraduate students, I particularly want to acknowledge Kazuhiro Terao and Adrain Kaho Chan, their help with the muon system was invaluable.

I am grateful to Anne Takizawa and Donna Sakima in the Berkeley Physics Department and to Karen Hope, Melissa Barclay and Tami Blackwell at Lawrence Berkeley National Lab for helping me navigate the various administrative issues I

encountered over years.

I'd like to acknowledge and thank Seán O' Brien my mathematics and chemistry teacher at CBS for encouraging me in my very early days. I'm very grateful to Profs. Stephen Fahy and Colm O'Sullivan of the Physics Department at National University of Ireland, Cork (UCC) and Drs. Tom Carroll and Gareth Thomas of the Mathematics and Applied Mathematics Departments at UCC for their advice and mentorship during my undergraduate years at Cork.

My work on KamLAND necessitated many trips to the Kamioka site and to Tohoku University in Sendai over the years. I'm extremely grateful to Drs. Kengo Nakamura, Masayuki Koga and Sei Yoshida for their patience and for helping me get by, and enjoy life in Mozumi and Toyama, especially during the longer trips. Katsuko Shimizu was extremely kind and welcoming during all my trips, I always looked forward to hunting for mountain grapes, fried tofu and english circle with her. Of course I especially want to thank Dr. Christopher Mauger for introducing me to the Asanaru Coffee Shop a.k.a 'the little kamioka coffee shop', it was always an oasis of serenity after a day spent in the mine surrounded by the dulled cacophony of pumps, chillers, fans and alarms that keep the detector in check.

I need to thank Drs. Sanshiro Enomoto, Kazumi Tolich, and Nicolai Tolich for answering my questions on the trigger system and for being wonderful collaborators. Thanks to Dr. Greg Keefer for being a reliable collaborator, and for the good times over our years together on KamLAND — especially Munich! I also owe much gratitude to all the KamLAND members at Tohoku University with whom I spent time onsite and who made my trips to Sendai memorable, especially Drs. Koichi Ichimura and Koyhei Nakajima, Hiroko Watanabe, Hisitaka Yoshida, and Yasuhiro Takemoto. I worked closely with Dr. Chao Zhang especially in the last two years of my research, I had a lot of fun discussing problems and ideas with him.

Second to last, I need to thank all my friends who encouraged and supported me during my research. I'm fortunate to be able to claim that the list is too long to write down here.

Lastly I owe much thanks and gratitude to my parents and my sisters for everything they have done for me. While coming to Berkeley has been an excellent opportunity and a wonderful experience it has come at the great cost of spending less time with them. I thank them for always supporting and encouraging me.

Chapter 1

Introduction

There is by now a large body of data, coming from numerous different experiments, that support the notion that the flavor content of a neutrino beam changes as the beam propagates; this flavor evolution is called *neutrino flavor-oscillation*, or simply *neutrino oscillation*. A compelling explanation of the data is achieved by assuming the existence of three neutrino mass-states which do not have definite flavor and at least two of which have nonzero masses. This is the first positive lower bound on neutrino masses!

This chapter provides an overview of the phenomenological consequences of mixing between neutrino eigenstates of flavor and of mass and reviews some of the experimental evidence which compels us to accept that this mixing occurs in nature — more detailed reviews can be found in [1–3]. The KamLAND experiment, which is the main focus of this thesis, is one source of the data that led to the discovery that neutrinos have finite masses and will be described in detail in the subsequent chapters.

1.1 Neutrino oscillation

In this section we outline the consequences if one assumes the existence of three neutrino mass states, $\nu_1\,, \nu_2$ and ν_3, with masses m_1, m_2 and m_3, which are not eigenstates of the weak interaction. In this case there exists a non-trivial unitary transformation, U, between the the mass-eigenstates and the flavor-eigenstates; we write

$$|\nu_\alpha\rangle = \sum_i U^*_{\alpha i} |\nu_i\rangle\,, \tag{1.1}$$

where the subscript α runs over the three known flavor states, $\alpha = e, \mu, \tau$ and the index i labels the mass states. The 3×3 unitary matrix U is known as the PMNS mixing matrix in honor of the contributions of Pontecorvo, Maki, Nakagawa and Sakata. Neglecting possible Majorana phases which do not affect the mixing phenomenology,

U can be parametrized by 4 parameters; three of these are identified as mixing angles, denoted θ_{12}, θ_{23} and θ_{13}; the fourth is a complex phase and is usually denoted δ. A common representation for U is

$$U = \begin{pmatrix} c_{12}c_{13} & s_{12}c_{13} & s_{13}e^{-i\delta} \\ -s_{12}c_{23} - c_{12}s_{23}s_{13}e^{i\delta} & c_{12}c_{23} - s_{12}s_{23}s_{13}e^{i\delta} & s_{23}c_{13} \\ s_{12}s_{23} - c_{12}c_{23}s_{13}e^{i\delta} & -c_{12}s_{23} - s_{12}c_{23}s_{13}e^{i\delta} & c_{23}c_{13} \end{pmatrix}, \quad (1.2)$$

where $s_{ij} = \sin\theta_{ij}$ and $c_{ij} = \cos\theta_{ij}$. Throughout this thesis we assume these mixing parameters are the same for neutrinos and antineutrinos as demanded by *CPT* invariance.

1.1.1 Neutrino oscillation in vacuum

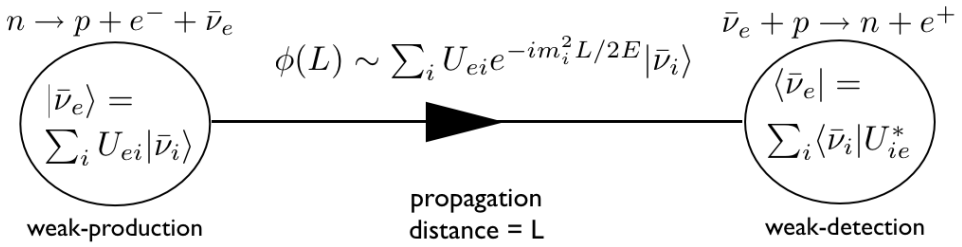

Figure 1.1: Illustration of a neutrino oscillation experiment.

An oscillation experiment is sketched in Figure 1.1, in this example an electron antineutrino is produced on the left through neutron beta decay, the state propagates as a superposition of the mass eigenstates ($\bar{\nu}_i$) which as a consequence of their different masses develop different phases with time — the form of this phase will be motivated presently. After a distance L the neutrino state behaves as an electron-flavor state and is detected through inverse beta decay (on the right). The standard model of particle physics (SM), with massless neutrinos and no neutrino-mixing, predicts the probability of observing a flavor-state other than electron-type is identically zero. If the model is extended to allow nonzero mixing angles and a neutrino mass spectrum which is not exactly degenerate then this probability can be greater than zero. Results of oscillation experiments are commonly reported as either: (i) the *survival-probability*, which is the probability to detect a flavor-state identical to the original flavor-state, or (ii) the *transition probability*, which is the probability of detecting a flavor-state different to the original. If one measures either of these probabilities for a mono-energetic neutrino beam as a function of time (or equivalently distance travelled by the beam) an interference pattern with a frequency related to the difference in the masses-squared of the neutrino mass-states emerges.

A rigorous derivation of this conclusion requires a full wavepacket treatment of the neutrino states and can be found in [4], for the moment we suspend rigor and assume that the neutrinos in the beam have a common, fixed momentum $\mathbf{p}$ but are localized in space (so that an interference pattern can be observed). It is shown in [4] that for likely experimental scenarios this naive approach yields the same final expression for the experimental observables as the more rigorous analysis. As mentioned above the state (Equation 1.1) evolves as a superposition of the vacuum Hamiltonian eigenstates, after a time t quantum mechanics predicts the following state:

$$|\nu_\alpha(t)\rangle = \sum_i U_{\alpha i} e^{-iE_i t} |\nu_i\rangle \,, \tag{1.3}$$

where the E_i are the vacuum Hamiltonian eigenvalues. The flavor-state is determined in a detector a distance L from the source, the amplitude to determine a flavor β is

$$\langle \nu_\beta | \nu_\alpha(t)\rangle = \sum_{i,j} \langle \nu_j | U^\dagger_{j,\beta} U_{\alpha i} e^{-iE_i t} |\nu_i\rangle = \sum_i U^*_{\beta i} U_{\alpha i} e^{-iE_i t} \,, \tag{1.4}$$

and the probability is the square of this amplitude

$$\begin{aligned} P(\nu_\alpha \to \nu_\beta) &= |\langle \nu_\beta | \nu_\alpha(t)\rangle|^2 \\ &= \sum_{i,j} U^*_{\beta i} U_{\alpha i} U_{\beta j} U^*_{\alpha j} e^{-i(E_i - E_j)t} \,. \end{aligned} \tag{1.5}$$

We next examine the phase in Equation 1.5. In vacuum the energy eigenvalues are

$$E_i = \sqrt{\mathbf{p}^2 + m_i^2} \simeq |\mathbf{p}| + \frac{m_i^2}{2|\mathbf{p}|} \,. \tag{1.6}$$

The approximation above is valid for relativistic neutrinos. Thus, assuming a common momentum, the relative phase to first order in $\dfrac{m_i^2}{\mathbf{p}^2}$ is

$$(E_i - E_j)\cdot t = \frac{(m_i^2 - m_j^2)L}{2E} = \frac{\Delta m^2_{ij} L}{2E} \,, \tag{1.7}$$

where $\Delta m^2_{ij} = m_i^2 - m_j^2$ and the limit $|\mathbf{p}| \to E$ has been taken — which is a valid approximation for relativistic neutrinos. Employing this approximation the transition probability for neutrinos (ν^{+l}) or antineutrinos (ν^{-l}) can be written as

$$\begin{aligned} P(\nu^{\pm l}_\alpha \to \nu^{\pm l}_\beta) &= \delta_{\alpha\beta} \\ &\quad - 4 \sum_{i>j} \mathcal{R}(U^*_{\alpha i} U_{\beta i} U_{\alpha j} U^*_{\beta j}) \sin^2 \Delta m^2_{ij} L/4E \\ &\quad \pm 2 \sum_{i>j} \mathcal{I}(U^*_{\alpha i} U_{\beta i} U_{\alpha j} U^*_{\beta j}) \sin \Delta m^2_{ij} L/2E \,, \end{aligned} \tag{1.8}$$

where $\delta_{\alpha\beta}$ is the Kronecker δ-function. The survival or transition probability is a sinusoidal function of L/E hence the term neutrino oscillation. Equation 1.8 reveals that flavor change cannot take place via this mechanism unless there is at least one massive neutrino state.

It is common to discuss the survival probability and experimental results in the context of only two neutrino species. In this case Equation 1.8 simplifies considerably, U becomes a 2×2 matrix parametrized by a single mixing angle θ and the survival probability can be written as

$$P(\nu_\alpha^{\pm l} \to \nu_\alpha^{\pm l}) = 1 - \sin^2 2\theta \sin^2 \frac{1.27 \Delta m^2[\mathrm{eV}^2]\mathrm{L[m]}}{E[\mathrm{MeV}]} \,. \tag{1.9}$$

The quantity $E/\Delta m^2$ sets a length scale for the oscillation and is called the *oscillation length*. Typically in an experiment one can control, to some extent, L/E. To have maximum sensitivity to the oscillation effect one should choose L/E such that the argument of the second sinusoidal factor in Equation 1.9 is close to $\pi/2$. Thus for neutrinos with energy $\mathcal{O}(1\,\mathrm{MeV})$ and $\Delta m^2 \simeq 1\,\mathrm{eV}^2$ a baseline of $\sim 1\,\mathrm{m}$ is needed, for $\Delta m^2 \simeq 1 \times 10^{-5}\,\mathrm{eV}^2$ a baseline of $\sim 1 \times 10^5\,\mathrm{m}$ is appropriate. If the neutrino source is extended over a distance large compared to the oscillation-length the second sinusoidal factor averages to $1/2$ and the average survival probability reduces to

$$P(\nu_\alpha^{\pm l} \to \nu_\alpha^{\pm l}) = 1 - \frac{1}{2} \sin^2 2\theta \,. \tag{1.10}$$

1.1.2 Neutrino oscillation in uniform matter

When neutrinos propagate in matter the pattern of mixing and the survival probability can alter significantly. Below we treat the simplified scenario of just two neutrino species, say ν_e and $\tilde{\nu}_\mu$, since the effects are more transparent in this case. It is shown in [5] that for the mixing parameters now favored by experiment and for matter densities of practical interest, two flavors decouple from the third and the three-flavor problem can be treated as a two-flavor problem. Thus despite the simplification just adopted the conclusions are relevant to situations of physical interest.

In matter the Hamiltonian is altered by weak interactions, in the weak eigenbasis the new Hamiltonian is

$$H' = U^\dagger H_{vac} U + H_{weak} \,, \tag{1.11}$$

where H_{vac} is the vacuum Hamiltonian in the vacuum representation:

$$H_{vac} = \begin{pmatrix} E_1 & 0 \\ 0 & E_2 \end{pmatrix} \simeq E \cdot \mathbf{1} + \begin{pmatrix} \dfrac{m_1^2}{2E} & 0 \\ 0 & \dfrac{m_2^2}{2E} \end{pmatrix} . \tag{1.12}$$

In normal matter — matter containing just electrons, protons and neutrons — electron neutrinos have both charged- and neutral-current interactions, whereas the non-electron flavor ($\tilde{\nu}_\mu$) experiences only neutral-current interactions. Therefore, in the flavor-basis the weak interaction Hamiltonian is

$$H_{weak} = \begin{pmatrix} V_{cc} + V_{NC} & 0 \\ 0 & V_{NC} \end{pmatrix} . \tag{1.13}$$

The quantities V_{NC} and V_{CC} are the charged-current and neutral-current Wolfenstein potentials [2, 6] and are given by

$$V_{CC} = F \cdot \sqrt{2} G_F n_e \, , \tag{1.14}$$

$$V_{NC} = -F \cdot \frac{G_F n_n}{\sqrt{2}} \, , \tag{1.15}$$

where G_F is the Fermi constant, n_e and n_n are the electron-density and neutron-density, and $F = 1$ for neutrinos and -1 for antineutrinos. The neutral-current contribution is the same for all flavors (at tree level) so this component is proportional to the identity matrix; since only relative phases are important terms proportional to the identity can be ignored. Expanding Equation 1.11 and omitting terms proportional to the identity the Hamiltonian in matter is

$$H' = \begin{pmatrix} -\dfrac{\Delta m^2 \cos 2\theta}{4E} + V_{CC} & \dfrac{\Delta m^2 \sin 2\theta}{4E} \\ \dfrac{\Delta m^2 \sin 2\theta}{4E} & \dfrac{\Delta m^2 \cos 2\theta}{4E} \end{pmatrix} . \tag{1.16}$$

The effective masses $\tilde{m}_1$ and $\tilde{m}_2$ are the eigenvalues of H' and the states of definite mass, $\tilde{\nu}_1$ and $\tilde{\nu}_2$, are the eigenvectors of H'. As before the flavor states are related to these new mass-eigenstates by

$$\begin{pmatrix} \nu_e \\ \tilde{\nu}_\mu \end{pmatrix} = \begin{pmatrix} \cos\theta_M & -\sin\theta_M \\ \sin\theta_M & \cos\theta_M \end{pmatrix} \begin{pmatrix} \tilde{\nu}_1 \\ \tilde{\nu}_2 \end{pmatrix} . \tag{1.17}$$

The parameter θ_M is the *matter mixing-angle* which is related to the parameters in H' by

$$\sin 2\theta_M = \frac{\sin 2\theta_v}{\sqrt{(A - \cos 2\theta_v)^2 + (\sin 2\theta_v)^2}} \, , \tag{1.18}$$

where the vacuum mixing-parameters are now qualified with the subscript v and

$$A = F \cdot \frac{2\sqrt{2} G_F n_e E}{\Delta m_v^2} \tag{1.19}$$

with $F = +1(-1)$ for neutrinos (antineutrinos). For a constant matter density the solution to the Schrödinger equation is the same as the result of the previous section but with the vacuum mixing-parameters replaced by their matter-modified counterparts. Thus the electron neutrino (antineutrino) survival probability in matter is

$$P_M(\nu_e^{\pm l} \rightarrow \nu_e^{\pm l}) = 1 - \sin^2 2\theta_M \sin^2 \frac{1.27\Delta m_M^2[\mathrm{eV}^2]\mathrm{L[m]}}{E[\mathrm{MeV}]}\,, \tag{1.20}$$

where Δm_M^2 is the difference in the effective mass squares and is related to the vacuum mass-splitting (Δm_v^2) by

$$\Delta m_M^2 = \Delta m_v^2 \sqrt{(A - \cos 2\theta_v)^2 + \sin^2 2\theta_v}\,. \tag{1.21}$$

Implicit in Equation 1.20 is a difference between the survival probabilities $P_M(\bar{\nu}_e \rightarrow \bar{\nu}_e)$ and $P_M(\nu_e \rightarrow \nu_e)$ because the sign of A depends on whether the beam is composed of neutrinos or antineutrinos. We note that in Equation 1.18 resonant mixing is possible if $A = \cos 2\theta_v$. For neutrinos, V_{CC} is positive, thus if $\Delta m^2 > 0$ and $\theta_v < \pi/4$, a resonant density ($n_{e,res}$) exists:

$$n_{e,res} = \frac{\Delta m_v^2 \cos 2\theta_v}{2\sqrt{2} G_F E}\,. \tag{1.22}$$

For this density $\theta_M \longrightarrow \pi/4$ and the mixing is maximal even if the vacuum mixing angle is small.

1.1.3 Neutrino oscillation in matter of varying density

In this section we consider neutrino propagation in matter of varying density, in particular the special case of a source in dense matter with the density monotonically decreasing as neutrinos propagate away from the source. This situation is of particular relevance for solar neutrinos. The evolution of the flavor states at any time t is

$$i\frac{d}{dt}\begin{pmatrix} \nu_e \\ \tilde{\nu}_\mu \end{pmatrix} = U_M^\dagger(t) H_M(t) \begin{pmatrix} \tilde{\nu}_1 \\ \tilde{\nu}_2 \end{pmatrix}\,, \tag{1.23}$$

where U_M is the mixing-matrix in matter. The transformation, U_M and H_M are now time dependent owing to the changing matter density. Equation 1.23 can be rearranged as follows:

$$i\frac{d}{dt}\begin{pmatrix} \tilde{\nu}_1 \\ \tilde{\nu}_2 \end{pmatrix} = [H_M - U_M i\frac{dU_M^\dagger}{dt}] \begin{pmatrix} \tilde{\nu}_1 \\ \tilde{\nu}_2 \end{pmatrix}\,. \tag{1.24}$$

When expanded and terms proportional to the identity are omitted this reduces to

$$i\frac{d}{dt}\begin{pmatrix}\tilde{\nu}_1\\ \tilde{\nu}_2\end{pmatrix} = \begin{pmatrix}\tilde{m}_1^2/2E & -i\,d\theta_M/dt\\ i\,d\theta_M/dt & \tilde{m}_2^2/2E\end{pmatrix}\begin{pmatrix}\tilde{\nu}_1\\ \tilde{\nu}_2\end{pmatrix} \tag{1.25}$$

$$= \begin{pmatrix}\Delta m_M^2/4E & -i\,d\theta_M/dt\\ i\,d\theta_M/dt & \Delta m_M^2/4E\end{pmatrix}\begin{pmatrix}\tilde{\nu}_1\\ \tilde{\nu}_2\end{pmatrix}. \tag{1.26}$$

The transition from Equation 1.25 to 1.26 is made by adding and subtracting $[\tilde{m}_1^2 + \tilde{m}_2^2]/4E \times \mathbf{1}$ on the right hand side and dropping any net terms proportional to the identity.

Equation 1.26 may be solved either numerically or analytically depending on the functional form of the density profile. However one limiting case is of particular interest. Suppose an electron neutrino is produced at the core of the Sun where the density is large, in the limit of infinite matter density $\theta_M(0) \to \pi/2$ and

$$|\nu_e\rangle = [\cos\theta_M(0)|\nu_1\rangle + \sin\theta_M(0)|\nu_2\rangle] \to |\nu_2\rangle\,, \tag{1.27}$$

where $\theta_M(0)$ denotes the matter mixing angle at the neutrino production point. In this limit $|\nu_e\rangle$ begins its journey exclusively as $|\nu_2\rangle$. If the quantity $\left|\frac{d\theta_M}{dt}\right| << \left|\frac{\Delta m_M^2}{4E}\right|$ (adiabatic propagation) the matrix in Equation 1.26 is diagonal to a good approximation and the state remains $|\nu_2\rangle$ as it propagates. However in vacuum

$$|\nu_2\rangle = \sin\theta_v|\nu_e\rangle + \cos\theta_v|\tilde{\nu}_\mu\rangle\,, \tag{1.28}$$

thus in the limit of infinite matter density at production and adiabatic propagation to vacuum the electron neutrino survival probability is

$$\lim_{\text{adiabatic},n_e(0)\to\infty} P(\nu_e \to \nu_e) \longrightarrow \sin^2\theta_v\,. \tag{1.29}$$

This limit is called the matter dominated regime. If the density is large, but not infinite, and propagation is adiabatic then a more general expression holds:

$$\lim_{\text{adiabatic}} P(\nu_e \to \nu_e) \to \cos^2\theta_M(0)\cos^2\theta_v + \sin^2\theta_M(0)\sin^2\theta_v \tag{1.30}$$

$$= \frac{1}{2}[1 + \cos 2\theta_M \cos 2\theta_v]\,. \tag{1.31}$$

The first term in Equation 1.30 is due to adiabatic propagation as $|\nu_1\rangle$ and the second is due to adiabatic propagation as $|\nu_2\rangle$.

In cases where the adiabatic approximation fails, the Hamiltonian becomes non-diagonal and the differential equation is much more difficult to solve. Some solutions for a number of different density profiles are discussed in [3]. For density profiles of

practical interest the adiabatic limit only fails near the resonance density and the results are usually stated in terms of a *jumping-probability*($P_{\rm jump}$) near the resonance point, this is the probability that the state $|\nu_1\rangle$ evolves into state $|\nu_2\rangle$ or vice-versa near the resonance region and continues adiabatically. In this case the electron neutrino survival probability [3] is

$$\begin{aligned} P_{Non-Ad}(\nu_e \to \nu_e) &= (1 - P_{\rm jump}) \cdot P_{Ad}(\nu_e \to \nu_e) + P_{\rm jump} \cdot (1 - P_{Ad}(\nu_e \to \nu_e)) \\ &= \frac{1}{2}[1 + (1 - 2P_{\rm jump}) \cos 2\theta_M \cos 2\theta_v] \,. \end{aligned} \tag{1.32}$$

Finally we consider the case where the matter effect is small at production and the vacuum mixing pattern is approximately realized. If matter effects are small at production they remain small as we consider only decreasing density profiles. This is called the *vacuum-dominated* regime. In this case the electron neutrino survival probability averaged over a large number of oscillation lengths is

$$P(\nu_e \to \nu_e) \to 1 - \frac{1}{2} \sin^2 2\theta_v \,. \tag{1.33}$$

We note that for small vacuum-mixing-angle there is a dramatic difference between vacuum-dominated and matter-dominated adiabatic neutrino propagation:

$$P(\nu_e \to \nu_e)|_{\theta_v \to 0} \begin{cases} \to 1 & \text{vacuum dominated} \\ \to 0 & \text{matter dominated} \,. \end{cases} \tag{1.34}$$

The dramatic transition in the flavor content of the beam in the matter-dominated regime is generally referred to as matter-enhanced neutrino oscillation. The matter effect is sometimes called the MSW effect in honor of the work of Mikheyev, Smirnov and Wolfenstein in the discovery and understanding of the effect.

1.2 Sources of neutrinos and experiments

Having outlined the effects of neutrino mixing on the experimental observables we now proceed to describe the results of experiments with different neutrino sources.

1.2.1 Solar neutrinos

The Sun is an intense source of electron neutrinos, Table 1.1 lists the neutrino producing reactions and fluxes predicted by the standard solar model (SSM) [7], the neutrino energy spectra are shown in Figure 1.2. During the last four decades there have been numerous experiments dedicated to the search for solar neutrinos. The initial aim was to use the neutrino flux to test the predictions of solar models, but as time progressed an anomaly emerged; the quest to resolve this anomaly led to further experiments and ultimately the discovery of neutrino mass. Below we describe some of the different types of solar experiments and the results.

Table 1.1: Neutrino producing reactions and fluxes predicted by the standard solar model [7].

Name	Reaction	Flux ($\mathrm{cm}^{-2}\mathrm{s}^{-1}$)
pp	$pp \rightarrow de^{+}\nu$	$5.99(1.00 \pm 0.01) \times 10^{10}$
pep	$pe^{-}p \rightarrow d\nu$	$1.42(1.00 \pm 0.02) \times 10^{8}$
Hep	${}^{3}Hep \rightarrow {}^{4}Hee^{+}\nu$	$7.93(1.00 \pm 0.16 \times 10^{3}$
${}^{7}Be$	${}^{7}Be\, e^{-} \rightarrow {}^{7}Li\, \nu$	$4.34(1.00 \pm 0.11) \times 10^{9}$
	${}^{7}Be\, e^{-} \rightarrow {}^{7}Li\, \nu + \gamma$	$0.50(1.00 \pm 0.11) \times 10^{9}$
${}^{8}B$	${}^{8}B \rightarrow {}^{8}Be^{*}\, e^{+}\nu$	$5.69(1.00 \pm 0.16) \times 10^{6}$
CNO	${}^{13}N \rightarrow {}^{13}C\, e^{+}\nu$	$3.07(1.00^{+0.31}_{-0.28}) \times 10^{8}$
	${}^{15}O \rightarrow {}^{15}N\, e^{+}\nu$	$2.33(1.00^{+0.33}_{-0.29}) \times 10^{8}$
	${}^{17}F \rightarrow {}^{17}O\, e^{+}\nu$	$5.84(1.00 \pm 0.52) \times 10^{8}$

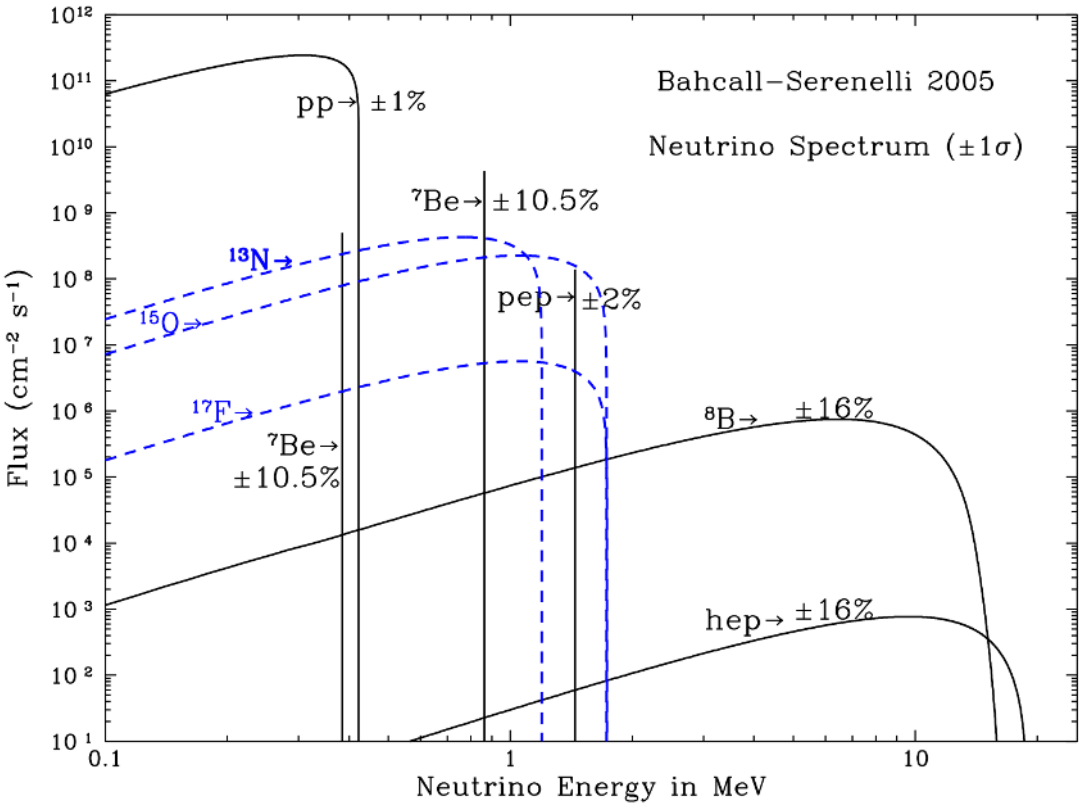

Figure 1.2: Energy spectra of solar neutrinos expected based on the standard solar model of Bahcall and Serenelli. This figure is reproduced from [7].

1.2.1.1 Radiochemical neutrino detectors

Radiochemical detectors were the first class of solar neutrino experiments. Generally this method involves searching for neutrino-induced products in a target made up of stable nuclei. The target nucleus is the product of an electron-capture decay

$$P + e^- \longrightarrow D + \nu_e \,, \tag{1.35}$$

where P denotes the parent nucleus, and D is the stable daughter. Neutrinos of sufficient energy can drive the inverse reaction producing radioactive P-nuclei in the stable target. Periodically an extraction process is performed to remove the radioactive product from the target and decays of the product are counted in an auxiliary detector by tagging Auger-electrons accompanying the decay. From the observed P-production rate an integrated neutrino flux above the production threshold can be inferred. Since the detection reaction proceeds only via charge-current interactions these experiments are sensitive only to electron-flavor neutrinos. Two radiochemical targets have been used to date, ^{37}Cl and ^{71}Ga.

1.2.1.2 The Homestake chlorine detector

The chlorine-based detector of Davis et. al [8] was the first solar neutrino experiment. It exploited the reaction

$$\nu_e + {}^{37}Cl \rightarrow {}^{37}Ar + e^- \tag{1.36}$$

which has a threshold of 0.814 MeV. With this threshold the experiment was sensitive to neutrinos from the ^7Be, CNO, pep and ^8B branches. The final result of the Homestake experiment based on over $\sim$ 25 years of operation is an ^{37}Ar production rate above background of $2.56 \pm 0.16\,(stat) \pm 0.16\,(syst)$ SNU[1] , this is about 30% of the SSM-predicted production rate of 8.1 ± 1.3 SNU. Figure 1.3 shows the solar-neutrino-induced ^{37}Ar production rate inferred by the Homestake chlorine experiment as a function of extraction date for 108 Ar extractions which were preformed during the lifetime of the experiment. The persistent deficit relative to the SSM expectation sparked what became known are the Solar Neutrino Problem, this anomaly was the genesis for more than three decades of neutrino experiments which ultimately led to the discovery of neutrino flavor oscillation.

1.2.1.3 Gallium based detectors

Following the anomaly that emerged from the chlorine experiment ^{71}Ga was used the detect neutrinos using the radiochemical method. There have been several Ga-based experiments — SAGE [9], GALLEX [10] and GNO [11]. They exploit the

[1] 1 SNU is equal to 1 capture per 10^{36} per targets per second.

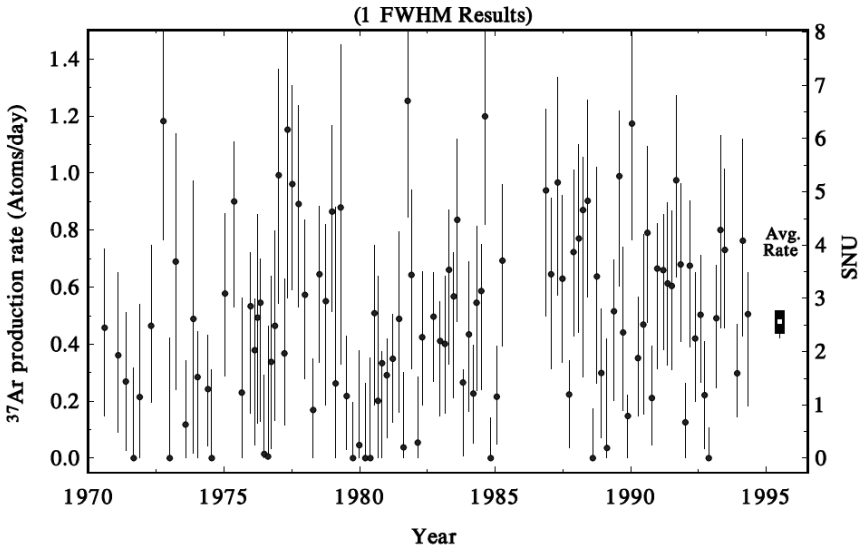

Figure 1.3: Solar-neutrino-induced ^{37}Ar production rate from 108 extractions from the Homestake Chlorine Detector. This figure is reproduced from [8].

reaction

$$\nu_e + ^{71}Ga \rightarrow ^{71}Ge + e^- \tag{1.37}$$

which has a threshold of 0.233 MeV. Consequently this method is sensitive to a larger fraction of solar neutrinos, particularly *pp*-neutrinos, than the Cl method. Table 1.2 summarizes the results of the Ga solar neutrino experiments. These experiments consistently observed only ∼60% of the expected ^{71}Ge production rate and provided independent evidence for a solar neutrino anomaly.

Table 1.2: ^{71}Ge production rate from ^{71}Ga-based solar neutrino experiments together with the SSM prediction.

Experiment	Result (SNU)
GALLEX [10]	$77.5 \pm 6.2\,(stat)\,^{+4.3}_{-4.7}\,(syst)$
GNO [11]	$62.9\,^{+5.5}_{-5.3}\,(stat)\,\pm 2.5\,(syst)$
SAGE [9]	$70.8\,^{+5.3}_{-5.2}\,(stat)\,^{+3.7}_{-3.2}\,(syst)$
SSM prediction [7]	126 ± 10 SNU

1.2.1.4 Water Cerenkov detectors

One drawback of the radiochemical approach is that the experiments only provide information on the integrated neutrino flux above the threshold for the production reaction, time information is very limited as the neutrino interaction can occur at any time between extractions. Water Cerenkov detectors, on the other hand, record the Cerenkov light produced by recoil electrons from neutrino-electron elastic scattering,

$$\nu + e^- \rightarrow \nu + e^- \,, \tag{1.38}$$

in real-time. All three neutrino flavors can participate in this process although the cross section for ν_μ and ν_τ is about 6 times smaller than that of ν_e. This method has several advantages: the scattered electron energy and event timestamp can be recorded on an event-by-event basis; and the direction of the recoiling electron, which is strongly correlated with the direction of the incident neutrino, can be measured. Water Cerenkov detectors which operated at Kamioka Mine in Japan and at Sudbury Mine in Canada made important contributions and are described next.

1.2.1.5 Kamiokande and Super-Kamiokande

The Kamiokande experiment and its larger, more sophisticated successor, Super-Kamiokande (SK) are examples of water Cerenkov solar experiments. Due to intrinsic radioactive backgrounds the recoil-electron signal is only separable above energies of several MeV — ultimately SK achieved an analysis threshold of ~ 5 MeV — these relatively high thresholds limit water Cerenkov experiments to study high-energy ^{8}B solar neutrinos.

A major triumph of Kamiokande was the observation of an excess of events whose recoil direction pointed away from the direction of the Sun, indicating that the events were indeed due to solar neutrinos. The significance of this observation has increased with time; the top plot of Figure 1.4, from a recent publication of the SK collaboration [12], shows this directional correlation, the ratio of the observed to expected electron-recoil spectrum, also from [12], is shown in the lower panel of the figure.

The experiments measure the ^8B ν-e elastic scattering rate and convert this to a ^{8}B neutrino flux assuming a purely electron-flavor beam. The final result from Kamiokande and the most recent result from SK are given in Table 1.3. Both experiments found evidence for a solar neutrino deficit, only $\sim 40 - 50\%$ of the expected scattering rate was observed .

1.2.1.6 Sudbury Neutrino Observatory (SNO)

A tremendous advance was made with the Sudbury Neutrino Observatory (SNO), this was also a water Cerenkov detector, but in this case heavy water (D_2O) rather than light-water (H_2O) was used as the target. As well as neutrino-electron elastic

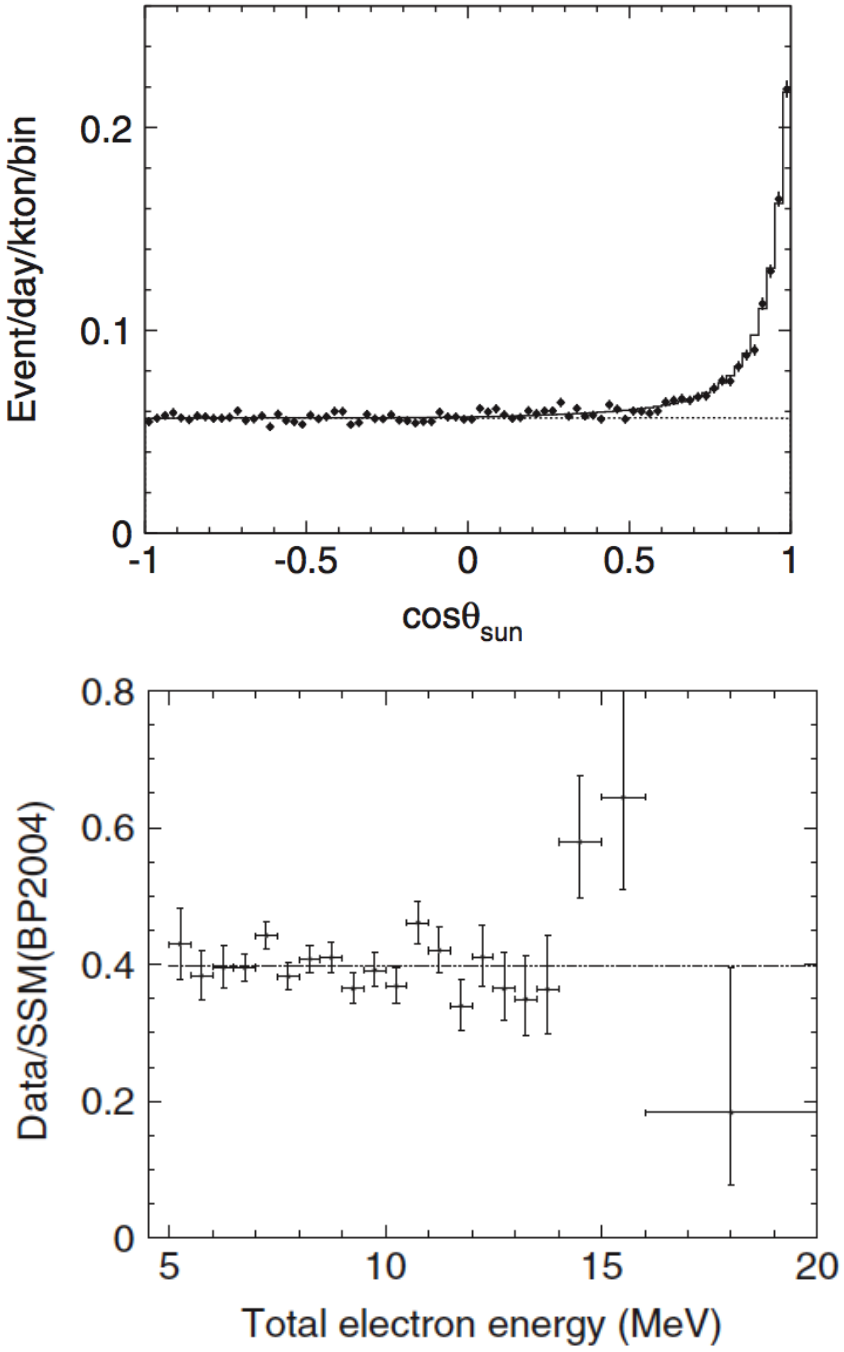

Figure 1.4: Distribution of $\cos\theta_{\rm Sun}$ for recoil-electron candidates in Super-Kamiokande, where $\theta_{\rm Sun}$ is the angle between the recoil-electron momentum and the vector pointing from the SK detector to the Sun at the time the electron was detected (top). Ratio of observed to expected recoil-electron spectrum (bottom). Both plots are reproduced from [12].

Table 1.3: The ^{8}B solar neutrino flux inferred from measurements by Kamiokande and Super-Kamiokande together with the SSM prediction.

Experiment	^8B flux ($\mathrm{cm^{-2}s^{-1}}$)
Kamiokande [13]	$2.80 \pm 0.19\,(stat) \pm 0.33\,(syst)$
Super-Kamiokande [12]	$2.32 \pm 0.04\,(stat) \pm 0.05\,(syst)$
SSM prediction [7]	$5.69(1.00 \pm 0.16)$

scattering, addition of the deuterium target made possible the following reactions:

$$\nu_e + d \;\rightarrow e^- + p + p\,, \tag{1.39}$$

$$\nu + d \;\rightarrow \nu + p + n\,. \tag{1.40}$$

The first reaction is charged-current breakup of the deuteron, which is sensitive only to electron-type neutrinos. The second reaction, neutral-current breakup of the deuteron is equally sensitive to all active flavors of neutrino. The SNO collaboration was able to tag each event type in their analysis and simultaneously provide measurements of the electron-flavor flux (ϕ_{CC}), the total active-flavor flux (ϕ_{NC}) and the flux inferred from ν-e^- elastic scattering (ϕ_{ES}).

Table 1.4: Results from the three phases of the SNO experiment, for comparison the SSM prediction is included.

Phase	Reaction	Flux ($\times 10^6\,\mathrm{cm^{-2}s^{-1}}$)
D_2O [14]	ϕ_{CC}	$1.76^{+0.06}_{-0.05}(\mathrm{stat})^{+0.09}_{-0.09}(\mathrm{syst})$
	ϕ_{ES}	$2.39^{+0.24}_{-0.23}(\mathrm{stat})^{+0.12}_{-0.12}(\mathrm{syst})$
	ϕ_{NC}	$5.09^{+0.44}_{-0.43}(\mathrm{stat})^{+0.46}_{-0.43}(\mathrm{syst})$
SALT [15]	ϕ_{CC}	$1.68^{+0.06}_{-0.06}(\mathrm{stat})^{+0.08}_{-0.09}(\mathrm{syst})$
	ϕ_{ES}	$2.35^{+0.22}_{-0.22}(\mathrm{stat})^{+0.15}_{-0.15}(\mathrm{syst})$
	ϕ_{NC}	$4.94^{+0.21}_{-0.21}(\mathrm{stat})^{+0.38}_{-0.34}(\mathrm{syst})$
NDC [16]	ϕ_{CC}	$1.67^{+0.05}_{-0.04}(\mathrm{stat})^{+0.07}_{-0.08}(\mathrm{syst})$
	ϕ_{ES}	$1.77^{+0.24}_{-0.21}(\mathrm{stat})^{+0.09}_{-0.10}(\mathrm{syst})$
	ϕ_{NC}	$5.54^{+0.33}_{-0.31}(\mathrm{stat})^{+0.36}_{-0.34}(\mathrm{syst})$
SSM ($\phi_{NC} = \phi_{ES} = \phi_{CC}$)		$5.69(1.00 \pm 0.16)$

The experiment was done in three phases, in each phase a different method to detect the neutron from the NC reaction was employed. In the first phase, called

the D_2O phase, the neutron was detected via the ∼6.25 MeV gamma ray released when a neutron captures on a deuteron. In the second phase, called the SALT phase, NaCl was added to the heavy water, neutrons preferentially capture on ^{35}Cl and produce a cascade of gammas with total energy of ∼8.6 MeV. In the third and final phase, called the neutral current detector (NCD) phase, discrete neutron detectors — ^{3}He-filled proportional tube counters — were distributed throughout the heavy water volume. The results of the three phases are summarized in Table 1.4.

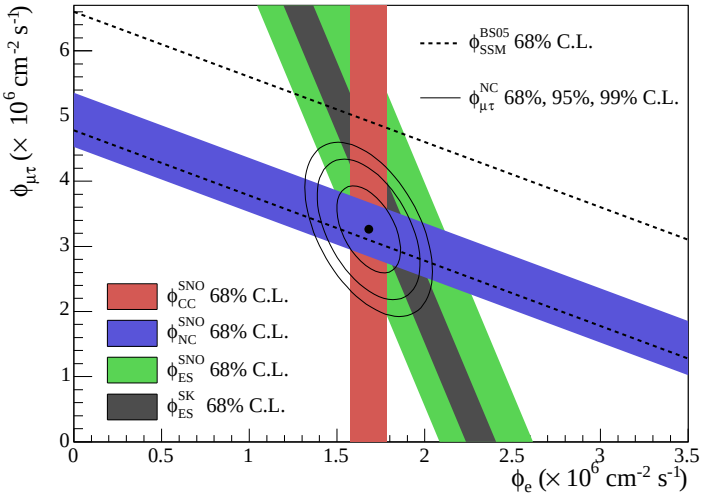

Figure 1.5: ^{8}B solar neutrino fluxes deduced from the CC (ϕ_e), ν-e^- elastic scattering (ϕ_{ES}), and NC ($\phi_{\mu\tau}$) measurements from the SALT phase of SNO [15] and the elastic scattering flux from Super-K. The BS05(OP) standard solar model prediction [7] is also shown. The bands represent the 1σ error. The contours show the 68%, 95%, and 99% joint probability for ϕ_e and $\phi_{\mu\tau}$. This figure is reproduced from [1].

Remarkably SNO found that the NC-flux and CC-flux were significantly different. This was the first direct evidence for the presence of an active flavor other than electron-type in the solar neutrino flux. Moreover the NC-flux is consistent with the standard solar model prediction but the neutrino-electron elastic scattering flux ϕ_{ES} is consistent with the results of Kamiokande and Super-K. Since there is no known way to produce a large flux of ν_μ and ν_τ in the Sun it became clear that the flavor content of the solar neutrino flux changes during propagation and that this is responsible for the solar neutrino deficit in detectors expecting a pure-ν_e flux.

1.2.2 Atmospheric neutrinos

By the time SNO announced their first results in 2001 there was already evidence for disappearance of neutrinos from a completely different source — atmo-

spheric neutrinos. We outline here the now definitive results from Super-K, although Kamiokande [17], IMB [18] and others played important roles in the early stages of this discovery.

Decays of pions and kaons produced by interactions of high-energy cosmic-ray protons with atmospheric nuclei are a source of electron and muon neutrinos. For example, for pions we have

$$\begin{aligned} \pi^{\pm} \rightarrow & \mu^{\pm} + \nu_{\mu}^{\pm l} \\ & \downarrow \\ & \mu^{\pm} \rightarrow e^{\pm} + \nu_{\mu}^{\mp l} + \nu_{e}^{\pm l} \,, \end{aligned} \tag{1.41}$$

where the $\pm l$ is used to distinguish antineutrinos from neutrinos by the sign of their lepton number. The experiments measured the tracks of charged leptons produced by these neutrinos in the detector, they had the ability to distinguish electron-tracks from muon-tracks but not the charge of the lepton. To first order based on Equation 1.41 one expects the ratio of electron-like tracks to muon-like tracks to be about ~ 2.

The experiments studied the double ratio

$$R \equiv \frac{\left(\frac{\mu}{e}\right)_{Obs}}{\left(\frac{\mu}{e}\right)_{MC}} \,, \tag{1.42}$$

where $(\mu/e)_{Obs}$ is the observed ratio of the number of muon-like and electron-like tracks and $(\mu/e)_{MC}$ is the ratio predicted from a Monte Carlo simulation. Surprisingly the double ratio was found to deviate significantly from unity. For example Super-K [**?**] found

$$R = \begin{cases} 0.638^{+0.016}_{-0.016} \pm 0.050 & \text{sub} - \text{GeV events} \\ 0.658^{+0.030}_{-0.028} \pm 0.078 & \text{multi} - \text{GeV events} \,. \end{cases}$$

Upon further investigation is was found that the double ratio had considerable zenith angle dependence. Figure 1.6 taken from [19] summarizes the findings found, in the figure $\cos\theta = -1$ signifies *upward-going* neutrinos, that is neutrinos produced in the atmosphere on the far side of the Earth which must travel through the Earth before interacting in the detector, $\cos\theta = +1$ signifies *downward-going* neutrinos, that is neutrinos produced in the atmosphere above the detector which propagate a short distance the detector. The muon-like flux was significantly suppressed for upward-going neutrinos which travel a large distance $\sim 13,000$ km through the Earth, but agreed with predictions for downward-going neutrinos (top and middle right panels of the figure). On the other hand the electron-like flux agreed well with expectations in both directions. This finding became known as the atmospheric neutrino anomaly and provided evidence that the flavor content of the atmospheric muon-neutrino flux depends on the distance traveled by the beam.

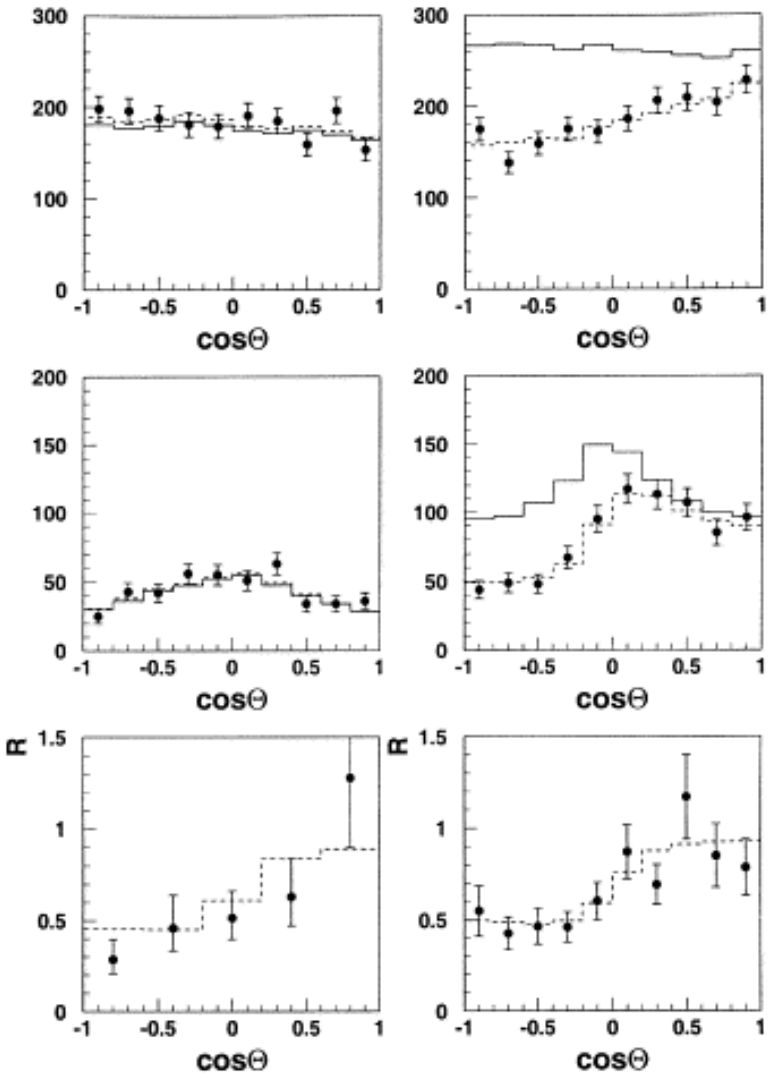

Figure 1.6: Zenith-angle distributions of sub-GeV e-like events (upper left), sub-GeV μ-like events (upper right), multi-GeV e-like events (middle left), multi-GeV μ-like events (middle right) and the double ratio (R) (lower right). The lower left figure shows the R distribution obtained in Kamiokande. The solid histograms show the expected distributions from a Monte-Carlo simulation (without oscillation). The dashed histograms show the Monte-Carlo prediction for $\nu_\mu \leftrightarrow \nu_\tau$ oscillations. This figure is reproduced from [19].

1.2.3 Accelerator Experiments

Proton accelerators can produce beams of muon and electron neutrinos in much the same way atmospheric neutrinos are produced by cosmic-ray protons. However at accelerator facilities the energy and charge sign of the intermediate $\pi^{\pm}$ or $K^{\pm}$ beam can be selected magnetically and the beam can be focused before the particles decay to produce neutrinos. Accelerator neutrino beams have been used to search for muon-neutrino disappearance as was found by Super-K. The results for two such experiments, MINOS [20] and K2K [21] are summarized in Table 1.5; Both experiments found significant evidence for muon-neutrino disappearance.

Table 1.5: Summary of results from accelerator muon-neutrino experiments.

Name	E_ν	L(km)	N_{exp}	N_{Obs}
K2K [21]	$\langle E \rangle = 1.3$ GeV	250	$158.1^{+9.2}_{-8.6}$	112
MINOS [22]	$1 \sim 5$ GeV	735	1065 ± 60	848

1.2.4 Reactor neutrino experiments

Nuclear reactors are intense sources of electron antineutrinos with $\mathcal{O}(1\,\mathrm{MeV})$ energy, the associated fluxes and spectra can be well predicted. Details on how such predictions are made for KamLAND are expanded in Chapter 5. As the solar neutrino anomaly emerged physicists began to search for disappearance of neutrinos from reactors. Historically detectors were placed at relatively short baselines, between $\sim 10\,\mathrm{m}$ and $\sim 1\,\mathrm{km}$ from the reactors and no significant evidence for neutrino disappearance was found, see Table 1.6 and Figure 1.7. The KamLAND detector was built at an unprecedented baseline of $\sim 180\,\mathrm{km}$ from its reactor sources and announced the first statistically significant observation of reactor neutrino disappearance in 2002 [23]. The KamLAND result confirmed neutrino disappearance with a man-made well-understood neutrino source.

1.3 Interpretation of neutrino disappearance data

The Super-K collaboration found that a two-flavor neutrino oscillation model (Equation 1.9) could explain the atmospheric neutrino anomaly if a mass-splitting $\Delta m^2 \simeq 2.5 \times 10^{-3}\,\mathrm{eV}^2$ and mixing angle $\theta \simeq 45^\circ$ were assumed. This oscillation model continues to describe the observations very well even as more data are accumulated. A particularly telling test, published in [32], is to examine the dependence of the observed survival probability on L/E; the oscillation model and competing models such as neutrino decay [33] and neutrino decoherence [34], exhibit different

Table 1.6: Baseline and ratio of the number of observed candidates to expected for different reactor neutrino experiments.

Name	Baseline (m)	Result (N_{Obs}/N_{exp})
ILL [24]	8.76	$0.955 \pm 0.035 \pm 0.110$
Grosgen [25]	37.9	$1.018 \pm 0.019\,(stat)\,^{\pm 0.015\,(uncorr\ syst)}_{\pm 0.06\,(corr\ syst)}$
	45.9	$1.045 \pm 0.019\,(stat)\,^{\pm 0.015\,(uncorr\ syst)}_{\pm 0.06\,(corr\ syst)}$
	64.7	$1.018 \pm 0.019\,(stat)\,^{\pm 0.015\,(uncorr\ syst)}_{\pm 0.06\,(corr\ syst)}$
Savannagh river [26]	18.2	$0.987 \pm 0.006 \pm 0.037$
Bugey [27]	15	$0.988 \pm 0.004 \pm 0.05$
	40	$0.994 \pm 0.010 \pm 0.05$
	95	$0.915 \pm 0.132 \pm 0.05$
Rovno [28]	$12 \sim 18$	$0.976 \pm 0.020 \pm 0.015$
Krasnoyarsk [29]	34	1.00 ± 0.04
CHOOZ [30]	1000	$1.00 \pm 0.028 \pm 0.027$
Palo Verde [31]	$750 \sim 890$	$1.01 \pm 0.024 \pm 0.053$
KamLAND [23]	$\sim 1.8 \times 10^5$	$0.611 \pm 0.085 \pm 0.041$

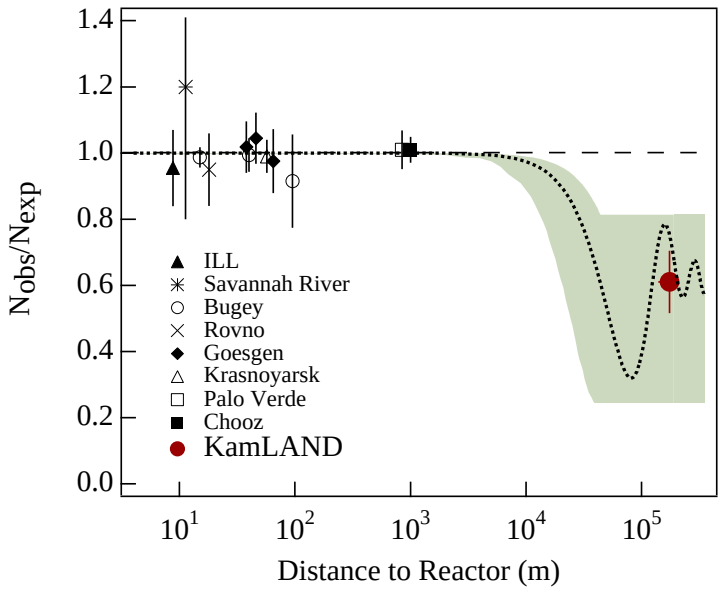

Figure 1.7: The ratio of measured to expected $\bar{\nu}_e$ flux found by a selection of reactor experiments. This figure is reproduced from [23].

dependence on L/E. The oscillation model is found to best describe the observed distribution (Figure 1.8). Further corroboration of this interpretation was achieved independently in the accelerator neutrino experiments at K2K and MINOS; The same oscillation model with statistically identical values of the oscillation parameters was found to describe all three independent experiments (Figure 1.10).

Since they emerged in atmospheric neutrino experiments the associated mass-splitting and mixing angle have come to be known as Δm^2_{atm} and θ_{atm}. The available data are not sensitive to the sign of Δm^2_{atm}. The current best-fit values for these parameters are $|\Delta m^2_{atm}| = 2.32^{+0.12}_{-0.08} \times 10^{-3}\,\mathrm{eV}^2$ and $\sin^2 2\theta_{atm} > 0.90$ at the 90% confidence level [20].

If a significant number of ν_μ oscillate into ν_e, $P(\nu_\mu \rightarrow \nu_e) >> 0$, then by CPT invariance $P(\bar{\nu}_e \rightarrow \bar{\nu}_\mu) >> 0$ and significant $\bar{\nu}_e$ disappearance should occur for $\mathcal{O}1$ MeV reactor antineutrinos at short-baselines ($L \sim E/\Delta m^2 \sim 1000\,\mathrm{m}$). The null results from short-baseline reactor experiments, Chooz and Palo Verde, largely exclude this possibility. Thus we conclude that ν_μ oscillate almost exclusively into ν_τ.

The solar neutrino data can also be explained by a neutrino oscillation model. Experiments that study high-energy ^{8}B solar neutrinos find $P(\nu_e \rightarrow \nu_e) \simeq 0.30$ and the disappearance is independent of neutrino energy; The Ga experiments where the rate is dominated by lower energy pp and ^{7}Be solar neutrinos find $P(\nu_e \rightarrow \nu_e) \simeq 0.60$. These can be explained with a vacuum mixing angle $\theta_v \simeq 33^\circ$ if the higher energy neutrinos experience matter-dominated oscillation but the lower energy neutrinos

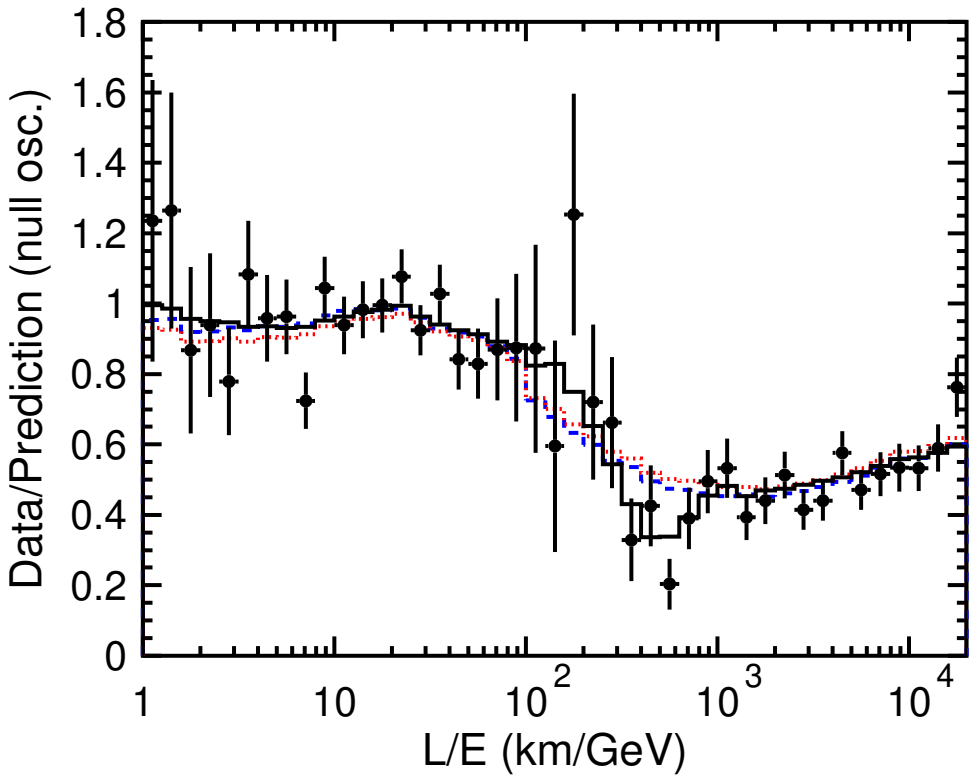

Figure 1.8: The points are the survival probability deduced from the SK data, the black line is the best-fit expectation for two-flavor $\nu_\mu \leftrightarrow \nu_\tau$ neutrino oscillation. The (red) dotted line and (blue) dashed line are the best-fit expectation for neutrino decoherence and neutrino decay. This figure is reproduced from [32].

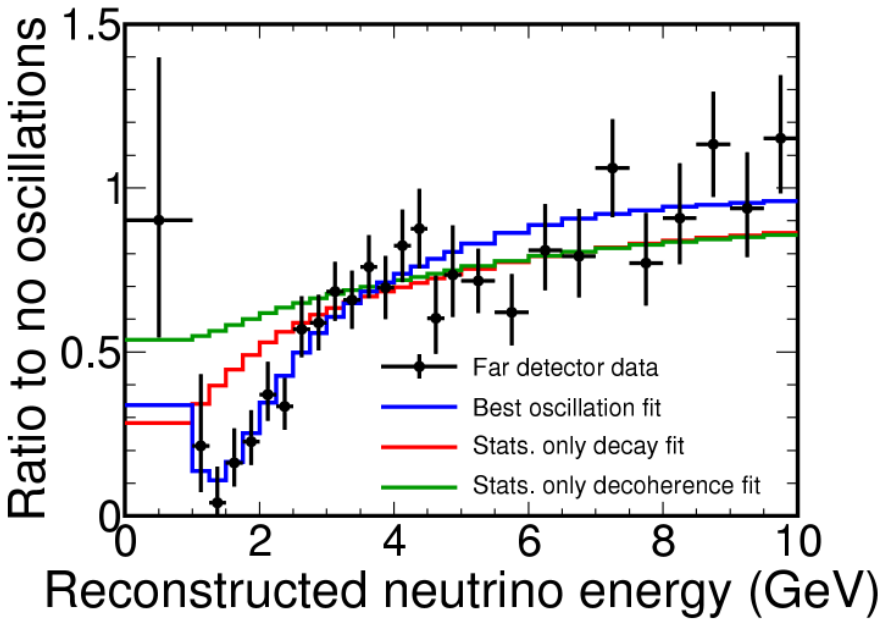

Figure 1.9: The points are the survival probability deduced from the MINOS data, the blue line is the best-fit expectation for two-flavor $\nu_\mu \leftrightarrow \nu_\tau$ neutrino oscillation. The red line and green line are the best-fit expectation for neutrino decay and neutrino decoherence respectively. This figure is reproduced from [20].

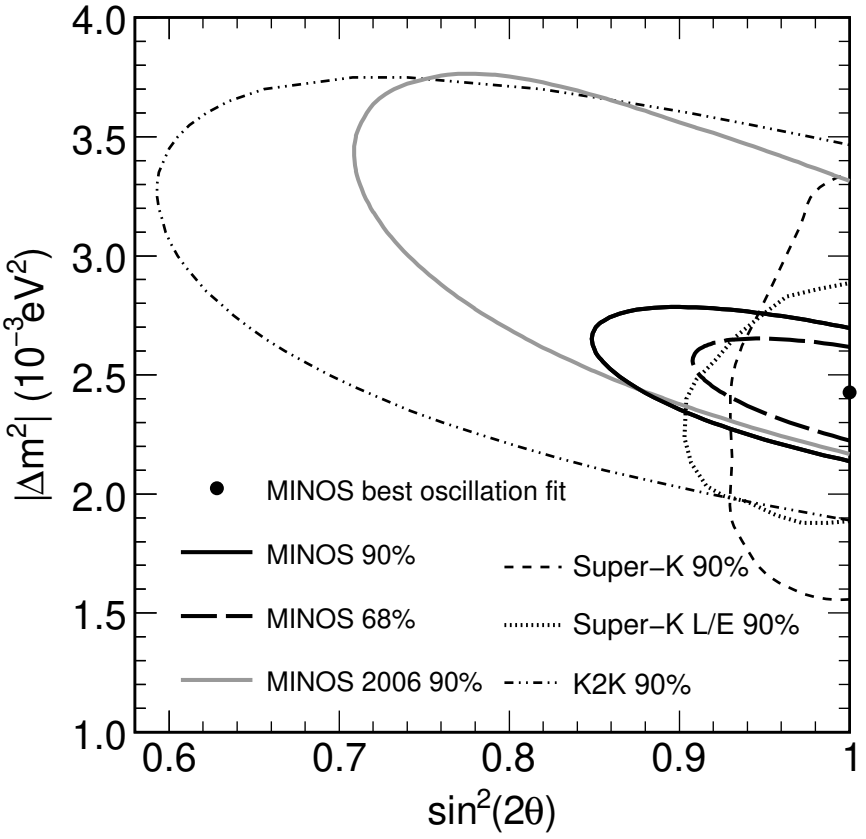

Figure 1.10: Allowed regions of oscillation parameter space for two-flavor analyses of each of atmospheric (SK), and accelerator (MINOS and K2K) neutrino experiments. [20].

experience vacuum-dominated oscillation:

$$P(\nu_e \to \nu_e)|_{\theta_v=33^\circ} = \begin{cases} 1 - 0.5\sin^2 2\theta_v = 0.58 & \text{vacuum dominated} \\ \sin^2\theta_v = 0.30 & \text{matter dominated .} \end{cases} \quad (1.43)$$

This of course requires that the mass-splitting Δm^2 be such that the matter-to-vacuum dominated transition actually takes place as the neutrino energy dials down. One region of the parameter space satisfying this constraint, with $\theta_v \sim 33^\circ$ and $10^{-5} \lesssim \Delta m^2[\text{eV}^2] \lesssim 10^{-4}$, became known as the LMA-MSW solution to the solar neutrino problem. KamLAND, with an average baseline of $\sim 180\,\text{km}$ exposed to antineutrino sources with energies in the $1 \sim 8\,\text{MeV}$ range was proposed to test solution.

KamLAND indeed found evidence for reactor antineutrino disappearance [23] and subsequently, as more data were collected, found distortion of the measured antineutrino spectrum [35, 36]. The data is well described by a two-flavor oscillation model with $\Delta m^2 \simeq 7.5 \times 10^{-5}\,\text{eV}^2$ and $\theta \simeq 33^\circ$. Figure 1.11 shows the regions in the Δm^2-$\tan^2\theta$ parameter space favored by the KamLAND data, and by the solar data. The same neutrino oscillation model with statistically compatible values of the oscillation parameters describes both sets of data. The mass-splitting and mixing angle are referred to as the solar mass-splitting $\Delta m^2_\odot$ and the solar mixing-angle $\theta_\odot$. As shown in Chapter 7 the best-fit values for the solar mixing parameters are $|\Delta m^2_\odot| = 7.6^{+0.2}_{-0.2} \times 10^{-5}\,\text{eV}^2$ and $\theta_\odot = 33.5^{+1.0}_{-1.1}$ degrees.

Matter effects in the Sun reveal that $\Delta m^2_\odot = m_2^2 - m_1^2 > 0$. The standard solar model and solar neutrino data support the conclusion that oscillation of high-energy solar neutrinos is matter-dominated and that their propagation is adiabatic. In the matter-dominated regime the effective mass $\tilde{m}_2$ is larger than $\tilde{m}_1$, and so $|\tilde{\nu}_2\rangle$ is the heavier mass state. Since propagation is adiabatic the electron-neutrino which begins as $|\tilde{\nu}_2\rangle$ remains the heavier mass state as it propagates to vacuum. Thus $|\nu_2\rangle$ in vacuum is heavier than $|\nu_1\rangle$.

1.4 Summary

The experimental results outlined above can be explained in a consistent way by assuming mixing between neutrino flavor-states and mass-states. The mixing parameters θ_{12}, Δm^2_{21}, and θ_{23}, Δm^2_{23} have been well measured in solar+reactor experiments and atmospheric+accelerator experiments respectively. The details of the KamLAND measurement and data analysis are the subject of the subsequent chapters. Our knowledge of the neutrino mass spectrum is summarized pictorially in Figure 1.12. Although the offset from zero is not known, we know that one mass-state must have a mass of at least $\sim 40\,\text{meV}$.

The absence of neutrino disappearance at short-baseline ($\sim 1\,\text{km}$) reactor experiments indicates θ_{13} is small, $\sin^2 2\theta_{13} < 0.15$ at the 90% confidence level [1]. A

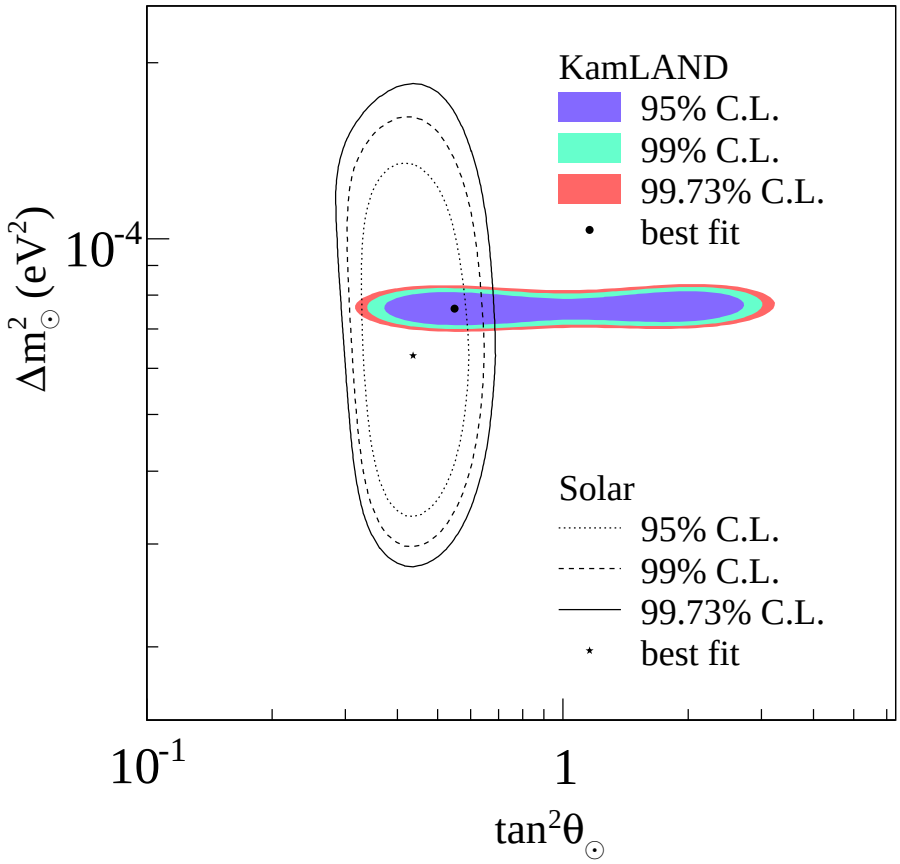

Figure 1.11: Allowed regions of oscillation parameter space for two-flavor analyses of solar and KamLAND data [36].

three-flavor analysis of the KamLAND and solar data described in Chapter 7 provides an upper bound on $\sin^2\theta_{13}$ which is consistent with existing limits. This unknown parameter is currently under investigation at next generation short-baseline reactor experiments and at accelerator neutrino experiments searching for electron-neutrino appearance in ν_μ-beams [37, 38].

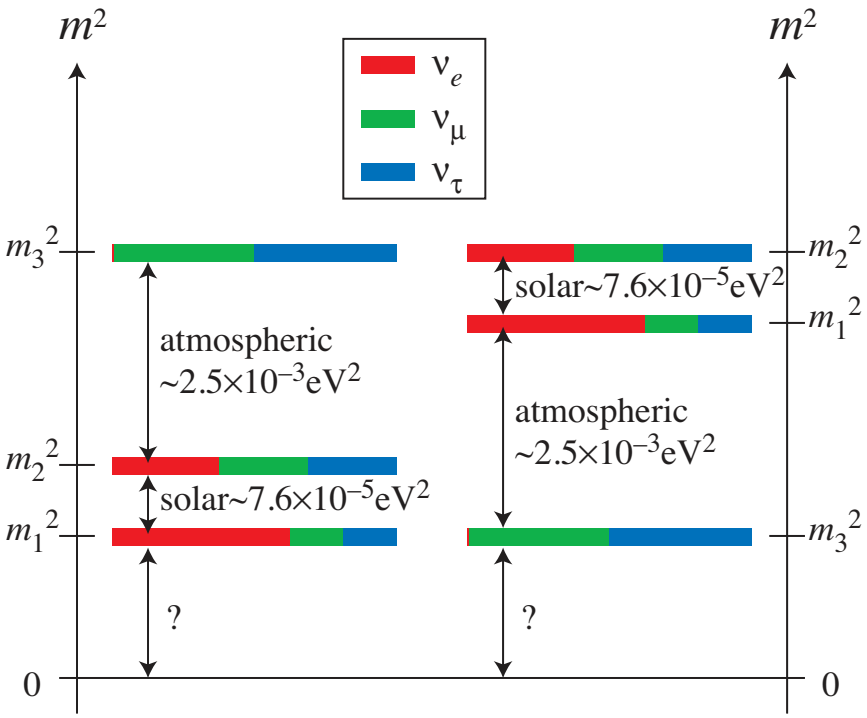

Figure 1.12: Neutrino mass spectra allowed by neutrino oscillation data, the left spectrum is called normal hierarchy, the right is called inverted hierarchy. This figure reproduced from at www.hitoshi.berkeley.edu/neutrino.

Chapter 2

KamLAND Detector

This chapter introduces the main KamLAND detector, the data acquisition system, and some terminology which will be useful for the subsequent chapters. Much more detailed descriptions of the detector can be found in several earlier works, for example [39–42].

2.1 Detector description

The KamLAND detector is located in the Kamioka Mine, Gifu, Japan. The site benefits from a vertical rock overburden of approximately 2700 m.w.e[1] which reduces the cosmic-ray muon flux in the detector by a factor of $\sim 10^6$ relative to sea level. The experiment hall, which is a cylindrical rock cavity about 20 m in diameter and 30 m high, can be accessed via a ∼2.5-km-long horizontal tunnel. Figure 2.1 shows a simplified schematic of the detector, it can be broadly divided into two sub-regions which we call the inner detector (ID) and outer detector (OD).

The ID is housed inside an 18-m-diameter spherical stainless-steel tank (SST). It contains $1171 \pm 25\,\mathrm{m}^3$ ($\sim$ 1kton) of liquid scintillator (LS) which is constrained by a thin, transparent balloon to an approximately spherical volume of radius 6.5 m, the center of this volume coincides with the center of the SST. The liquid scintillator was developed at Tohoku University [39, 40, 43], the composition and some key properties are listed in Tables 2.1 and 2.2. The LS-filled balloon is surrounded by a layer of transparent, non-scintillating mineral oil which fills the volume between the outer surface of the balloon and the inner surface of the SST ($1800\,\mathrm{m}^3$). This buffer oil (BO) volume both supports the LS and provides shielding from external gamma rays and neutrons. The LS composition was tuned so that its density exceeds that of the BO by 0.04%; the excess weight is supported by the balloon which is itself supported by a net of 44 lateral and 22 longitudinal ropes.

[1] meters water equivalent

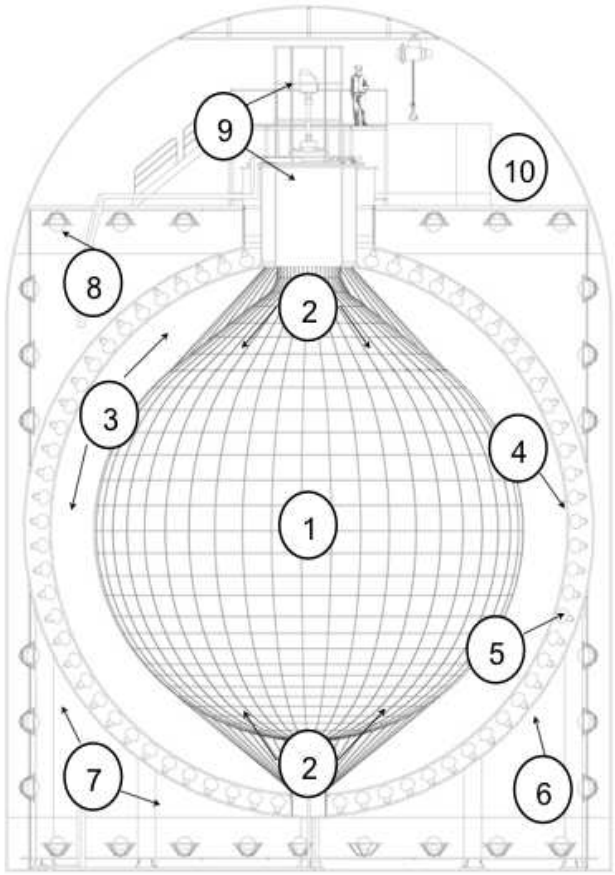

1. Liquid scintillator volume $\oslash = 13\,\mathrm{m}$
2. LS support balloon and ropes
3. Mineral oil buffer
4. Spherical acrylic shell, $\oslash = 16.7\,\mathrm{m}$, 3 mm thick
5. ID PMT array
6. Stainless-steel tank $\oslash = 18\,\mathrm{m}$
7. Water Cerenkov muon veto
8. OD PMT array
9. Chimney area, calibration port, glove-box
10. Dome area

Figure 2.1: Simplified schematic of the KamLAND detector.

Table 2.1: Liquid scintillator composition.

Component	Chemical formula	Fraction
Dodecane	$C_{12}H_{26}$	80.2%(by volume)
Pseudocumene	C_9H_{12}	19.8%(by volume)
PPO	$C_{15}H_{11}NO$	1.35 g/l

Table 2.2: Some properties of the liquid scintillator from test-bench measurements taken during LS development [39].

Density	$0.778\,\mathrm{g/cm^3}$ @ 15°C
Light output	57% anthracene
Attenuation length	10 m @ 400 nm
Refractive index	1.44 @ 400 nm
Fast response time constant	6.9 ns [44]
Slow response time constant	12.8 ns [44]

An array of 1879 PMTs mounted on the inside of the SST measures the light output of the LS. A subset (554) of these, known as the 20-inch tubes, are Hamamatsu model R3600-02; they have a 20-inch diameter photocathode surface and were reused from the Kamiokande experiment [45]. The remaining 1325 PMTs, known as the 17-inch tubes, are Hamamatsu model R7250. These are identical to the 20-inch tubes in geometry but their photocathode area is masked down to a 17-inch diameter active surface. Furthermore they have a different dynode[2] structure which results in improved timing and single photo-electron resolution relative to the 20-inch tubes [40, 46]. The spectral response of both types of PMT peaks at ∼400 nm which is well matched to the emission spectrum of the LS. The total photocathode coverage is 34%, with 22% and 12% coming from the 17- and 20-inch tubes respectively.

A 3-mm-thick, 8.35-m-radius, transparent acrylic sphere divides the BO volume, separating the inner BO region and the LS from the PMTs. This was included to limit diffusion of ^{222}Rn into the active LS volume; ^{222}Rn is a daughter of ^{238}U which is present in trace amounts in the PMT glass.

The OD consists of the volume bounded by the outer surface of the SST, the rock cavity and the steel plate which caps the cavity and forms the dome area floor. This volume is filled with 3.2 ktons of high-purity water and instrumented with 225 20-inch PMTs. The OD is divided into four optically isolated sub-volumes referred to as: OD-top, OD-upper, OD-lower and OD-bottom. The OD serves as a water Cerenkov muon-veto and further shields the ID from external gamma rays and fast neutrons.

Near the top of the detector the LS and BO volumes taper to concentric cylindrical shapes. This *neck-* or *chimney-area* is instrumented with 6 downward looking 5-inch PMTs which are attached to the plate that caps the neck of the detector. A long, 16-inch-diameter stainless-steel tube with a gate valve which can be remotely operated connects the LS volume to the outside of the detector and forms the sole conduit

[2]The dynode structure of the R7250 is the 'box-and-line' design whereas the R3600-02 has a 'venetian-blind' dynode structure [46].

for lowering calibration sources into the LS. This tube terminates in a glove-box on top of the detector which functions as a clean-space to manipulate and prepare calibration hardware. The calibration systems and procedures will be described more in Chapter 4. The environment and materials transferred into the glove-box are strictly controlled to safeguard the radio-purity of the LS.

The space above and outside the detector is called the dome area, this area contains a humidity controlled cabin or E-Hut which houses the data acquisition electronics and a clean-room for storing and preparing calibration sources prior to deployment.

2.2 Data Acquisition

The data acquisition system (DAQ) records the output of the PMTs. Data taking periods, during which all the detector and DAQ parameters are fixed, are called *runs* and are typically one day long. We use a software package called KiNOKO to control and manage the DAQ. KiNOKO was first developed for KamLAND, although the design is flexible enough that it can be easily adapted for use in other applications[3]. The DAQ has two main hardware components which are housed in the E-Hut in the dome area: (i) the *KamLAND FrontEnd Electronics* (KamFEE), a set of 200, 12-channel-boards which were custom designed at LBNL [48] and (ii) the *trigger system* which was designed at Stanford University [41].

2.2.1 Trigger system

The trigger system manages timing, monitors the number of PMTs that have been hit and controls whether or not to readout the PMTs. To keep time it has a $\sim 40\,\mathrm{MHz}$ oscillator which it distributes to each KamFEE board. A single oscillator cycle is called a *clocktick* and is $\sim 25\,\mathrm{ns}$ long. The trigger continuously records the number of clockticks that elapse relative to the start of a run. This is called the *timestamp* and is used to keep KamLAND data records time-ordered and to study temporal correlations between events recorded in the same run. To have the possibility of relating data recorded in KamLAND to observations recorded in other experiments a GPS[4] timing system is integrated into the DAQ. The GPS receiver, which is located outside the mine, outputs an IRIG-B time-code and a *one-pulse-per-second* or 1PPS pulse which are transferred via an optical fibre to the trigger unit in the E-Hut. The trigger is configured to record both the GPS time-code and the oscillator-based timestamp in the data stream once every $32\,\mathrm{s}$. Using this information the GPS time

[3]KiNOKO and KiNOKO-compatible drivers for a wide variety of commonly used hardware are freely available [42, 47].

[4]Global positioning system: a satellite-based global navigation system that provides time and position information when four or more satellites can communicate with the receiver. GPS time is a widely adopted time reference.

of any event in KamLAND can be determined and compared to other observations for which a valid GPS time is available.

2.2.2 KamFEE

The KamFEE electronics record the pulses output by the PMTs, each PMT is connected by a 40-m-long cable to a dedicated channel. Each board has 12 channels and an FPGA[5] (*board FPGA*) which handles communication between the board and the trigger system. Each channel has a discriminator, two Analog Transient Waveform Digitizers (ATWD) [49], and a *channel FPGA* which controls the digitizers and communicates with the board FPGA.

The high speed (GHz) ATWDs are a crucial component of the frontend electronics and make it possible to make high-fidelity digital copies of the $\sim$ 20-ns-long, milli-volt scale photo-electron pulses from the PMTs. Each ATWD has four inputs which we denote: H, M, L and C. Input C is reserved for clock pulses from the DAQ oscillator. Three different copies of the PMT output are sent to inputs H, M and L; each copy corresponds to the original pulse amplified by an associated factor — 20$\times$ on H (High gain), 4$\times$ on M (Medium gain), and 0.5$\times$ on L (Low gain). Each input has a dedicated 128-element switched capacitor array (SCA) which allows all four inputs to be recorded simultaneously. The switching time or sample width is programmable, we choose approximately $\sim$ 1.5 ns but ultimately this is precisely calibrated using the clock pulses recorded on input C. If a *launch command* is received the ATWD switching cycle is initiated and each input cycles through its train of 128 capacitors, capturing and holding a $\sim$ 200-ns-long record of the input. The holding time, which we call the *acquisition hold time*, is programmed to be 7 clockticks (175 ns) which is approximately twice the time it takes a photon to cross the diameter of the detector. If the ATWD receives a *digitize command* from the trigger within the hold time the waveforms are digitized. Each ATWD has a single bank of 128 10-bit ADCs which simultaneously digitizes the 128-samples on one SCA, each input-SCA (H, M or L) is digitized successively in order of decreasing amplification factor. The lower-amplification input-SCA is only digitized if the preceding, higher gain SCA saturates. The use of three amplifications allows a wide range of pulse charges, ranging from single to hundreds of photoelectrons, to be faithfully captured. Each 128$\times$10-bit-word waveform is written to an on-board memory buffer, it takes about 25 μs to digitize and write one SCA. If no digitize signal is received the SCAs are reset, it takes about 1 μs to reset the ATWD. To reduce dead-time associated with digitization and writeout, each channel has two ATWDs which we denote ATWD-A and -B. If ATWD-A is busy the launch command is routed to the backup digitizer. The channel FPGA records the number of clockticks elapsed between the ATWD launch command and

[5] A field programmable gate array (FPGA) is an integrated circuit whose logic functions may be reprogrammed after manufacture by the end-user.

the digitize command. This quantity is called the *launch offset* and is important for time ordering the pulses relative to the trigger timestamp.

2.2.3 Triggering

The command to digitize and write out the ATWD inputs is called a *trigger*. There a two basic types of triggers which we call (i) *forced-acquisition* and (ii) *global-acquisition*. A forced-acquisition trigger causes all ATWDs to acquire and digitize regardless of any input to the channel or the status of other channels. On the other hand a global-acquisition trigger is based on coincidence between input pulses on several channels. The sequence of steps leading to a global-acquisition trigger is outlined below.

1. The input of the KamFEE channel is split into two copies.

2. One copy is sent to the channel discriminator, the second proceeds via a delay line after which it is multiplexed to the three amplifier lines ($20\times, 4\times, 0.5\times$) whose outputs respectively go to the ATWD inputs H, M and L. The delay line is long enough ensure an available ATWD will be launched before pulses arrive at its inputs.

3. If the signal is above the discriminator threshold the FPGA sends a launch command to the ATWDs. The channel FPGA also starts a 5-clocktick-long (125 ns) logic pulse, called the *hit-channel pulse*, which indicates the incoming PMT signal was above the discriminator threshold.

4. On each clocktick (every 25 ns) the board FPGA sums the number of hit-channel pulses from the channels above threshold. This is called *board-NSum* and is communicated to the trigger unit.

5. From the board-NSum data the trigger unit determines the total number of channels above threshold, called the *trigger-NSum*. There are several different trigger-NSums based on the type or location of the PMTs connected to the board inputs, for example $\mathrm{NSum}_{\mathrm{OD-Top}}$ or $\mathrm{NSum}_{\mathrm{ID}_{17}}$ refers to the number of OD-Top or 17-inch ID PMTs above threshold.

6. If a trigger-NSum is above a certain predefined programmable threshold then the trigger signals ATWDs that acquired or are acquiring waveforms to digitize.

We next describe a few important named-triggers of each type which were programmed to capture certain types of physics signals or to monitor the the status of the hardware.

2.2.3.1 Some important global acquisition triggers

ID-prompt trigger

This trigger is based on the value of $\mathrm{NSum}_{\mathrm{ID}_{17}}$ which is used as a proxy for the amount of energy deposited in the detector. The NSum threshold for this trigger was typically set at $\mathrm{NSum}_{\mathrm{ID}_{17}} \geq 200$ which corresponds to an electron depositing ~ 1 MeV of energy near the center of the detector.

ID-delayed trigger

This trigger is also based on the value of $\mathrm{NSum}_{\mathrm{ID}_{17}}$. It is designed to capture lower energy events correlated with an ID-prompt trigger. For 1000 μs following a prompt trigger the NSum threshold is reduced to a lower value, typically $\mathrm{NSum}_{\mathrm{ID}_{17}} \geq 120$, which corresponds to an electron depositing approximately 0.5 MeV of energy near the center of the detector. This trigger was introduced to record the quenched energy of delayed alphas from ^{214}Bi-^{214}Po and ^{212}Bi-^{212}Po coincidences in the decay chains of ^{238}U and ^{232}Th .

OD NSum triggers

These are triggers based the values of $\mathrm{NSum}_{\mathrm{OD-Top}}$, $\mathrm{NSum}_{\mathrm{OD-Upper}}$, $\mathrm{NSum}_{\mathrm{OD-Lower}}$, $\mathrm{NSum}_{\mathrm{OD-Bottom}}$, and $\mathrm{NSum}_{\mathrm{Chimney}}$ — the number of PMTs that fired in each of the optically isolated OD regions and the chimney area.

ID-OD trigger

This is a digitization command sent to OD and chimney PMTs if an ID trigger is issued. This is used to study possible sub-threshold activity in the OD correlated with ID events.

OD-ID trigger

This is a digitization command sent to the ID PMTs if one of the OD triggers is issued. This is to monitor and characterize possible ID activity associated with OD events, for example muons crossing the OD are expected to produce fast neutrons which may scatter into the LS.

Prescale trigger

The prescale trigger is also based on $\mathrm{NSum}_{\mathrm{ID}_{17}}$. In prescale mode, a non-trivial DAQ duty cycle is introduced to control the data rate. The fraction of time the DAQ is active is called the prescale fraction. The purpose of this trigger is to study low-energy (<1MeV) background levels which for the first several years of data taking where high enough to generate very high data rates when the trigger threshold was lowered. Typical settings were $\mathrm{NSum}_{\mathrm{ID}_{17}} \geq 35$, corresponding to an electron energy deposit of ~ 0.15 MeV at the detector center, and a prescale fraction of 10%. Prescale triggers are also used when very active calibration sources are deployed in the LS.

Snapshot or 1PPS trigger

This is a global acquisition trigger issued when the trigger unit receives a 1PPS pulse from the GPS unit outside the mine. Since this trigger is not correlated any event in KamLAND this allows the dark rate of the PMTs to be monitored. Also since the frequency of 1PPS triggers is known very precisely, it can be used to monitor drifts in the DAQ oscillator frequency.

2.2.3.2 Some important forced acquisition triggers

GPS trigger

This is a forced acquisition trigger issued every 32 s, the GPS time-code is saved in the data record. By combining the GPS time-code, the oscillator timestamp, and the oscillator frequency we can determine the GPS time of events in KamLAND to better than 1 μs. The uncertainty is dominated by the uncertainty on the signal propagation time from the receiver outside the mine into the E-Hut.

Clock and pedestal triggers

These are 50 forced acquisition triggers issued at the start of every run. The purpose is to record clock waveforms to calibrate the ATWD sampling interval. The waveforms recorded on the other three ATWD inputs are called *pedestals*. These are taken to measure average ADC offsets of the ATWDs. The role of pedestal and clock waveforms in event reconstruction will be described in Chapter 3.

2.2.4 Event building

When a trigger is issued, a trigger record, which includes the timestamp, the type of trigger and the trigger-NSums, is generated and written to a data file. The digitized waveforms are recorded separately. Each waveform record includes: the timestamp of the trigger digitize command, the ATWD launch offset, the PMT channel connected to the ATWD, the ATWD ID (A or B), the ATWD input that was digitized (H, M, L or C), and the 128 pulse-height samples. To optimize data readout, the waveform records are stored in an on-board memory buffer and later written to data files as the buffer fills. The event builder process sorts through trigger and waveform records and assembles them into events according to the trigger-command timestamp. The logic of the decision to issue a global-acquisition trigger means that photons arriving within a $\sim$350 ns window will be recorded with the same timestamp and thus grouped into a single KamLAND-event. If multiple physical events occur within this time window these will pile up and be recorded as one event. Thus in the subsequent analysis we impose a minimum difference between KamLAND-event timestamps of 500 ns.

The event-built data is compressed [50] and transferred to mass storage facilities at Tohoku University in Japan and the HPSS facility at NERSC in Oakland CA,

USA. The Japanese and US groups then proceed with independent analyses. The analysis presented in the remainder of this thesis describes work carried out by the author with the US analysis group.

2.3 Detector operations and radio-purity upgrades

The data analyzed in this thesis was collected between April 3^{rd} 2002 and November 2009. The detector operated stably between April 2002 and May 2007, this period is referred to as T-I in subsequent chapters. In May 2007 the KamLAND collaboration began purifying the LS in order to remove long-lived sources of low-energy backgrounds such as ^{85}Kr and ^{210}Pb which were introduced during construction. This first purification campaign ended in September 2007 and normal data taking resumed. A second purification campaign began in July 2008. The period between September 2007 and July 2008 is referred to as T-II. The second purification campaign ended in February 2009 and normal data taking continued. The period between February 2009 and November 2009 is referred to as T-III.

Summary

In this chapter the main features of the detector and data acquisition were described. A glossary of important terms associated with the DAQ can be found in Table 2.3.

Table 2.3: Glossary of terms associated with the DAQ.

Term	Meaning
run	a data taking period, normally 24 hours long
clocktick	one cycle of the DAQ 40MHz oscillator (25 ns)
timestamp	the number of oscillator cycles elapsed since the start of a run
SCA	128-element switched capacitor array
ATWD	Analog Transient Waveform Digitizer, there are 2 per channel designated ATWD-A and -B
waveform sample	a single voltage level captured by an element of the SCA connected to the ATWD input
sample interval	the switching time of the SCA, typically 1.5 ns
waveform (WF)	set of 128 waveform samples taken at the sample interval
launch command	signal to ATWD from the channel FPGA to acquire waveforms on its inputs
acquisition-hold time	time for which ATWD holds acquired waveforms before discarding them (175 ns)
trigger command	signal to ATWD to digitize and write out acquired waveforms
launch-offset	number of clockticks between receipt of the launch command and the digitize command
clock input	one ATWD input dedicated to capturing pulses from the DAQ oscillator
gain	a term for one of the other 3 non-clock inputs of an ATWD; it may be qualified by high (H), medium (M) or low (L) to indicate which of the amplification or gain factors: 20×, 4× or 0.5×, is captured by that input

Chapter 3

Waveform analysis and event reconstruction

This chapter describes how PMT hit-times and charges are extracted from the waveform data and how event properties such as energy and position are reconstructed.

3.1 Waveform analysis

Waveform analysis (WA) is the process of extracting PMT hit-time (T) and number of photoelectrons or hit-charge (Q) from the waveforms in the event. Two waveform analyses are used by the US group, they are called *primary-WA* and *threshold-WA*. As the name suggests primary-WA is used for almost all the energy and position reconstruction; threshold-WA is only used for reconstruction of tracks associated with cosmic-ray muons.

3.1.1 Raw waveform to underlying waveform

As described in Chapter 2, a raw waveform ($\overrightarrow{W}$) is a ∼200-ns-long record of the PMT output digitized as a sequence of 128, ten-bit samples,

$$\overrightarrow{W} = \{w_1, w_2, \cdots, w_{128}\}\,. \tag{3.1}$$

Each waveform is assumed to have three contributions: (i) small sample-index-dependent fluctuations called the *pedestal*, (ii) a common sample-index-independent offset called the *baseline*, and (iii) the contribution from the PMT pulse in question which is called the *underlying waveform*. To extract the underlying waveform the pedestal and baseline must be determined and subtracted. Moreover, to convert sample-index to time elapsed since the ATWD launch the sampling time must be calibrated. We note that in this chapter the term channel is used to refer to a PMT-ATWD combination, thus a PMT corresponds to two channels.

3.1.1.1 Pedestal subtraction

The pedestal waveform ($\overrightarrow{W}_{\rm ped}$) for each input H, M, L of each channel is determined following the procedure below.

1. On each input of each channel a set of 50 forced-acquisition waveforms is collected at the start of the run. Let $\mathcal{W}_{FA}$ denote one such set,

$$\mathcal{W}_{FA} = \{\overrightarrow{W}_1, \overrightarrow{W}_2, \cdots, \overrightarrow{W}_{50}\}\,. \tag{3.2}$$

   Ideally these are all empty waveforms so that the measured pulse-height is due to residual charge on the ADCs or SCAs rather than any output of the PMT.

2. For each waveform, $\overrightarrow{W}_j$, the mean of the waveform-samples,

$$\mu_j = \frac{1}{128}\sum_{i=1}^{128} w_{j,i}\,, \tag{3.3}$$

   is calculated. The quantity $w_{j,i}$ is the i^{th} waveform-sample of the j^{th} waveform in $\mathcal{W}_{FA}$.

3. An average waveform,

$$\overrightarrow{W}_{\rm avg} = \{a_1, \cdots, a_i, \cdots, a_{128}\}\,, \tag{3.4}$$

   is constructed. The a_i are defined as

$$a_i = \frac{1}{N_{FA}}\sum_{j=1}^{N_{FA}} w_{j,i}\,, \tag{3.5}$$

   where N_{FA} is the number of waveforms being considered — initially $N_{FA} = 50$.

4. Next, an r.m.s waveform,

$$\overrightarrow{W}_{\rm rms} = \{\delta_1, \cdots, \delta_i, \cdots, \delta_{128}\}\,, \tag{3.6}$$

   with $\delta_i = \sqrt{\dfrac{1}{N_{FA}-1}(w_{j,i}-\mu_j)^2 - a_i^2}$, is formed.

5. To exclude forced-acquisition waveforms that might coincide with physical pulses, we remove waveforms $\overrightarrow{W}_j$ for which any sample satisfies $|w_{j,i} - \mu_j - a_i| > 4\cdot\delta_i$.

6. $\overrightarrow{W}_{\rm avg}$ is recalculated from the remaining waveforms in $\mathcal{W}_{FA}$.

This final average waveform is used as the pedestal for the associated channel-input and is subtracted from all waveforms collected on this input during the run. The pedestal is determined in the same way for both the primary and threshold waveform analysis.

3.1.1.2 Baseline subtraction

Once the pedestal waveform is subtracted from the raw waveform the baseline and underlying waveform remain. For the threshold waveform analysis the baseline is taken as the average of the first 10 waveform-samples and this value is subtracted from each sample. For the primary waveform analysis, the baseline is calculated from segments of the waveform that do not have peaks consistent with an underlying pulse. It is calculated iteratively following the steps below.

1. For the first iteration the baseline (b_0) is simply the average of the waveform samples,

$$b_0 = \frac{1}{128} \sum_{i=1}^{128} w_i \,. \tag{3.7}$$

2. For the n^{th} iteration, with $n > 0$, the baseline (b_n) is defined as

$$b_n = \frac{1}{\mathcal{N}_n} \sum_{i=1}^{128} w_i \,; \tag{3.8}$$

the sum is restricted to samples that satisfy

$$|w_i - b_{n-1}| < \delta \,, \tag{3.9}$$

with δ fixed at the average pulse-height of a pedestal waveform, $\delta = 0.025$. The normalization $\mathcal{N}_n$ is the number of entries that are included in the sum.

The iteration stops if $b_{n+1} = b_n$. This happens when all remaining waveform-samples are close, in the sense of Equation 3.9, to the previous value of the baseline. Once the baseline is found it is subtracted from each waveform sample.

3.1.2 Sample-index to time conversion

As mentioned in Chapter 2 waveforms from the DAQ 40 MHz oscillator are captured on the C input of each ATWD. The forced-acquisition waveforms taken on this input are used to calibrate the SCA switching time. Empty waveforms for pedestal estimation cannot be acquired on this channel because of the continuous clock input, instead the average of the M and L channel pedestals is subtracted from the clock waveforms. A fourier-analysis is carried out on the resulting clock waveforms to determine the clock frequency in units of sample-index. Knowing the true oscillator frequency the duration of the sample interval can be determined. The sample interval is found to be ~ 1.5 ns for all ATWDs.

3.1.3 Waveform smoothing

Once the pedestal waveform and baseline have been subtracted from the raw waveform the result is smoothed using a Savitzky-Golay filter [51]. This final waveform is assumed to be due to a physical PMT hit and is processed for hit-time and charge extraction.

An example of a raw waveform and the smoothed, underlying waveform is shown in Figure 3.1. In the sequel, the term waveform — used without qualification — will mean the smoothed, baseline-and-pedestal subtracted waveform.

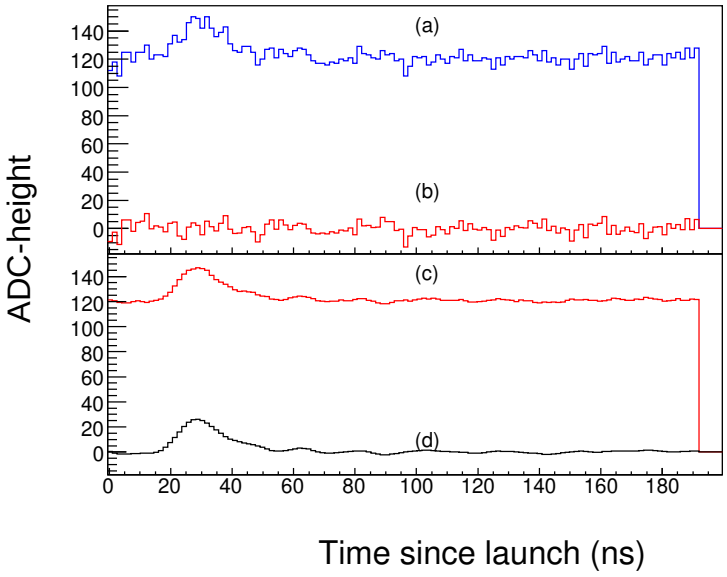

Figure 3.1: Steps in the waveform analysis. The curve labeled (a) is a raw waveform, curve (b) is the pedestal of the associated channel, curve (c) is the raw waveform after pedestal subtraction, curve (d) is the smoothed waveform with the baseline subtracted. On the horizontal axis sample-index has been converted to nanoseconds since ATWD launch using the clock waveforms.

3.1.4 Primary pulse extraction

Once the underlying waveform is found it is scanned for pulses. The primary-WA pulse finding method is called the *contiguous-area* method. A pulse is defined to be any consecutive sequence of positive waveform samples. The pulse-finder loops over the time-ordered samples in the waveform, if a positive sample is found a sequence is initiated and consecutive samples are added to the sequence if they are positive.

If a non-positive sample is found, the sequence is ended. The loop continues, a new pulse-sequence is started if another positive sample is found and so on until all 128 samples are exhausted. The result is a set of one[1] or more pulse-sequences ($\vec{p}_j$) of various lengths:

$$\begin{aligned}
\vec{p}_1 &= \{w_{i_1}, w_{i_1+1}, w_{i_1+2}, \cdots, w_{i_1+N_1}\}, \\
\vec{p}_2 &= \{w_{i_2}, w_{i_2+1}, w_{i_1+2}, \cdots, w_{i_2+N_2}\}, \\
&\vdots \\
\vec{p}_j &= \{w_{i_j}, w_{i_j+1}, w_{i_j+2}, \cdots, w_{i_j+N_j}\},
\end{aligned} \tag{3.10}$$

where the index i_j is the index in the parent waveform of the first entry of the j^{th} pulse-sequence and N_j is the number of consecutive positive waveform-samples added to this pulse. In most cases only one or two pulses are found in a single waveform. The algorithm accepts at most 16 pulse-sequences. If more than this are found they are merged.

3.1.4.1 Pulse charge

The pulse charge ($Q(\vec{p})$) is proportional to the area of the pulse

$$Q_j \equiv Q(\vec{p}_j) = \delta t \times (w_{i_j} + w_{i_j+1} + \cdots + w_{i_j+N_j}), \tag{3.11}$$

where δt is the sample interval. The units of charge at this stage are ADC-height $\times$ ns; the connection with photoelectrons is made using pulses from calibration data. Pulses with charge less than 15% of the total positive area in the waveform $\left(Q_{Tot} = \sum_j Q_j\right)$ are assumed to be spurious and are ignored in subsequent analysis.

3.1.4.2 Pulse arrival time

The PMT hit-time or photon arrival time associated with a pulse, called *TofQ*, is taken as the time of the maximum height of the pulse. A parabola is constructed on the three pairs centered on the maximum sample:

$$\{(t_{M-1}, w_{i_j+M-1}), (t_M, w_{i_j+M}), (t_{M+1}, w_{i_j+M+1})\}, \tag{3.12}$$

where w_{i_j+M} is the maximum sample in the j^{th} pulse and t_M is the time associated with sample number $i_j + M$. The maximum of this parabola is taken as TofQ for the pulse. By construction this time is relative to the launch of the ATWD; using the launch offset of the parent waveform all pulses in the event can be time ordered.

[1] Of course it is possible that no pulse is found, in which case there is no further processing of the waveform.

3.1.5 Threshold waveform analysis

The threshold waveform analysis is reserved for high-energy events where pile-up of photoelectrons makes it difficult to reliably resolve individual pulses. This waveform analysis is used only in muon track reconstruction. In this method the charge of the waveform is taken simply as the area of the first pulse found, where a pulse is defined as a sequence of at least 20 consecutive waveform-samples above a certain nonzero ADC-height threshold (ADC height $\geq$50). The hit-time of the pulse is taken as the time of the first sample above the ADC-height threshold.

3.1.6 TQ files

The result of the waveform analysis is a time (T) and a charge (Q) for each pulse found in the waveform of each channel-input (H, M, L) that was digitized. Intermediate data files are prepared with the waveform samples replaced by their TQ summary. With the default trigger settings about 300 GB of event-built data are collected per day in KamLAND. The TQ files are a factor of $\sim$10 smaller and are the starting point for event reconstruction.

3.2 Low level detector calibration

Before proceeding with event reconstruction some information about the detector response is needed. Calibration runs with a ^{60}Co source positioned at the center of the detector provide the reference data to establish the detector response. Reference runs are performed regularly — approximately once per fortnight. A number of low-level response parameters, introduced in Table 3.1, are determined from each reference data set. The procedures employed for this are described next [3].

3.2.1 Single-photoelectron charge $Q0$

The single-photoelectron (SPE) charge is a channel-dependent renormalization parameter which approximately converts the area of a pulse to a number of photoelectrons. Figure 3.2 shows an example of the distribution of pulse areas collected on the high-gain input for a single channel during a calibration run; only pulses with area above a charge threshold of $Q_t = 5$ ADC-height$\times$ ns are included in this distribution. The area of a single-photoelectron pulse on this channel is defined to be the mean of this distribution. The charge in units of photoelectrons (p.e) assigned to a pulse $\vec{p}$, captured on ATWD-A or -B of PMT i $\left(\frac{Q(\vec{p})}{Q0_{i-A}} \text{ or } \frac{Q(\vec{p})}{Q0_{i-B}}\right)$ is denoted $\hat{q}(\vec{p})$. This

[3] Many of calibration procedures were established in the early days of the experiment before the author joined the group and have only received minor modification since then. However, the details are included here to have a complete reference.

Table 3.1: Low level detector response parameters.

Symbol	Description
$Q0_{i-A}$, $Q0_{i-B}$	single-photoelectron charge on ATWD-A or ATWD-B of the i^{th} PMT, called *Q-zero*.
$\mathrm{T0}_{i-A}$, $\mathrm{T0}_{i-B}$	correction for systematic timing drifts observed on each channel, called *T-zero*.
$\mu_{i,spe}$, $\sigma_{i,spe}$	mean and width of the distribution of single photoelectron pulse charges — in units of $Q0_{i-A}$ or $Q0_{i-B}$ — collected on the i^{th} PMT.
$\Delta T_{i,Evt}$	average time over which pulses are collected from PMT i during an event, called the *event window*.
$Y_{i,\delta}$	expected number of dark photoelectrons [2] on the i^{th} PMT during an event window, called the *dark-photoelectron yield*.
$Y_{i,ref}$	expected number of photoelectrons on the i^{th} PMT per MeV of visible energy deposited in the LS, called the *reference photoelectron yield*.

rationalized charge largely factors out the channel dependence and allows for more direct comparison of the charge collected across channels. For the subsequent analysis a pulse is used only if $\hat{q} \geq 0.2\,\mathrm{p.e.}$

3.2.2 Dark-photoelectron yield $Y_{i,\delta}$

There are two methods to determine $Y_{i,\delta}$ which we call the *PPS method* and the *prepulse method*. As the name suggests the PPS method uses the 1PPS global-acquisition triggers; since these triggers are random, any charge found on a PMT is likely not related to an energy deposit in the detector. The dark occupancy ($\Omega_{i,\delta}$) is defined as the fraction of 1PPS events in which PMT i was hit. Let N_{PPS} be the number of 1PPS events under consideration and let $n_{i,\delta}$ be the size of the subset of these events that include a hit on PMT i, then

$$\Omega_{i,\delta} = \frac{n_{i,\delta}}{N_{PPS}}\,. \tag{3.13}$$

To filter out hits due to coincidence with physical events in the detector only 1PPS events with a low value of $\mathrm{NSum}_{\mathrm{ID}-17}$ ($\lesssim 20$) [4] are considered in Equation 3.13. We

[4] $\mathrm{NSum}_{\mathrm{ID}-17}$ for an event is the number of 17-inch PMTs in the inner detector array with a signal above the channel threshold during the event (Chapter 2).

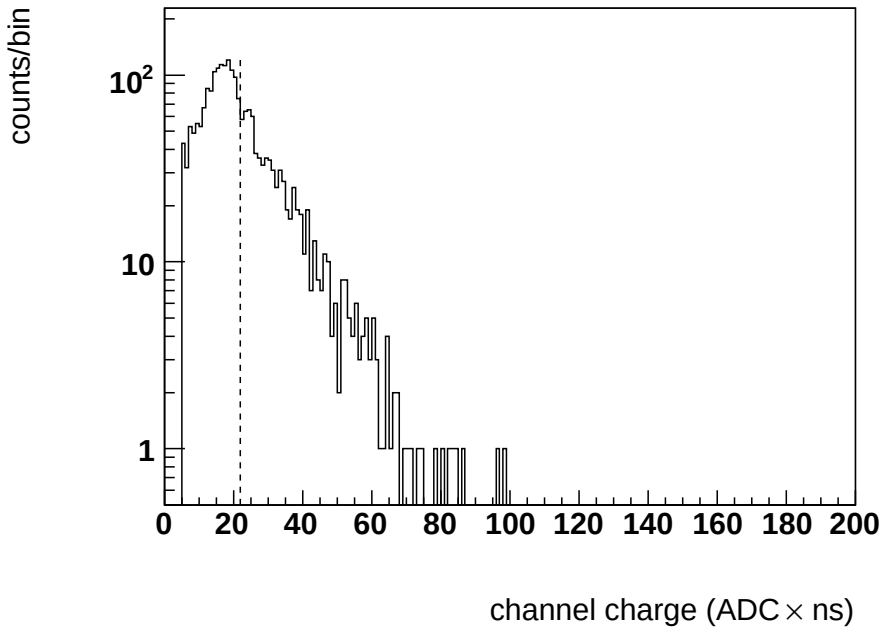

Figure 3.2: Charge per event on a single channel for a sample of events taken during a ^{60}Co calibration run. The mean of this charge distribution, indicated by the vertical dashed line, is taken as the single-photoelectron charge ($Q0$) for this channel.

can connect $Y_{i,\delta}$ to the dark occupancy by noting that

$$\begin{aligned} n_{i,\delta} &= \sum_{\text{events}} P_i(n_{p.e} > 0 | Y_{i,\delta}) \\ &= \sum_{\text{events}} \{1 - P_i(n_{p.e} = 0 | Y_{i,\delta})\} . \end{aligned} \tag{3.14}$$

The quantity $P_i(n_{p.e}|Y_{i,\delta})$ above, is the probability of observing $n_{p.e}$ photoelectrons on PMT i given an expectation $Y_{i,\delta}$ and the sum is over events that pass the $\text{NSum}_{\text{ID}-17}$ selection. Assuming P_i is a Poisson distribution — which neglects the effect of the charge threshold and channel dead-time — we have

$$n_{i,\delta} = N_{PPS} \cdot \{1 - e^{-Y_{i,\delta}}\} \tag{3.15}$$

and therefore

$$Y_{i,\delta} = -\ln(1 - \Omega_{i,\delta}) . \tag{3.16}$$

The second method used to estimate $Y_{i,\delta}$ is called the prepulse method. Figure 3.7 shows the launch-offset-corrected pulse arrival times for all ID PMTs accumulated over a reference run. Pulses that arrive well before the trigger command — in the window $(-475\,\text{ns}, -345\,\text{ns})$ — are assumed to be dark pulses. This 130 ns sample-window is denoted ΔT_δ. Let $n_{i,\delta}$ be the size of the subset of events, out of a total of N_{Tot} events, in which PMT i registers a pulse in the dark sample window, following similar reasoning to the PPS method, the dark-photoelectron yield during the dark window (ΔT_δ) can be found from the dark occupancy ($n_{i,\delta}/N_{Tot}$). To arrive at the dark yield over the full event window we must rescale this result by the duration of the event relative to ΔT_δ. The average duration of an event for PMT i, denoted $\Delta T_{i,Evt}$, is estimated from the range of launch offsets for that PMT accumulated over the calibration run. We have

$$\Delta T_{i,Evt} = (l_{i,max} - l_{i,min}) \times 25\,\text{ns} , \tag{3.17}$$

where $l_{i,max}$ and $l_{i,min}$ are the maximum and minimum launch offsets observed on the PMT — see Figure 3.4 for a sample launch offset distribution. Following Equation 3.14, the dark-photoelectron yield is

$$Y_{i,\delta} = -\frac{\Delta T_{i,Evt}}{\Delta T_\delta} \times \ln\left(1 - \frac{n_{i,\delta}}{N_{Tot}}\right) . \tag{3.18}$$

The results of the PPS- and prepulse-method were found to agree well. The US group adopted the prepulse method as the default method to determine the PMT dark-yields, this was mainly for computational convenience. The yields were updated after every reference run and written to a database whence they were used during

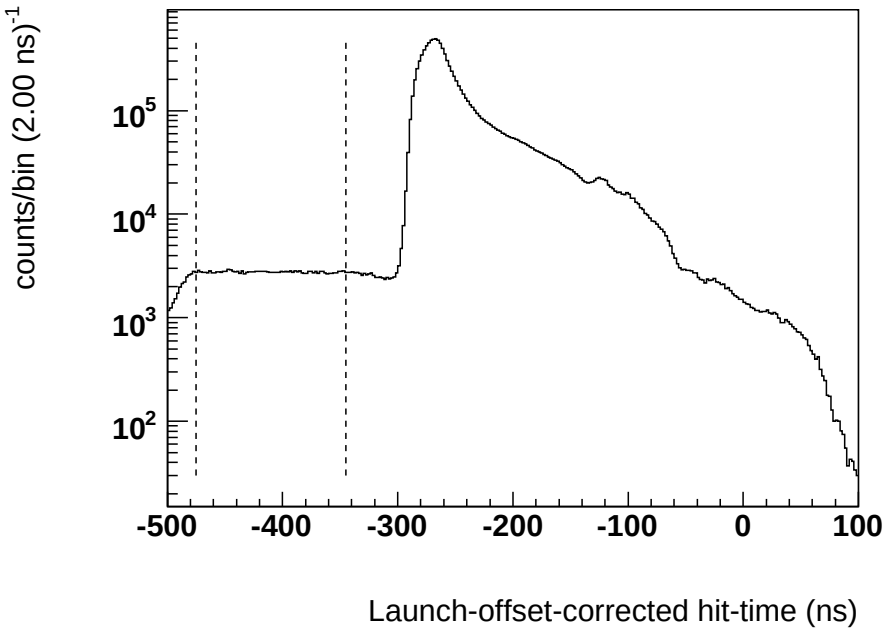

Figure 3.3: Launch-offset-corrected hit-time for all ID PMTs accumulated over a ^{60}Co calibration run. Pulses arriving in the time window delineated by the vertical lines are assumed to be from dark photoelectrons.

regular reconstruction. The PPS yields typically served as a cross-check and were calculated for each run after reconstruction. For most of the data taking period the dark yields of the PMTs were very stable and varied little between reference runs, hence fortnightly updates were more than sufficient. On some occasions it was found that the dark yields varied from run-to-run, particularly during LS purification in 2007 and 2008, the reason for this is not fully understood. During these periods the PPS method was used to update the dark yields in (*near*) real-time for the purposes of detector monitoring. However, these periods of instability are not included in the neutrino-oscillation data set.

3.2.3 Photoelectron yield per MeV of visible energy $Y_{i,ref}$

The photoelectron yield per MeV of visible energy is also determined from the ^{60}Co reference runs. Following Equation 3.14 the expected photoelectron yield per

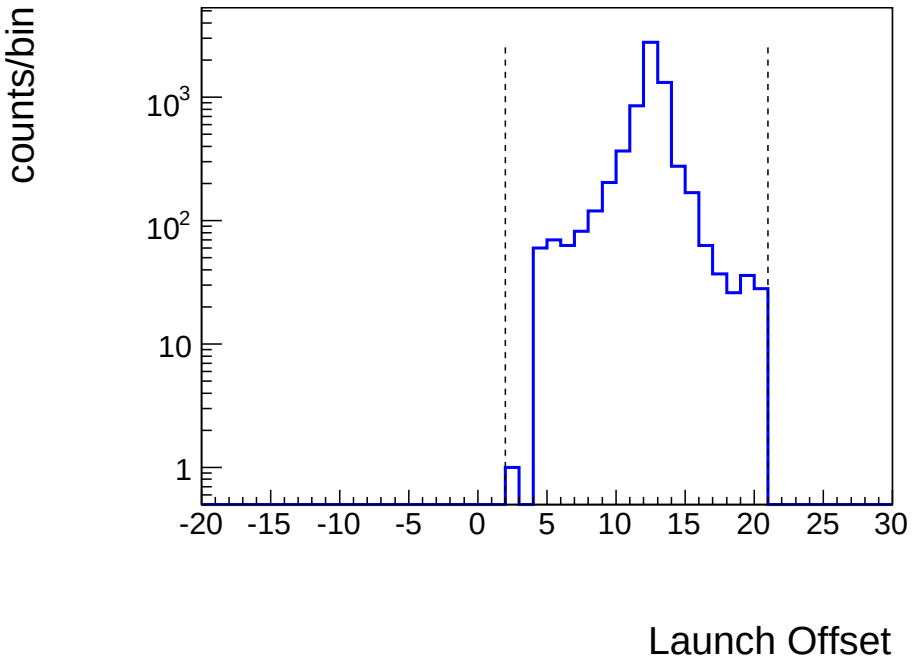

Figure 3.4: Launch offset distribution for a single PMT for events collected during a ^{60}Co calibration run.

reference event in PMT i is

$$Y_{i,Tot} = -\ln\left(1 - \frac{n_{i,hit}}{N_{Tot}}\right) , \tag{3.19}$$

where $n_{i,hit}$ is the number of times PMT i registers a hit out of N_{Tot} events. While the activity of the source ensures most events are due to the source, there is a small contribution from non-source events, for example from natural activity in the detector. To reduce the effect of such events, only triggers with $\mathrm{NSum}_{\mathrm{ID}-17}$ within two standard deviations of the mean $\mathrm{NSum}_{\mathrm{ID}-17}$ recorded during the run are considered. The normalisation of the visible energy scale is arbitrary, the US group defines the visible energy of ^{60}Co events at the center the detector, E_{ref}, to coincide with the expected physical energy deposit in the LS from gammas that escape the source capsule; $E_{ref} = 2.506\,\mathrm{MeV}$. Accounting for the dark-photoelectron yield and assuming linearity of the scintillator response, the photoelectron yield per MeV of visible energy is defined as

$$Y_{i,ref} = \frac{1}{E_{ref}} \times (Y_{i,Tot} - Y_{i,\delta}) . \tag{3.20}$$

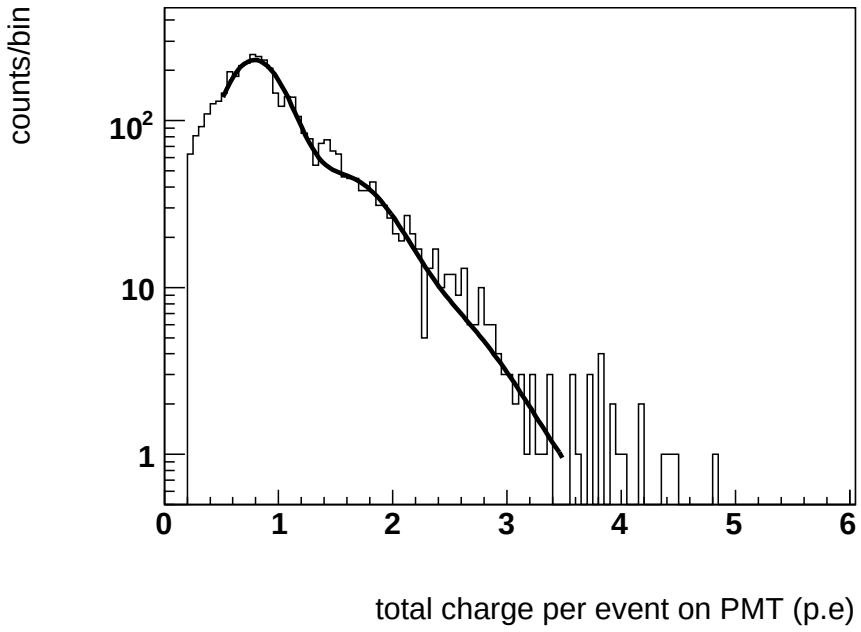

Figure 3.5: The histogram is the distribution of total charge per event, in units of photoelectrons, on a PMT for a sample of events collected during a ^{60}Co calibration run. The line is the best-fit shape function (Equation 3.22) for this distribution.

3.2.4 Mean and width of single-photoelectron charge distribution

For each PMT i, we assume the PDF which connects the number of photoelectrons to the collected charge is a gaussian-function with a mean and width-squared that scale linearly with the number of photoelectrons. To fix the PDF for PMT i the mean ($\mu_{i,spe}$) and width ($\sigma_{i,spe}$) of the single-photoelectron case must be determined. Based on the distribution of total charge per event collected on each PMT during a reference run the following iterative procedure is used to simultaneously determine $\mu_{i,spe}$, $\sigma_{i,spe}$, $Y_{i,\delta}$ and $Y_{i,ref}$ in a way that includes the charge threshold effect.

1. The initial values of $Y_{i,\delta}$ and $Y_{i,ref}$ are taken from Equations 3.18 and 3.20, which ignore threshold effects.

2. Based on the current values of $Y_{i,\delta}$ and $Y_{i,ref}$ the expected photoelectron yield

in PMT i is calculated

$$Y_{i,Tot} = E_{ref} \cdot Y_{i,ref} + Y_{i,\delta}\,. \tag{3.21}$$

3. Fixing $Y_{i,Tot}$ to its current value, new values for $\mu_{i,spe}$ and $\sigma_{i,spe}$ are found by fitting the following charge shape-function to the PMT charge distribution:

$$F(\hat{q}, \mu_i, \sigma_i | Y_{i,Tot}) = \mathcal{N} \sum_{j=1}^{\infty} \frac{1}{\sqrt{2\pi j}\sigma_i} e^{-(\hat{q}-j\cdot\mu_i)^2/2j\cdot\sigma_i^2} \times \frac{Y_{i,Tot}^j e^{-Y_{i,Tot}}}{j!}\,, \tag{3.22}$$

where $\mathcal{N}$ is a normalization parameter. Each term in the sum is the product of the poisson probability to produce j photoelectrons given an expectation of Y_{Tot} and the gaussian probability of observing a charge $\hat{q}$ given an expected mean charge equal to j photoelectrons. In practice the summation is truncated at $j = 10$.

4. Fixing $\mu_{i,spe}$ and $\sigma_{i,spe}$ at their current values, the dark yield is recalculated

$$Y_{i,\delta} = \frac{\Delta T_{i,Tot}}{\Delta T_\delta} \times \nu\,, \tag{3.23}$$

where ν is chosen to minimize

$$P_i(n_{p.e} = 0|\nu) - (1 - \Omega_{i,\delta})\,. \tag{3.24}$$

Here $\Omega_{i,\delta}$ is the dark occupancy of the PMT and $P_i(n_{p.e} = 0|\nu)$ is the probability — including threshold effects — that the PMT does not register a hit when ν photoelectrons are expected,

$$P_i(n_{p.e} = 0|\nu) = e^{-\nu} + \sum_{j=1}^{\infty} \frac{\nu^j}{j!} e^{-\nu} \int_{-\infty}^{\hat{q}_t} \frac{1}{\sqrt{2\pi j}\,\sigma_i} e^{-(q-j\cdot\mu_i)^2/2j\cdot\sigma_i^2} dq\,. \tag{3.25}$$

The second term above accounts for the charge threshold ($\hat{q}_t = 0.2\,\text{p.e}$) and in practice the sum is truncated at $j = 3$.

5. With $Y_{i,\delta}$, $\mu_{i,spe}$ and $\sigma_{i,spe}$ fixed at their current values a new value of $Y_{i,ref}$ is found by fitting the function in Equation 3.22 to the charge distribution.

Steps 2-5 are repeated 6 times and the final best-fit values of $Y_{i,\delta}$, $Y_{i,ref}$, $\mu_{i,spe}$ and $\sigma_{i,spe}$ are saved to a database. An example of the best-fit charge shape-function, Equation 3.22, overlaid with the input charge distribution is shown in Figure 3.5.

3.2.5 T-zero

The T-zero correction is a correction to account for systematic differences in the timing response of each channel. For any channel, the pulse arrival time distribution depends on the scintillator response, the propagation time to the PMT and finally the channel response. For events occurring at the center of the detector, we expect, assuming spherical geometry, that the distribution of propagation times to each PMT will be statistically the same when many events are considered. Furthermore, when integrated over many events the effect of the scintillator response should be the same for each channel. Thus by comparing the hit-time distribution on each channel accumulated over many center-events we can constrain systematic timing differences across channels. The T-zero-finding algorithm determines the offset for each channel required so that the center-event hit-time distributions of all channels have a common mean. These offsets calculated for each reference run and stored in a database for use in subsequent event reconstruction.

3.3 Event reconstruction

Once the TQs have been generated and the detector response parameters have been fixed the next step in processing is to combine the TQ data from each hit PMT to reconstruct the event energy and position. If an event is classified as an inner-detector muon then an attempt is also made to reconstruct the associated muon track. The event types and event classification are described in Appendix B.

3.3.1 Position Reconstruction

The position fitter, called the *Peak Time Fitter* (PTF) relies on the pulse times to estimate an event vertex ($\vec{V}$). Only pulses from 17-inch PMTs are used due to their superior timing and single-photoelectron resolution, pulse hit-times are based on the pulses recorded on the highest unsaturated gain of the ATWD, and pulses with charge less than 0.2 p.e are omitted from the fit. Once the input pulses for the fit have been selected, the T-zero correction of the channel is applied. To reduce energy dependence of the position reconstruction, a charge-based time correction of the following form is applied:

$$t'_{hit,i} = t_{hit,i} - a \cdot \hat{q}_i^{\,b} \,. \tag{3.26}$$

Here $t_{hit,i}$ denotes the hit-time associated with the i^{th} pulse selected for the fit. The pair $(a, b) = (0.9, 0.65)$ was found to minimize the energy dependence of the reconstruction. Subsequent references to hit-time will mean this T-zero-corrected, charge-corrected hit-time.

The algorithm finds the best-fit vertex by following a sequence of n iterations. Let $\vec{V}(n)$ be the estimated vertex at step n, the next position is found by applying a push, $\vec{\delta}[\vec{V}(n)]$, to the current position so that

$$\vec{V}(n+1) = \vec{V}(n) + \vec{\delta}[\vec{V}(n)] \ . \tag{3.27}$$

This continues until $|\vec{\delta}[\vec{V}(n)]| < 1\,\text{mm}$ or a maximum number of iterations ($n = 100$) is reached. The procedure to calculate the push at each step is outlined below.

1. The expected photon time-of-flight (t_F^{exp}) from the current position $\vec{V}(n)$ to the PMT associated with the i^{th} pulse is calculated assuming the relation

$$t_F^{exp}(n,i) = \frac{d_{LS}(\vec{V}(n),i)}{c_{LS}} + \frac{d_{BO}(\vec{V}(n),i)}{c_{BO}} \, . \tag{3.28}$$

   The quantities $d_{LS}(\vec{V},i)$ and $d_{BO}(\vec{V},i)$ are the distances in the LS and BO along the ray joining $\vec{V}$ to the center of the photocathode of PMT i. The parameters c_{LS} and c_{BO} are nominally the speed of light in the LS and BO respectively. However, these are effective speeds; they are tuned using calibration data to minimize systematic position-dependent biases in the reconstruction rather than being fixed at the values measured during detector development. The values $c_{LS} = 196\,\text{mm/ns}$ and $c_{BO} = 220\,\text{mm/ns}$ were found to give the best performance.

2. Next, the time-of-flight residual distribution is constructed. For the i^{th} pulse the time-of-flight residual (Δt) is

$$\Delta t(n,i) = t_{hit,i} - t_F^{exp}(n,i) \, . \tag{3.29}$$

   The position of the peak of this distribution at the n^{th} iteration is denoted Δt_n^{peak}.

3. A parameter called the *peak-mean* of the time-of-flight residual distribution, defined as

$$\langle \Delta t \rangle_n^{peak} = \frac{1}{N_n} \sum_i \Delta t(n,i) \, , \tag{3.30}$$

   is calculated. The sum is over the pulses near the peak of the distribution, where near is defined by the relation $-10\,\text{ns} < \Delta t(n,i) - \Delta t_n^{peak} < 5\,\text{ns}$; the number of pulses admitted to the sum is N_n.

4. For each pulse we construct the time-of-flight ratio, R_{ToF}, defined as

$$R_{ToF}(n,i) = \frac{t_{hit,i} - \langle \Delta t \rangle_{n-1}^{peak}}{t_F^{exp}(n,i)} \, . \tag{3.31}$$

   We call the numerator the *preceding average time-of-flight* for PMT i.

5. The push is defined as

$$\vec{\delta}[\vec{V}(n)] = \sum_i (1 - R_{ToF}(n,i)) \cdot (\vec{r}_i - \vec{V}(n)) \,, \tag{3.32}$$

where the sum ranges over the pulses that satisfy

$$-10\,ns < \Delta t(n,i) - \langle \Delta t \rangle_{n-1}^{peak} < 5\,ns \,. \tag{3.33}$$

The effect of the push is to nudge the current vertex towards PMTs for which the preceding average time-of-flight is shorter than the current expected time-of-flight, thus decreasing the expected time-of-flight for the new vertex. If the preceding average time-of-flight is longer than expected the push nudges the vertex away from the PMT, thus increasing the expected time-of-flight when evaluated at the new vertex. As the preceding average time-of-flight and the expected time-of-flight converge to similar values for each channel the push becomes small and the fit converges. The fraction of pulses satisfying Equation 3.33 and admitted into the sum in Equation 3.32 is called the *pulse ratio*. This is an important parameter used to classify the quality of the vertex fit.

The initial vertex in the iteration ($\vec{V}(0)$) is based on the charge-weighted average position of the hit PMTs,

$$\vec{V}(0) = \alpha \frac{\sum_i Q_i \vec{r}_i}{\sum_i Q_i} \,. \tag{3.34}$$

The pair $(Q_i, \vec{r}_i)$ above indicate the charge of the i^{th} pulse and the position of the center of the photocathode of the associated PMT. The value $\alpha = 1.62$ was found in calibration runs to give the best initial guess for the vertex. The initial value of the peak mean ($\langle t \rangle_0^{peak}$) is taken as the mean of entries within a 10 ns window of the peak of the initial time-of-flight residual distribution.

Along with the best-fit position the PTF fitter records some fit-quality parameters based on the failure modes listed in Table 3.2. Only vertices that pass all five of these quality tests are considered *good-vertices* and are used in the final antineutrino analysis. The efficiency of this selection is studied in Chapter 6.

3.3.2 Visible energy reconstruction

The visible energy (E_{vis}) of an event is based on the photoelectron yield in the PMT array. One must distinguish between the visible energy and the real, or physical, energy deposited by a particle. The scintillation-photon yield — and consequently the photoelectron yield — per MeV of physical energy is particle and energy dependent. For example, due to quenching effects it is found that a ∼7 MeV alpha particle and a ∼0.6 MeV electron have similar scintillation-photon yields, and thus have similar

Table 3.2: Vertex fitter failure modes.

Mode Name	Description
Bad Fit	fitter did not converge within 100 iterations
Invalid	fitter converged but the fit vertex is outside the detector
Bad RMS	fitter converged but the RMS of the final time-of-flight residual distribution was too large
Bad Pulse Ratio	fitter converged but the pulse ratio for the final iteration was not within the acceptable range
Bad Peak RMS	fitter converged but RMS of the time-of-flight residuals of the final iteration within the peak window $(t_n^{peak} - 10, t_n^{peak} + 5)$ was not within acceptable range

visible energy. The final antineutrino analysis is carried out as a function of positron visible energy, thus ultimately all expectations must be converted from real to visible energy. An energy-scale model which accounts for the particle- and energy-dependent non-linearities of the scintillator is described in Chapter 4. In this section we focus on how the visible energy of an event is determined.

As mentioned above the visible energy reconstruction is based on the observed hit pattern in the PMT array, including the multiplicity of hits in each PMT. A PMT is considered hit if the charge collected on the PMT is greater than 0.2 p.e. The form of the PDF connecting charge to hit-multiplicity was introduced in subsection 3.2.4. Using a model for light propagation and geometric effects in the detector, the fitter predicts the number of photoelectrons expected in each PMT as a function of E_{vis}; for a given PMT we denote this quantity $\bar{n}(E_{vis})$. Given the expected photoelectron yield in each PMT, the probability that each PMT registers a hit or not is calculated; these are then combined to form the joint likelihood for the hit/not-hit pattern observed in the PMT array.

The PMT not-hit probability is given by

$$\begin{aligned} P_i^{no-hit}(\bar{n}(E_{vis})) &= P(n_{p.e} = 0|\bar{n}) + P(n_{p.e} > 0|\bar{n}) \cap P_i(\hat{q} < \hat{q}_t|n_{p.e}) \\ &= e^{-\bar{n}} + \sum_{j>0} \frac{\bar{n}^j e^{-\bar{n}}}{j!} \int_{-\infty}^{\hat{q}_t} dq \, \frac{e^{-(q-j\cdot\mu_i)^2/2j\sigma_i^2}}{\sqrt{2\pi j}\,\sigma_i}\,, \end{aligned} \tag{3.35}$$

where $\hat{q}_t$ is the charge threshold of the analysis, and μ_i and σ_i are the mean and

width of the single-photoelectron charge distribution of PMT i, as determined with the calibration data (subsection 3.2.4). The probability that a PMT is hit and a charge $\hat{q}$ is observed is

$$\begin{aligned} P_i^{hit}(\hat{q}|\bar{n}(E_{vis})) &= P(n_{p.e} > 0|\bar{n}) \cap P_i(\hat{q}|n_{p.e}) \\ &= \sum_{j>0} \frac{\bar{n}^j e^{-\bar{n}}}{j!} \int_{\hat{q}_t}^{\infty} dq \, \frac{e^{-(q-j\cdot\mu_i)^2/2j\sigma_i^2}}{\sqrt{2\pi j}\,\sigma_i} \delta(q-\hat{q}) \,, \end{aligned} \tag{3.36}$$

where δ is the Dirac δ-function.

The best-fit value of E_{vis} is then found my maximizing the likelihood of the observed hit/not-hit pattern,

$$L(E_{vis}) = \prod_i \mathcal{P}_{avail,i} \cdot P_i^{hit} \times \prod_j \left\{ (1 - \mathcal{P}_{avail,j}) + \mathcal{P}_{avail,j} \cdot P_j^{no-hit} \right\} \,, \tag{3.37}$$

where the $\mathcal{P}_{avail,i}$ is the probability that the output of PMT i can be recorded on one of the ATWDs, the index i ranges over the PMTs that register a hit, and the index j ranges over the PMTs that register no hits during the event. For each PMT, $\mathcal{P}_{avail}$ is defined as follows:

$$\mathcal{P}_{avail} = \begin{cases} 0 & \text{if both ATWDs had a pulse in the previous } 30\mu\,\text{s} \\ 0.94 & \text{if only one of the ATWDs had a pulse in the previous } 30\mu\,\text{s} \\ 1 & \text{if none of the ATWDs had a pulse in the previous } 30\ \mu\,\text{s} \,. \end{cases} \tag{3.38}$$

This corrects for dead-time introduced when an ATWD digitizes. The probability of recording a hit in the case of only one available ATWD ($\mathcal{P}_{avail} = 0.94$) was tuned using calibration data from a ^{241}Am^{9}Be neutron source. This source sometimes emits prompt photons in association with the product neutron. The reconstructed energy of neutron-capture gammas occurring within 30μs of the accompanying prompt photon was found to be systematically lower than for captures occurring more than $30\mu\,$s after the prompt photon. This systematic effect was remedied by introducing $\mathcal{P}_{avail}$ as defined in Equation 3.38.

The ROOT [52] interface to the *Minuit* minimization routine [53] (*TMinuit*) is used to perform the fit. The fitter uses the exit status from *Minuit* to determine the fit quality. If the exit status is good the energy is tagged as a good fit. Only events with a good energy-fit are used in the antineutrino analysis, the efficiency of this restriction is estimated in Chapter 6.

It remains to describe how $\bar{n}(E_{vis})$ is determined for each PMT. The model assumes the PTF event vertex is an isotropic source of scintillation light. The photoelectron yield in the i^{th} PMT is assumed to have the following form:

$$\bar{n}_i(E_{vis}, \vec{V}, \vec{R}_i) = \alpha(i, \vec{V}, \vec{R}_i) \times E_{vis} + Y_{i,\delta} \,, \tag{3.39}$$

where $\vec{V}$ is the event vertex returned by the PTF fitter, $\vec{R}_i$ is the position of the center of the photocathode of the PMT, α is an energy independent function, and $Y_{i,\delta}$ is the dark-photoelectron yield of the PMT. This form is based on the fact that for a fixed particle type, the scintillation-light yield varies approximately linearly with real energy and that the charge collected in the PMT array varies approximately linearly with the light yield[5].

By construction $\alpha(i, \vec{V} = 0, \vec{R}_i)$ is just the photoelectron yield per MeV of visible energy determined from the ^{60}Co reference runs, $Y_{i,ref}$, which was introduced in subsection 3.2.3. For an arbitrary event position $\vec{V}$, $\alpha(i, \vec{V}, \vec{R}_i)$ is estimated by correcting $\alpha(i, \vec{V} = 0, \vec{R}_i)$ for the following geometric effects: (i) solid angle correction, (ii) light attenuation correction, and (iii) corrections for absorption of light by non-active detector elements, for example by the balloon ropes; this last correction is called the *shadowing-correction*. Thus an arbitrary α can be written

$$\frac{\alpha(i, \vec{V}, \vec{R}_i)}{Y_{i,ref}} \equiv \frac{\alpha(i, \vec{V}, \vec{R}_i)}{\alpha(i, \vec{V} = 0, \vec{R}_i)} \tag{3.40}$$

$$= \frac{\Omega(\vec{V}, \vec{R}_i)}{\Omega(\vec{V} = 0, \vec{R}_i)} \times \frac{f_{Att}(\vec{V}, \vec{R}_i)}{f_{Att}(\vec{V} = 0, \vec{R}_i)} \times \frac{S(\vec{V}, \vec{R}_i)}{S(\vec{V} = 0, \vec{R}_i)}\,, \tag{3.41}$$

where $\Omega(\vec{V}, \vec{R}_i)$ is the solid angle subtended by the PMT photocathode at the event vertex $\vec{V}$, $f_{Att}(\vec{V}, \vec{R}_i)$ is a function that describes attenuation of the scintillation light in the LS and BO, and $S(\vec{V}, \vec{R}_i)$ describes the effect of shadowing by the balloon ropes. The solid angle correction is straight forward to calculate, the shadowing correction is estimated from an analytic model of the balloon support ropes and cross-checked using a ray-tracing simulation. The attenuation model assumes exponential attenuation parametrized by two attenuation lengths,

$$f_{Att}(\vec{V}, \vec{R}_i) \propto e^{-d_{LS}/\lambda_{LS}} \cdot e^{-d_{BO}/\lambda_{BO}}\,. \tag{3.42}$$

The quantities d_{LS} and d_{BO} are the distances in LS and BO respectively along the ray joining the event vertex to the center of the photocathode of PMT i. The parameters λ_{LS} and λ_{BO} represent the attenuation lengths in each volume; these are effective parameters, rather than fixing them at their nominal values measured during detector development they are tuned to minimize systematic source-position-dependent biases in the reconstructed energy of calibration data.

3.3.3 Muon track reconstruction

High energy muons traversing the ID can produce short-lived light nuclei which are a source of background for antineutrino detection [54]. It is advantageous to

[5]It is expected that this assumption breaks down for high energy events ($E_{vis} \gtrsim 20$MeV) when high-multiplicity multi-photoelectron pulses become increasingly common. The fitting algorithm has not been calibrated in this regime.

reconstruct the tracks of muons to help tag and veto the associated backgrounds. Muons passing through the ID are identified by the large amount of charge they generate in the PMT array. If an event is tagged as a muon candidate an attempt is made to estimate the associated muon track. The muon fitter, called the *Fastest Light Fitter* [50] is described below.

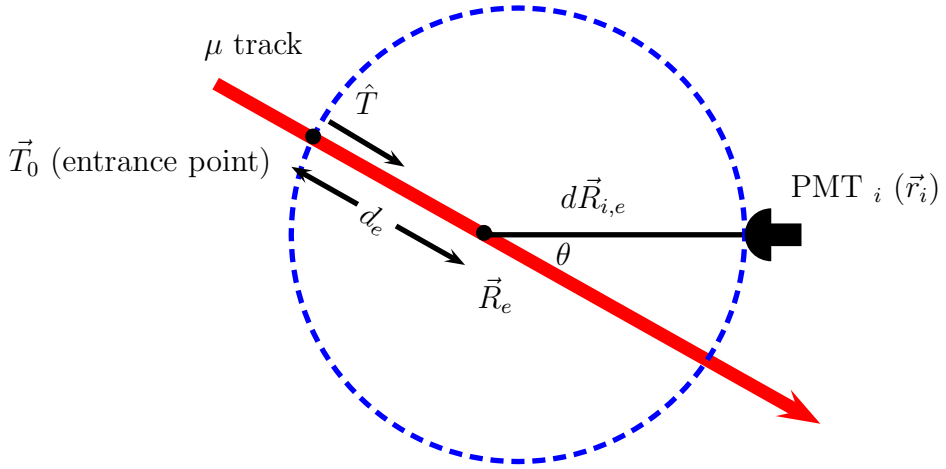

Figure 3.6: Illustration of parameters relevant for muon track reconstruction. $\vec{T}_0$ is the first point on the track in the detector; $\hat{T}$ is the unit vector describing the track direction. d_e is the distance travelled by the muon in the detector before the emission of the photon being considered, $\vec{R}_e$ is the position at which this photon is emitted, $d\vec{R}_{i,e}$ is the vector connecting $\vec{R}_e$ and the photocathode of the i^{th} PMT.

The Fastest Light Fitter takes advantage of the fact that in the limit of instantaneous detector response and ultra-relativistic muons the angle between the muon track and the path followed by the first photon to arrive at a PMT is fixed by the index of refraction of the medium. To see this, consider the situation depicted in Figure 3.6. Here each point on the muon track is assumed to be an isotropic source of scintillation photons. Ignoring delays due to the detector response, the PMT hit-time has two components: (i) the time for the scintillation photon to propagate from its emission point $\vec{R}_e$ to PMT i, denoted $TOF_{i,e}$, and (ii) the time for the muon to travel from the point where it enters the detector to the point where it causes emission of the photon in question; this time to emission is denoted $t_{i,e}$, where the subscript i specifies the PMT hit by the photon. Thus we can write the hit-time of PMT i,

$$t_{i,hit} = t_{i,e} + TOF_{i,e} = \frac{d_e}{c_\mu} + \frac{|d\vec{R}_{i,e}|}{c_{LS}}\,. \tag{3.43}$$

Referring to Figure 3.6, d_e is the distance traveled by the muon in the detector before it causes emission of the photon in question; $d\vec{R}_{i,e}$ is the vector joining the photon emission point to the PMT photocathode, the photon is assumed to travel directly along this vector; c_μ is the speed of the muon and c_{LS} is the propagation speed of photons in the LS. Although photons must also traverse the BO, a single medium with photon speed of c_{LS} is assumed for simplicity. This is a reasonable assumption since the LS and BO have similar indices of refraction. The second term in Equation 3.43 may be reparametrized in terms of the muon track

$$t_{i,hit} = \frac{d_e}{c_\mu} + \frac{|\vec{r_i} - (\vec{T_0} + d_e \cdot \hat{T})|}{c_{LS}}\,, \tag{3.44}$$

where $\vec{r_i}$ is the center of the photocathode of PMT i, $\vec{T_0}$ is the entrance point of the track in the detector and $\hat{T}$ is the unit vector describing the track direction. To find the minimum value of $t_{i,hit}$ we consider the derivative with respect to d_e:

$$\frac{\partial\, t_{i,hit}}{\partial\, d_e} = \frac{1}{c_\mu} - \frac{1}{c_{LS}} \cdot \frac{(\vec{r_i} - (\vec{T_0} + d_e \cdot \hat{T})) \cdot \hat{T}}{|\vec{r_i} - (\vec{T_0} + d_e \cdot \hat{T})|} \tag{3.45}$$

$$= \frac{1}{c_\mu} - \frac{1}{c_{LS}} \cdot \frac{d\vec{R}_{i,e} \cdot \hat{T}}{|d\vec{R}_{i,e}|} \tag{3.46}$$

$$= \frac{1}{c_\mu} - \frac{1}{c_{LS}} \cdot d\hat{R}_{i,e} \cdot \hat{T}\,. \tag{3.47}$$

We see that the minimum of $t_{i,hit}$ is realized when θ, the angle between the track and the path followed by the photon, satisfies

$$\cos\theta = \frac{c_{LS}}{c_\mu}\,. \tag{3.48}$$

Thus for ultra relativistic muons, the angle between the muon track and the path of the first-hit photon at any PMT obeys: $\cos\theta = 1/n_{LS}$, where n_{LS} is the emission-spectrum averaged index of refraction of the LS. Knowing this angle it is straightforward to calculate the first hit-time of each PMT for any trial track and compare it to the observed first-hit-time distribution in the PMT array.

3.3.3.1 Observed first-hit-time distribution

Only pulses on the 17-inch tubes are used for the muon track fit, the 20-inch tubes are not used due to their larger transit time spread. The TQs from the threshold waveform analysis are used for this reconstruction. The pulse hit time ($t_{i,hit}$) is determined from the highest-gain input, regardless of whether or not it saturates, and the T-zero correction for the appropriate ATWD is applied. Only the first pulse

found on each PMT is used in the fit [6]. A smoothing operation is applied to each hit-time, this operator corrects the time based on the average difference between the pulse time and the hit-times of pulses on neighbouring PMTs; explicitly we write

$$t'_{i,hit} = t_{i,hit} + \frac{1}{N_{Tot}} \sum_j (t_{i,hit} - t_{j,hit}) \,, \tag{3.49}$$

where the index j is over pulses satisfying $|\vec{r}_i - \vec{r}_j| < 1\text{m}$ and $|t_{i,hit} - t_{j,hit}| < 10$ ns, and N_{Tot} is the total number of pulses that enter the sum. The resulting hit-time distribution is the input for the fit. For the remainder of this section $t_{i,hit}$ will refer to this T-zero-corrected, smoothed hit-time. The pulse charge is estimated from the highest unsaturated gain, this information is only used to construct an initial guess of the track for the fit.

3.3.3.2 Fitting the track

As mentioned earlier, Equation 3.43 is only valid in the limit of instantaneous detector response. For a given track, there are many effects which can cause the first-hit-time to deviate from the expected value. These include, for example, the decay time of the scintillator, the rise time and transit time of the PMTs, and artifacts of the waveform analysis. To find the best-fit track we consider the difference between the expected first-hit-time and the observed first-hit-time

$$\Delta t_i(\vec{T}) = t^{exp}_{hit,i}(\vec{T}) - t_{hit,i} \,, \tag{3.50}$$

where $t^{exp}_{hit,i}(\vec{T})$ is the expected first-hit-time of PMT i which is a function of the muon track $\vec{T}$. The best-fit muon track is chosen as the one with the most probable Δt distribution. To realize this fit we need a PDF for Δt.

3.3.3.3 Probability density function for Δt

The PDF for Δt is assumed to have the following form:

$$\begin{aligned} P(\Delta t) =& f_p \cdot \frac{e^{-\Delta t^2/2\sigma^2_{PMT}}}{\sqrt{2\pi}\sigma_{PMT}} \\ &+ \frac{f_d}{2\tau_d} \cdot \left\{ e^{\sigma^2_{PMT}/2\cdot\tau_d} \times e^{-\Delta t/\tau_d} \times Erfc\left(\frac{\frac{\sigma^2_{PMT}}{\tau_d} - \Delta t}{\sqrt{2}\sigma_{PMT}} \right) \right\} \\ &+ (1 - f_p - f_d) \times \left\{ \frac{e^{-|\Delta t|/\tau_\delta}}{2 \cdot \tau_\delta} \right\} . \end{aligned} \tag{3.51}$$

The meaning of the parameters σ_{PMT}, f_p, f_d, τ_d and τ_δ are summarized in Table 3.3.

The first term in Equation 3.51 is due to light from the prompt component of the

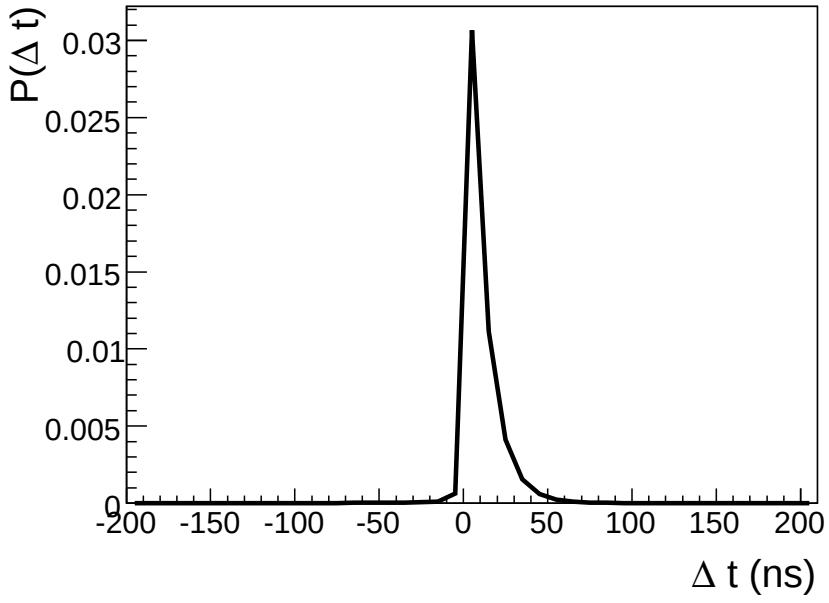

Figure 3.7: PDF for the difference between the observed first-photon hit-time and the first-photon hit-time predicted with the simple model of Equation 3.43.

Table 3.3: Description of parameters appearing in the Δt-PDF (Equation 3.51) used in muon track reconstruction.

Parameter	Description
σ_{PMT}	width of the gaussian function used to describe the combined response of the PMT, ATWD and waveform analysis. This is fixed at $\sigma_{PMT} = 1.5\,\text{ns}$ for all PMTs.
f_p	fraction of scintillation light produced by the fast component of the LS. This is fixed at $f_p = 0.5$.
f_d	fraction of scintillation light produced by the slow component of the LS. This is fixed at $f_d = 0.49$.
τ_d	characteristic time of the slow component of the LS, which is fixed at $\tau_d = 10\,\text{ns}$.
τ_δ	the model treats dark hits as being distributed in time according to an exponential function with a long characteristic time, τ_δ. This is fixed at $\tau_\delta = 40\,\text{ns}$.

LS. The form of this term is motivated by the assumptions that:

1. The prompt component is responsible for 50% of the LS emission.
2. The emission time of the prompt component is negligible.
3. Δt is due to the width of the distribution that describes the channel timing response — combining the effects of the PMT, ATWD and waveform analysis. This distribution is assumed to be gaussian; the mean is assumed to be zero as the T-zero correction has been applied and a uniform width, $\sigma_{PMT} = 1.5\,\text{ns}$, is assumed across all channels.

The second term is due to scintillation light from the delayed or slow component of the LS, which is assumed to contribute 49% of emission. In this term Δt is due to the convolution of the finite exponential response of the LS with the gaussian response of the channel which was described above. The third term accounts for possible dark hits, this term is normalized to a 1% contribution. The dark hits are assumed to be distributed in time according to an exponential function with a characteristic time $\tau_\delta = 40\,\text{ns}$ [7].

[6] The threshold waveform analysis finds only one pulse in each waveform (subsection 3.1.5). In the case where both ATWDs connected to a PMT digitize pulses only the first pulse is used.

[7] A flat distribution might have been a more intuitive choice for this random hit-time component however the form given was adopted. Since the normalization of this contribution is small the form has little impact; any slowly varying function is sufficient.

The same fitting routine is used to fit muons that pass through the LS volume (LS-muons) and muons that pass only through the BO volume (oil-muons). These two classes of events can be distinguished by the amount of charge collected in the PMT array. LS-muons generally produce an order of magnitude more charge than oil-muons since they produce both scintillation and Cherenkov light. Cherenkov photons are emitted along the path of the first-hit photon thus the same routine can be used to predict the first-hit-time distribution for both LS- and BO-muons. Since the PDF for Δt is poorly known and rather crudely estimated we use the same Δt-PDF for both the LS and BO.

The likelihood associated with the Δt distribution for each track is

$$L_{\Delta t}(\vec{T}) = \prod_i P(\Delta t_i(\vec{T}))\,, \tag{3.52}$$

where the index i ranges over the PMTs that were hit. A track is parametrized by a point on the track and a unit direction vector — five free parameters. We choose the point on the track closest to the center of the detector, which we call the *impact parameter* ($\vec{b}_\mu$), as the reference point. During fitter development it was found that many tracks were either pushed towards the center of the detector or towards the LS balloon boundary. To help counteract this, a penalty term of the following form was added to the likelihood:

$$L_{pen}(\vec{T}) = \begin{cases} \left(\dfrac{|\vec{b}_\mu(\vec{T})|}{1\,\mathrm{cm}} - 4\right)^2 & \text{if } |\vec{b}_\mu(\vec{T})|<4 \text{ cm} \\ \left(\dfrac{|\vec{b}_\mu(\vec{T})| - |\vec{b}_{\mu,max}|}{1\,\mathrm{cm}} - 4\right)^2 & \text{if } |\vec{b}_{\mu,max}| - |\vec{b}_\mu(\vec{T})|<4 \text{ cm} \\ 0 & \text{otherwise .} \end{cases}$$

Here $\vec{b}_{\mu,max}$ is the maximum track impact parameter allowed in the fit. If the muon is tagged as an LS-muon, then $\vec{b}_{\mu,max} = 650\,\mathrm{cm}$ — the radius of the LS balloon. If the muon is tagged as a BO-muon then $\vec{b}_{\mu,max} = 850\,\mathrm{cm}$ — the radius of the acrylic radon barrier. The form of this penalty is rather arbitrary but this was found to reduce the boundary effect. The best-fit track is the one that maximizes the total likelihood ($L_{\Delta t} + L_{pen}$). The maximization is done using Minuit. To begin the fit an initial guess for the track is required. The initial value for the impact parameter is taken as the charge weighted average position of the hit PMTs,

$$\vec{b}_\mu(0) = 1.62 \times \frac{\sum_i Q_i \vec{r}_i}{\sum_i Q_i}\,,$$

and the initial direction of the track is taken as the most downward pointing vector perpendicular to $\vec{b}_\mu(0)$.

Once the fit is complete the fit quality must be assessed. The track is required to pass two quality tests. The first is based on the exit status of Minuit, if it exits unsuccessfully the track is considered a bad track. If the track survives this test, a second test based on the following figure of merit ($FOM(\vec{T})$) is performed. The figure of merit is

$$FOM(\vec{T}) = \frac{1}{NDF} \sum_i \frac{\Delta t_i^2(\vec{T})}{\sigma_{PMT}^2}, \tag{3.53}$$

where NDF is the number of degrees of freedom in the fit — the number of pulses less the 5 track parameters — and σ_{PMT} is as defined in the Δt-PDF. If $FOM(\vec{T}) > 6$ the track is considered a bad fit. Tracks that pass both these tests are considered good and are used in the subsequent analysis.

Summary

In this chapter the steps to derive high-level event quantities such as position, energy, and track, from low-level waveform data were described. Events with their TQ data replaced by the best-fit position, energy and track are written to summary files called RECON files; these are the starting point for the antineutrino analysis. The performance of the reconstruction is discussed in the next chapter.

Chapter 4

Reconstruction performance and energy scale

This chapter summarizes the calibration and performance of the vertex and energy reconstruction and describes how the visible energy scale of the detector is determined.

4.1 Calibration

4.1.1 Deployment systems

Three deployment systems have been used thus far in KamLAND. From 2002-05 a simple system known as the *z-axis system* was used which could position calibration sources to an arbitrary point along the central z-axis of the detector. One shortcoming of this was the inability to study the reconstruction performance away from this axis other than with events samples from cosmogenic and intrinsic radioactivity which are less controlled than calibration event samples. The z-axis system was superceded by the so-called *4π system* [55] in 2006. This system can be operated in z-axis or full-volume mode. In the latter mode sources can be positioned to almost any point within the LS. Full-volume calibrations are a delicate and labor intensive operation, consequently the 4π was mostly operated in z-axis mode. An exhaustive full-volume calibration campaign was carried out in late 2006 and early 2007 [50]. After purification was completed in 2009 the 4π was removed in favor of a simpler system called *miniCAL* [56] which has similar functionality to the old z-axis system but surpasses it and the 4π in terms of radiopurity. This was necessary to meet the more stringent radiopurity controls imposed on equipment coming into direct contact with the LS after purification.

4.1.2 Calibration sources

The calibration sources used in KamLAND and associated visible particles[1] are listed in Table 4.1. The ^{60}Co calibrations at the detector center were performed on a $\sim$ fortnightly basis and were used to generate the reference constants for event reconstruction as described in Chapter 3. Calibrations with other sources and at other positions along the z-axis were done less frequently, this data is used to quantify position- and energy-dependent systematic biases in the reconstruction. The ^{68}Ge

Table 4.1: Calibration sources used in KamLAND with the total physical energy deposit expected in the LS [57] and the particle species associated with the events. The gamma energies from neutron capture are listed in the last two rows.

Source name	Energy (MeV)	Visible particle(s)
^{60}Co	2.506	$\gamma + \gamma$
^{68}Ge	1.022	$\gamma + \gamma$
^{65}Zn	1.115	γ
^{137}Cs	0.662	γ
^{203}Hg	0.279	γ
^{241}Am^{9}Be	$0 < E_n < 11$	n + γ
^{210}Po^{13}C	$2.5 < E_n < 7.5$	n + γ
$n + p \rightarrow d + \gamma$	2.223	γ
$n +^{12}$ C $\rightarrow^{13}$ C $+ \gamma$	4.495	γ

visible event comes from the annihilation-photons produced by positrons that stop in the source capsule, this sample is particularly important since it mimics events near the antineutrino detection threshold — the antineutrino detection method will be described in detail in Chapter 5. The other γ-sources help fix the energy scale at low energies.

The AmBe and ^{210}Po^{13}C neutron sources rely on α-n reactions; they produce neutrons with energies in the $1 \sim 10$ MeV range and provide a sample of prompt-delayed coincidence (PDC) events. As described in Chapter 5 this coincidence event structure is important for tagging antineutrino candidates. In the case of α-n reactions the prompt event comes from neutron scattering on protons and carbon nuclei in the LS. Elastic scattering on protons is the dominant process and results in a continuous prompt spectrum with energy up to about 4 MeV for AmBe and ^{210}Po^{13}C . If the

[1]Visible particles are those that escape the source and deposit enough energy in the scintillator to trigger the DAQ. Source capsules were made from 2 mm thick stainless-steel which stops short range radiation: $e^{\pm}, \alpha$. Only penetrating particles — neutrons and γ-rays — escape the capsule and deposit energy in the scintillator.

Table 4.2: Best-fit vertex resolution parameters (Equation 4.1) for each of the data periods.

Parameter	T I	T II	T III
$\sigma_{R,0}$(mm)	118 ± 1	118 ± 3	92 ± 4
$\sigma_{R,1}$(mm)	80 ± 1	83 ± 5	127 ± 6

heavy product of the α-n reaction is produced in an excited state, prompt radiation from the excited nuclear state also contributes to the prompt event. The delayed event comes from neutron capture on protons or ^{12}C. The ^{210}Po^{13}C source was not deployed regularly, it was constructed and deployed in 2006 specifically to study the ^{13}C$(\alpha, \mathrm{n})^{16}$O reaction which is one of the largest backgrounds to detection of $\bar{\nu}_e$with energies below $\sim 4\,$MeV in KamLAND [58]. This will be discussed more in Chapter 6. For now we focus on using the calibration data to measure the reconstruction performance.

4.1.3 Reconstruction performance

The calibration runs provide a sample of events with well known positions and energies with which to quantify the performance of the reconstruction processes. Figure 4.1 shows the difference between the mean reconstructed z-position of the source events and the nominal z-position of the source determined from the deployment system. The systematic error on the nominal position of the source is estimated to be 2 mm. The difference between the reconstructed and nominal position is found to be less than 30 mm for the positions probed along the z-axis. A systematic bias of similar magnitude was found with the 4π off-axis calibrations [50]. The vertex resolution is also determined from the calibration data. A gaussian resolution function with a width, σ_R, of the form

$$\sigma_R^2 = \sigma_{R,0}^2 + \sigma_{R,1}^2 / E_{vis}[\mathrm{MeV}]\,, \tag{4.1}$$

is assumed. The best-fit values of ($\sigma_{R,0}$, $\sigma_{R,1}$) are determined by fitting Equation 4.1 to the distribution of resolutions measured from each calibration run. The results are summarized in Table 4.2. The vertex resolution at 1 MeV is $\sim 200\,$mm.

Figure 4.2 shows the variation of the mean reconstructed energy for each source as a function of the source z-position for all the z-axis calibration data taken during T-I, T-II and T-III. The spread in energies at a fixed position is due to time variation in the reconstruction. For periods T-I and T-II, the systematic variation with position has a roughly symmetric 'M' shape and has been dubbed the 'M-bias'. The shape of the bias is somewhat different for period T-II, which is the period between the first and second purification cycles. The change is due to variations in the quality and concentration of PPO in the LS which occurred as it was cycled through the purification system. This

Figure 4.1: Systematic bias of position reconstruction vs z-position for all z-axis deployments performed during T-I, T-II and T-III. For each calibration, Z_{fit} is the mean reconstructed z-position of the source events, Z_{nom} is the nominal source position determined from the deployment system.

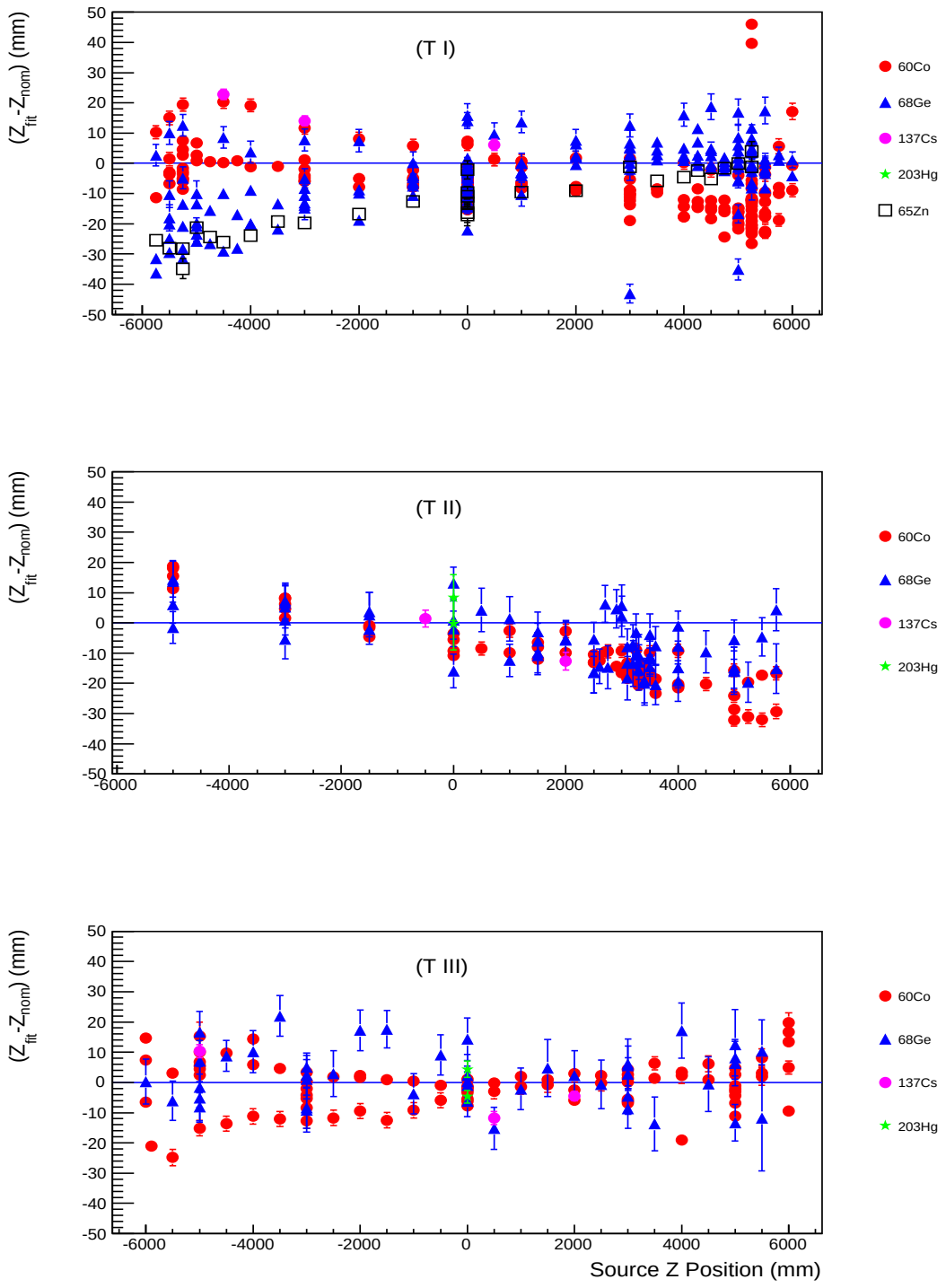

gave rise to a position dependence of the LS light yield; the volume with $Z > 2000\,\text{mm}$ was cycled twice and the photoelectron yield per MeV in this volume was found to be $\sim 15\%$ lower than the yield in the region with $Z < 2000\,\text{mm}$, where the LS had been processed once. The T-II bias has similar magnitude to the T-I bias, thus it was decided not to implement position-dependent reference photoelectron yields in the reconstruction but rather to include it in the energy scale systematic error. With the experience of the first purification campaign much more consistent control of the LS quality and uniformity was achieved in subsequent campaign.

4.2 Energy scale model

4.2.1 Overview of the model

The energy scale chosen for the neutrino oscillation analysis is the visible-energy scale. By visible energy one means the reconstructed energy returned by the fitting tools rather than the real or physical energy [2] deposited in the LS during the event. As discussed in Chapter 3, the visible energy output by the fitter is, by construction, an approximately linear function of the photoelectron yield with an offset for dark photoelectrons. The relationship between LS-photon yield, the PMT photoelectron yields, and the real energy of photons from ^{60}Co is fixed by the reference constants calculated from ^{60}Co center-calibrations. For events that reconstruct away from the centre of the detector, the fitter corrects for the expected attenuation and geometric effects to remove most of the position dependence; variations on the $\sim 3\%$ level remain and are evident in Figure 4.2. The relationship between the photoelectron yield of an arbitrary particle to the photoelectron yield of ^{60}Co photons is described by the energy scale model [3].

The effects considered in the energy scale model are quenching [4] and energy loss through Cherenkov radiation. These corrections are estimated in [59], using the EGSnrc simulation utility [60]. The real-to-visible energy conversion function is constructed to have the following form:

$$\frac{\langle E_{vis}(i,E)\rangle}{E} = A_0 \times \left(1 + \delta^i_q(E,k_B) + k_c\delta^i_c(E) + k_0\delta_0(E)\right), \tag{4.2}$$

where the index i runs over each of the particle types considered: α, $\beta^{+/-}$, γ and proton; E is the real energy deposited by the particle in the LS; and $\langle E_{vis}\rangle$ is the mean visible energy resulting from E. The parameter A_0 represents the overall scale

[2] The term real energy refers to the energy deposited by a particle unaltered by any detection or reconstruction effects.

[3] Arbitrary, but of course it must be within in the limits of the model.

[4] Quenching refers to the dependence of scintillation yield of a particle on its ionisation density, generally particles with a higher ionisation density yield fewer scintillation photons per MeV than particles with lower ionisation density

Figure 4.2: Systematic bias of energy reconstruction vs z-position for all z-axis deployments performed during TI, TII and TIII. For each calibration E_{fit} is the mean reconstructed energy of the source events, E_{nom} is a reference energy and is taken as the mean of E_{fit} from the centre calibrations for each source.

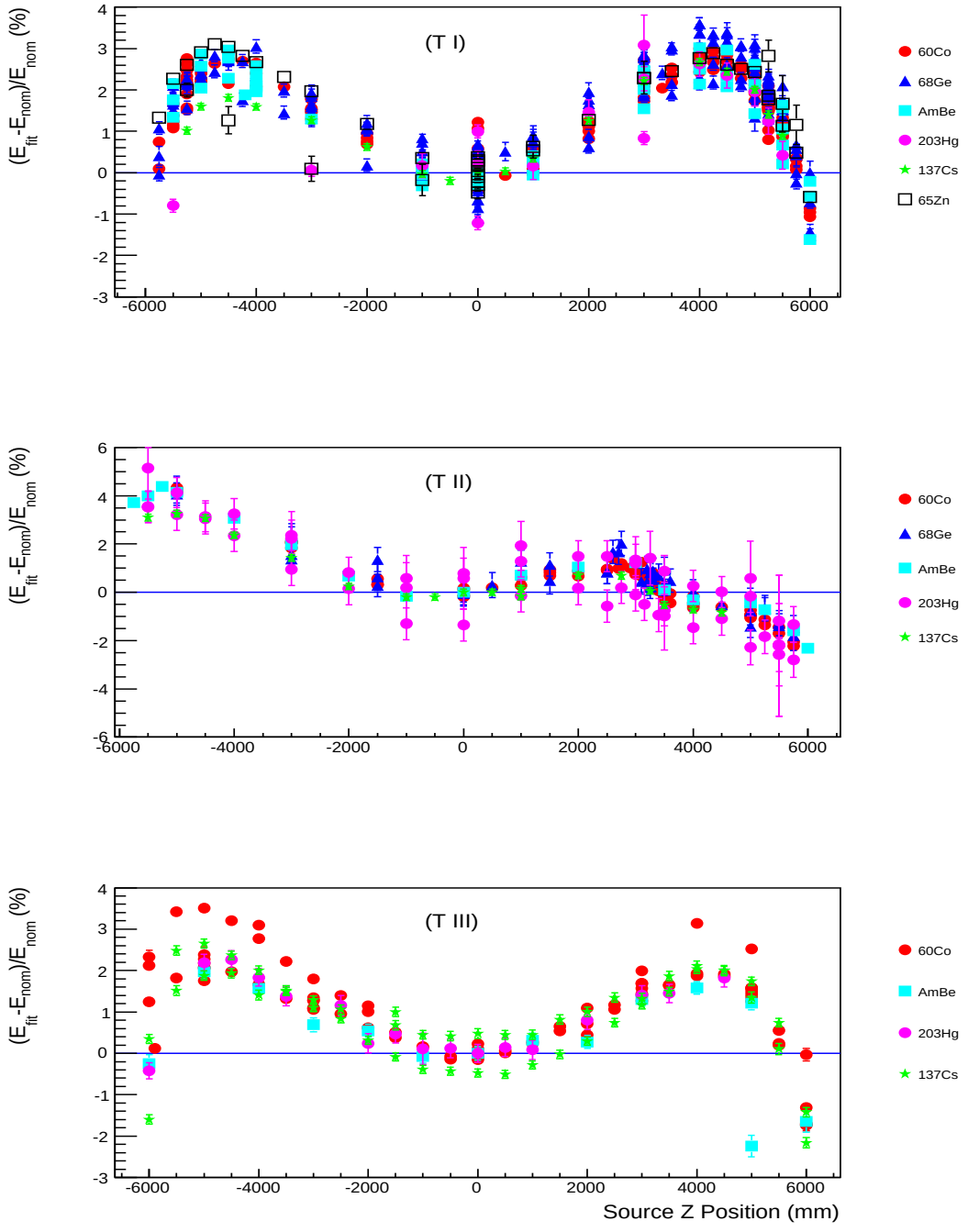

of the conversion. The function δ_q accounts for the quenching effect and is calculated for each particle using a *first order Birks quenching* model which assumes the following relationship between the scintillation light yield of a particle and its real energy deposit:

$$\frac{dL}{dx} \propto \frac{dE/dx}{1 + k_B dE/dx}\,. \tag{4.3}$$

Here dL/dx is the scintillation light per unit length, dE/dx is the stopping power of the particle and k_B is a particle-independent, scintillator-dependant constant, called *Birk's constant*, which must be determined for the KamLAND scintillator. The stopping power for each particle is taken from the SRIM utility [61]. The function δ_c is a particle-dependent function which describes the energy lost through Cherenkov radiation and k_c parametrizes the fraction of Cherenkov light that contributes to the photoelectron yield. Thus k_c is a particle-independent parameter but depends on the efficiency for Cherenkov light to be absorbed and re-emitted as scintillation light and the photocathode efficiency integrated over the Cerenkov spectrum transmitted to the PMTs. The function δ_0 and constant k_0 account for artificial energy-loss due to the tracking threshold of the simulation. The conversion function (Equation 4.2) is precalculated on a grid of the energy-scale parameter space spanned by (A_0, k_B, k_c, k_0) and stored in a database whence it can be conveniently retrieved for use in the oscillation analysis.

4.2.2 Energy resolution

The final step in the real to visible energy conversion is to apply the detector energy resolution to $\langle E_{vis} \rangle$. A gaussian resolution with a width, σ_E, given by

$$\sigma_E^2 = \sigma_{E,0}^2 + \sigma_{E,1}^2 \cdot E_{vis}[\mathrm{MeV}]\,, \tag{4.4}$$

is assumed. The first and second terms parametrize the contribution from fluctuations in (i) the dark photoelectron yield and (2) the photoelectron yield per MeV of energy deposited. The resolution at several values of E_{vis} was determined from the γ-calibration sources, Equation 4.4 was then fit to the distribution of these resolutions to determine the best-fit values of $\sigma_{E,0}$ and $\sigma_{E,1}$ for each of the three data periods. A systematic error of 2.5% was added to improve the χ^2 of the full fit. This additional error accounts for the time and position variation of the energy resolution. The result is summarized in Table 4.3. A deterioration of the energy resolution is evident in T-II and T-III, this is due to a reduction in scintillator light yield that occurred during successive purification cycles.

4.2.3 Energy scale parameters

The values of energy-scale parameters are determined from a joint fit of Equation 4.2 to the calibration data and events from cosmogenic and intrinsic-α radioactivity.

Table 4.3: Best-fit energy resolution parameters (Equation 4.4) for each of the data periods.

Parameter	T-I	T-II	T-III
$\sigma_{E,0}$(MeV)	0.0056 ± 0.0008	0.0186 ± 0.0003	0.0177 ± 0.0007
$\sigma_{E,1}$(MeV)	0.0726 ± 0.0001	0.0755 ± 0.0001	0.0807 ± 0.0002

Table 4.4: Best-fit energy scale parameters for each of the data periods.

Parameter	T-I	T-II	T-III
A_0	1.106 ± 0.038	1.08 ± 0.04	1.10 ± 0.05
k_B (g/cm^2/MeV $\times 10^{-2}$)	1.08 ± 0.06	1.07 ± 0.09	1.05 ± 0.08
k_0	0.74 ± 0.18	0.84 ± 0.18	0.63 ± 0.25
k_C	0.24 ± 0.09	0.28 ± 0.11	0.22 ± 0.12

Alphas from ^{212}Po and ^{214}Po decays can be tagged by their coincidence with the preceding ^{212}Bi and ^{214}Bi decays respectively. The α samples are important to constrain k_B since the quenching effect is largest for α particles. The spallation product ^{12}B is a source of electrons with energy up to 14 MeV which can be tagged by coincidence with muons [62]; ^{12}B candidates are included to help constrain the Cherenkov parameter of the model. Although the effect of the energy resolution can be decoupled for the discrete (α ,γ) sources it is difficult to do this for the ^{12}B sample. Therefore, when the joint fit is performed, $\sigma_{E,0}$ and $\sigma_{E,1}$ are included as free parameters but are constrained with a gaussian-penalty to the previously determined values. The best-fit values for the energy scale parameters are summarized in Table 4.4.

4.3 Summary and results

The best-fit energy scale conversion function (equation 4.2) for photons is shown in Figure 4.3 together with the conversion factors determined from the γ -calibration data. For events with multiple particles the conversion has to be applied to each particle individually and then summed. For this reason data for ^{60}Co appears at $E_{real} = 1.25$ MeV which is the average energy of the two photons in the event; the data for ^{68}Ge appears at $E_{real} = 0.511$ MeV. The conversion function for alphas and the conversion factors measured for intrinsic ^{210}Po, ^{212}Po and ^{214}Po α-samples are shown in Figure 4.4. Figures 4.5 and 4.6 show the conversion function for positrons and electrons respectively. Finally, Figure 4.7 shows the tagged- ^{12}B candidate spectrum for T-I together with the predicted visible energy spectrum.

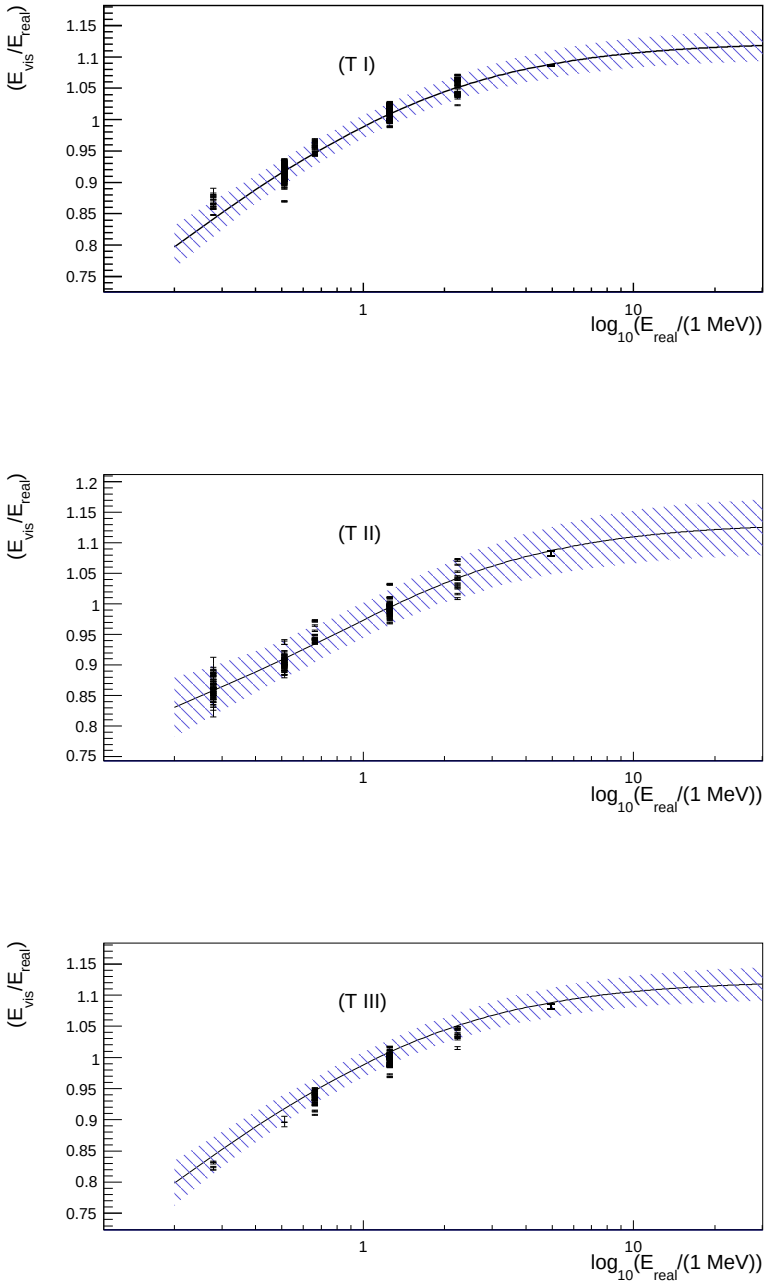

Figure 4.3: Energy scale conversion function for photons. The shaded band represents the width of the conversion factor distribution obtained by simultaneously and independently varying the energy-scale parameters within 3σ of the best-fit values. The data points are the conversion factors determined from each z-axis calibration run; ^{60}Co and ^{68}Ge appear at $E_{real} = 1.25\,MeV$ and $0.511\,MeV$ respectively.

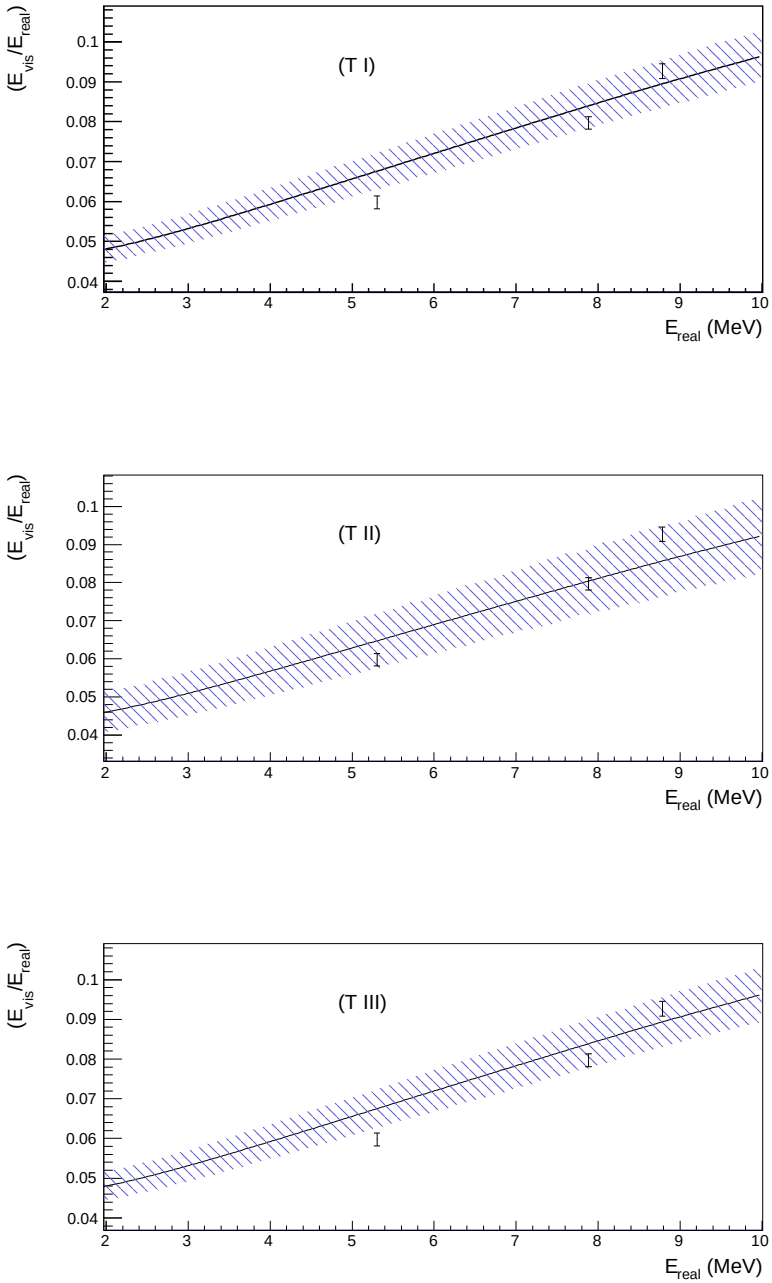

Figure 4.4: Energy scale conversion function for alphas. The meaning of the shaded band is given in the caption of Figure 4.3. The data points are the conversion factors determined from the ^{210}Po, ^{212}Po and ^{214}Po alpha samples.

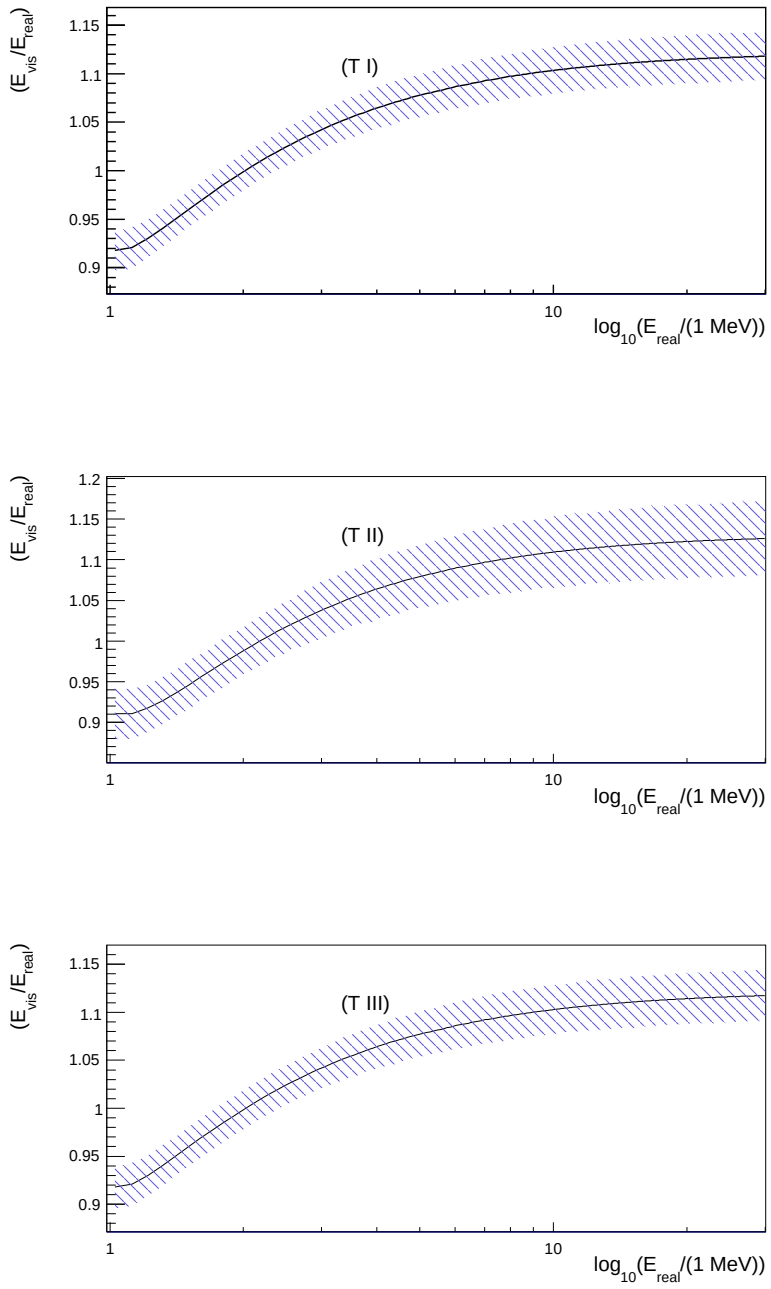

Figure 4.5: Energy scale conversion function for positrons. The meaning of the shaded band is given in the caption of Figure 4.3. By convention the positron visible energy is defined to include the contribution from the annilihation-γs, therefore the function is only defined above 1.022 MeV.

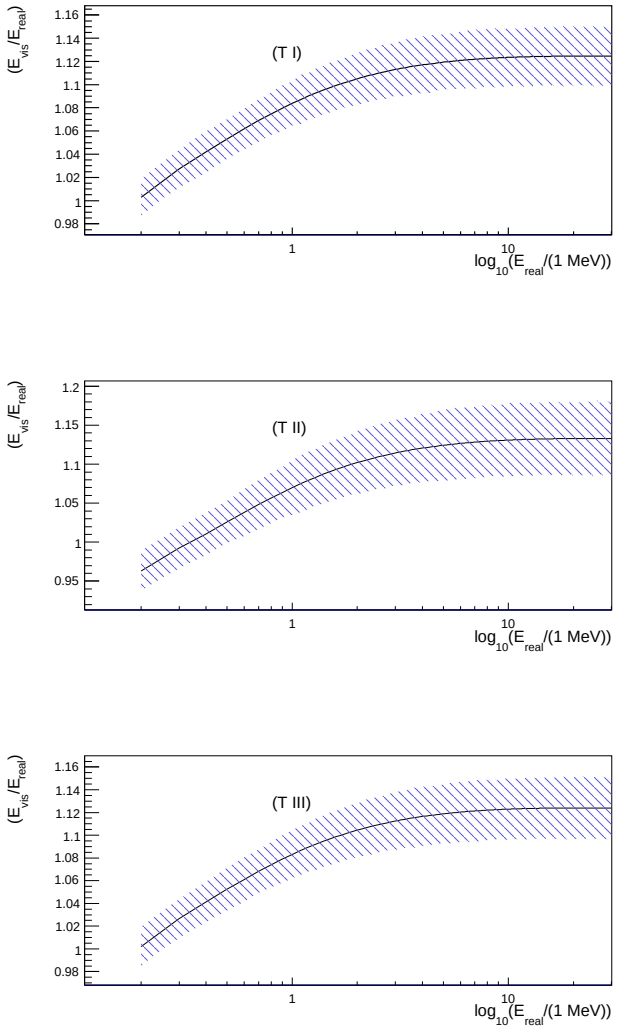

Figure 4.6: Energy scale conversion function for electrons. The meaning of the shaded band is given in the caption of Figure 4.3.

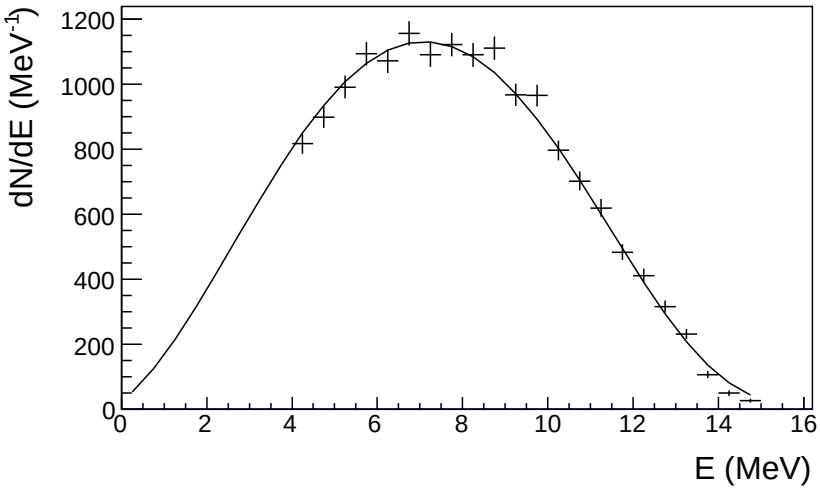

Figure 4.7: Fit of the ^{12}B visible energy spectrum predicted with the energy scale model to the ^{12}B candidate event spectrum for T-I data, $\chi^2/\mathrm{dof} = 23/17$.

Chapter 5

Antineutrino detection and sources at KamLAND

For the data set under study, the flux of antineutrinos at KamLAND is dominated by $\bar{\nu}_e$produced at nearby nuclear reactors. This chapter covers the antineutrino detection method at KamLAND and how the expected reactor-$\bar{\nu}_e$spectrum is determined.

5.1 Antineutrino detection via inverse beta decay

The inverse beta decay reaction,

$$\bar{\nu}_e + p \rightarrow e^+ + n\,, \tag{5.1}$$

is the most favorable reaction for detecting $\bar{\nu}_e$at KamLAND. For the energies typical of reactor antineutrinos this is by far — by almost 100 fold — the most probable interaction in the LS. Furthermore, the prompt-delayed coincidence (PDC) pair signature of the positron and neutron offers excellent background suppression. Each PDC pair is described by the set of parameters $\overrightarrow{PDC} = (E_{\rm p}, E_{\rm d}, \vec{R}_{\rm p}, \vec{R}_{\rm d}, \Delta R, \Delta T, t)$, Table 5.1 summarizes the meaning of this notation. The prompt event of the pair is due to the positron which quickly desposits its kinetic energy in the LS and annihilates on an electron. The neutron undergoes radiative capture in the LS, the mean capture time is $207.5\,\mu s$ (Chapter 6) and the radiated photon produces the delayed event. In 99.5% of cases the neutron captures on a proton, $n + p \rightarrow d + \gamma(2.223\,\mathrm{MeV})$.

The inverse beta decay cross section is well known, the calculation by Vogel et al. [63, 64] which includes recoil corrections of order $1/M$ (M is the nucleon mass) is plotted in Figure 5.1. For the energy range shown, the function includes all corrections greater than 0.2%. The energy of the incident antineutrino ($E_{\bar{\nu}_e}$) is related to the

Table 5.1: Description of parameters that define a prompt-delayed coincidence pair.

Variable	Description
$E_{\rm p}$	Prompt event energy
$\rm E_d$	Delayed event energy
$\vec{R}_{\rm p}$	Prompt event position
$\vec{R}_{\rm d}$	Delayed event position
ΔR	Distance between prompt and delayed events
ΔT	Time between prompt and delayed events
t	Global time assigned to PDC event pair

positron energy (E_{e^+}) by

$$E_{\bar{\nu}_e} = E_{e^+} + \Delta M_{np} + \delta E_n \quad (5.2)$$
$$\simeq E_{\rm p} + \Delta M_{np} - m_e\,, \quad (5.3)$$

where ΔM_{np} is the difference between the neutron and proton mass (1.293 MeV), m_e is the electron mass, δE_n is the recoil energy of the neutron, and $E_{\rm p}$ is the prompt event energy which we define to include the positron kinetic energy and the energy of both annihilation photons. The division of the available energy between the final state particles depends on the angular correlation between the incoming antineutrino and the outgoing positron. In KamLAND this angular correlation cannot be measured and this in principle degrades the resolution on $E_{\bar{\nu}_e}$. However, the effect is very small, δE_n is $\mathcal{O}$(10keV); ultimately the resolution on $E_{\bar{\nu}_e}$ is dominated by the reconstruction resolution of $E_{\rm p}$ (Chapter 3). Assuming protons are at rest in the lab frame, the threshold for the inverse beta decay reaction is 1.806 MeV.

5.2 Reactor sources

It is convenient to divide the reactor sources into three categories according to how well their $\bar{\nu}_e$spectrum is determined. The first category (R1) consists of commercial nuclear power reactors operating in Japan. The operators of these reactors kindly provide detailed data, such as thermal power output, fuel-enrichment, and enriched-fuel volume ratios, to the KamLAND collaboration which allows us to predict the $\bar{\nu}_e$spectrum of these reactors with a systematic error of $\sim 3.5\%$. The second category (R2) is commercial power reactors operating in Korea, the spectrum of these reactors is estimated from publicly available data gathered by international regulatory agencies [65]. We assign a $\sim 10\%$ systematic error to this estimate. The final category (R3) is all other reactors, including distant power reactors and research reactors operating

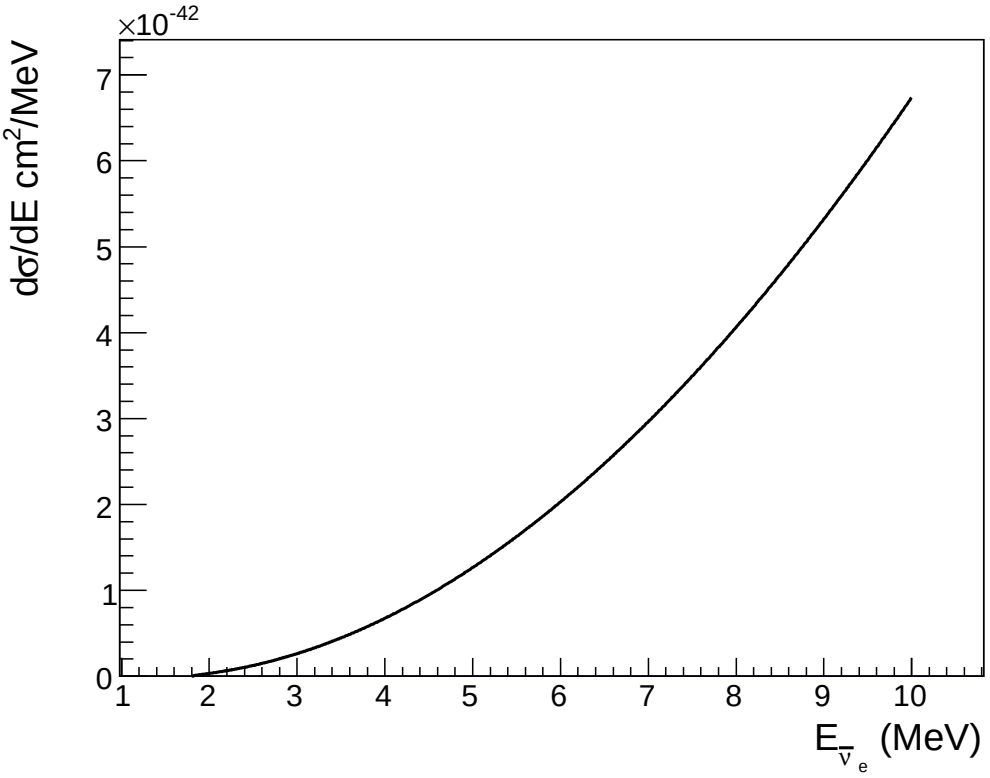

Figure 5.1: Inverse beta decay cross section [63].

in Japan and elsewhere. These are characterized by their specifications and publicly available data, we assign a 50% uncertainty to the R3 contribution. Although the uncertainties on R2 and R3 are relatively large their contributions to the flux at KamLAND, averaged over the data set, are only 3.4% and 1.0% respectively, thus they do not add significantly to the overall source uncertainty.

5.3 Calculation of the antineutrino spectrum of a reactor

Reactors are a very intense antineutrino source, approximately 10^{20} $\bar{\nu}_e$from β decay of fission products are produced per GJ thermal output. Only $\sim 25\%$ of these have energy above the inverse beta decay threshold [66]. In the following sections the steps to calculate the reactor antineutrino spectrum at KamLAND are described, we focus only on the part of the spectrum above the inverse beta decay threshold.

The antineutrino rate above threshold per unit energy at time t of a reactor is

$$\frac{d\mathcal{N}(E,t)}{dt} = \mathcal{F}(t)\sum_j f_j(t)\hat{S}_j(E,t) + \delta_{EQ}(E,t,dt_{\mathrm{turn-on}})\,. \tag{5.4}$$

The first term describes the contribution from fission products that have reached equilibrium. The function $\mathcal{F}(t)$ is the total fission rate at time t, the index j labels the constituent isotopes of the reactor fuel, $f_j(t)$ is the fraction of fissions at time t due to isotope j, and $\hat{S}_j(E)$ is the $\bar{\nu}_e$spectrum per fission of isotope j. The index j runs over the four isotopes: ^{235}U, ^{238}U, ^{239}Pu and ^{241}Pu which produce more than 99.9% of fissions in a typical reactor [67]. The term δ_{EQ} is a correction for out-of-equilibrium fission products, the importance of this term depends on how long the reactor has been running ($dt_{\mathrm{turn-on}}$).

5.3.1 Spectrum normalization- $\mathcal{F}(t)$

If the fission fractions are known the fission rate can be determined from the thermal power output of the core (P_{Th})

$$P_{\mathrm{Th}}(t) = \mathcal{F}(t)\sum_j f_j(t)\cdot\Delta E_j, \tag{5.5}$$

where ΔE_j is the energy released per fission of fuel isotope j. The quantities f_j and ΔE_j can be determined rather precisely, thus the uncertainty of $\mathcal{F}(t)$ is dominated by the uncertainty of P_{Th}. For R1 reactors P_{Th} is determined from thermal power output measurements taken regularly by the reactor operators, the reported uncertainty of these measurements is 2%. For R2, P_{Th} is estimated from the electrical power output reported to regulatory bodies [65], the uncertainty in converting electrical power to thermal power is $\sim$ 10% [67]. An uncertainty of 50% is assumed for the R3 contribution.

5.3.2 Fission fractions - $f_j(t)$

Fission fractions can be calculated using detailed simulations that follow the microscopic processes in the core. Such detailed simulation of all 56 R1-cores is impractical, instead the collaboration adopted a simplified core model [68]. In [68] the authors use the results from detailed simulations of several reference cores to develop an effective model parametrized by the core burnup, fuel enrichment and enriched-fuel volume fractions to predict the time evolution of the fission rate of each fuel. As shown in Figure 5.2 the predictions for the fission rates using this model versus a detailed core simulation agree to within 1% after the third fuel cycle, the agreement is worse (2%) for cores in earlier fuel cycles. A fuel cycle typically lasts for one year, since most R1 cores started operation many years before KamLAND data taking began we adopt

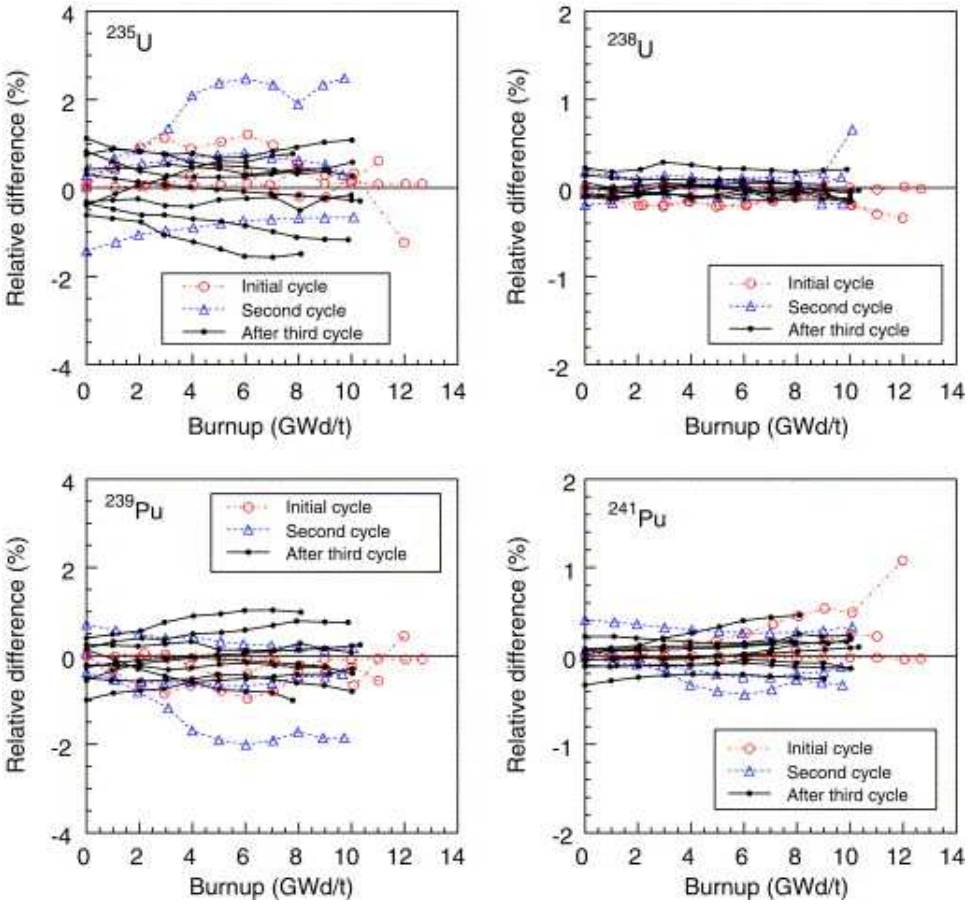

Figure 5.2: The relative difference between the fission rate of the four main reactor fuels predicted by the simplified reactor model [68] and by a detailed simulation for a number of reference cores. The set of reference cores included cores in their first, second and third or later fuel cycles. The agreement between the simplified model and detailed simulation is best for cores at or beyond the third fuel cycle. The figure was reproduced with permission from [68].

1% as the additional uncertainty of the simplified model over the detailed simulation. The uncertainties of detailed core simulations were studied in [69]. Based on the difference between simulated and measured isotopic composition of the spent fuel the authors estimate an uncertainty of 0.9% in the fission fraction predictions. For R2 cores, detailed operation data is not available. The fission fraction as a function of burnup for a 'typical reactor' was assumed for these cores. The estimates for f_j based on detailed simulation and typical-reactor data agree to within 10%.

5.3.3 Antineutrino spectrum per fission

The problem of calculating the antineutrino spectrum per fission for reactors has a long history dating back to 1949 [66]. The approaches in the literature fall into two categories: (i) the *direct approach* and (ii) the *semi-empirical approach*.

In the *direct approach*, fission-yield and nuclear-beta-decay data are used to directly calculate the sum of the antineutrino spectra of all β decay branches in the decay chain of each fission product. Unfortunately the decay schemes of many relevant nuclei are not completely known and nuclear models, with often large uncertainties, must be used to supplement the nuclear data. The $\bar{\nu}_e$spectra calculated by Vogel et al. [70] are an example of the direct approach and have uncertainties of $\sim 10\%$ (Figure 5.3).

In the *semi-empirical approach*, a particular fuel isotope is caused to fission by exposing it to an appropriate neutron flux for approximately one day. This is enough time for most of the fission products to come to equilibrium. The spectrum of electrons emitted from the sample is then measured and this β spectrum is converted to an antineutrino spectrum. While this approach circumvents incompleteness of the nuclear decay data, the procedure for converting the total β-spectrum of many decays to a total $\bar{\nu}_e$-spectrum is not unique and introduces its own uncertainties.

The spectra for ^{235}U [71], ^{239}Pu and ^{241}Pu [72] have been estimated following the semi-empirical approach. For each fuel, a sample was exposed to a thermal neutron flux at the ILL research reactor and the spectrum of β's emitted from the irradiated sample was measured, yielding a total β spectrum $S_{Tot,\beta}(Y)$, where Y specifies the irradiated fuel-type. The conversion procedure involves fitting a series of 30 virtual allowed-beta-decay spectra to $S_{Tot,\beta}(Y)$, yielding a set of 30 Q-values and branch-intensities (I):

$$S_{Tot,\beta}(Y) \longrightarrow \begin{cases} \delta S_{1,\beta}(Q_1, I_1, Y), \\ \quad\vdots \\ \delta S_{i,\beta}(Q_i, I_i, Y), \\ \quad\vdots \\ \delta S_{30,\beta}(Q_{30}, I_{30}, Y)\ . \end{cases} \tag{5.6}$$

Each virtual beta-spectrum $\delta S_{i,\beta}$ is converted to an antineutrino spectrum,

$$\delta S_{i,\beta}(Q_i, I_i, Y) \longrightarrow \delta S_{i,\bar{\nu}_e}(Q_i, I_i, Y)\,. \tag{5.7}$$

Then the total antineutrino spectrum from the fission products of fuel Y is taken as

$$S_{Tot,\bar{\nu}_e}(Y) = \sum_{i=1}^{30} I_i \cdot \delta S_{i,\bar{\nu}_e}(Q_i, I_i, Y)\,. \tag{5.8}$$

To first order, the conversion (Equation 5.7) is based on the assumption that each branch has an allowed shape. However there are corrections to this shape that depend on the identity of the initial and final state nuclei, for example forbidden-ness corrections, radiative corrections, and finite nuclear size corrections [73]. Since the branches are imaginary, the decomposition (Equation 5.6) contains no information about the identity of parent and daughter nuclei; it is not obvious what properties to give the virtual fission fragments so that they reproduce the effects of the physical fission fragments in the final spectrum. The authors of [71] and [72] use corrections based on calculations averaged over the known physical fission fragments. Based on simulation they estimate the uncertainty introduced by the conversion procedure is $\sim 2.7\%$ (Figure 5.3) for $2\,\mathrm{MeV} \lesssim \mathrm{E}_{\bar{\nu}_e} \lesssim 8\,\mathrm{MeV}$. The conversion algorithm used as well as some general perspectives on the semi-empirical approach are discussed in detail in [73].

For the KamLAND analysis the reactor spectrum (Equation 5.4) is evaluated using a semi-empirical spectrum for ^{235}U [71], ^{239}Pu, and ^{241}Pu [72]; a direct-approach estimate for ^{238}U [70] is used. These spectra and their uncertainties are shown in Figure 5.3. To date there is no semi-empirical estimate of the ^{238}U $\bar{\nu}_e$-spectrum as the total electron spectrum of the fission fragments has not been measured; however work is underway to remedy this [74]. The choice of which approach to adopt for each fuel was investigated by the Bugey-3 short-baseline (15 m, 40 m) reactor neutrino experiment [27]. This collaboration recorded a large number (1.2×10^5) of inverse beta decay events. Figure 5.4, reproduced from [27], shows the ratio of the measured positron spectrum for inverse beta decay candidates to the positron spectrum predicted by their detector simulation for three different input models of the incident $\bar{\nu}_e$spectrum. The upper two panels, Model 1 [75] and Model 2 [76], use the direct-approach. The bottom panel, Model 3, uses the semi-empirical approach for ^{235}U [71], ^{239}Pu and ^{241}Pu [72], and the direct-approach calculation of [75] for ^{238}U, this is the choice adopted for the KamLAND analysis. It is evident that the Bugey-3 data favors this choice.

The final term in Equation 5.4, δ_{EQ}, is a correction for long-lived, out-of-equilibrium fission products such as $^{90}\mathrm{Sr}\,(T_{\frac{1}{2}} = 28.8\,\mathrm{yr})$, $^{106}\mathrm{Ru}\,(T_{\frac{1}{2}} = 372\,\mathrm{d})$, and $^{144}\mathrm{Ce}\,(T_{\frac{1}{2}} = 295\,\mathrm{d})$. These are not included in the spectra per fission determined by the semi-empirical approach since the total β-spectrum in each case was measured after a

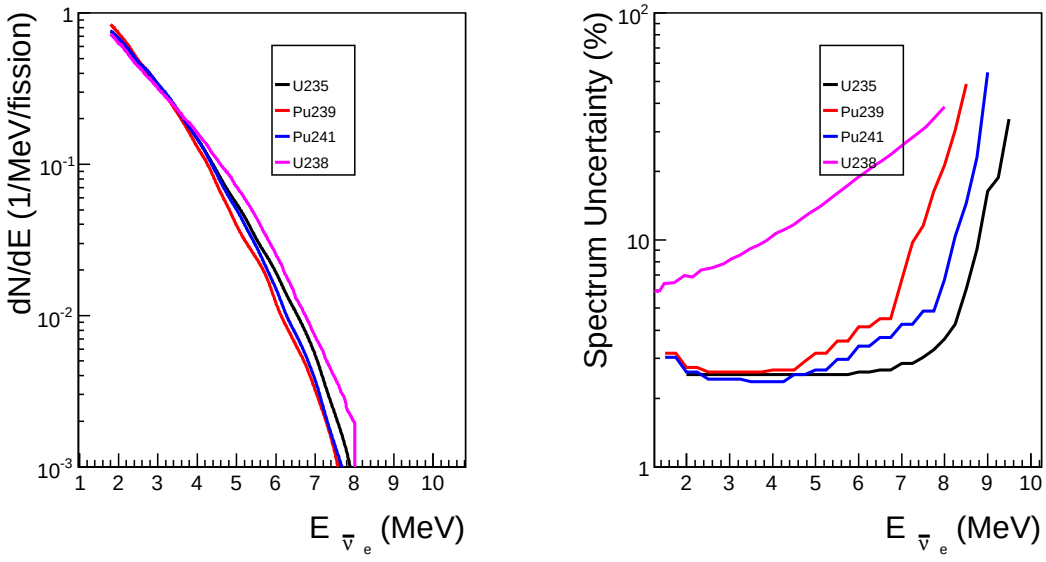

Figure 5.3: Antineutrino spectra and uncertainties. The left panel shows the antineutrino spectrum per fission for each of the four fuel isotopes. The $1\,\sigma$ spectrum uncertainty is shown in the right panel.

relatively short ($\sim$ 1 day) exposure. To estimate the contribution to the $\bar{\nu}_e$rate at any particular time, the history of the reactor operation and spent fuel storage over several years needs to be considered. From the data released by the R1-reactor operators we estimate that out-of-equilibrium fission products contribute $(0.6 \pm 0.3)\%$ of the total flux above the inverse beta decay threshold. The uncertainty of this quantity is large (50%) since the operation data prior to the beginning of KamLAND is not available and the final locations of spent fuel after the initial $\sim$ 4 years of storage at the reactor site is not known by the KamLAND collaboration. Almost all the fission products come into equilibrium within approximately 10 hours of reactor turn-on, the out-of-equilibrium fission products only affect the spectrum for $E_\nu < 3.5\,\mathrm{MeV}$ [77].

5.3.3.1 New developments related to the antineutrino spectra per fission

Recently the question of the antineutrino spectra per fission has been revisited by Mueller et al [78]. Their approach can be considered a hybrid of the direct and semi-empirical approaches outlined above. They used up-to-date nuclear beta-decay databases to directly calculate, to the extent possible, the total beta spectrum expected from the fissions of each reactor fuel. For each fuel Y, we label this theoretical

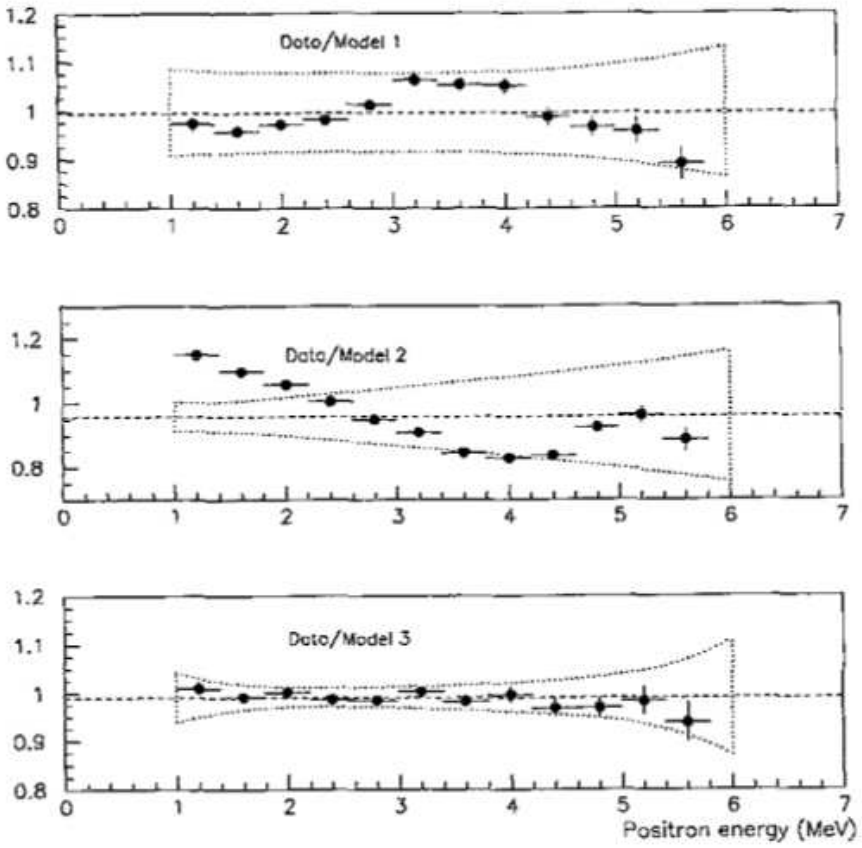

Figure 5.4: Ratio of the positron spectrum from inverse beta decays measured at Bugey-3 to the prediction of the detector simulation for three different input $\bar{\nu}_e$-spectrum models. The errors on the data points are due to the statistical error on the measured and simulated positron spectra. The dotted lines are the quadratic sum of the model uncertainty and deformation when the the energy scale in the detector simulation is modified by $1\,\sigma$. Model 3, described in the main text, is similar to that adopted for the KamLAND analysis. This figure is reproduced with permission from [27].

β-spectrum $S_{DB,\beta}(Y)$ and we write it as

$$S_{DB,\beta}(Y) = \sum_i I_{i,DB}(Y) \sum_{j(i)} w_j \delta S_{j,DB,\beta}(Q_{j,DB}, [A_j, Z_j]_{1,DB}, [A_j, Z_j]_{2,DB}) \,, \tag{5.9}$$

where the subscript DB is used to emphasize the spectrum is constructed from nuclear databases, the index i labels the fission fragments of Y, $I_{i,DB}$ is the relative yield of fragment i, the index j labels the decay branches of fragment i, w_j is the relative intensity of branch j, $[A_j, Z_j]_{1,DB}$ and $[A_j, Z_j]_{2,DB}$ identify the initial and final nucleus of the branch. They then subtract this database-based spectrum from the measured total beta spectrum to produce a residual spectrum:

$$\Delta S_{Res,\beta}(Y) = S_{Tot,\beta}(Y) - S_{DB,\beta}(Y) \,. \tag{5.10}$$

This residual spectrum is then decomposed into 5 virtual branches:

$$\Delta S_{Res,\beta}(Y) \longrightarrow \begin{cases} \delta S_{1,vir,\beta}(Q_1, I_{1,vir}, Y), \\ \quad \vdots \\ \delta S_{5,vir,\beta}(Q_5, I_{5,vir}, Y) \,, \end{cases} \tag{5.11}$$

following a procedure similar to Equation 5.6. The subscript *vir* has been added above to emphasize these branches are not physical decays. The physical and virtual component beta-spectra are then converted to antineutrino spectra:

$$\delta S_{j,DB,\beta} \longrightarrow \delta S_{j,DB,\bar{\nu}_e} \,, \tag{5.12}$$

$$\delta S_{i,vir,\beta} \longrightarrow \delta S_{i,vir,\bar{\nu}_e} \,. \tag{5.13}$$

In the conversion of the database-based branches the identity of the initial and final state nuclei are known so the nucleus-dependent corrections can be applied on a branch-by-branch level. For the virtual branches averaged corrections are applied. The final total antineutrino spectrum is

$$S_{Tot,\bar{\nu}_e}(Y) = \sum_i I_{i,DB}(Y) \sum_{j(i)} w_j \delta S_{j,DB,\bar{\nu}_e} + \sum_{k=1}^{5} I_{k,vir}\, \delta S_{k,vir,\bar{\nu}_e} \,. \tag{5.14}$$

The authors of [78] apply their hybrid-method to ^{235}U, ^{239}Pu and ^{241}Pu; their spectrum for ^{238}U is based solely on their direct calculation with up-to-date nuclear databases since no measurement of the total beta spectrum from ^{238}U-fission is available. The shape and uncertainties of the resultant antineutrino spectra are similar to the existing estimates in [70], [71], and [72]; however the normalization of the hybrid spectra above $\sim$ 1.8 MeV is systematically higher, by $\sim$ 3%, relative to those estimates.

In the following chapters the term *default* or *canonical* reactor-spectrum denotes the expected reactor antineutrino spectrum calculated using the old spectra-per-fission based on [70–72], the term *new* or *hybrid* reactor-spectrum will denote the spectrum calculated using [78]. The oscillation analysis using the canonical reactor-spectrum is the main focus of Chapter 7, the results using the hybrid reactor-spectrum are summarized in Appendix A.

5.4 Expected antineutrino flux at KamLAND

Finally, the expected incident antineutrino rate per unit energy at time t from reactors at KamLAND is

$$\frac{d\mathcal{N}_{\mathrm{KL}}(E,t)}{dt} = \sum_{i}^{\mathrm{R1,R2,R3}} \frac{1}{4\pi L_i^2} P_{\bar{\nu}_e\to\bar{\nu}_e}(E,L_i)\frac{d\mathcal{N}_i}{dt}\,, \tag{5.15}$$

where the index i labels the reactors and runs over the set (R1,R2,R3), L_i is the distance from the i^{th} reactor to KamLAND, $P_{\bar{\nu}_e\to\bar{\nu}_e}$ is the antineutrino survival probability and $d\mathcal{N}_i/dt$ is the antineutrino spectrum of the i^{th} reactor defined in Equation 5.4. In the analysis both a two-flavor and three-flavor neutrino oscillation model are considered. For the two-flavor case the survival probability is (Equation 1.9)

$$P^{2\nu}_{\bar{\nu}_e\to\bar{\nu}_e}(E,L) = 1 - \sin^2 2\theta_{12}\sin^2\frac{1.27\Delta m^2_{21}[\mathrm{eV}^2]\mathrm{L[m]}}{E[\mathrm{MeV}]}\,; \tag{5.16}$$

For the three-flavor case, invoking the fact that $|\Delta m^2_{21}| << |\Delta m^2_{31}|$ the survival probability can be written

$$P^{3\nu}_{\bar{\nu}_e\to\bar{\nu}_e}(E,L) = \cos^4\theta_{13}\cdot P^{2\nu}_{\bar{\nu}_e\to\bar{\nu}_e}(E,L) + \sin^4\theta_{13}\,. \tag{5.17}$$

Since θ_{13} is known to be small only the lowest order terms in $\sin\theta_{13}$ need be considered, in this limit we have

$$P^{3\nu}_{\bar{\nu}_e\to\bar{\nu}_e}(E,L) \simeq (1 - 2\sin^2\theta_{13})\cdot P^{2\nu}_{\bar{\nu}_e\to\bar{\nu}_e}(E,L)\,. \tag{5.18}$$

5.5 Summary

We close this chapter with Table 5.2 which summarizes the systematic error on the expected reactor antineutrino spectrum at KamLAND.

Table 5.2: Summary of systematic uncertainty on the reactor spectrum at KamLAND.

Source	Uncertainty
Number of fissions ($\mathcal{F}$)	2%
Fission fractions (f_j)	1.3%
Spectra per fission $\hat{S}_j$	2.5%
Total	3.5%

Chapter 6

Data reduction and event selection

This chapter describes the conditions or cuts applied to the data to select inverse beta decay candidate pairs. The cuts can be divided, loosely, into two categories: (i) *level-I* cuts which are motivated by the expected characteristics of inverse beta decay events and (ii) *level-II* cuts which are driven largely by the characteristics of the residual backgrounds after the level-I selection.

6.1 Run selection

The first step is to select the runs to be used in the analysis. A near-continuous detector monitoring effort is maintained so that any problems which might compromise data quality — for example a high voltage failure or a KamFEE card malfunction — can be identified and remedied as promptly as possible. Records of the detector status and any problems encountered are maintained and stored in an operations database for later reference. All the data is processed for event reconstruction, once this is complete a series of quality checks called *diagnostics-checks* are performed to search for unusual features in the data, for example a sudden change in the reconstructed event spectrum is often indicative of a high voltage power supply failure. Combining the diagnostics-checks with information from the operations database we build up a list of runs which are considered *good runs* for the final neutrino-oscillation analysis. The total live-time of the good-runs for the present study 1834 days.

6.2 Coincidence pair selection

Recall from Chapter 5 that each prompt-delayed coincidence (PDC) pair is characterized by six parameters $\overrightarrow{PDC} = (\Delta T, E_{\rm p}, E_{\rm d}, \vec{R}_{\rm p}, \vec{R}_{\rm d}, \Delta R, t)$ — Table 5.1. The range of values for these parameters expected for inverse beta decay pairs are presented in the following subsections.

6.2.1 Prompt-delayed time separation ΔT

The time between the prompt and delayed events in each pair must be consistent with the mean neutron-capture time (τ_n). Using a simple model for the KamLAND LS we expect τ_n in the range 206 $\mu s < \tau_n <$ 216 μs [79]; however neutron calibration runs and spallation neutrons are used to estimate τ_n directly.

Reference PDC pair candidates are selected from the neutron-source data using the conditions given in Table 6.1. The ΔT distributions found for the PoC, moderated AmBe, and unmoderated AmBe sources [1] are shown in panels (a)-(c) of Figure 6.1. We estimate τ_n for each source by fitting the function

$$F(x) = \frac{A}{\tau_n} e^{-x/\tau_n} + B \tag{6.1}$$

to the associated ΔT distribution. The parameter A is a normalization constant and B is a time-independent constant added to model background from uncorrelated pairs. The results of these fits are summarized in Table 6.3.

Cosmic-ray muons which spall neutrons are also a source of reference PDC pairs. In this case the parent muon forms the prompt event and subsequent captures of any spallation neutrons form the delayed event. Table 6.2 lists the spallation PDC pair selection conditions. If multiple neutrons are produced, multiple PDC pairs can be found, however only muons are accepted as prompt events. To avoid pile up, muons are required to be separated in time by at least 0.02 s. Only low-multiplicity muons are selected — muon multiplicity is defined as the number of triggers that occur within 2 ms after the muon. This cut is imposed to reduce systematic biases in vertex and energy reconstruction caused by electronics dead-time and noise which often follow high-multiplicity muons. The ΔT distribution of the selected PDC pairs is shown in panel (d) of Figure 6.1. Again, τ_n is estimated by fitting Equation 6.1 to this distribution; the fit range is restricted to the interval 500 $\mu s < \Delta T <$ 1500 μs,. At earlier times post-muon electronics-noise can degrade the energy and position reconstruction and results in a time-dependent neutron tagging efficiency. Deviation of the observed ΔT distribution from the expected exponential form is evident for $\Delta T <$ 500 μs in Figure 6.1-(d). The result of the fit is shown in Table 6.3.

The average value of the four estimates of τ_n ($\tau_n = 207.7 \pm 1.0 \mu s$) is adopted in the analysis, we impose the cut $0.5\,\mu s < \Delta T < 1500$ μs for inverse beta decay pair candidates. Based on our estimate of τ_n the efficiency of this cut is $99.7 \pm 0.4\%$.

6.2.2 Prompt energy selection $E_{\rm p}$

Figure 6.2 shows the positron or prompt visible energy spectrum expected based on the best-fit energy scale model and an unoscillated reactor antineutrino flux at Kam-

[1] The moderated (unmoderated) AmBe source refers to the source with (without) the 3cm thick polyethylene outer-capsule.

Table 6.1: PDC pair selection conditions for neutron calibration data.

Variable	Cut
E_{p}	$2.0\,\mathrm{MeV} < E_{\mathrm{p}} < 6.0\,\mathrm{MeV}$
E_{d}	$2.2\,\mathrm{MeV} < E_{\mathrm{d}} < 2.6\,\mathrm{MeV}$
ΔR	$\Delta R < 1.0$ m
ΔT	$30\ \mu s < \Delta T < 1500\ \mu s$
Source position	within 2 m of center
$\vec{R}_{\mathrm{p}}$, $\vec{R}_{\mathrm{d}}$	within 2 m of the source
Reconstruction status	good

Table 6.2: Spallation PDC pair selection conditions.

Variable	Cut
Prompt event	Must be tagged as a muon
Time between muons	$> 0.02\,\mathrm{s}$
Muon multiplicity	< 10
ΔT	$30\ \mu s\ < \Delta T < 1500\ \mu s$
$\vec{R}_{\mathrm{d}}$	$\lvert\vec{R}_d\rvert < 5.5$ m
E_{d}	$2.2\,\mathrm{MeV} < E_{\mathrm{d}} < 2.6\,\mathrm{MeV}$
Delayed reconstruction status	good

Table 6.3: Best-fit mean neutron-capture time for multiple sources; Sig is the normalization estimator to be identified with A in Equation **??**,τ is estimator for $\tau_n$and Bkg is the estimator for the background, B.

Source	Best-fit $\tau_n\,(\mu s)$	χ^2/ndf
AmBe (Moderated)	208.5 ± 1.9	98/94
AmBe (Unmoderated)	206.2 ± 2.0	98/94
PoC	208.1 ± 2.7	83/94
Spallation	208.3 ± 2.4	114 /97
Weighted average	$\tau_n = 207.7 \pm 1.0\ \mu s$	

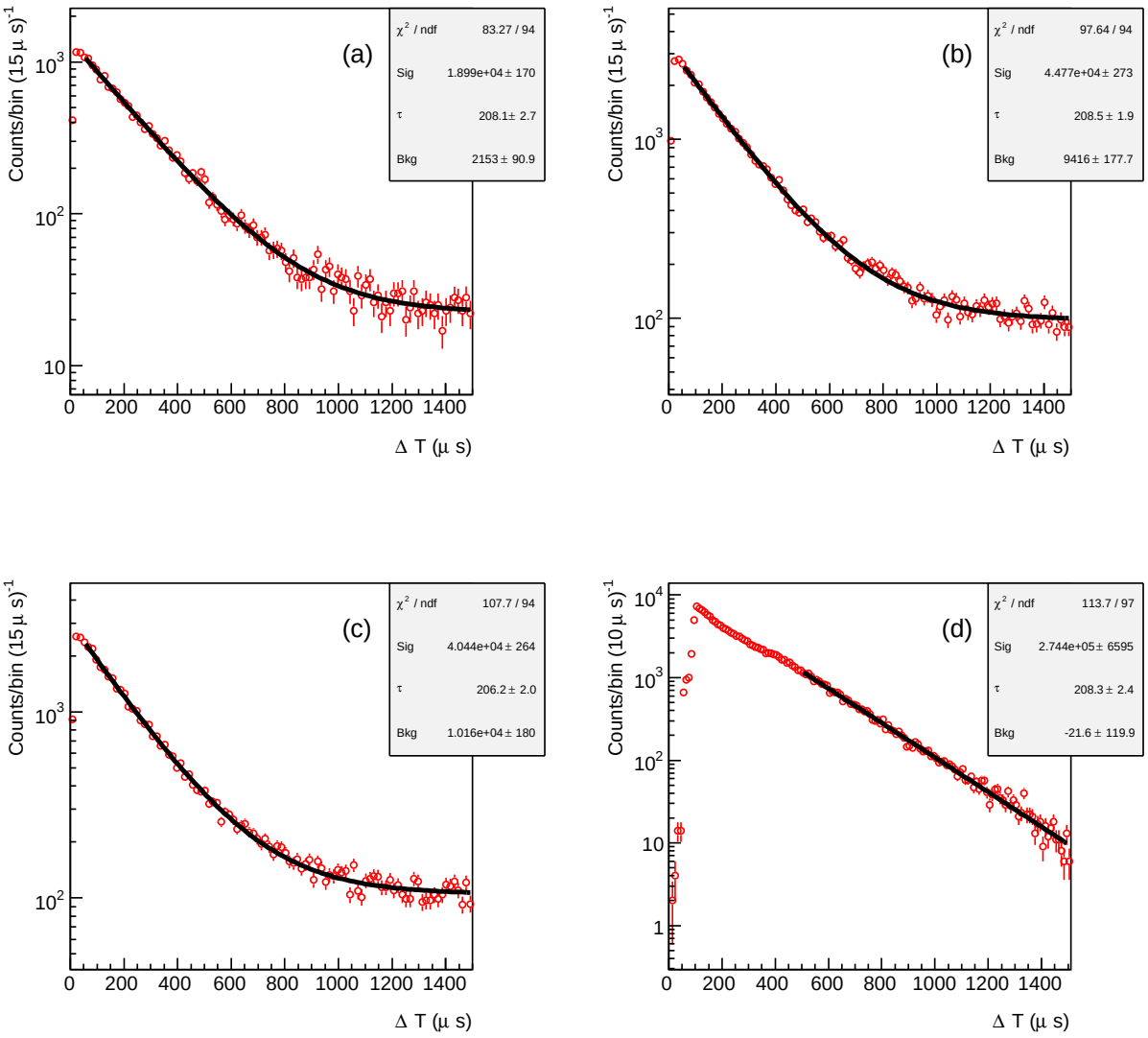

Figure 6.1: Distribution of ΔT for PDC pairs selected from: (a) PoC, (b) Moderated AmBe, (c) Unmoderated AmBe, and (d) spallation neutron sources. The solid line is the best-fit model of the data.

LAND; most prompt events are expected to reconstruct between $\sim 1\,\mathrm{MeV}$ and $\sim 10\,\mathrm{MeV}$.

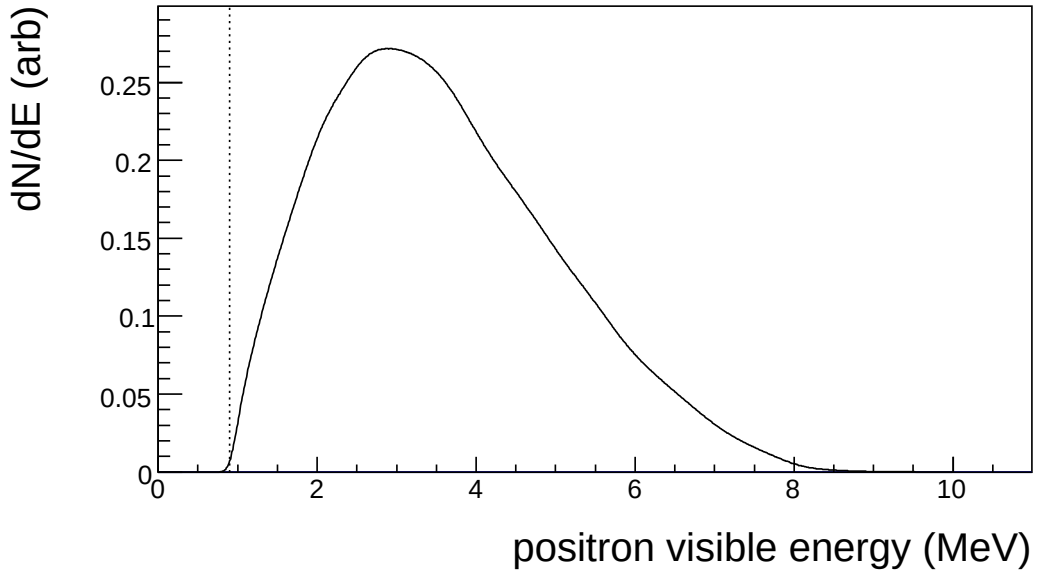

Figure 6.2: Expected prompt positron spectrum for an unoscillated reactor flux at KamLAND. The dashed vertical line indicates the E_{p} selection threshold used in the analysis.

To select inverse beta decay candidates we adopt the cut $0.9\,\mathrm{MeV} < E_{\mathrm{p}} < 20.0\,\mathrm{MeV}$. The upper limit, which extends well beyond the maximum expected for inverse beta decay positrons, is chosen to have a signal-free window to study backgrounds with prompt visible-energy spectra that extend beyond $\sim 10\,\mathrm{MeV}$. The lower limit is driven by the DAQ trigger threshold. Ultimately the efficiency of this cut depends on the shape of the prompt positron visible energy spectrum which in turn is a function of the oscillation and detector-response parameters. Thus the relevant efficiency is calculated during the final oscillation-parameter fit. For reference, the efficiency assuming an unoscillated reactor flux with the T-I detector response is 99.97 ± 0.02 % — the uncertainty comes mainly from the uncertainty of the detector response model.

6.2.3 Delayed energy selection E_{d}

The neutron produced in inverse beta decay thermalizes and captures radiatively on a proton, producing a $2.224\,\mathrm{MeV}$ photon, or on $^{12}\mathrm{C}$ releasing a $4.448\,\mathrm{MeV}$ photon.

From the relative abundances of p and ^{12}C in the LS and the thermal capture cross sections we expect 99.5% of neutrons to undergo np-capture [79]. We choose to ignore n-^{12}C captures and apply the cut $2.0\,\mathrm{MeV} < E_\mathrm{d} < 2.8\,\mathrm{MeV}$ to select candidates. From the detector response model we expect the np-capture photon to reconstruct with mean visible energy $\langle E_{vis} \rangle \simeq 2.35\,\mathrm{MeV}$ and resolution $\sigma \simeq 0.11\,\mathrm{MeV}$. Table 6.4 lists the efficiency to accept an np-capture photon for each data period. The increase in uncertainty for periods T-II and T-III is due to poorer energy resolution and larger energy scale uncertainty for these periods.

Table 6.4: Efficiency of E_d cut.

	Data period		
	T-I	T-II	T-III
E_d efficiency (%)	99.87 ± 0.06	99 ± 1	98 ± 2

6.2.4 Prompt-delayed spatial separation (ΔR)

PDC pairs from neutron calibration data are used to estimate the PDF for ΔR. Pairs are selected as per Table 6.1 but the ΔR and $\vec{R}_\mathrm{d}$ cuts are relaxed. The PDFs for AmBe and PoC data are shown in panels (a) and (b) of Figure 6.3. For both sources we find that $\sim 99\%$ of PDC pairs have $\Delta R <$ 1.6 m; we adopt this cut for inverse beta decay candidate selection. The ΔR-PDF shape for neutron-source pairs and antineutrino-induced pairs are not expected to be identical. The shape is governed by the resolution of the vertex reconstruction and the range of the prompt and delayed particles in the LS. In the case of AmBe for example, the prompt event comes mostly from a combination of neutron scattering and a prompt $\sim$4.4 MeV photon; for antineutrinos the prompt event is from stopping and annihilation of a positron. To estimate the difference in shape of the ΔR-PDF between these cases a sample of inverse beta decay events from antineutrinos with incident kinetic energy ranging from 2.0 MeV to 10.0 MeV was simulated using Geant4 [80]. For each event, waveform data was generated and processed with the standard reconstruction software. Similarly, samples of PoC and AmBe PDC-pairs were generated. For the subsequent discussion we adopt the notation $\Delta R^{\mathrm{source}}_{\mathrm{method}}$ to refer to a particular ΔR construction, so for example $\Delta R^{\mathrm{AmBe}}_{\mathrm{sim}}$ is the ΔR PDF from the AmBe simulation and $\Delta R^{\mathrm{PoC}}_{\mathrm{Data}}$ is from the PoC data. The results for the simulations, $\Delta R^{\mathrm{AmBe}}_{\mathrm{sim}}$ and $\Delta R^{\bar{\nu}_\mathrm{e}}_{\mathrm{sim}}$, are shown in panels (c) and (d) respectively of Figure 6.3. All four ΔR PDFs yield consistent estimates for the ΔR cut efficiency (Table 6.5), the average of the PoC- and AmBe-data results ($\xi_{\Delta R} = 98.8 \pm 0.6\%$) is adopted. The ratios of $\Delta R^{\mathrm{AmBe}}_{\mathrm{Data}}$ to $\Delta R^{\mathrm{AmBe}}_{\mathrm{sim}}$ and of $\Delta R^{\bar{\nu}_\mathrm{e}}_{\mathrm{sim}}$ to $\Delta R^{\mathrm{AmBe}}_{\mathrm{sim}}$ are shown in Figure 6.4. The ratio $\Delta R^{\bar{\nu}_\mathrm{e}}_{\mathrm{sim}} / \Delta R^{\mathrm{AmBe}}_{\mathrm{sim}}$ indicates that $\bar{\nu}_e$-pairs tend to reconstruct closer together than AmBe pairs, as expected since the prompt

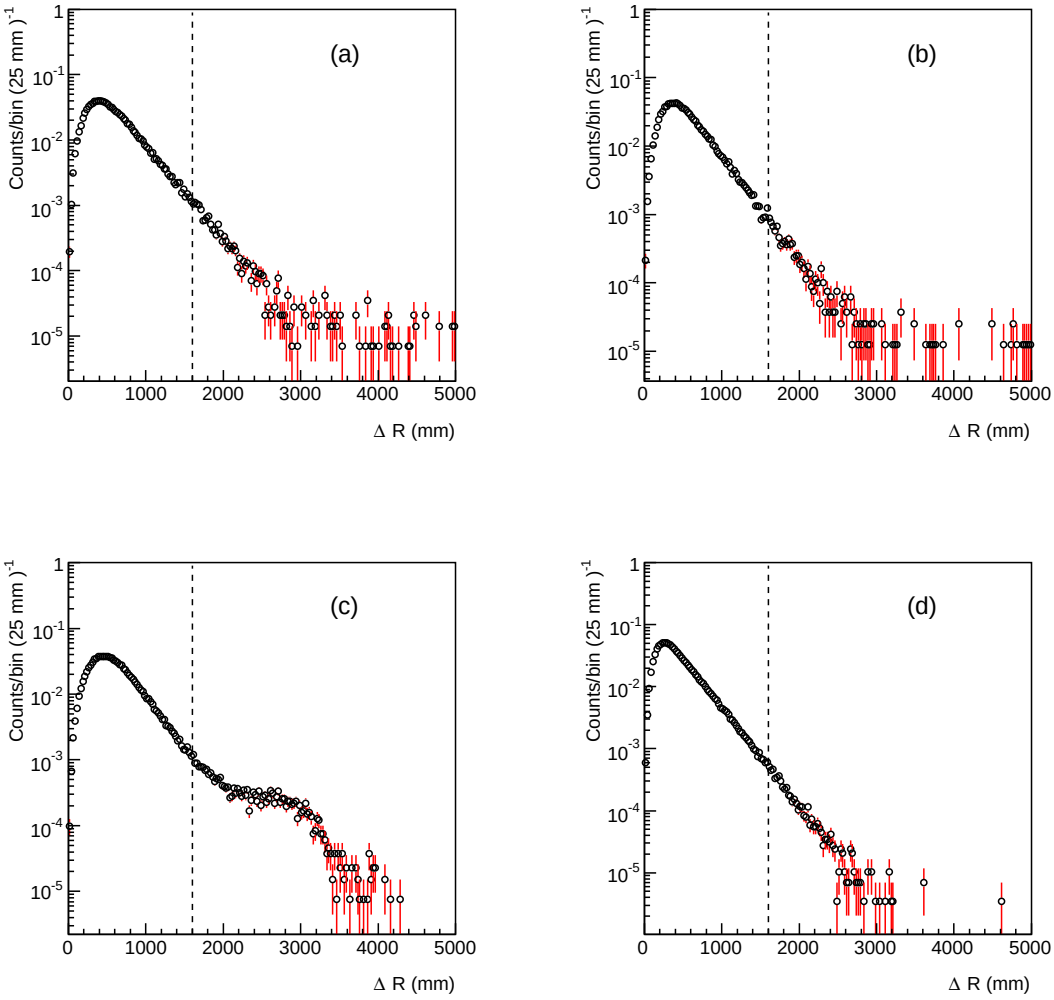

Figure 6.3: ΔR for PDC pairs from (a) AmBe data, (b) PoC data, (c) AmBe simulation and (d) $\bar{\nu}_e$simulation. The dashed vertical line indicates the ΔR cut adopted in the analysis.

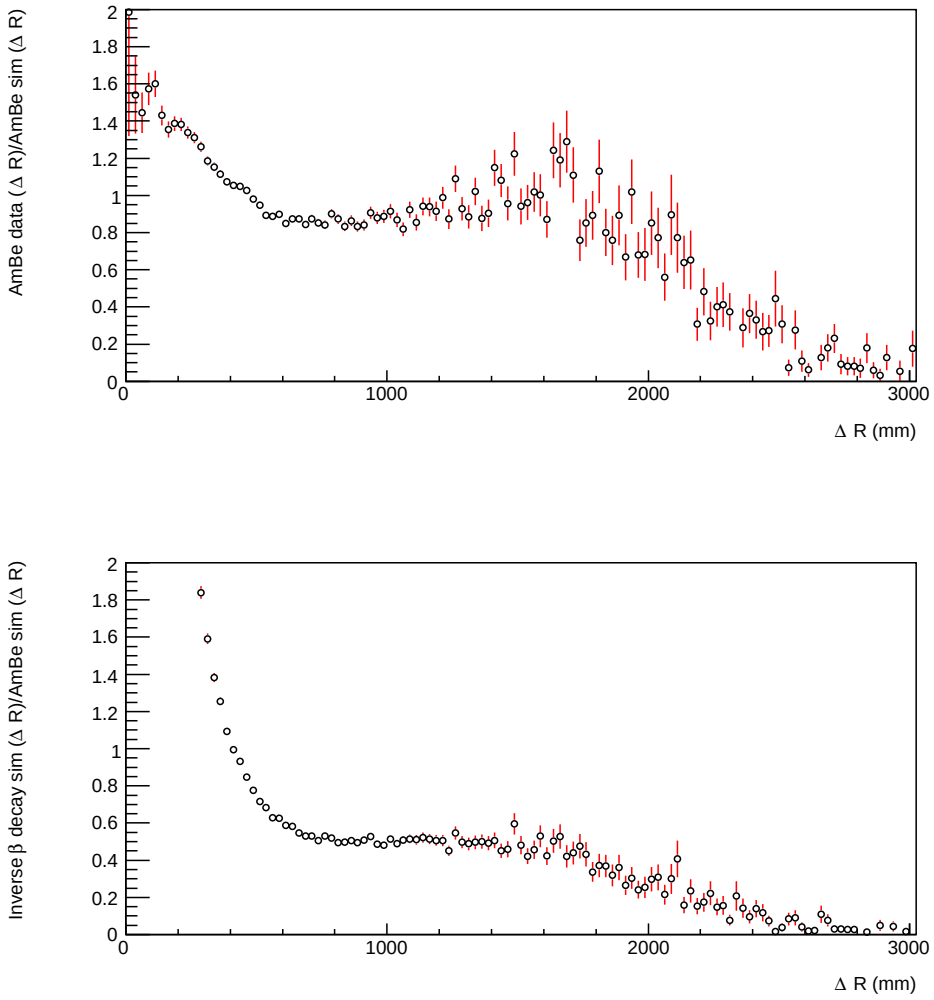

Figure 6.4: Ratio of the ΔR PDFs for different PDC sources. The upper plot is AmBe-data/AmBe-simulation, the lower plot is $\bar{\nu}_e$-simulation/AmBe-simulation.

particle for AmBe has a longer range than the prompt particle for $\bar{\nu}_e$. However, the ratio $\Delta R_{\rm Data}^{\rm AmBe}/\Delta R_{\rm sim}^{\rm AmBe}$ indicates that the simulation tends to underestimate the fraction of pairs with shorter ΔR relative to the data. We use the different ΔR PDFs to estimate the systematic error from assuming that $\bar{\nu}_e$-data pairs and AmBe-data pairs follow the same ΔR distribution.

Table 6.5: Efficiency of ΔR cut for different sources of PDC pairs.

Source	Efficiency of ΔR cut (%)
AmBe (data)	98.7 ± 0.5
PoC (data)	99.1 ± 0.7
AmBe (sim)	99.2 ± 1.0
Inverse β decay (sim)	99.5 ± 0.3

6.2.5 Prompt event and delayed event position ($\vec{R}_{\rm p}$, $\vec{R}_{\rm d}$)

To avoid background from radioactive contaminants on the balloon and support ropes we reject PDC pairs for which either the prompt or delayed event reconstruct with a radius greater than 6.0 m. The volume defined by the $\vec{R}_{\rm p} < 6.0$ m cut is called the *fiducial volume* and the fraction of exposure remaining after this cut is called the *fiducial-volume fraction*(FVF). We estimate FVF from calibration data and the reconstructed vertex distribution of tagged spallation ^{12}B. We expect ^{12}B to be produced uniformly in the LS, thus the fraction of ^{12}B candidates that reconstruct inside the fiducial volume provides an estimate of FVF. The results are listed in Table 6.6, for comparison we note the nominal value of FVF, assuming a truly spherical volume and ignoring vertex reconstruction error, is 0.786. The estimates for period T-II and T-III have larger uncertainties than that of T-I. This is because spallation data alone were used to estimate FVF for T-II and T-III; T-I benefited from a full-volume calibration campaign which allowed the systematic biases throughout most of the analysis volume to be measured [2].

Table 6.6: Fiducial volume fraction.

	Data period		
	T-I	T-II	T-III
Fiducial volume fraction	0.741 ± 0.018	0.772 ± 0.035	0.793 ± 0.045

[2] A new full volume calibration applicable to T-II and T-III has recently been performed and will be incorporated into a future analysis.

The efficiency associated with the $\vec{R}_{\rm d}$ cut is called the *edge-efficiency*, pairs near the edge of the fiducial volume will not be tagged if the delayed event reconstructs outside the volume defined by $\vec{R}_{\rm d} < 6.0$ m. A toy Monte-Carlo was used to estimate this efficiency: a large number of pairs was generated, the prompt event vertices were generated uniformly inside a 6-m sphere, for each prompt vertex $\vec{R}_{\rm p}$ a delayed vertex $\vec{R}_{\rm d}$ was generated with the constraint that the spatial separation follow the nominal ΔR}-PDF — $\Delta R^{\rm AmBe}_{\rm data}$. The edge-efficiency is taken as

$$\xi_{\rm Edge} = \frac{N_{\vec{R}_p+\Delta R+\vec{R}_d}}{N_{\vec{R}_p+\Delta R}}\,, \tag{6.2}$$

where the denominator is the number of pairs that satisfy the $\vec{R}_{\rm p}$ and ΔR cuts and the numerator is the number of pairs that satisfy the $\vec{R}_{\rm p}$, ΔR and $\vec{R}_{\rm d}$ cuts. The result depends on the shape of the PDF used; to estimate the systematic error due to the ΔR-shape uncertainty and vertex reconstruction biases the calculation was repeated with different choices of the ΔR PDF — $\Delta R^{\rm AmBe}_{\rm Sim}$, $\Delta R^{\rm PoC}_{\rm Data}$ and $\Delta R^{\bar{\nu}_e}_{\rm Sim}$. Additionally, each calculation was repeated by biasing the previously uniform prompt position according to the vertex reconstruction bias functions determined from calibration data (Chapter 4). The systematic error of the efficiency is taken as the RMS of the resulting estimates. Figure 6.5 shows the efficiency curves for several such simulations. The efficiency is $\xi_{\rm Edge} = 92.6 \pm 0.5$ %.

6.2.6 Trigger threshold efficiency

The DAQ NSumMax[3] trigger threshold introduces an effective energy threshold. The relationship between NSumMax and visible energy is position and energy dependent, since NSumMax is the number of PMTs that received at least one hit in an event while visible energy is based on the number of photoelectrons observed in the event. Figure 6.6 shows the prompt- and delayed- trigger threshold settings as a function of run date for the data set.

The delayed-trigger threshold was at or below NSumMax = 120 for all good-runs. From neutron calibration data we find the NSumMax distribution of *np*-capture events is well modeled by a gaussian function. The mean NSumMax is in the range $430 \lesssim \mu_{NSUM} \lesssim 520$, where the lower value is found for data collected close to the fiducial volume boundary at $Z = \pm 6.0$ m and the upper value is found when the source is at the detector center; the typical width these distributions is $\sigma_{NSUM} \simeq 25$. Therefore the probability for an *np*-capture to generate NSumMax less than 120 and thus fail to trigger the DAQ is vanishingly small.

The prompt threshold was set at NSumMax = $\{200\,, 180\,, 200\,, 80\,, 90$ and $70\}$ at various times during the data taking period. Calibrations with ^{68}Ge are a source

[3]NSumMax is the maximum value of NSum recorded during a $\sim$ 300-ns-long event window.

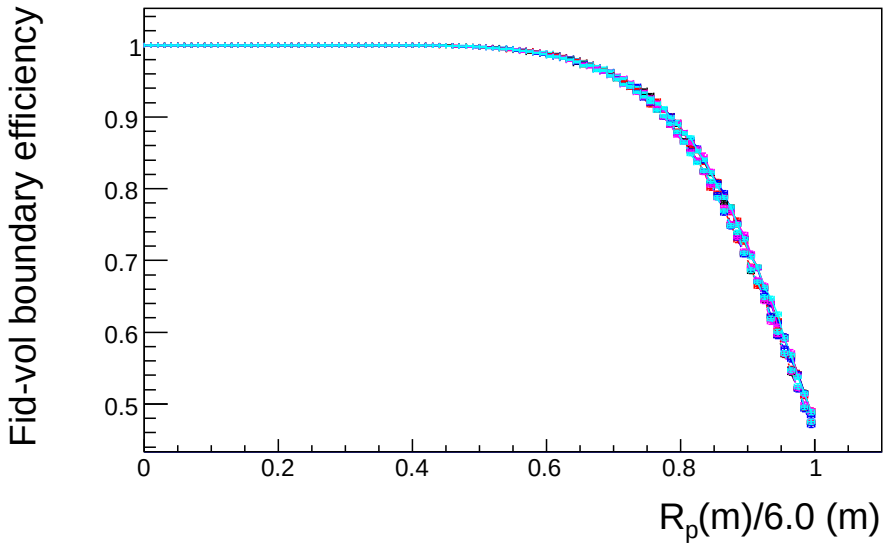

Figure 6.5: Fiducial volume edge efficiency curves, where the efficiency is the fraction of events which passing the R_p and ΔR cut which also pass the R_d. Each curve is calculated from a simulation with a difference choice of the ΔR PDF, and with and without application of the measured vertex reconstruction biases.

of positron annihilation gammas which together reconstruct with visible energy close to the 0.9 MeV cut threshold. The mean NSumMax of ^{68}Ge events is in the range $190 \lesssim \mu_{^{68}\mathrm{Ge}} \lesssim 240$, where the lower value is at the fiducial volume edge and the upper value is at the detector center; the NSumMax width for these events is $\sigma_{^{68}\mathrm{Ge}} \simeq 18$. Therefore, at prompt-trigger thresholds of 70, 80 and 90 the probability not to trigger on an event with $E_\mathrm{p} \geq 0.9\,\mathrm{MeV}$ is negligible. However for the threshold of 200 or 180 the efficiency is non-trivial. For both of these cases we use delayed-trigger events to investigate the efficiency; we take

$$\xi_{trig}(E) = \frac{\int_{E-0.1}^{E+0.1} S_{d+p}(E')dE'}{\int_{E-0.1}^{E+0.1} S_d(E')dE'}\,, \tag{6.3}$$

where S_d is the visible-energy spectrum of events that satisfy the delayed trigger (NSumMax $\geq$ 120) and S_{d+p} is the subset of S_d that also satisfy the prompt-trigger threshold. To study the position dependence of this efficiency the fiducial volume was divided into 10 concentric spherical shells and Equation 6.3 was evaluated for the events in each shell. The efficiency curves for data period T-I and T-II are shown in

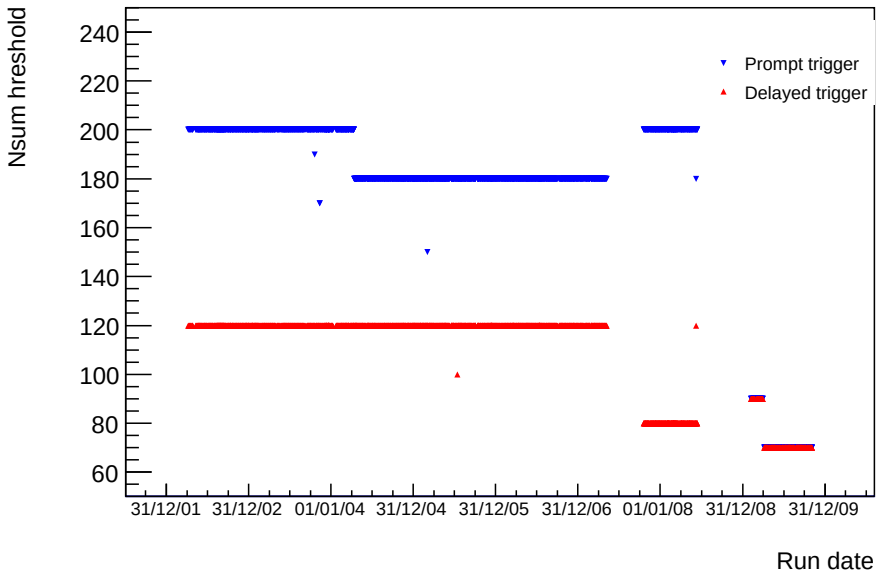

Figure 6.6: NSumMax trigger threshold settings.

the upper two panels of Figure 6.7 — for clarity the 10 volumes are rebinned into five volumes. For period T-III the prompt trigger threshold was low enough that the efficiency is 100%. Variation of the efficiency with event position is evident — as expected the outer-most volume is the most inefficient.

Equation 6.3 may over estimate the prompt-trigger efficiency unless the delayed trigger is 100% efficient at the prompt-energy threshold. The delayed-trigger efficiency as a function of visible energy is studied using *background runs*. These are special runs taken with very low trigger thresholds — typically NSumMax = 30, which corresponds to a visible energy threshold of about 0.1 MeV. Following similar reasoning as above, the efficiency of the delayed trigger is estimated by comparing the spectrum of all background triggers to the spectrum of background triggers that also pass the delayed-NSumMax threshold. The bottom panel of Figure 6.7 shows the result of this study, for simplicity only the efficiency for the outermost shell — the most inefficient — is shown for each data period. The delayed trigger is found to be 100% efficient at the prompt-energy threshold.

6.2.7 Reconstruction status efficiency

The events in each pair are required to have valid reconstruction status. We estimate the efficiency of this cut as a function of NSumMax using the fraction of

events that reconstruct successfully — more explicitly,

$$\xi_{\mathrm{RECON}}(x) = \frac{\int_{x-\Delta x}^{x+\Delta x} N_{\mathrm{good-RECON}}(x')dx'}{\int_{x-\Delta x}^{x+\Delta x} N_{\mathrm{all-RECON}}(x')dx'}\,, \tag{6.4}$$

where $N_{\mathrm{all-RECON}}$ and $N_{\mathrm{good-RECON}}$ are the NSumMax spectra of all reconstructed events and of well-reconstructed events respectively.

Natural radioactivity in the detector provides a large sample of physical events contained in the LS with NSumMax ranging from the trigger threshold up to ~ 450, this corresponds to visible energy up to about $2.0 \sim 2.5$MeV depending on the position of the event in the LS. Figure 6.8 shows the efficiency curves from low-NSum data for each of the periods T-I,T-II and T-III. Events expected to have poor reconstruction performance are excluded from this study if they can be tagged independently of their vertex information — for example events within 2 ms of muons or events within 100 μs of forced acquisition triggers.

For most of the spectrum the efficiency is better than 99%. Beyond NSum $\simeq 450$ the efficiency starts to fall, these higher energy events are expected to come mostly from ^{208}Tl on the balloon or outside LS volume. The reconstruction algorithms are not well tested on these peripheral events. For period T-II there is a sharp decrease of the efficiency for events with NSumMax below ~ 240. This was found to be due to spurious TQs on some PMTs. When the T-II data was processed this problem had not been identified. The reconstruction algorithms were updated to correct for this in time for T-III data processing. To estimate the reconstruction efficiency for higher energy events ^{12}B spallation candidates were used. The efficiency is estimated following Equation 6.4 using the NSumMax spectra of ^{12}B candidates. Figure 6.9 shows the resulting efficiency curves for each data period, the efficiency is better than 98% over the NSumMax range.

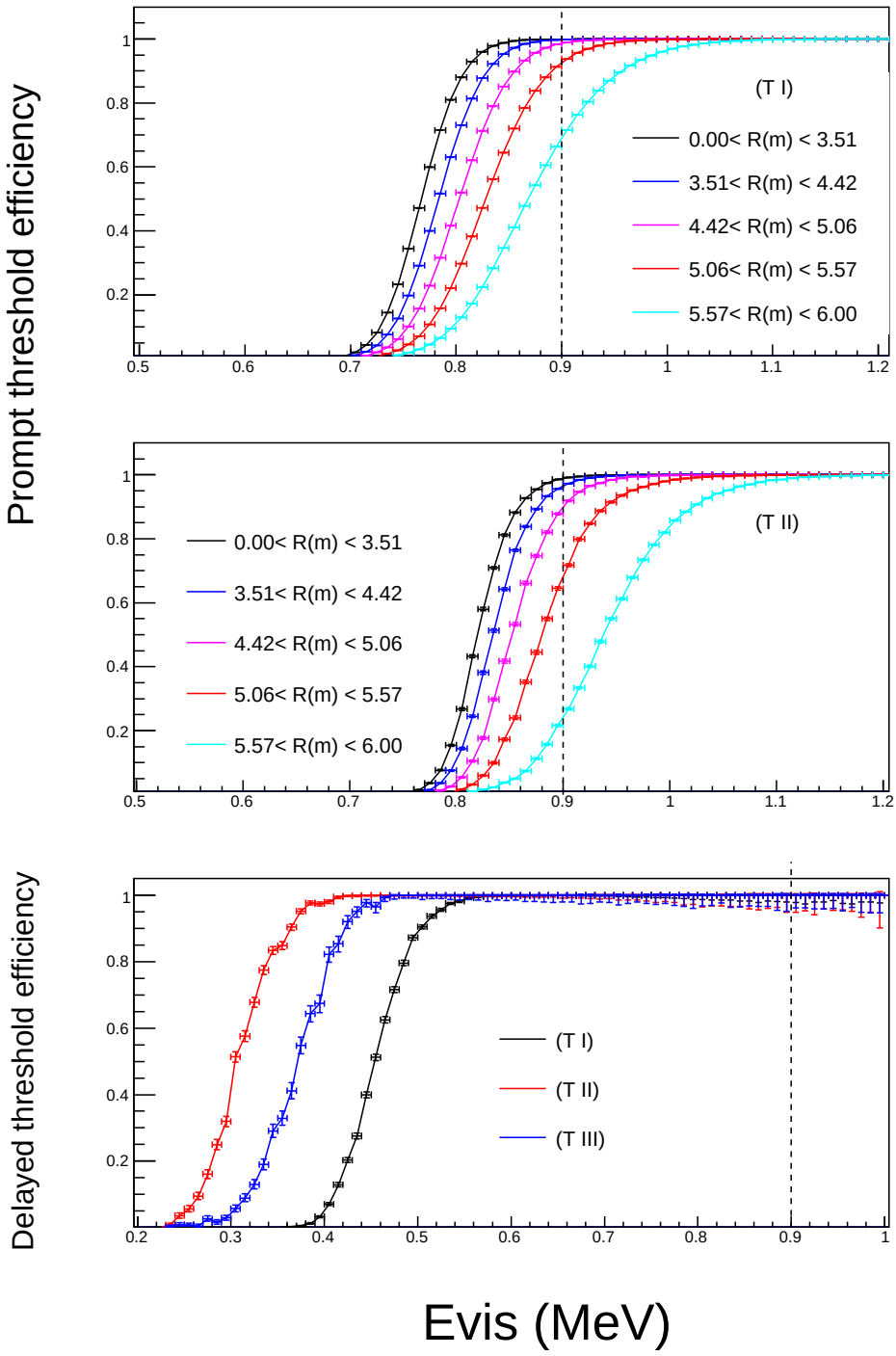

Figure 6.7: Trigger efficiency as a function of visible energy for prompt and delayed triggers. The prompt-energy threshold of the analysis is indicated by the vertical dashed line.

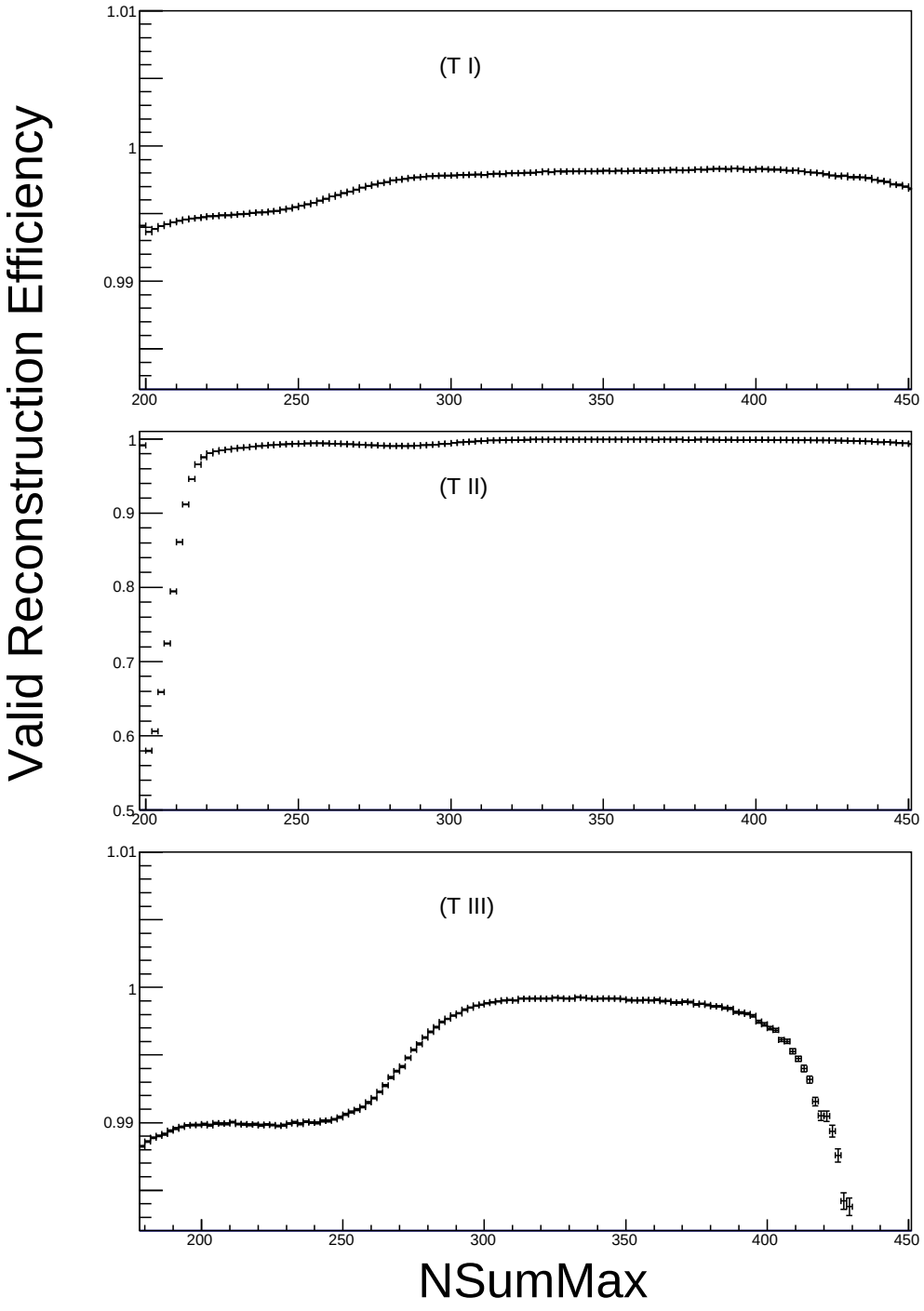

Figure 6.8: Good reconstruction cut efficiency estimated from singles events for each data period.

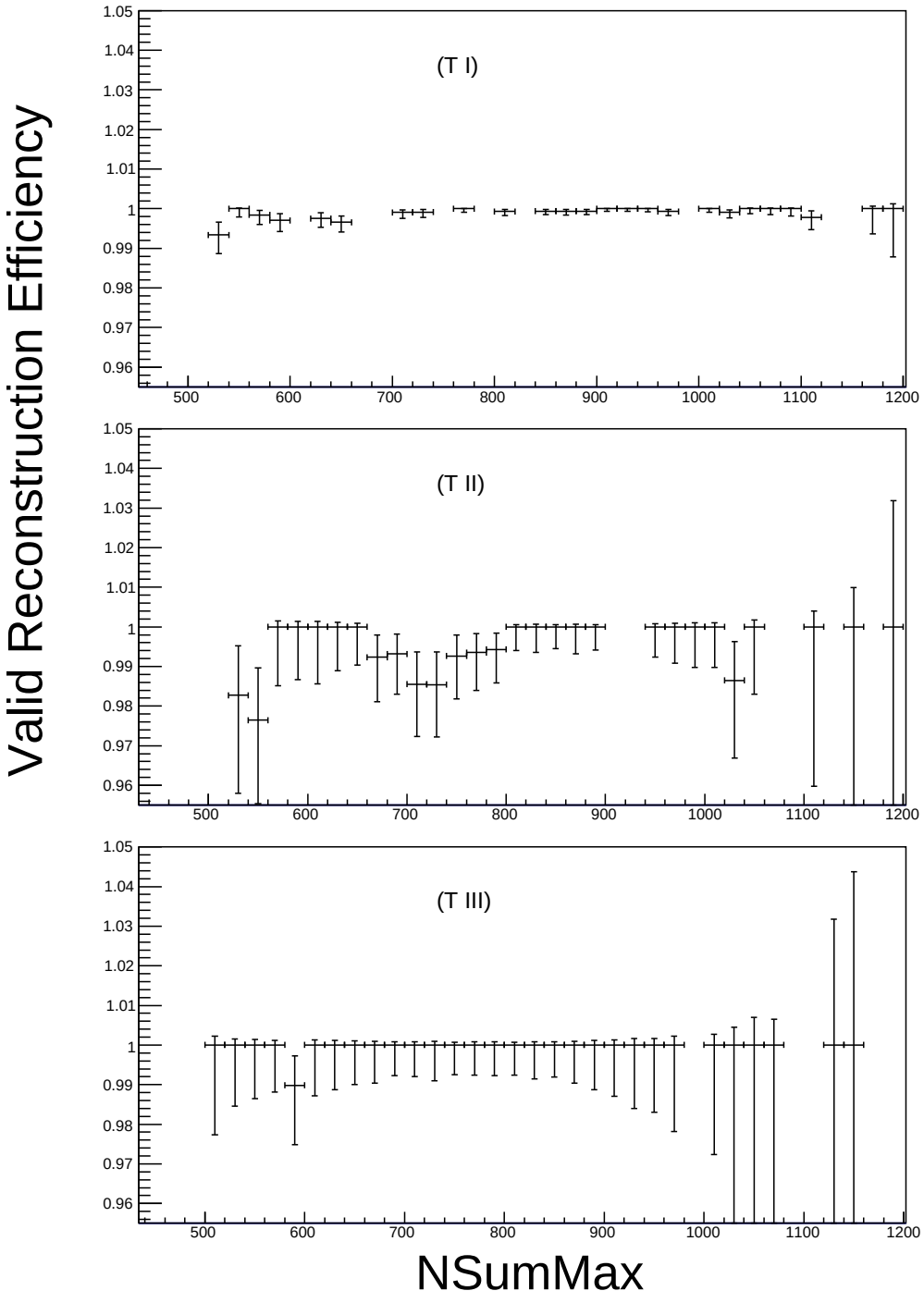

Figure 6.9: Good reconstruction cut efficiency estimated from ^{12}B candidates for each data period.

Having outlined the level-I candidate selection cuts we now proceed to describe the backgrounds. Additional cuts, to further reduce the backgrounds, called the level-II cuts will be introduced as we proceed.

6.3 Accidental background

Accidental background refers to PDC pairs made up of uncorrelated events that happen to pass the level-I cuts. To measure this background, pairs are selected according to the level-I cuts except the ΔT condition is replaced with the requirement that 10 s$< \Delta T <$20 s. This choice excludes pairs containing truly correlated neutrons and allows accumulation of a large sample of accidental pairs. The accidental background level expected in the $\bar{\nu}_e$-candidate sample is then found by scaling for the relative lengths of the accidental- and $\bar{\nu}_e$-ΔT windows.

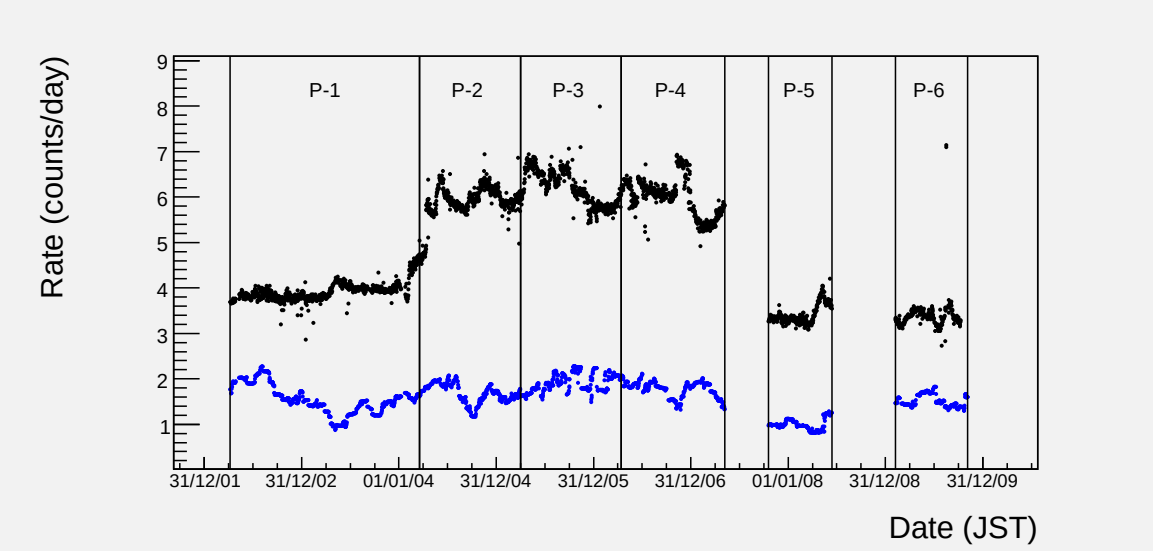

Figure 6.10: Accidental background rate and expected reactor signal rate — for an unoscillated reactor-flux — as a function of time. For the accidentals study the data is divided into 6 periods: P1, $\cdots$, P6; the vertical lines mark the boundaries of these periods.

Figure 6.10 shows the resultant accidental rate in the fiducial volume as a function of run date, for comparison the expected signal rate due to the reactor flux described in Chapter 5 (without oscillation) is also shown. The accidental rate shows some time dependence, to exploit this in the analysis the data set is coarsely divided into 6 periods, denoted P-1, P-2, $\cdots$, P-6. The period boundaries are delineated in Figure 6.10. The large changes can be traced to changes in the trigger settings and radiopurity of the LS, for example the increase in rate during P-2 is due to reduction

of the prompt-trigger threshold from NSumMax=200 to 180, the rate of low-energy events triggering the DAQ consequently increased resulting in more accidental pairs with low $E_{\rm p}$. The decrease in late 2007 is due to LS purification, sources of low-energy background such as ^{210}Bi were removed from the LS resulting in a lower accidental-coincidence rate.

It is evident from Figure 6.10 that accidental background after the level-I cuts is several times larger than the expected signal. However it is advantageous to compare how accidental pairs and signal-like pairs populate PDC parameter space. For example, referring to Figure 6.11, one can see that accidental pairs are more likely to occur with large $\vec{R}_{\rm p}$ and large ΔR than signal-like pairs. The accidental PDFs in this figure were constructed from the accidental sample described above and the signal-like PDFs were constructed using a simple simulation. In this simulation $E_{\rm p}$ is generated assuming the positron visible-energy spectrum from inverse beta decay induced by the expected (without oscillation) reactor-flux, $E_{\rm d}$ is drawn from a gaussian PDF with a mean and width determined by the energy of the neutron capture gamma and the energy-scale model, $\vec{R}_{\rm p}$ follows a uniform spherical distribution, $\vec{R}_{\rm d}$ is generated using $\Delta R^{\rm AmBe}_{\rm Data}$, and ΔT follows an exponential distribution parametrized by τ_n[4].

We can divide the space spanned by ($E_{\rm p}$, $E_{\rm d}$, $\vec{R}_{\rm p}$, $\vec{R}_{\rm d}$, ΔR) into sub-volumes and categorize them according to how likely an accidental pair is to populate a given sub-volume versus the expected likelihood for a signal-like pair to populate this volume. To that end we introduce a parameter called the *likelihood-asymmetry* ($\mathcal{A}$). Let ($\vec{\xi}_0\,, \Delta T_0$) denote a point in PDC parameter space, the likelihood asymmetry of the sub-volume containing ($\vec{\xi}_0\,, \Delta T_0$) is

$$\mathcal{A}(\vec{\xi}_0\ , \Delta T_0) \equiv \frac{P_{\bar{\nu}_e}(\vec{\xi}_0\ , \Delta T_0) - P_{\rm Acc}(\vec{\xi}_0\ , \Delta T_0)}{P_{\bar{\nu}_e}(\vec{\xi}_0\ , \Delta T_0) + P_{\rm Acc}(\vec{\xi}_0\ , \Delta T_0)}\,, \tag{6.5}$$

where $P_{\bar{\nu}_e}(\vec{\xi}_0\ , \Delta T_0)$ is the probability that a $\bar{\nu}_e$-like pair occurs with PDC parameters ($\vec{\xi}_0\ , \Delta T_0$) and likewise for $P_{\rm Acc}$. No correlation is observed between ΔR and ΔT in neutron calibration runs so one can write

$$P_{\bar{\nu}_e}(\vec{\xi}_0\ , \Delta T_0) = P_{\bar{\nu}_e}(\vec{\xi}_0) \times \frac{1\mu s}{\tau_n} e^{-\Delta T/\tau_n} \tag{6.6}$$

and

$$P_{\rm Acc}(\vec{\xi}_0\ , \Delta T_0) = P_{\rm Acc}(\vec{\xi}_0) \times \frac{1\mu s}{W_{\Delta T}}\,, \tag{6.7}$$

[4]The advantage of the simple simulation over the full Geant4-based simulation is that large samples can be generated relatively quickly and agreement with the detector response can be enforced by using measured response functions. Moreover it is straight forward to vary the parameters of the response functions and regenerate the sample.

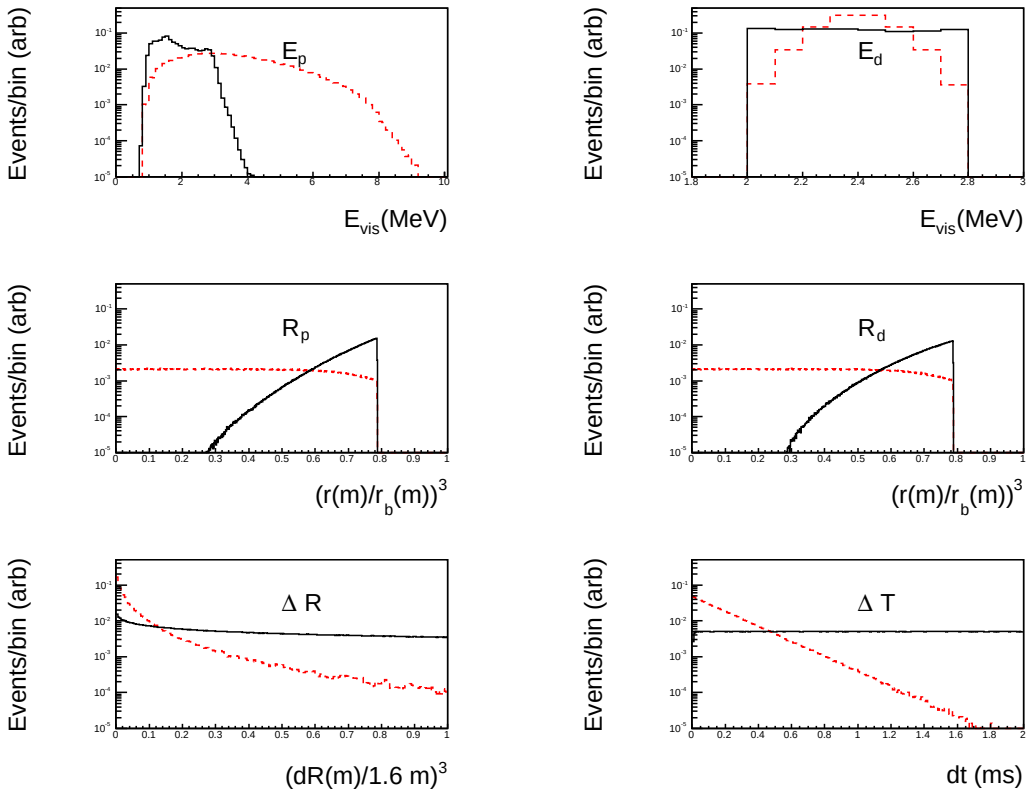

Figure 6.11: PDFs for each of the PDC selection parameters: $E_{\rm p}$, $E_{\rm d}$, $R_{\rm p}$, $R_{\rm d}$, ΔR, and ΔT for P-6. The red (dashed) curves are for accidentals, the black (solid) curves are for $\bar{\nu}_e$-like pairs.

where $W_{\Delta T}$ is the width of the ΔT window used in the analysis ($1499.5\,\mathrm{P}\,\mu s$). For both accidental and simulated-$\bar{\nu}_e$pairs we approximate $P(\vec{\xi}_0)$ as the fraction of pairs that populate the sub-volume of $\vec{\xi}$-space containing $\vec{\xi}_0$:

$$P_{\mathrm{Acc}}(\vec{\xi}_0\,) \simeq \frac{N_{\mathrm{Acc}}(\vec{\xi}_0 \pm \Delta\vec{\xi}\,)}{N_{\mathrm{Acc}}^{\mathrm{Tot}}} \qquad \text{and} \qquad P_{\bar{\nu}_e}(\vec{\xi}_0\,) \simeq \frac{N_{\bar{\nu}_e}(\vec{\xi}_0 \pm \Delta\vec{\xi}\,)}{N_{\bar{\nu}_e}^{tot}}\,. \tag{6.8}$$

P_{Acc} is estimated from the accidental sample, and $P_{\bar{\nu}_e}$ is estimated from the simulated-$\bar{\nu}_e$sample. In both cases the sample size is large, $N^{\mathrm{Tot}} > 10^7$, so the statistical error is small; the systematic error will be addressed later.

With this prescription in hand we partition $\vec{\xi}$-space into sub-volumes and calculate P_{Acc} and $P_{\bar{\nu}_e}$ for each volume; the partition is outlined in Table 6.7. An asymmetry can then be assigned to any candidate pair according to the sub-volume of $\vec{\xi}$-space it populates and the ΔT value of the pair. Figure 6.12 shows the $\mathcal{A}$ distributions

Table 6.7: Division of PDC parameter space used to define the likelihood asymmetry.

Parameter	Number of bins	Division
E_{p}	60	46 0.1-MeV bins from 0.9 MeV to 5.5 MeV 14 1.0-MeV bins from 5.5 MeV to 19.5 MeV
E_{d}	8	8 0.1-MeV bins from 2.0 MeV to 2.8 MeV
$R_{\mathrm{p}}(R_{\mathrm{d}})$	33	3 1-m bins from 0 m to 3 m 30 0.1-m bins from 3 m to 6 m
ΔR	16	16 0.1-m bins from 0.0 m to 1.6 m

for accidental and simulated-$\bar{\nu}_e$ pairs for four different ranges of E_{p}. By construction accidentals predominately occupy sub-volumes with negative $\mathcal{A}$ and $\bar{\nu}_e$-like pairs tend to occupy volumes with positive $\mathcal{A}$. By cutting sub-volumes with large accidental content but small signal-like content we can improve the signal-to-accidental-background ratio.

To choose which sub-volumes to cut we introduce the following figure-of-merit which is based on the statistical significance of the expected remaining $\bar{\nu}_e$-signal level,

$$\mathcal{FOM}(\mathcal{A}, E_p) = \frac{\Sigma_{\bar{\nu}_e}(\mathcal{A}\,, E_p)}{\sqrt{\Sigma_{\bar{\nu}_e}(\mathcal{A}\,, E_p) + \Sigma_{\mathrm{Acc}}(\mathcal{A}\,, E_p)}}\,. \tag{6.9}$$

The quantity $\Sigma_{\bar{\nu}_e}(A' \,|\, E'_p)$ is the expected number of $\bar{\nu}_e$-signal events with $\mathcal{A} > \mathcal{A}'$, summed over all the sub-volumes of PDC-space that contain pairs with $E_p = E'_p$ (Table 6.7); the term $\Sigma_{\mathrm{Acc}}(A' \,|\, E'_p)$ is similarly defined. The figure-of-merit depends on the relative normalization of the accidental and simulated-$\bar{\nu}_e$samples. In the analysis the $\bar{\nu}_e$sample is normalized to the number candidates expected from the reactor-flux

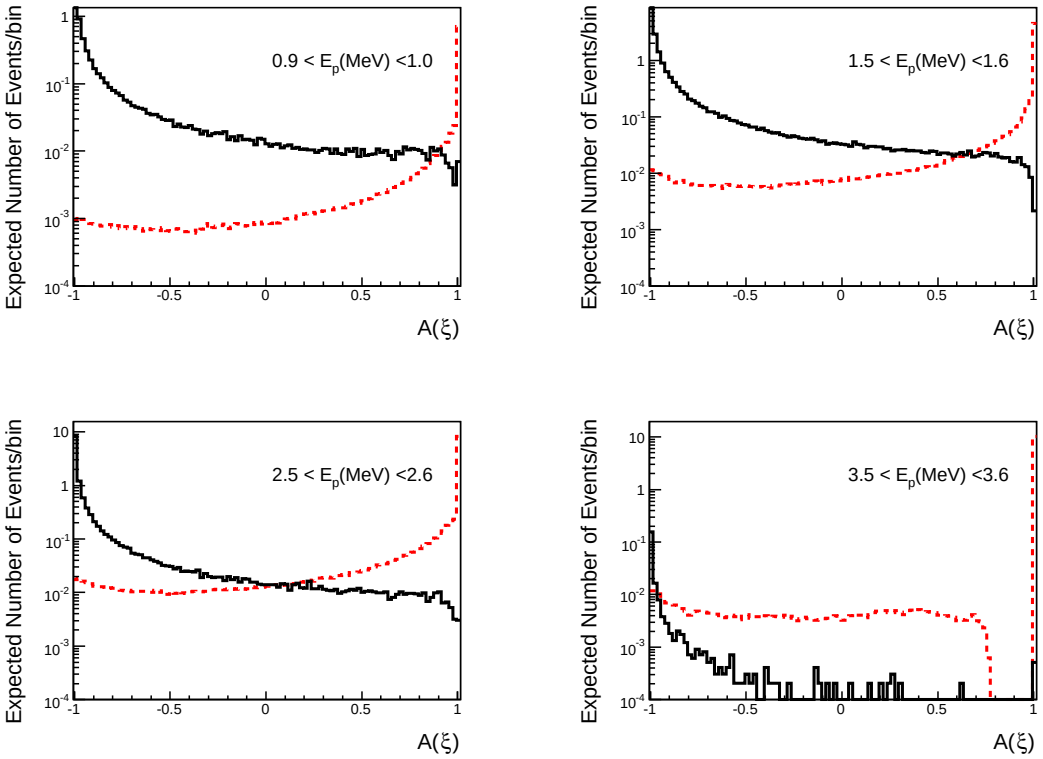

Figure 6.12: Likelihood asymmetry for accidental and simulated-$\bar{\nu}_e$ pairs for four prompt-energy intervals. The red (dashed) curve is for accidentals, the black (solid) is for $\bar{\nu}_e$-like pairs.

(without oscillation) described in Chapter 5. Figure 6.13 shows the figure-of-merit and signal selection efficiency for four different intervals of $E_{\rm p}$. For each bin in $E_{\rm p}$ and each period P-1, P-2, $\cdots$, P-6, the cut threshold ($\mathcal{A}_{\rm Cut}(E_{\rm p})$) is chosen to maximize $\mathcal{FOM}$, and pairs with $\mathcal{A}(E_{\rm p}) < \mathcal{A}_{\rm Cut}(E_{\rm p})$ are rejected. Referring to Figure 6.13, one can see that for low $E_{\rm p}$, due to the high accidental-rate, $\mathcal{FOM}$ is only maximized near $\mathcal{A} = +1$, with a signal selection efficiency of $\sim 50\%$. As one moves to higher $E_{\rm p}$, the accidental-background rate decreases and the cut becomes increasingly efficient for signal. The expected accidental-background levels with and without the $\mathcal{A}$-cut

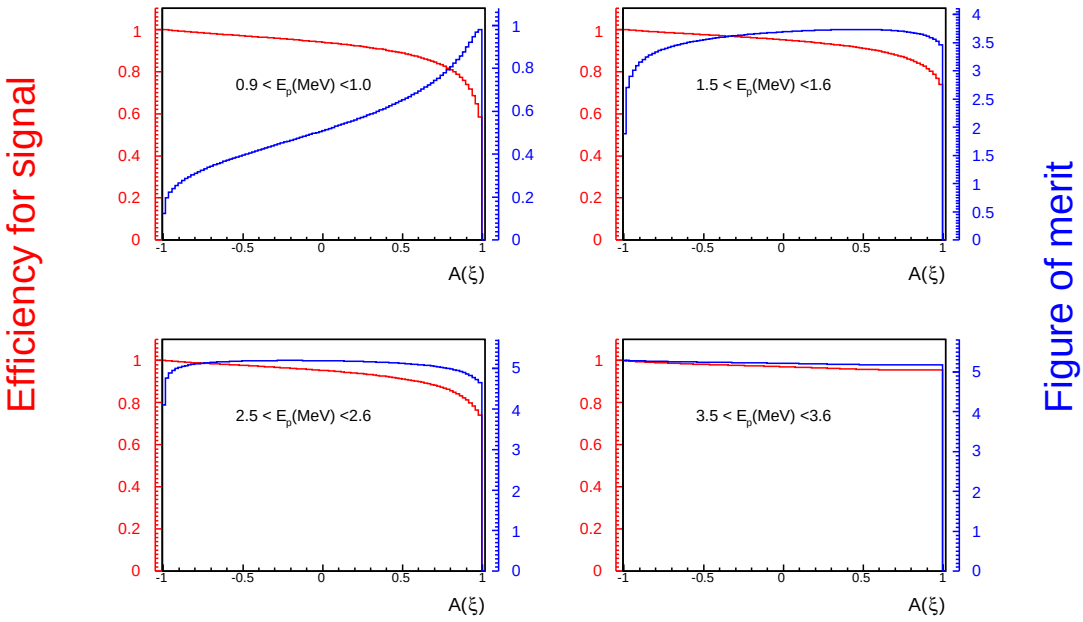

Figure 6.13: Examples of signal selection efficiency (red curve, left axis) and figure-of-merit (blue curve, right axis) versus likelihood asymmetry for 4 different prompt-energy intervals.

applied are summarized in Table 6.8. An almost 50-fold reduction of the background level is achieved with only 3% loss in expected signal.

The efficiency of the $\mathcal{A}$-cut to select signal-like pairs is estimated using the simple simulation and the results are shown for each period in Figure 6.14. The improvement in efficiency for P-5 and P-6 is due LS purification. Beyond $E_{\rm p} = 4.0$ MeV the efficiency is 100% for all periods. To estimate the systematic uncertainty due to vertex reconstruction biases, the ΔR-shape and energy-scale uncertainties, the simulation

Table 6.8: Expected number of candidates from accidental coincidences in the $\bar{\nu}_e$ candidate sample after just the level-I cuts and after both the level-I and -II cuts.

	Accidental Background	
Period	Level-I	Level-I + II
P-1	1101.0 ± 0.4	22.80 ± 0.06
P-2	912.6 ± 0.4	14.40 ± 0.05
P-3	909.3 ± 0.4	15.86 ± 0.05
P-4	890.4 ± 0.4	15.41 ± 0.05
P-5	448.5 ± 0.3	5.88 ± 0.03
P-6	415.4 ± 0.2	8.90 ± 0.04
Total	4677.3 ± 0.8	83.2 ± 0.1

was repeated with different choices of the ΔR PDF, with and without application of the measured vertex reconstruction bias functions, and with the energy scale parameters perturbed within their uncertainties. Figure 6.15 shows the relative change in the efficiency for a number of such simulations for P-6. Similar results are found for the other 5 periods. The efficiency changes by at-most 0.8%, this value is taken as the systematic uncertainty on the level-II cut efficiency.

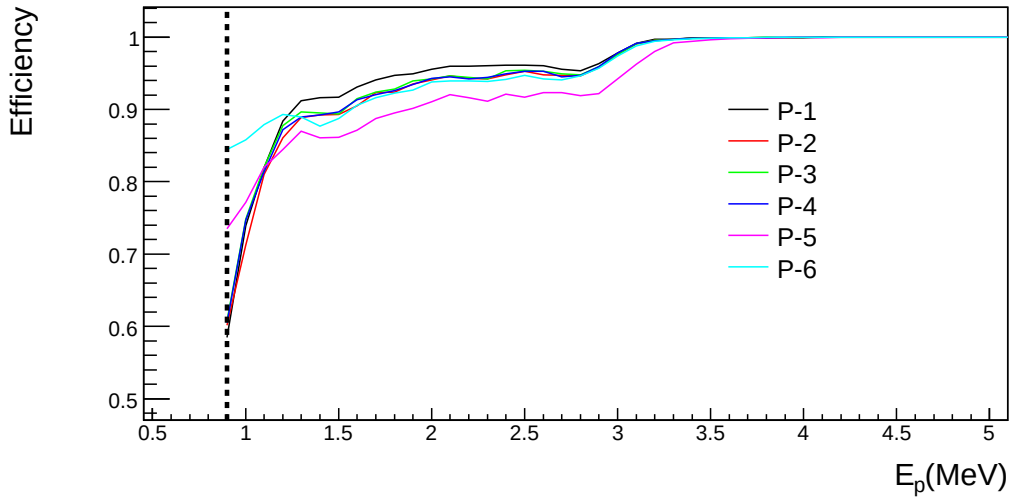

Figure 6.14: Efficiency to select a PDC pair as a function $E_{\rm p}$ with the level-II cut for each accidental period; the efficiency is only valid for pairs that populate ($E_{\rm d}$, $R_{\rm p}$, $R_{\rm d}$, ΔR, ΔT) space in the same way as $\bar{\nu}_e$-like pairs.

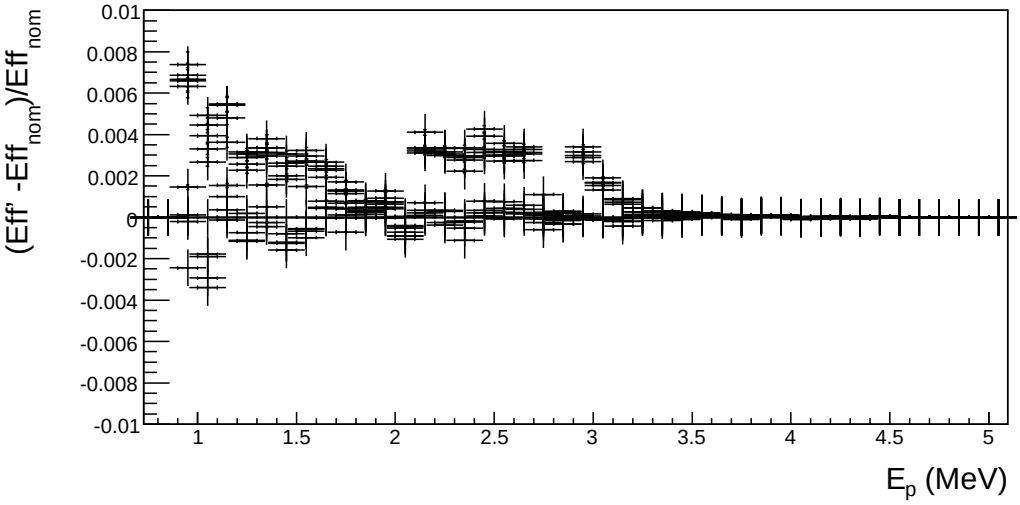

Figure 6.15: Relative change in the level-II cut efficiency as a function of $E_{\rm p}$ found by varying the input PDFs of the efficiency calculation.

6.4 Alpha-n background

Alpha-n reactions are a source of fast neutrons which form a background for $\bar{\nu}_e$detection. Figure 6.16 shows the α-n cross section weighted by the number of target nuclei for the most numerous targets in the LS [81], below α energies of ~ 11 MeV the $^{13}\mathrm{C}(\alpha,\mathrm{n})^{16}\mathrm{O}$ reaction is evidently the dominant one. The most significant α-source in the LS — by more than a factor of 10^5 — is the 5.304 MeV decay of ^{210}Po [82]. Thus only the $^{13}\mathrm{C}(\alpha,\mathrm{n})^{16}\mathrm{O}$ reaction with a ^{210}Po α-source (denoted by $^{210}\mathrm{Po}^{13}\mathrm{C}$) is considered in the background estimate.

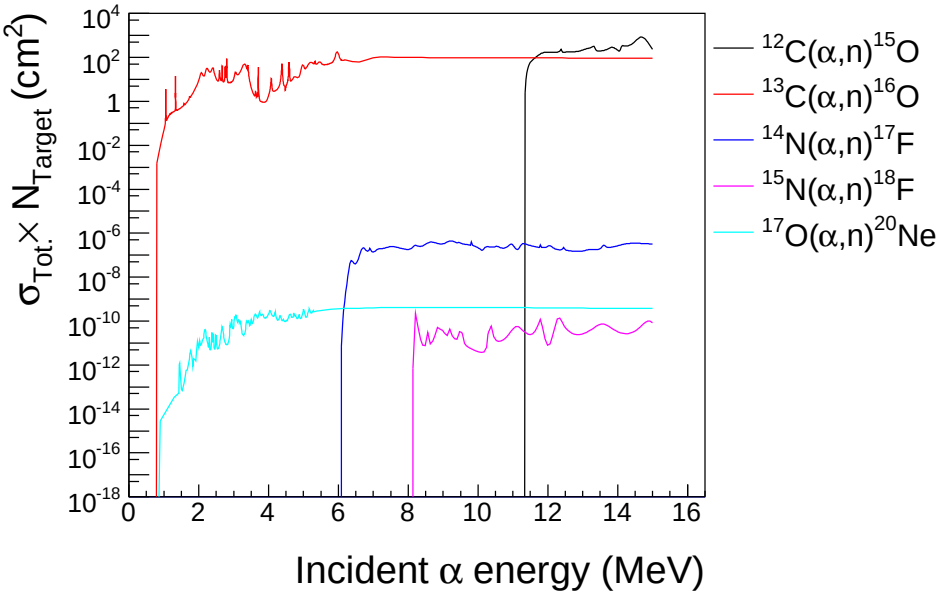

Figure 6.16: α-n cross section for the most abundant isotopes in KamLAND, each curve is weighted by the corresponding number of targets in the LS.

6.4.0.1 Expected neutron yield and real-energy spectrum

For a mono-energetic α-source with energy E_α the total neutron yield is

$$N_{Tot} = n_{\mathrm{target}}\,\mathcal{N}_\alpha \int_0^{E_\alpha} dE' \frac{\sigma_{Tot}(E')}{dE/dX(E')}\,, \tag{6.10}$$

where n_{target} in the number density of target nuclei, $\mathcal{N}_\alpha$ is the number of incident alphas, dE/dX is the alpha stopping power in the target material and σ_{Tot} is the

Table 6.9: Final states of ^{16}O accessible in the ^{13}C(α(5.304 MeV), n)^{16}O reaction, α-energy threshold for each state and decay radiation of excited states.

^{16}O-level	E-level(MeV)	Production threshold(MeV)	Decay radiation
g.s	0.0	0.0	stable
1^{st}	6.049	5.013	e^+/e^-
2^{nd}	6.130	5.119	γ

total α-n cross section. To evaluate Equation 6.10 for the ^{210}Po^{13}C reaction we use the total cross section measurement from [83], which has a 4% uncertainty, and use alpha stopping power tables from SRIM [61]. The neutron yield per alpha per target density is found to be $(1.64 \pm 0.07) \times 10^{-28}\,\mathrm{cm}^3$; the uncertainty is driven by the uncertainty on σ_{Tot}. Combining this with the ^{13}C number-density in the LS, $(3.71 \pm 0.04) \times 10^{20}\,\mathrm{cm}^{-3}$, we expect $(6.1 \pm 0.3) \times 10^{-8}$ neutrons per ^{210}Po decay.

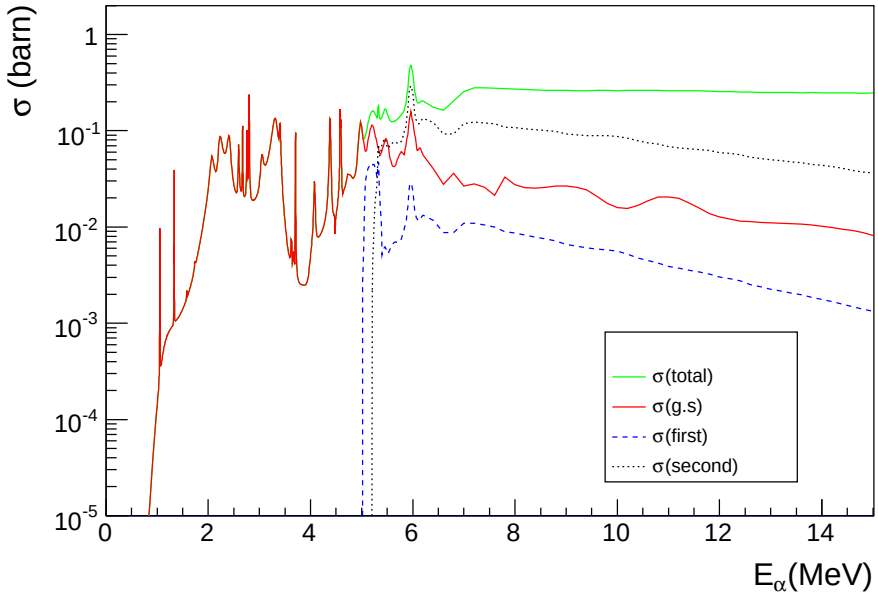

Figure 6.17: Total cross section and final-state partial cross sections for ^{13}C(α, n)^{16}O. Only final states accessible to ^{210}Po α-decays are shown.

The neutron energy spectrum depends on the ^{16}O final state and the direction of neutron emission. The accessible final states and accompanying decay radiation are

listed in Table 6.9. Following Equation 6.10, the spectrum for each final state is

$$N_i(E_n) = n_{\text{target}}\,\mathcal{N}_\alpha \int_0^{4\pi} d\Omega \int_0^{E_\alpha} dE' \frac{\sigma_{p,i}(E')}{dE/dX(E')} \frac{dP_i}{d\Omega}(E',\Omega)\,\delta(f(E',\Omega),E_n)\,, \quad (6.11)$$

where the index i labels the final state of $^{16}\text{O}(i = g.s, 1^{st}, 2^{nd})$, $\sigma_{p,i}$ is cross section to produce the i^{th} final state (partial cross section), $dP/d\Omega$ is the probability that the outgoing neutron is scattered the direction Ω, and the δ-function imposes the kinematic constraint between the incoming alpha energy and the outgoing neutron energy.

Equation 6.11 is evaluated using Monte-Carlo integration. The $\sigma_{p,i}$ were retrieved from the JENDL [81] database, below 5.013 MeV we substitute σ_{Tot} from Harissopulos et al. [83] for $\sigma_{p,0}$ since below this threshold the ground state is the only accessible final state, we refer to this combination as the JENDL-Harissopulos cross section. The total and partial cross sections are shown in Figure 6.17. We write the function $\frac{dP}{d\Omega}$ using an eighth order Legendre polynomial expansion:

$$\frac{dP}{d\Omega}(E) = \frac{1}{\mathcal{N}} \sum_{l=0}^{8} a_l(E) A_l(\cos(\theta))\,, \quad (6.12)$$

where $\mathcal{N}$ is a normalization constant, $\mathcal{A}_l$ is the Legendre polynomial of order l, and θ is the angle between the momenta of the incoming α and outgoing neutron. The coefficients $a_l(E)$ were taken from angular correlation measurements found for this reaction in the literature [84, 85] Figure 6.18 shows the resultant neutron real-energy spectra associated with each final state.

6.4.0.2 Prompt visible-energy spectrum

With the neutron real-energy spectra in hand the next step is to estimate the prompt visible-energy spectrum in the LS. A neutron produces scintillation light indirectly by scattering on protons and carbon nuclei. Figure 6.19 shows the cross sections for the neutron scattering processes considered in the analysis. The visible-energy spectrum was calculated using a Monte-Carlo. A large number of alphas were simulated, for each alpha the energy lost before undergoing the α-n reaction was recorded; a neutron with real-energy distributed according to Equation 6.11 was produced; each neutron was allowed to undergo p or C scattering, at each scatter the real energy and identity of secondary particles — scattered p, C nucleus, or photon from inelastic scattering — was recorded. For simplicity isotropic scattering in the CM frame was assumed for all neutron scatters. Each neutron was tracked down to 1 eV. The real energy of each secondary particle was converted to visible energy — without smearing for detector resolution — and these were summed together. The unsmeared visible energy deposited by the alpha and decay radiation from $^{16}\text{O}^*$ were also added. The sum was then smeared with the detector energy-resolution function.

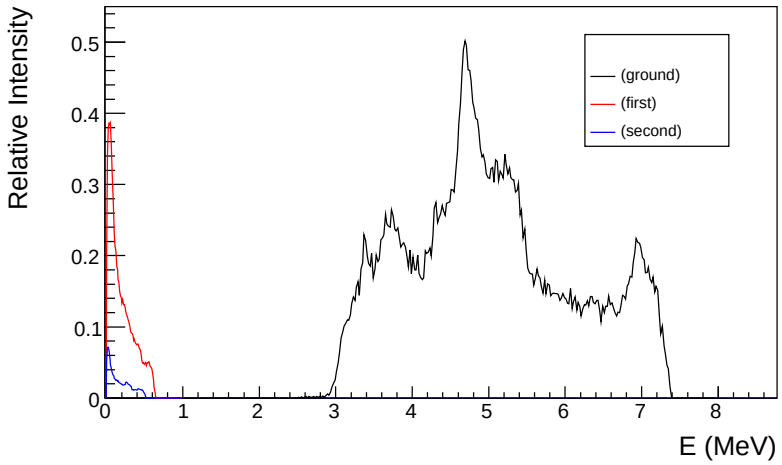

Figure 6.18: Real-energy spectra of neutrons produced in association with each accessible final state of ^{16}O in the ^{210}Po^{13}C reaction.

A ^{210}Po^{13}C calibration source was constructed and deployed in late 2006 to study the ^{210}Po^{13}C background. We use this data to directly constrain the branching fractions to each ^{16}O final state and check the validity of the simulated prompt visible-energy spectrum. The ^{210}Po^{13}C source is described in detail in [58], it consisted of 100μCi of ^{210}Po uniformly mixed with 0.3g of ^{13}C powder, the source mixture was doubly encapsulated in two 1-mm-thick stainless-steel capsules, a schematic is shown in Figure 6.20. Delayed coincidence pairs were selected from the calibration data using the same level-I selection conditions as for $\bar{\nu}_e$candidates. A background-subtracted prompt-energy spectrum was constructed by subtracting an off-time (510 $\mu s < \Delta T <$ 1000 μs) $E_{\rm p}$ spectrum from an on-time (10 $\mu s < \Delta T <$ 510 μs) $E_{\rm p}$ spectrum. An expected real-energy spectrum was prepared for each final state branch. These were then fed to a fitting routine which converted them to visible energy and fitted them to the observed prompt visible-energy spectrum using a binned maximum likelihood. The relative normalizations of the branches and the energy scale parameters were allowed to vary in the fit, however a penalty term was added to the likelihood to constrain the energy scale parameters to the best-fit values found in Chapter 4.

Figure 6.21 shows the observed prompt-energy spectrum from the calibration source together with the best-fit components from the simulation. The resulting best-fit branching fractions (b_0 , b_1 , b_2) together with those expected based on the JENDL-Harissopulos cross sections are listed in Table 6.10. In the case of b_1, the e^+/e^- stop in the source and only the e^+-annihilation photons contribute to the visible energy, consequently these events have visible energy of $\sim$ 1 MeV and are obscured by events from b_0. We find b_1 and b_0 are strongly anticorrelated and the uncertainty

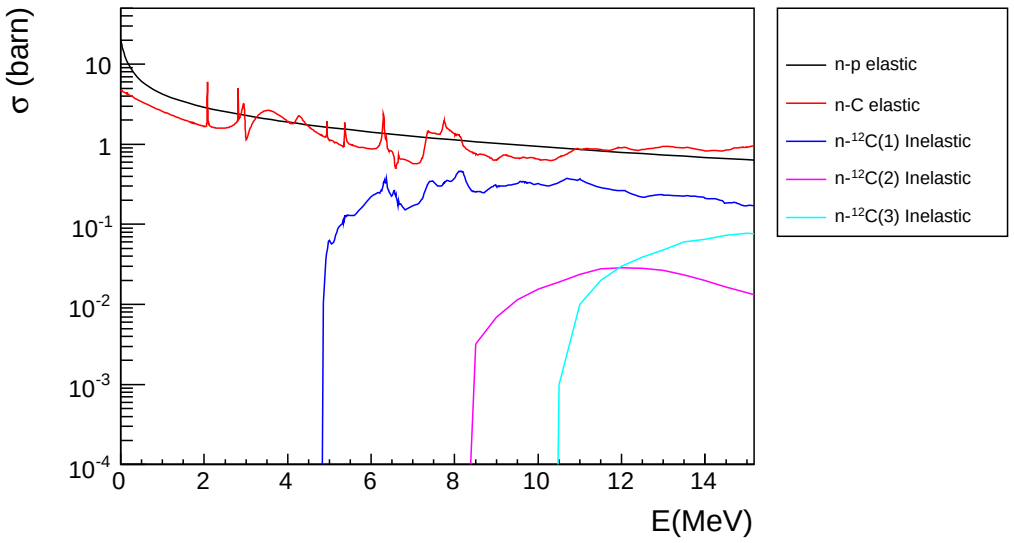

Figure 6.19: Cross sections for the processes considered in the neutron real-to-visible energy conversion.

on b_1 is relatively large.

The spectrum predicted by the simple simulation does not replicate all the features of the measured spectrum. A more complete Geant4-based simulation was also done by adding an α-n process to the Geant4 toolkit. This simulation indicates that the features between $3 \sim 4.5$ MeV and $5.5 \sim 6.2$ MeV come from a combination of positron annihilation in flight, neutron inelastic scattering on ^{13}C and shadowing by the calibration hardware. Although the simple simulation does not model these effects, it was adopted it in preference to the full Geant4 simulation because it is reproduces the main features of the spectrum and it is computationally more convenient to propagate the energy-scale and branching fraction uncertainties to the final spectrum.

The branching fractions for ^{210}Po^{13}C events in the LS differ slightly to those from the ^{210}Po^{13}C source since the stopping power of α's in the LS and source material are different. When constructing the visible-energy spectrum for ^{210}Po^{13}C events in the LS we define the branching fraction for each final state (b_i^{LS}) as

$$b_i^{LS} = \frac{b_{\mathrm{JENDL,i}}^{\mathrm{source}}}{b_{\mathrm{JENDL,i}}^{LS}} \times b_i^{\mathrm{source}}\,, \tag{6.13}$$

where b_i^{source} is the best-fit branching fraction using the ^{210}Po^{13}C-source data and $b_{\mathrm{JENDL,i}}^{LS}$ and $b_{\mathrm{JENDL,i}}^{\mathrm{source}}$ are the branching fractions in the LS and source materials calcu-

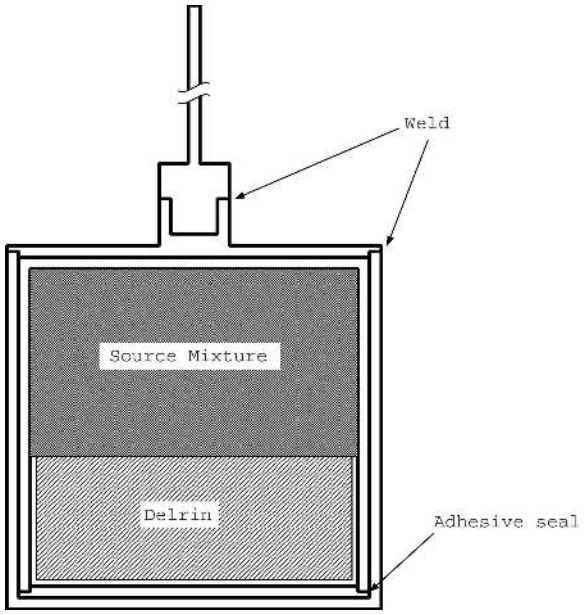

Figure 6.20: Schematic of the ^{210}Po^{13}C source, reproduced from [58].

lated using the JENDL-Harissopulos cross sections. Figure 6.22 shows the expected prompt visible-energy spectrum for ^{210}Po^{13}C events in the LS, the spectra expected after level-I and level-II cuts are also shown.

Table 6.10: Comparison of best-fit and expected branching fractions for each of the accessible ^{16}O final states for the ^{210}Po^{13}C source data.

^{16}O State	Branching fraction	
	Best-fit	Expected (JENDL-Harissopulos)
g.s (b_0)	0.928 ± 0.023	0.898
1^{st} (b_1)	0.062 ± 0.010	0.089
2^{nd} (b_2)	0.0098 ± 0.0003	0.013

6.4.0.3 Estimate of the ^{210}Po α-decay rate

The final quantity needed to normalize the ^{210}Po^{13}C background is the ^{210}Po decay rate. This is somewhat difficult to determine, unlike ^{214}Po or ^{212}Po alpha-decays which can be tagged by their coincidence with a preceding ^{214}Bi or ^{212}Bi decay, the ^{210}Po rate must be extracted from a fit to the total event spectrum. Due to quenching the ~5.3 MeV alphas are expected to reconstruct with mean visible

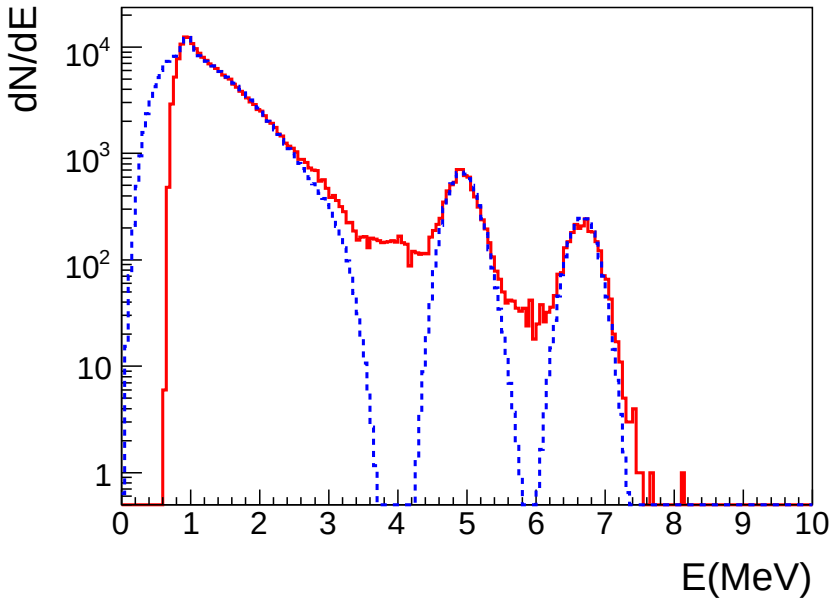

Figure 6.21: The solid (red) histogram is the prompt-energy spectrum of ^{210}Po^{13}C calibration events. The dashed (blue) histogram is the best-fit model. The model does not replicate all the features of the measured spectrum, so the fit is restricted to the intervals: 0.9 MeV $<E_{\rm p}<$2.5 MeV, 4.4 MeV $<E_{\rm p}<$5.6 MeV and 6.2 MeV $<E_{\rm p}<$7.2 MeV.

energy $\langle E_{vis}\rangle \simeq 0.3$ MeV, in this region the reconstruction tools are more likely to fail the default quality requirements imposed at higher energies and we expect a large background from ^{14}C, ^{85}Kr and ^{210}Bi decays in the LS. The impact of reconstruction failure on the shape of the visible-energy spectrum is difficult to model reliably and incorporate into the real-to-visible energy conversion so instead we estimate the ^{210}Po decay rate from a fit to the NSumMax spectrum.

Figure 6.23 shows the NSumMax distributions for events with reconstructed position inside the fiducial volume; when selecting events the reconstruction-quality cut was relaxed, only events for which the position reconstruction failed to converge were rejected. We find 97% of events pass this cut. The NSumMax spectrum is modeled assuming a gaussian signal from ^{210}Po and a second order polynomial to describe the background, there is no particular motivation for this choice of background shape except that it is the simplest choice that fit the NSumMax spectrum. The best-fit model

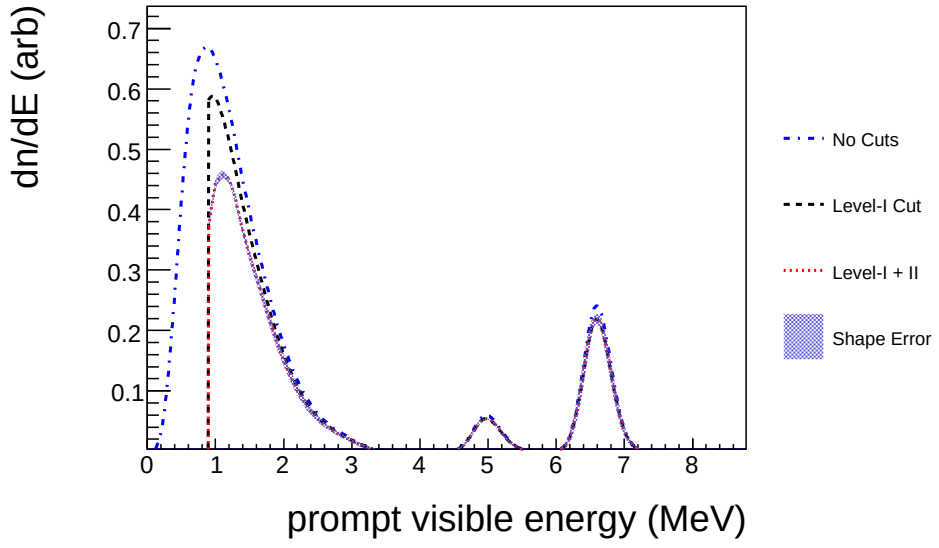

Figure 6.22: Expected prompt energy spectrum of ^{210}Po^{13}C PDC pairs. The shape error is estimated by varying the energy-scale parameters and branching fractions within their uncertainties.

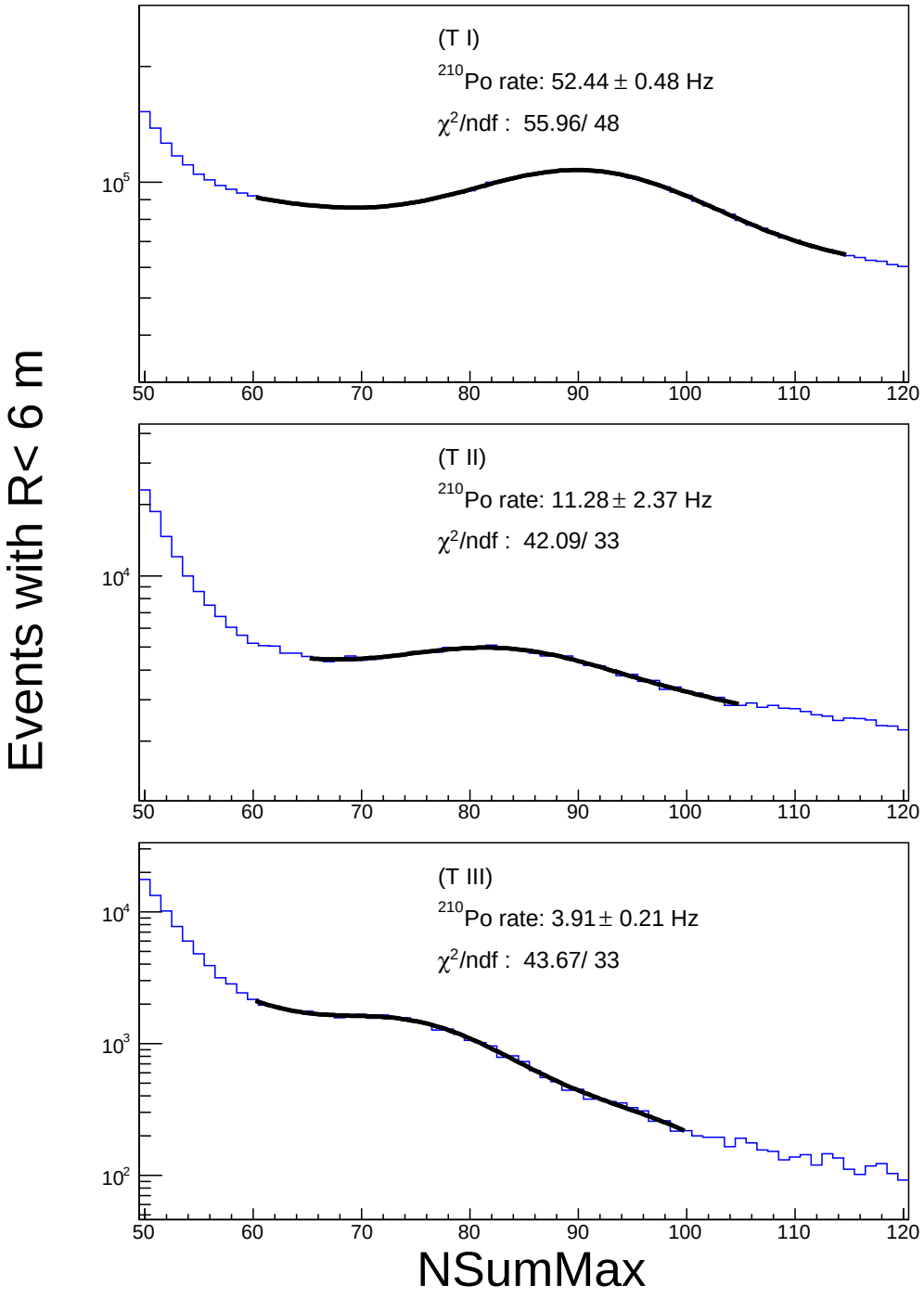

Figure 6.23: Each panel corresponds to a data period: T-I, T-II and T-III. Each histogram is the NSumMax distribution for low-energy events that reconstruct inside the fiducial volume. The curve is the best-fit model assuming a gaussian signal from ^{210}Po decays and a quadratic background function.

and resultant ^{210}Po decay rate for each period are shown in Figure 6.23. To estimate the systematic error of this analysis, waveform data were generated using Geant4 for uniformly distributed sources of ^{210}Po and each of the expected backgrounds: ^{14}C, ^{85}Kr and ^{210}Bi. The simulated NSumMax distributions were then summed together assuming random values for the normalization of each component. The model was fit to the resultant NSumMax spectrum and the best-fit ^{210}Po rate was compared to the known rate used to construct the spectrum. This process was repeated a large number of times. This study indicates a 20% systematic error on the best-fit ^{210}Po rate. The expected ^{210}Po decay rates for each period are summarized in Table 6.11. The successive reduction in rate for T-II and T-III is due to LS purification.

Table 6.11: Best-fit ^{210}Po decay rate for each data period.

	T-I	T-II	T-III
Rate (Hz)	52 ± 11	11 ± 3	3.9 ± 0.8

6.4.0.4 ^{210}Po^{13}C summary

Table 6.12 summarizes the expected background level from ^{210}Po^{13}C . In all, after the level-I and -II cuts we expect 145 ± 30 events from ^{210}Po^{13}C in the $\bar{\nu}_e$candidate sample.

Table 6.12: Summary of the expected number of ^{210}Po^{13}C events for the three data periods. The first two rows give the number of alpha decays and total number ^{210}Po^{13}C reactions expected for each period. The third row lists the total number of events expected after the level-I and -II cuts.

	TI		TII		TIII	
$\mathcal{N}_\alpha$	$(5 \pm 1) \times 10^9$		$(1.7 \pm 0.3) \times 10^8$		$(2.9 \pm 0.6) \times 10^7$	
$N_{\alpha-\mathrm{n}}$	258 ± 52		10 ± 2		1.8 ± 0.4	
	Level-I	Level-II	Level-I	Level-II	Level-I	Level-II
$N_{\alpha-\mathrm{n}}$	158.3	139.8	4.6	4.0	1.57	1.42

6.5 Cosmogenic backgrounds

In this section we describe backgrounds caused by cosmic-rays muons that pass through or close to the detector.

6.5.1 Spallation ^{9}Li and ^{8}He

^{9}Li and ^{8}He are delayed neutron β emitters which are produced by muons traversing KamLAND [54]. Coincidence of a prompt beta-decay and capture of the associated delayed neutron represents a background for antineutrino detection. Some decay parameters for these nuclei are listed in Table 6.13 [86]. To study this background

Table 6.13: Some decay data for ^{9}Li and ^{8}He.

Nucleus	Q-value	Half life	$\beta - n$ fraction
^{9}Li	13.61 MeV	178.3 $\pm$0.4 ms	0.508
^{8}He	10.7 MeV	119.1 $\pm$0.1 ms	0.16

PDC pairs occurring between 0.002 s and 2 s after tagged LS muons were selected. To reduce background from other low-energy spallation products a prompt-energy threshold of 4 MeV was imposed. Figure 6.24 shows how the prompt events of the selected pairs are distributed in time following muons. The distribution was fit with the following function:

$$\frac{dN}{dt} = \frac{A}{\tau} e^{-t/\tau} + B\,, \tag{6.14}$$

which assumes a single decaying species with a mean lifetime τ and a time-independent background B. The best-fit lifetime is $\tau = 258 \pm 24$ μs, which is consistent with the established lifetime of ^{9}Li (257.3 ± 0.1 μs [57]); the total yield of spallation candidates with prompt energy greater than 4 MeV is 856 ± 46. A fit was also done using a model which included a second decaying species, however the best-fit lifetimes were not consistent with the expected lifetimes of either ^{9}Li or ^{8}He. When the lifetimes were fixed at their established values the ^{8}He yield was consistent with zero and the ^{9}Li yield agreed well with the result of the single-species fit.

To reduce the background from these long-lived spallation products in the antineutrino candidate sample we introduce the following cuts:

- **Bad LS-muon cut**
  All candidates occurring between 0.002 s and 2 s after an LS showering-muon or an LS muon with a poorly reconstructed track are rejected.

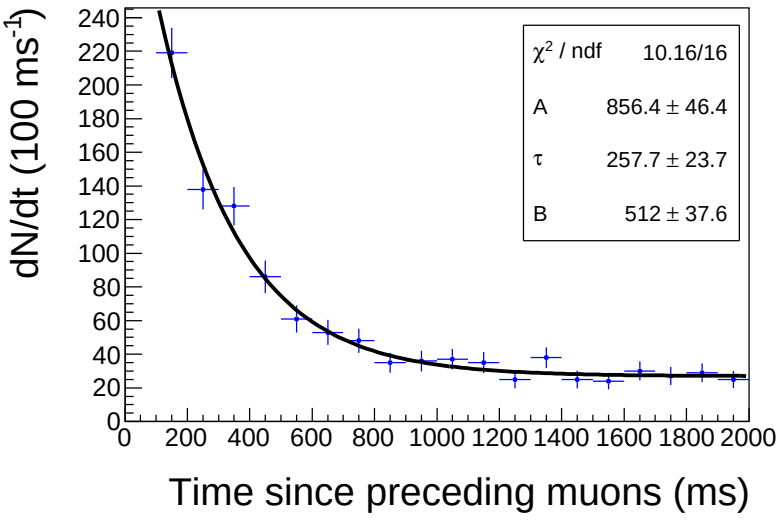

Figure 6.24: The histogram is the time since muon for the prompt event of all PDC candidates occurring within 0.002 s and 2 s of an LS muon. The curve is the best-fit model assuming a single decaying species and a constant background.

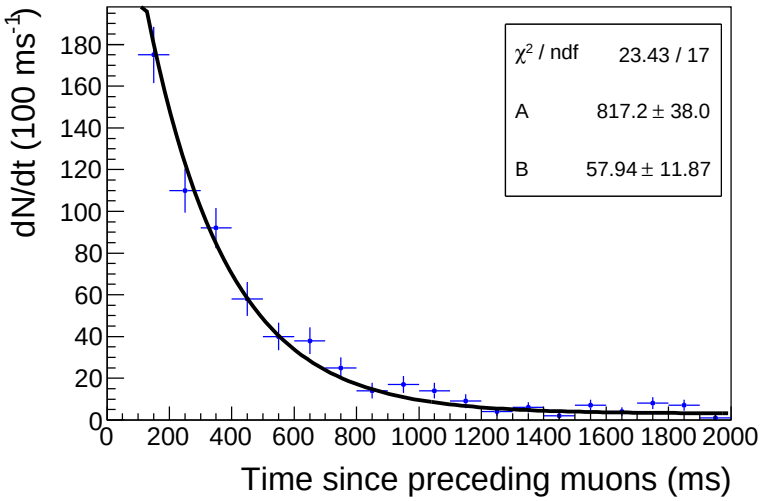

Figure 6.25: The histogram is the time since muon for the prompt event of all PDC candidates occurring within 0.002 s and 2 s of a showering or poorly-reconstructed LS muon. The curve is the best-fit model assuming decay of ^{9}Li and a constant background.

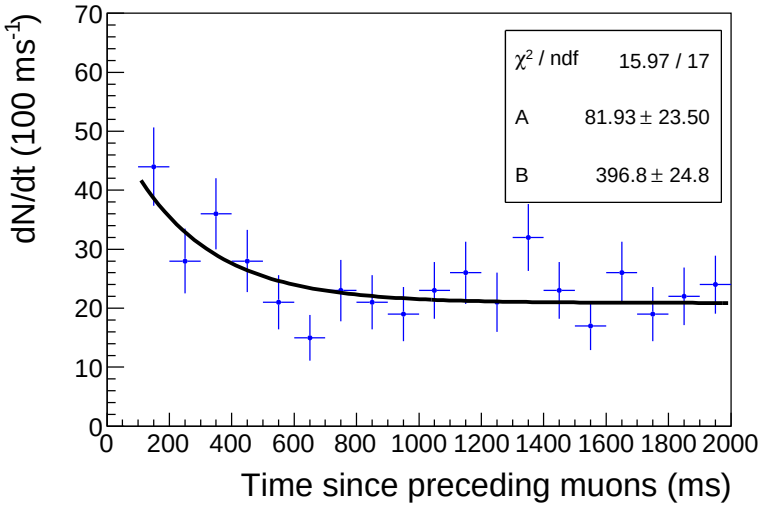

Figure 6.26: The histogram is the time since muon for the prompt event of all PDC candidates with only non-showering, well-reconstructed LS muons in the preceding 2 s. The curve is the best-fit model assuming decay of ^{9}Li and a constant background.

- **Good LS-muon cylinder cut**

  All candidates occurring between 0.002 s and 2 s after an LS muon with a well-reconstructed track are rejected if the prompt event reconstructs inside a 3-m-radius cylinder centered on the muon track.

We find that most ^{9}Li-^{8}He candidates occur after the first category of muons. Figure 6.25 shows how the prompt event of candidates occurring after showering and poorly-reconstucted muons are distributed in time relative to those muons. Again this distribution is fit with a model that assumes a single species decay and a constant background. With the lifetime fixed at $\tau = 257.3$ ms, the best-fit yield of spallation candidates with $E_{\rm p} > 4\,{\rm MeV}$ is 817 ± 38; we estimate 0.34 ± 0.44 of these remain in the $\bar{\nu}_e$-candidate set after the bad-LS-muon cut.

Figure 6.25 shows PDC candidates found between 0.002 s and 2 s after non-showering, well-reconstructed muons. Using the same fixed-lifetime model as before the best-fit candidate yield from this class of muon is 82 ± 24. The efficiency of the muon track cylinder cut is estimated from ^{12}B spallation candidates; we find $89 \pm 1\%$ of ^{12}B candidates reconstruct within a 3-m-radius cylinder of the associated muon track. Applying this efficiency to ^{9}Li we expect 9 ± 3 of spallation pairs to remain following the good-LS-muon cut. Figure 6.27 shows how candidates that pass the 2 s, 3-m-radius cut are distributed in time relative to the preceding muons. Using the fixed-lifetime model, the best-fit yield is 7 ± 16 which is consistent with the preceding estimate. The background levels after both classes of muon are summarized in Table 6.14.

Table 6.14: Summary of the long-lived spallation background levels.

Cut name	Cut efficiency(%)	Without cut	With cut
Bad LS μ	99.96 ± 0.05	817 ± 38	0.34 ± 0.44
Good LS μ cylinder	89 ± 1	82 ± 24	9 ± 3

Figure 6.5.1 shows the expected prompt visible-energy spectrum for PDC candidates from ^{9}Li. This spectrum was constructed using decay data for the delayed-neutron branches found in [86]; small corrections for the prompt visible-energy of the delayed neutron are not included. We find $73 \pm 1\%$ of the spectrum is above 4 MeV. Thus after the level-I and -II cuts we expect 11 ± 4 events from ^{9}Li in the $\bar{\nu}_e$-candidate sample.

6.5.1.1 Exposure loss due to long-lived spallation cuts

To estimate the loss of exposure due the cuts that target ^{9}Li a set of fake test-events distributed uniformly in time and in position were embedded into the data set. The top panel of Figure 6.29 shows the fraction of test events remaining after the spallation cuts, which we call the *spallation efficiency*, as a function of run date.

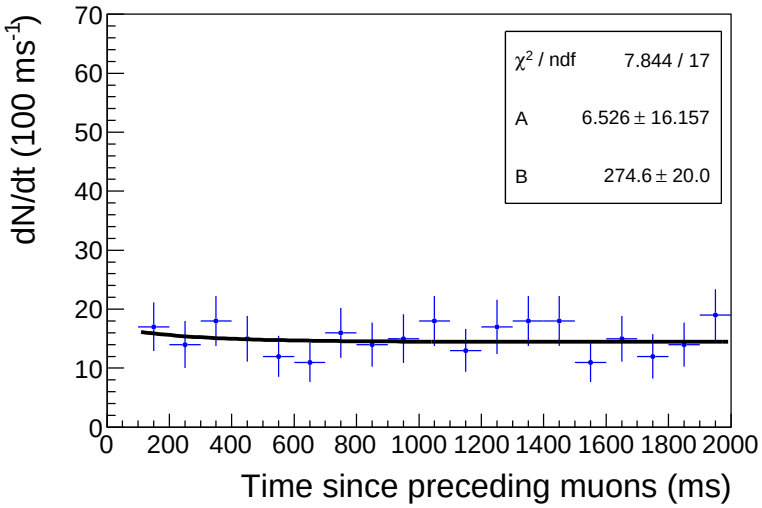

Figure 6.27: The histogram is the time since muon for the prompt event of all PDC candidates that pass the *Good LS-muon cylinder cut* described in the text. The curve is the best-fit model assuming decay of ^{9}Li and a constant background.

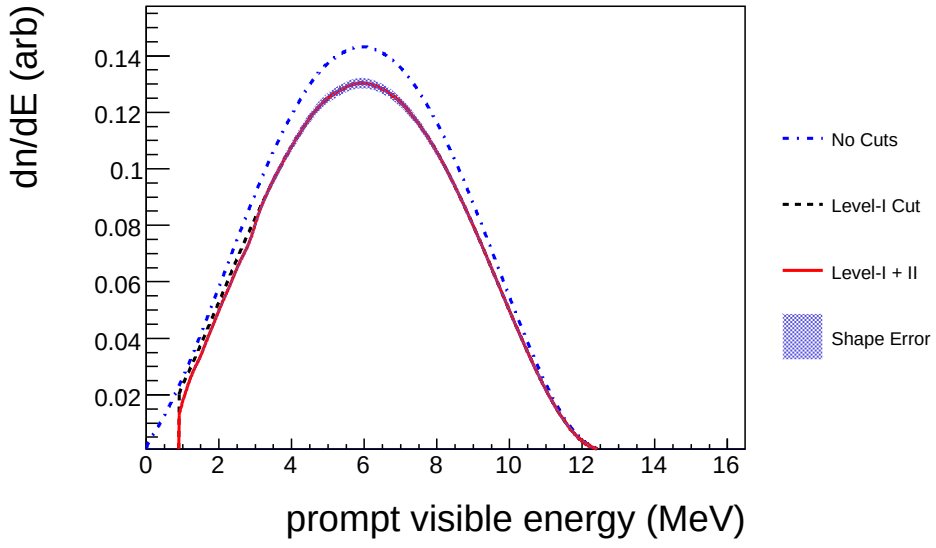

Figure 6.28: Expected prompt-energy spectrum of PDC pairs from ^{9}Li. The shape error is estimated by varying the energy-scale parameters and branching fractions within their uncertainties.

On average, the ^{9}Li cuts introduce a 10% loss of exposure. The spallation efficiency increased slightly in 2007 due to an electronics-upgrade which improved the data readout after muons.

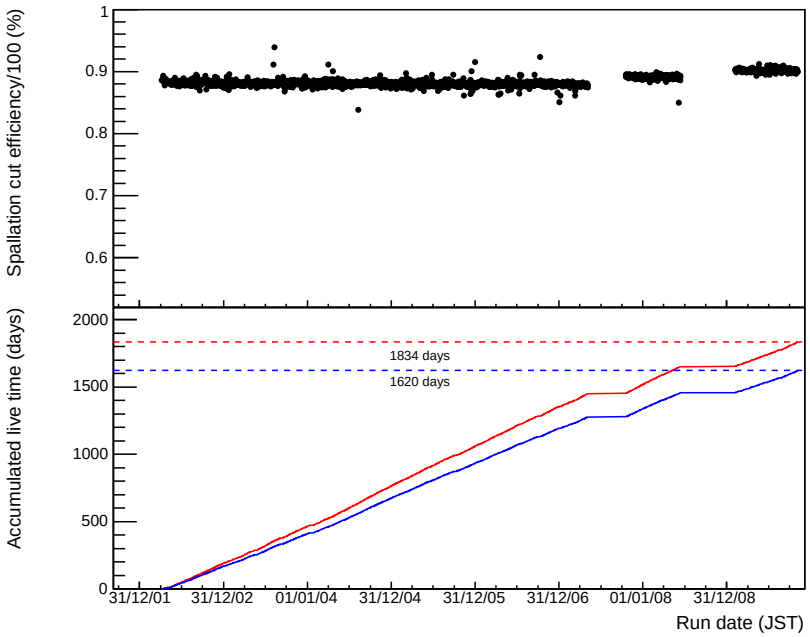

Figure 6.29: Spallation efficiency (top panel) and integrated live-time (bottom panel) versus run date. The red curve is the integrated live-time without the spallation cuts (1834 days) the blue curve is the live-time after the spallation cuts (1620 days).

6.5.2 OD fast neutrons

Just as with fast neutrons from α-n reactions, fast neutrons produced by untagged muons passing through the OD or the nearby rock can cause a background if the neutron scatters into the LS with a few MeV or more of energy. To study this background we select candidates that occur within 2 ms of OD-only muons, where an OD-only muon is one that triggers the OD but not the ID. Figure 6.30 shows how the

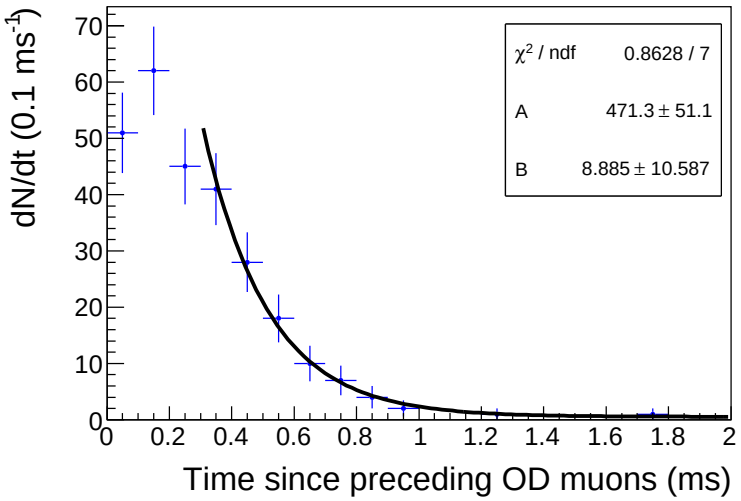

Figure 6.30: The histogram is the time since muon of the delayed event for all PDC candidates with only an OD muon in the preceding 2 ms. The curve is the best-fit model assuming a mean time-separation equal to the neutron capture time and a time-independent background.

delayed events for these candidates are distributed in time relative to the preceding muons. If we fit an exponential function and constant background to this distribution we find the mean time-separation is $212 \pm 30\,\mu s$, which is consistent with the expected mean neutron-capture-time, and the total candidate yield is found to be 487 ± 100. If we fix the mean time-separation in the model to the neutron capture time estimated in section 6.2.1 the yield is found to be 471 ± 51. Figure 6.31 shows the prompt energy spectrum of these candidates. There is a very clear peak in the bin containing the $\sim$2.2 MeV neutron capture gamma which indicates many PDC pairs are due to coincidence of multiple different neutron captures in the same ΔT window.

This background is reduced by applying a 2 ms veto after all tagged OD muons. We estimate the OD-muon tagging efficiency from the fraction of ID muons that also

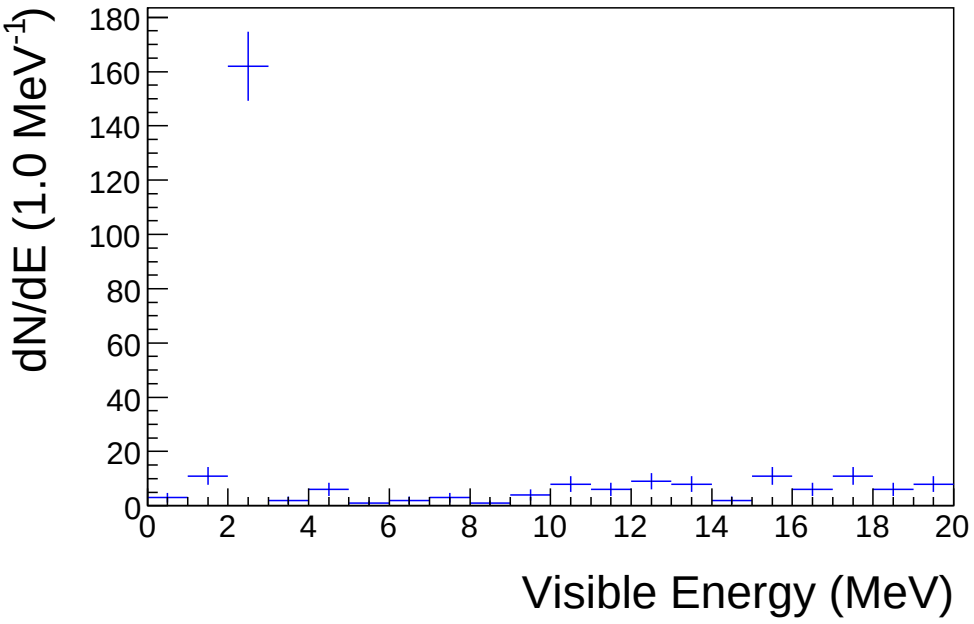

Figure 6.31: Prompt-energy spectrum of candidates preceded exclusively by OD-only muons in the previous 2 ms.

trigger the OD. Figure 6.32 shows the resultant efficiency as a function of time over the course of the data set. The efficiency is deteriorating with time, this is expected due to loss of PMTs in the OD. Using this efficiency curve we expect 4.7 ± 0.8 pairs from OD-neutrons in the $\bar{\nu}_e$ candidate sample. The exposure loss due to the 2 ms veto is negligible (<0.1 %).

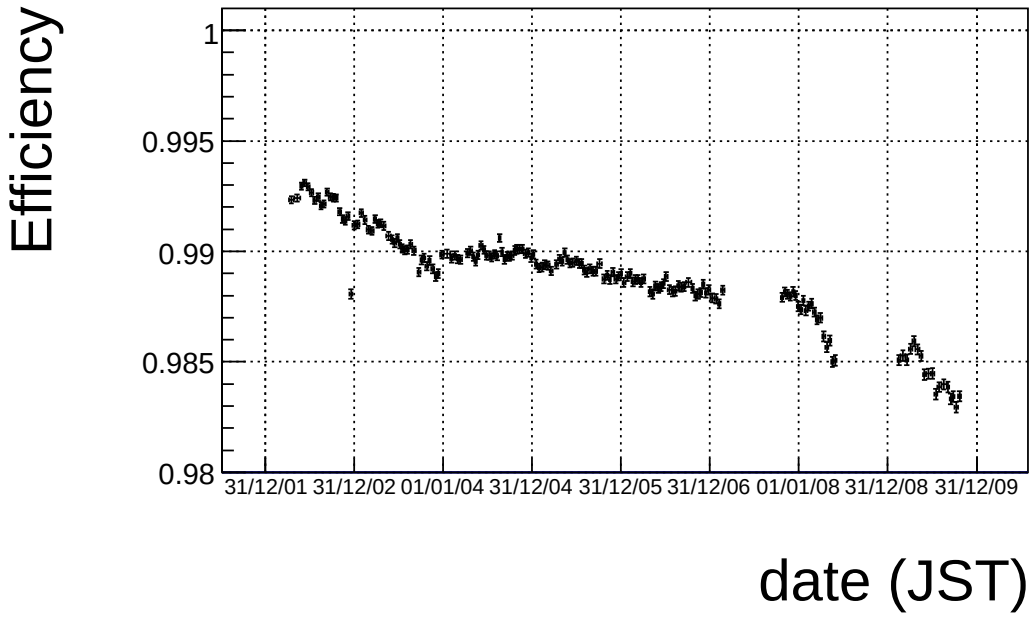

Figure 6.32: OD-muon tagging efficiency versus run date.

6.5.3 Atmospheric neutrinos

Atmospheric neutrinos, produced by cosmic ray interactions in the atmosphere, are expected to produce fast neutrons through quasi-elastic scattering on carbon in the LS. A simulation based on NUANCE and KLG4sim [5] [54] predicts that atmospheric-neutrino-induced candidates have an approximately flat prompt-energy spectrum [82]. We find 5 candidates in the interval 15 MeV $< E_{\rm p} <$20 MeV, assuming a flat prompt-energy spectrum for this class of pairs we estimate 20 atmospheric-neutrino-induced candidates. We assume a 100% uncertainty on this estimate.

[5]KLG4sim or KamLAND Geant4 simulation, is the name of the Geant4 application with the KamLAND detector response and geometry implemented.

6.6 Geo-neutrinos

Antineutrinos emitted from beta decays of ^{238}U, ^{232}Th and their daughters in the Earth are expected to contribute to the flux at KamLAND. These geologically produced neutrinos are dubbed *geo-neutrinos*. The total antineutrino spectrum shape expected for each of the ^{238}U and ^{232}Th chains can be constructed from known beta decay data [57]. The decays with Q-value above the inverse beta decay threshold are listed in Table 6.15. The expected rate as well as the relative contribution from

Table 6.15: Q-values and relative intensities for β decays in the ^{232}Th and ^{238}U series with Q-value above the inverse beta decay threshold.

	Decay	Q-value (MeV)	Relative Intensity (%)
^{232}Th	^{212}Bi $\rightarrow$ ^{212}Po	2.246	86.28
	^{228}Ac $\rightarrow$ ^{228}Th*	2.069	12.47
	^{228}Ac $\rightarrow$ ^{228}Th*	1.940	1.25
^{238}U	^{234}Pa $\rightarrow$ ^{234}U	2.207	77.75
	^{214}Bi $\rightarrow$ ^{214}Po	3.270	15.22
	^{214}Bi $\rightarrow$ ^{214}Po*	1.892	5.86
	^{214}Bi $\rightarrow$ ^{214}Po*	1.855	0.71
	^{214}Bi $\rightarrow$ ^{214}Po*	2.661	0.46

^{238}U and ^{232}Th depends on the distribution of the source nuclei in the Earth and one has to rely on models to predict these quantities. A reference Earth-model described in [42] predicts 30.52 TNU [6] from ^{238}U and 8.04 TNU from ^{232}Th. For the source distributions assumed in the oscillatory term $[\sin^2(\Delta m^2 L/E)]$ in the survival probability can be well approximated (to better than 1%) by the average value (1/2). Based on this we assume an undistorted antineutrino spectrum for geo-neutrinos in the analysis. The expected prompt-energy spectrum for geo-neutrino candidates with and without the selection cuts are shown in Figure 6.33. Given the assumptions above we expect 84 candidates from geo-neutrinos in the candidate sample after the level-I and -II cuts. This rate estimate is not used in the analysis since the Earth model is not well constrained, only the undistorted prompt-spectra from the ^{238}U and ^{232}Th chains are used in the final analysis.

[6] TNU: Terrestrial neutrino unit, this corresponds to one inverse beta decay event per 10^{32} protons per year.

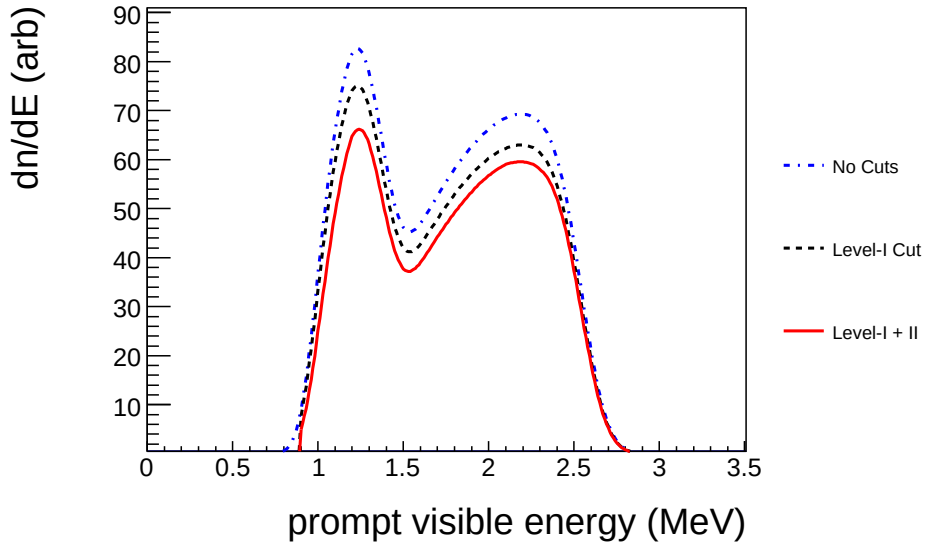

Figure 6.33: Expected prompt visible energy spectrum shape for geo-neutrinos assuming the ^{238}U and ^{232}Th rates predicted by the reference Earth-model [42].

6.7 Summary

We close this chapter with a summary of the data set, the candidate selection conditions, and the expected signal and background levels.

6.7.1 Live-time and exposure

The detector live-time and exposure are summarized in Table 6.16. The uncertainty on the exposure comes mainly from the fiducial-volume uncertainty, the uncertainty on the live-time is negligible.

Table 6.16: Summary of live-time and target exposure.

	live-time (days)	exposure ($\times 10^{32}$ proton-years)
T-I	1277.53	2.058 ± 0.037
T-II	178.75	0.297 ± 0.014
T-III	165.09	0.280 ± 0.015
Total	1621.36	2.64 ± 0.07

6.7.2 Summary of selection cuts and efficiency

The level-I and -II candidate selection cuts summarized below.

Level-I cuts

- Prompt visible-energy: 0.9 MeV $< E_{\rm p} <$ 20.0 MeV
- Trigger threshold — introduces an effective $E_{\rm p}$ cut
- Delayed visible-energy: 2.0 MeV $< E_{\rm d} <$ 2.8 MeV
- Prompt event position: $\vec{R}_{\rm p}$ <6.0 m
- Delayed event position: $\vec{R}_{\rm d}$ <6.0 m
- Prompt-delayed spatial separation: $\Delta R <$ 1.6 m
- Prompt-delayed time separation: 0.5 $\mu s < \Delta T <$ 1500 μs
- Good reconstruction status
- Global spallation muon cut: time separation between prompt events and all preceding muons must be greater than 2 ms

Level-II cuts

- Likelihood asymmetry cut
- Bad LS-muon/showering-muon 2 s cut
- Good LS-muon 2 s, 3-m-radius cylinder cut

The total selection efficiency with the 1σ uncertainty, averaged over the three data periods, is shown in Figure 6.34.

6.7.3 Expected signal and background levels

The expected background contributions after level-I and -II cuts are listed in Table 6.17. The expected geo-neutrino rate is not included in the analysis since the Earth model is not well constrained; the only Earth-model result used is that the geo-neutrino spectrum shape is undistorted by neutrino-oscillation. The number of candidates expected assuming the reactor flux described in Chapter 5 (without oscillation) for both the *default* and *new* reactor-spectra calculations are given in Table 6.18.

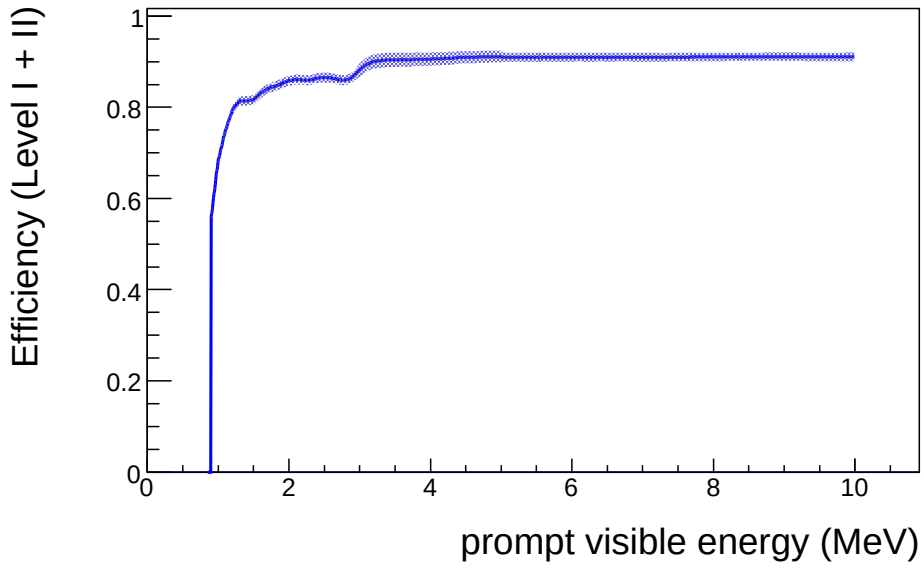

Figure 6.34: Efficiency, after all selection cuts, to select $\bar{\nu}_e$-like pairs as a function of prompt visible-energy. The curve shown is the average over the full data set. The shaded band is the 1σ uncertainty.

Table 6.17: Expected number of candidates from background.

Source	Expected counts
Accidentals	83.2 ± 0.1
Alpha-n	145 ± 30
^{9}Li	12 ± 4
Fast Neutron (OD + atm. ν)	25 ± 20
Total (excluding geo-ν)	265 ± 36
geo-ν	~ 84

Table 6.18: Expected number of candidates from reactor antineutrinos.

Source	Expected counts
Default reactor-spectra	2140 ± 74
New reactor-spectra	2250 ± 78

Chapter 7

Analysis

This chapter describes how the oscillation parameters are deduced from a fit of the oscillation model to the selected candidates and presents the results of the fit. An analysis combining KamLAND and a selection of solar neutrino data is also presented.

7.1 Observed candidates

After applying the selection cuts described in the preceding chapter we find 1614 candidates. Excluding geo-neutrinos, we expect 2397±81(syst) candidates; this deficit is interpreted as being due to neutrino oscillation. The energy spectrum of the candidates is used to estimate the mixing parameters Δm^2_{21}, θ_{12} and θ_{13}.

7.2 Likelihood model for oscillation parameters

We use the likelihood-profile method [87] to estimate best-fit values and confidence intervals for the oscillation parameters. The inputs for the analysis listed below.

1. The number of candidates observed (N_{obs}) and the prompt visible-energy and detection time of each candidate:

$$\{E_1, t_1\}, \{E_2, t_2\}, \cdots, \{E_{N_{obs}}, t_{N_{obs}}\}\,. \tag{7.1}$$

2. The reactor operation data which is used to calculate the flux and antineutrino spectrum of each reactor at zero baseline (Chapter 5).

3. The reactor baselines, the neutrino-oscillation model, and inverse beta decay cross section which are needed to calculate the expected prompt real-energy spectrum for $\bar{\nu}_e$ candidates.

4. The expected prompt real-energy spectra of the ^{9}Li, ^{210}Po^{13}C, and geo-neutrino backgrounds.

5. The visible-energy spectra of the accidental, OD-fast-neutron and atmospheric-neutrino-induced backgrounds.

6. The expected number of candidates from ^{9}Li, accidental, ^{210}Po^{13}C, fast neutron and atmospheric-neutrino backgrounds.

7. The detector response which includes:

   (a) The energy scale model used for real-to-visible energy conversion.

   (b) The efficiency curves which describe the $E_{\rm p}$-dependent efficiency to tag a candidate.

Using items 2-7 the likelihood of the observed candidate set, item 1, can be calculated.

The terms in the likelihood can be classified into three categories: (i) a normalization term, (ii) a shape-time term, and (iii) a penalty term. We write

$$\mathcal{L} = \mathcal{L}_{\rm Norm} \times \mathcal{L}_{\rm Shape-Time} \times \mathcal{L}_{\rm Penalty}\,. \tag{7.2}$$

The parameters of the likelihood model are listed in Table 7.2 ; there are 3 parameters of physical interest, namely the estimators for Δm^2_{21}, θ_{12} and θ_{13}; the other 19 parameters are nuisance parameters which are used to incorporate the uncertainties in the detector response and expected backgrounds into the analysis. The estimators for the nuisance parameters are assumed to be random variables but they are constrained using the studies presented in the preceding chapters. The following section describes the likelihood model and how the nuisance parameters are used in the analysis.

7.2.1 Energy scale nuisance parameters

Since it is pertinent to all terms in the likelihood model we first review how the energy scale and the associated nuisance parameters are used in the analysis. As described in Chapter 4, the visible-energy spectrum associated with a physical or real-energy spectrum is

$$S_{vis}(E) = \int_{-\infty}^{\infty} dE' \int_{0}^{E_{max}} dE_r S_r(E_r) \frac{e^{-(f(E_r)-E)^2/2\sigma^2((f(E_r)))}}{\sqrt{2\pi}\sigma(f(E_r))} \delta(f(E_r)-E'))\,, \tag{7.3}$$

where S_r is the real-energy spectrum in question, $f(E_r)$ is the particle-dependent function that maps real energy to quenched scintillation-energy (E_{scint}), $\sigma(E)$ is the detector resolution function and δ is the Dirac δ-function.

The real-to-visible energy conversion depends on 4 energy scale parameters,

$$E_{scint} = f(E_r|A_0, k_B, k_0, k_C)\,,$$

the best-fit estimators, and the covariance matrix for these parameters were found from a fit to calibration data (Chapter 4). The likelihood model has four energy-scale

nuisance parameters: η_{A_0}, η_{K_B}, η_{K_0}, η_{K_C}. When converting real energy to visible energy during the analysis, a shifted estimator, rather than the best-fit estimator, is used for each energy scale parameter. For example the shifted estimator for Birks' constant used for the data period containing timestamp t is

$$k'_B(t) = \hat{k}_B(t) + \eta_{k_B} \cdot \sigma_{k_B}(t)\,, \tag{7.4}$$

where $\hat{k}_B(t)$ and $\sigma_{k_B}(t)$ are the best-fit estimator and variance for Birks' constant. Similar relations hold for the other energy scale parameters. Although there is a set of energy scale parameters for each data period T-I, T-II, and T-III, a single set of nuisance parameters is used for all three data periods.

We add an energy scale term

$$\mathcal{L}_{ES,penalty} = \frac{1}{N} e^{-\frac{1}{2}\Delta\chi^2_{ES}} \tag{7.5}$$

to the penalty likelihood to constrain the nuisance parameters. The quantity N is a normalization constant which will cancel out in the final analysis. To define $\Delta\chi^2_{ES}$ we introduce the notation below.

- Let $\mathbf{X}_i = (A_0, k_B, k_0, k_C)_i$ be the vector of parameter estimators for data period i, where the index i runs over the three periods T-I, T-II and T-III.
- Let $\hat{\mathbf{X}}_i = (\hat{A}_0, \hat{k}_B, \hat{k}_0, \hat{k}_C)_i$ and $\mathbf{\Sigma}_i = (\sigma_{A_0}, \sigma_{k_B}, \sigma_{k_0}, \sigma_{k_C})_i$ be the best-fit estimators and variances for period i.
- Let $\vec{\eta} = (\eta_{A_0}, \eta_{K_B}, \eta_{K_0}, \eta_{K_C})$ be the vector of energy-scale nuisance parameters.
- Following Equation 7.4 we define a shifted estimator vector $\mathbf{X'}_i$ as

  $$[\mathbf{X'}_i]_j = [\mathbf{X}_i]_j + \eta_j \cdot [\mathbf{\Sigma}_i]_j\,, \tag{7.6}$$

  where the index i labels the data period and j labels the position in the 4-dimensional vector — a square bracket encloses the data-period-dependent object to help separate the two indices.
- For each data period we define

  $$\Delta\chi^2_i(\vec{\eta}) \equiv \sum_{j,k} [\hat{\mathbf{X}}_i - \mathbf{X'}_i]_j [\mathbf{V}_i^{-1}]_{jk} [\hat{\mathbf{X}}_i - \mathbf{X'}_i]_k \tag{7.7}$$

  $$= \sum_{j,k} \eta_j \eta_k [\mathbf{\Sigma}_i]_j [\mathbf{V}_i^{-1}]_{jk} [\mathbf{\Sigma}_i]_k \tag{7.8}$$

  where $\mathbf{V}_i^{-1}$ is the inverse of the covariance matrix for period i determined from the calibration data.

With the notation above in hand we define $\Delta\chi^2_{ES}$ as

$$\Delta\chi^2_{ES} = \frac{1}{T_{\rm Tot}} \sum_{i=1}^{3} T_i \cdot \Delta\chi^2_i \,, \tag{7.9}$$

where T_{Tot} is the total live-time of the data set and T_i is the live-time of period i.

Each nuisance parameter is the signed difference between the shifted estimator and the best-fit estimator in units of the estimator variance. In the analysis the nuisance parameters are allowed to vary between ± 5, values close to zero are favored as those have the largest likelihood.

7.2.2 Neutrino oscillation parameters

The expected prompt real-energy spectrum at time t from reactor antineutrinos is

$$S_{e^+,r}(E',t) = N_p \sum_j \left[\int_0^\infty dE \, \frac{P_{\bar{\nu}_e \to \bar{\nu}_e}(E, L_j, \Delta m^2, \theta_{12}, \theta_{13})}{4\pi L_j^2} \sigma(E) \frac{dN_{\bar{\nu}_e}(t,j)}{dE} \delta(f(E), E') \right] , \tag{7.10}$$

where N_p is the number of target protons in KamLAND, the index j runs over the reactor sources, L_j is the baseline from reactor j to KamLAND, $P_{\bar{\nu}_e \to \bar{\nu}_e}(E, L_j, \Delta m^2, \theta_{12}, \theta_{13})$ is the electron antineutrino survival probability, σ is the inverse beta decay cross section, $\frac{dN_{\bar{\nu}_e}(t,j)}{dE}$ is the number of neutrinos emitted per unit energy from source j, and the δ-function enforces the kinematic relationship between the incoming antineutrino and outgoing positron, Equation 5.2.

The positron visible energy spectrum, $S_{e^+,vis}(E,t)$, is found by applying the transformation in Equation 7.3. The energy scale parameters for the data period containing the timestamp t is used in the conversion.

7.2.3 Nuisance parameter for reactor normalization

The uncertainty in the number of target protons and the reactor-spectra are combined together as a single uncertainty on the expected reactor antineutrino spectrum normalization. The expected candidate rate at time t with energy E from reactor-antineutrinos is

$$R(E,t) = \int_{t-\Delta t}^{t+\Delta t} \int_{E-\Delta E}^{E+\Delta E} dE' \, dt' \, \xi(E',t') \cdot A(t') \cdot S_{e^+,vis}(E',t') \,. \tag{7.11}$$

The function $S_{e^+,vis}(E,t)$ is the positron visible energy spectrum defined above, $\xi(E,t)$ is the candidate tagging efficiency and $A(t)$ is a renormalization parameter,

$$A(t) = 1 + \eta_{\bar{\nu}_e} \cdot \delta_{\bar{\nu}_e}(t) \,, \tag{7.12}$$

where $\eta_{\bar{\nu}_e}$ is the nuisance parameter for the reactor normalization and $\delta_{\bar{\nu}_e}(t)$ is the combined normalization uncertainty. In the numerical integration of Equation 7.11 we use $\Delta T = 1\,s$ and $\Delta E = 10\,\mathrm{keV}$. We add a term

$$\mathcal{L}_{\bar{\nu}_e,penalty} = \frac{1}{N} e^{-\frac{1}{2}\Delta\chi^2_{\bar{\nu}_e}} = \frac{1}{N} e^{-\frac{1}{2}\eta^2_{\bar{\nu}_e}} \tag{7.13}$$

to the penalty likelihood to constrain this nuisance parameter. Again, N is a normalization constant which will cancel in the final analysis. As $\eta_{\bar{\nu}_e}$ varies in the fit, the reactor normalization will vary continuously about the expected value.

7.2.4 Nuisance parameters for geo-neutrinos

The parameters $\mathrm{N}_{^{238}\mathrm{U}}$ and $\mathrm{N}_{^{232}\mathrm{Th}}$ normalize the geo-neutrino contribution. In the likelihood model the candidate rate at time t with energy E from geo-neutrinos is

$$R(E,t) = \frac{1}{T_{Tot}} \times \int_{t-\Delta t}^{t+\Delta t} \int_{E-\Delta E}^{E+\Delta E} dE'\, dt'\, \xi(E',t') \times \Big[N_{^{238}\mathrm{U}} \cdot S_{^{238}\mathrm{U}}(E',t') + N_{^{232}\mathrm{Th}} \cdot S_{^{232}\mathrm{Th}}(E',t') \Big], \tag{7.14}$$

where T_{Tot} is the total experiment live-time, $\xi(E,t)$ is the efficiency to tag an antineutrino candidate, and $S_{^{238}\mathrm{U}}$ and $S_{^{232}\mathrm{Th}}$ are the prompt visible-energy spectra of geo-neutrinos from the ^{238}U- and ^{232}Th-chains respectively. Each spectrum is normalized such that

$$\int_0^\infty dE' S_{^{238}\mathrm{U}}(E',t') = \int_0^\infty dE' S_{^{232}\mathrm{Th}}(E',t') = 1\,. \tag{7.15}$$

We do not constrain the geo-neutrino rates so there is no associated term in the penalty likelihood.

7.2.5 Nuisance parameters for ^{210}Po^{13}C background

We introduce seven nuisance parameters for the ^{210}Po^{13}C background, four of them are associated with the shape and the other three are associated with the normalization for each data period. The rate of candidates at time t with energy E from ^{210}Po^{13}C is

$$R(E,t) = \frac{1}{T(t)} \int_{t-\Delta t}^{t+\Delta t} \int_{E-\Delta E}^{E+\Delta E} dE'\, dt'\, \xi(E',t') S(E',t')\,, \tag{7.16}$$

where $T(t)$ is the total live-time of the data period containing the timestamp t, $\xi(E,t)$ is the tagging efficiency, and $S(E,t)$ is the prompt visible energy spectrum of the

^{210}Po^{13}C background. Let $\hat{N}_{\alpha-n}(t)$ and $\sigma_{\alpha-n}(t)$ be the expected number of α-n candidates and associated uncertainty for the data period containing the timestamp t, as before we introduce a shifted estimator for this parameter:

$$N'_{\alpha-n}(t) \equiv \hat{N}_{\alpha-n}(t) + \eta_{N_{\alpha-n}}(t) \cdot \sigma_{\alpha-n}(t)\,, \tag{7.17}$$

where the $\eta_{N_{\alpha-n}}(t)$ is the nuisance parameter for the associated data period. At each step in the fit, the visible energy spectrum is normalized such that

$$N'_{\alpha-n}(t) = \int_{period(t)} dt' \int_0^\infty dE'\, S(E', t')\,. \tag{7.18}$$

The time integral goes over the live-time of the period containing t. To constrain these parameters we add the following term to the penalty likelihood:

$$\mathcal{L}_{N_{\alpha-n},penalty} = \frac{1}{N} e^{-\frac{1}{2}\Delta\chi^2_{N_{\alpha-n}}}\,, \tag{7.19}$$

where N is a normalization constant and

$$\Delta\chi^2_{N_{\alpha-n}} = \sum_{i=1}^{3} \frac{(N'_{\alpha-n}(i) - \hat{N}_{\alpha-n}(i))^2}{\sigma^2_{\alpha-n}(i)} = \sum_{i=1}^{3} \eta^2_{N_{\alpha-n}}(i)\,. \tag{7.20}$$

The index i labels the three data periods T-I, T-II and T-III.

As described in the preceding chapter the prompt events for this background can be classified into three event-types; here we further divide the first type — decays to the ^{16}O ground state — according to whether or not the neutron scatters inelastically on ^{12}C. Thus we have four event-types, we write the total visible energy spectrum as the sum of the 4 component spectra

$$S(E,t) = \frac{N'_{\alpha-n}(t)}{\sum_{i=1}^{4} b_i} \cdot \sum_{i=1}^{4} b_i \cdot S_i(E,t)\,. \tag{7.21}$$

The index i labels the event type, (see Table 7.1), b_i and S_i are the branching fraction and spectrum of component i. Each component spectrum is normalized such that $\int_0^{E_{max}} S_i(E', t)\, dE' = 1$.

We introduce a nuisance parameter for each branching-fraction estimator. Let $\hat{\mathbf{b}} = (\hat{b}_0, \hat{b}_1, \hat{b}_2, \hat{b}_3)$ and $\mathbf{\Sigma} = (\sigma_1, \sigma_2, \sigma_3, \sigma_4)$ be the best-fit branching fractions and variances determined from the ^{210}Po^{13}C calibration-source analysis, and let $\vec{\eta} = (\eta_{b,1}\,, \eta_{b,2}\,, \eta_{b,3}\,, \eta_{b,4}\,)$ be the vector of branching-fraction nuisance parameters. In the analysis the shifted branching-fractions, defined as

$$b'_i = \hat{b}_i + \eta_{b,i} \cdot \Sigma_i\,, \tag{7.22}$$

Table 7.1: ^{210}Po^{13}C event types.

Index	Description
1	decay to ^{16}O ground state, prompt energy from neutron-proton elastic scattering
2	decay to ^{16}O ground state, prompt energy from neutron-proton elastic scattering and neutron-^{12}C inelastic scattering
3	decay to ^{16}O first excited state, prompt energy from neutron-proton elastic scattering and prompt e^+/e^- emitted from ^{16}O
4	decay to ^{16}O second excited state, prompt energy from neutron-proton elastic scattering and prompt γ from ^{16}O

are used when evaluating Equation 7.21. To constrain these nuisance parameters we introduce the following penalty term:

$$\mathcal{L}_{S_{\alpha-n},penalty} = \frac{1}{N} e^{-\frac{1}{2}\Delta\chi^2_{S_{\alpha-n}}} , \tag{7.23}$$

where N is a normalization factor and

$$\Delta\chi^2_{S_{\alpha-n}} = \sum_{j,k} \eta_{b,j}\eta_{b,k}\Sigma_j V^{-1}_{jk}\Sigma_k . \tag{7.24}$$

The quantity V^{-1} above is the inverse of the covariance ^{210}Po^{13}C branching-fraction estimators from the ^{210}Po^{13}C calibration data analysis.

7.2.6 Nuisance parameters for normalization of other backgrounds

The nuisance parameters for the normalization of the accidental, ^{9}Li, OD-fast-neutron and atmospheric-neutrino-induced backgrounds are handled in the same way as the ^{210}Po^{13}C normalization nuisance parameters. The rate of candidates from each background at time t with prompt energy E is

$$R_i(E,t) = \frac{1}{T_{Tot}} \times \int_{t-\Delta t}^{t+\Delta t}\int_{E-\Delta E}^{E+\Delta E} dE'\,dt'\,\xi(E',t')\,S_i(E',t') , \tag{7.25}$$

where the index i labels the background source, T_{Tot} is the total experiment live-time, $\xi(E,t)$ is the efficiency to tag a candidate, and S_i is the prompt-visible energy

spectrum of background i. Each spectrum is normalized such that

$$N_i' \equiv \hat{N}_i + \eta_i \cdot \sigma_i = \int dt' \int_0^\infty dE'\, S(E', t') \tag{7.26}$$

where N_i' is the shifted estimator for the background normalization, $\hat{N}_i$ and σ_i are the best-fit estimate and uncertainty for the normalization found in Chapter 6, and η_i is the associated nuisance parameter. To constrain each nuisance parameter we add the term

$$\mathcal{L}_{\,\mathrm{Bkg\,,penalty}} = \frac{1}{N} e^{-\frac{1}{2}\Delta\chi^2_{\mathrm{Bkg}}} \tag{7.27}$$

to the penalty likelihood. The quantity N is a normalization constant and $\Delta\chi^2_{\mathrm{Bkg}}$ is

$$\Delta\chi^2_{\mathrm{Bkg}} = \sum_{i=1}^{i=3} \frac{(N'_{\mathrm{Bkg-i}} - \hat{N}_{\mathrm{Bkg-i}})^2}{\sigma^2_{\mathrm{Bkg-i}}} = \sum_{i=1}^{i=3} \eta_i^2\,, \tag{7.28}$$

where the sum is over the three background sources: accidentals, ^{9}Li, and OD-fast-neutrons and atmospheric neutrinos.

7.2.7 Nuisance parameters for detection efficiency

The total candidate tagging efficiency is a product of several factors which were described in Chapter 6. Let $\hat{\xi}_{Tot}(E,t)$ and $\sigma_\xi(E,t)$ be the estimated total efficiency and its uncertainty. The shifted efficiency estimator is defined as

$$\xi'_{Tot}(E,t) = \hat{\xi}_{Tot}(E,t) + \eta_\xi \cdot \sigma_\xi(E,t)\,, \tag{7.29}$$

where η_ξ is the efficiency nuisance parameter. The shifted efficiency estimator is used in the analysis rather than the best-fit estimator. We add the term

$$\mathcal{L}_{\xi,penalty} = \frac{1}{N} e^{-\frac{1}{2}\Delta\chi^2_\xi} = \frac{1}{N} e^{-\frac{1}{2}\eta^2_\xi} \tag{7.30}$$

to the penalty likelihood to constrain this parameter.

7.2.8 Normalization likelihood

Having outlined how the expected instantaneous rate from each candidate source is calculated in the likelihood model we can proceed to define the rate likelihood and the shape-time likelihood.

For a given set of parameter values ($\vec{\rho}$) the likelihood model can be used to calculate an expected number of candidates

$$N_{exp}(\vec{\rho}) = \sum_i \int_{data-set} dt \int_{E_{min}}^{E_{max}} dE\, R_i(E,t,\vec{\rho})\,, \tag{7.31}$$

Table 7.2: Parameters of the likelihood model used in the analysis.

Free parameters		
Oscillation	1	Δm^2_{21}
	2	θ_{12}
	3	$\sin^2\theta_{13}$
Geo-$\bar{\nu}_e$	4	N-^{238}U
	5	N-^{232}Th
Nuisance Parameters		
Reactor normalization	6	$\eta_{\bar{\nu}_e}$
Tagging efficiency	7	η_{ξ}
Energy scale	8	η_{A_0}
	9	η_{K_B}
	10	η_{K_0}
	11	η_{K_C}
PoC shape	12	$\eta_{b,1}$
	13	$\eta_{b,2}$
	14	$\eta_{b,3}$
	15	$\eta_{b,4}$
^{210}Po rate	16	$\eta_{N_{\alpha-n}}$(T-I)
	17	$\eta_{N_{\alpha-n}}$(T-II)
	18	$\eta_{N_{\alpha-n}}$(T-III)
Other background rates	19	η_{Acc}
	20	$\eta_{^9\mathrm{Li}}$
	21	$\eta_{\mathrm{Fast-N+atm-}\nu}$

where the index i runs over the event sources, $R_i(E, t, \vec{\rho})$ is the instantaneous rate expected from source i given the model parameters $\vec{\rho}$, and E_{min} and E_{max} are the limits of the $E_{\rm p}$ cut acceptance. The normalization likelihood is defined as the probability, given N_{exp}, of observing a number of candidates N' equal to the number actually observed (N_{obs}). Assuming Poisson statistics we have

$$\mathcal{L}_{\rm Norm}(\vec{\rho}) = \delta(N', N_{obs}) \cdot \frac{N_{exp}^{N'}}{N'!} e^{-N_{exp}} \,, \tag{7.32}$$

where $\delta(N', N_{obs}) = 1$ if $N' = N_{obs}$, and $\delta(N', N_{obs}) = 0$ if $N' \neq N_{obs}$.

7.2.9 Shape-time likelihood

To use the observed candidate spectrum and take advantage of time dependence of the reactor output and background levels we introduce the shape-time likelihood. The likelihood of observing a candidate with the same energy and timestamp as the i^{th} observed candidate is

$$\delta\mathcal{L}_{Shape-time}(\{E_i, t_i\}|\vec{\rho}) = \frac{\sum_j R_j(E_i, t_i)}{\sum_j \int_{E_{min}}^{E_{max}} R_j(E', t_i) dE'} \tag{7.33}$$

where j labels the sources — reactor, PoC etc. The shape-time likelihood is the joint likelihood for all the observed candidates,

$$\mathcal{L}_{Shape-time}(\vec{\rho}) = \prod_{i=1}^{N_{obs}} \delta\mathcal{L}_{Shape-time}(\{E_i, t_i\}|\vec{\rho}) \,. \tag{7.34}$$

7.2.10 Penalty likelihood

The elements of the penalty likelihood have been described in detail above in the description the likelihood model and the nuisance parameters. In summary we write

$$\mathcal{L}_{penalty} = \mathcal{L}_{ES} \cdot \mathcal{L}_{\bar{\nu}_e} \cdot \mathcal{L}_{\xi} \cdot \mathcal{L}_{N_{\alpha-n}} \cdot \mathcal{L}_{S_{\alpha-n}} \cdot \mathcal{L}_{Bkg} \,. \tag{7.35}$$

The penalty subscripts used earlier in defining the terms on the right hand side of Equation 7.35 have been dropped for convenience.

7.3 Likelihood ratio

Having described the likelihood model and how it depends on the physical and nuisance parameters, we proceed to define a likelihood ratio, or profile likelihood, which is a function of the physical parameters only. We introduce the following notation to help describe the likelihood ratio.

- Let N be the number of parameters in the likelihood model.
- Let $\vec{\nu}$ denote an n-vector subset of the parameters and let $\vec{\eta}(\vec{\nu})$ be the remaining N-n parameters. For example, if $\vec{\nu} = (\theta_{12}, \theta_{13})$ then $\vec{\eta}(\theta_{12}, \theta_{13})$ is the set of remaining parameters including Δm^2_{21}; if $\vec{\nu} = (\theta_{12})$ then $\vec{\eta}(\theta_{12})$ is the set of remaining parameters including Δm^2_{21} and θ_{13}.
- Let $\hat{\rho}$ denote the values of the parameters that maximize the likelihood.
- Let $\vec{\nu}_0$ denote a particular choice of values for the parameter subset $\vec{\nu}$ and let $\hat{\eta}(\vec{\nu}_0)$ be the values of the remaining parameters that maximize the likelihood when $\vec{\nu}$ is fixed at $\vec{\nu}_0$.

With this notation the likelihood ratio is

$$\lambda(\vec{\nu}) = \frac{\mathcal{L}(\vec{\nu}, \hat{\eta}(\vec{\nu}))}{\mathcal{L}(\hat{\rho})}\,. \tag{7.36}$$

The quantity $-2\ln(\lambda(\vec{\nu}))$ follows a χ^2 distribution with n degrees of freedom, where n is the size of $\vec{\nu}$ [87]. The best-fit estimators are those that maximize the likelihood ratio, or equivalently minimize the associated χ^2, and the confidence intervals are constructed using the statistical properties of the χ^2 distribution.

7.3.1 Construction of the likelihood ratio function

In practice the analysis is done by building up likelihood ratio function,

$$\lambda(\Delta m^2_{21}, \theta_{12}, \theta_{13}) = \frac{\mathcal{L}(\Delta m^2_{21}, \theta_{12}, \theta_{13}, \hat{\eta}(\Delta m^2_{21}, \theta_{12}, \theta_{13}))}{\mathcal{L}(\hat{\rho})}\,, \tag{7.37}$$

on a grid of points in the space spanned by Δm^2_{21}, θ_{12} and θ_{13}. For each point $\vec{\nu}_0$ on the grid, $\hat{\eta}(\vec{\nu}_0)$ is found using the ROOT interface to the Minuit minimiser. At each point, minimisation over the 19 nuisance parameters takes about 1 hour on the PDSF compute nodes (2.2 GHz lx24-amd64 QuadCore). Once the scan is complete, $\hat{\rho}$ is taken as the grid-point with the maximum value of the likelihood. In the following we will also use projections of the likelihood ratio onto subspaces of the (Δm^2_{21}, θ_{12} and θ_{13}) parameter space. For example the projection onto Δm^2_{21} is

$$\lambda_{\mathrm{Proj}}(\Delta m^2_{21}) = \lambda(\Delta m^2, \hat{\theta}_{12}, \hat{\theta}_{13})\,, \tag{7.38}$$

where for fixed Δm^2_{21}, $\hat{\theta}_{12}$ and $\hat{\theta}_{13}$ are the values of θ_{12} and θ_{13} that maximize $\lambda(\Delta m^2_{21}, \theta_{12}, \theta_{13})$.

7.4 KamLAND results

We now proceed to the results of the analysis. The main results are based on the expected reactor flux calculated using the default reactor-spectrum calculation presented in Chapter 5. A two-flavor (θ_{13} fixed at zero) and a three-flavor (θ_{13} allowed to vary) analysis was done. The results of a similar analysis based on the new reactor-spectra are presented in Appendix A.

7.4.1 Two-flavor result

The top panel of Figure 7.1 shows the profile likelihood, projected onto the Δm^2_{21} axis. The best-fit value and 1σ confidence interval is $\Delta m^2_{21} = 7.63^{+0.18}_{-0.19} \times 10^{-5}\text{eV}^2$. The bottom panel of Figure 7.1 shows the the profile likelihood projected onto the θ_{12} axis. There are two, almost degenerate minima. Without matter effects KamLAND is sensitive to θ_{12} through only the $\sin^2 2\theta_{12}$ term in the survival probability and thus cannot distinguish between $\theta_{12} > 45^\circ$ and $\theta_{12} < 45^\circ$. Including matter effects in the survival probability introduces $\cos 2\theta_{12}$ dependence (Equation 1.18), which breaks the degeneracy. The effect for KamLAND is very small; however, matter effects in the Sun are much larger and solar-neutrino experiments can distinguish between the two allowed regions. As shown in Figure 7.2 solar neutrino data reject the $\theta_{12} > 45^\circ$ region to very high significance. Assuming the oscillation parameters are the same for neutrinos and antineutrinos as demanded by *CPT* invariance, and appealing to the solar neutrino data we exclude $\theta_{12} > 45^\circ$ region for KamLAND. Thus the best-fit value and 1σ confidence interval is $\theta_{12} = 34.5^{+1.7}_{-1.8}$ degrees.

7.4.2 Three-flavor result

The analysis was repeated allowing θ_{13} to be nonzero. The parameter θ_{13} appears in the survival probability as a $\sin^2\theta_{13}$ term (Equation 5.18). Physically this quantity cannot take on negative values, however negative values are artificially allowed in the analysis since from short-baseline reactor experiments we expect the best-fit estimator of $\sin^2\theta_{13}$ to be close to this physical boundary. In this case the definition of the profile likelihood is modified slightly, the range of the parameters in denominator of Equation 7.36 is restricted to physically allowed values ($\sin^2\theta_{13} \geq 0$).

The top plot in Figure 7.3 shows the profile likelihood projected onto the Δm^2_{21} axis. The best-fit value and 1σ confidence interval is $\Delta m^2_{21} = 7.60^{+0.20}_{-0.19} \times 10^{-5}\text{eV}^2$. The lower plot in Figure 7.3 shows the projection onto the θ_{12} axis, appealing to the findings of solar neutrino experiments only the region $\theta_{12} < 45^\circ$ is considered. The best-fit value and 1σ confidence interval is $\theta_{12} = 32.5^{+2.9}_{-2.9}$ degrees. Figure 7.4 shows profile likelihood projected onto the $\sin^2\theta_{13}$ axis. Due to limited computing resources the scan was restricted to the interval $-0.1 < \sin^2\theta_{13} < 0.1$, since $\sin^2\theta_{13}$ is known to be small [88] this restriction just excludes regions of parameter space that are already

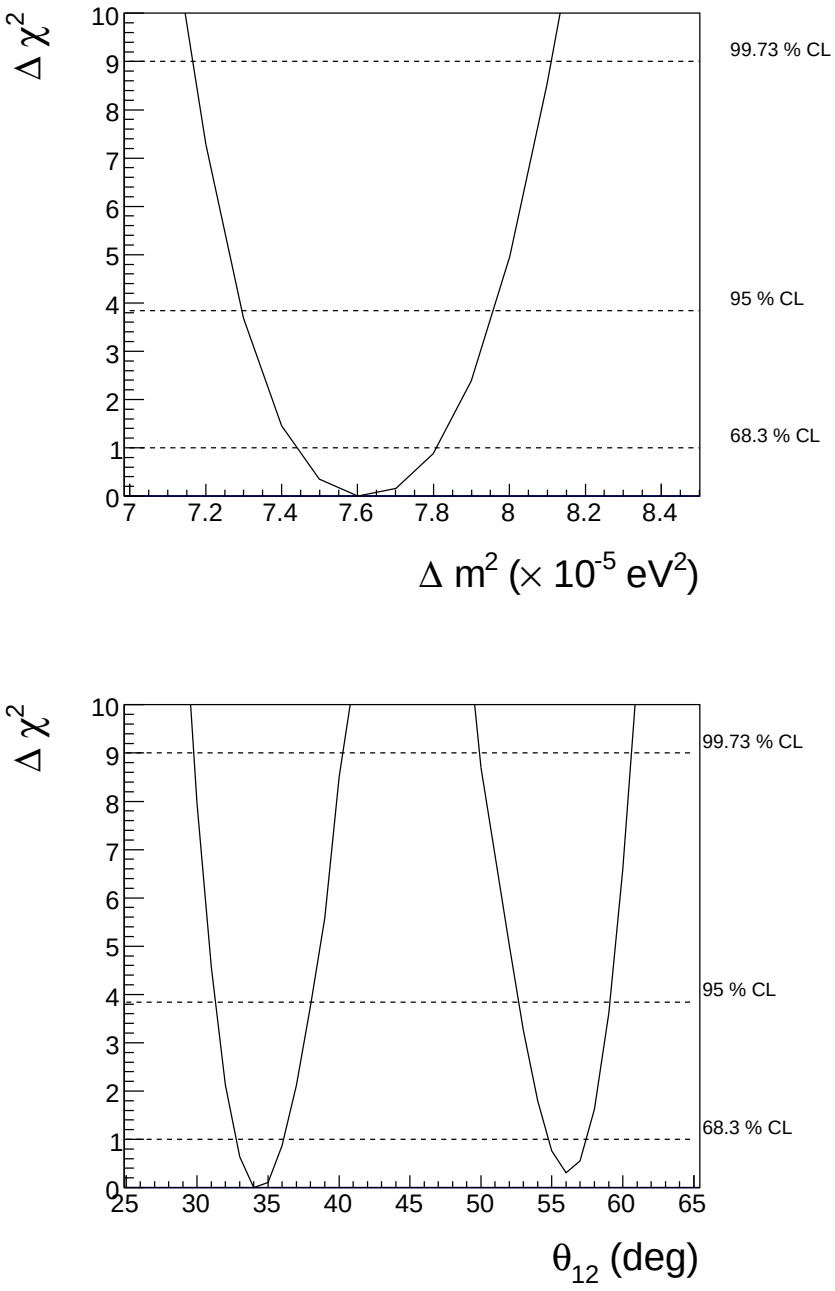

Figure 7.1: Projection of the profile likelihood onto the Δm^2_{21} axis (top) and θ_{12} axis (bottom) for a two-flavor analysis of the KamLAND data.

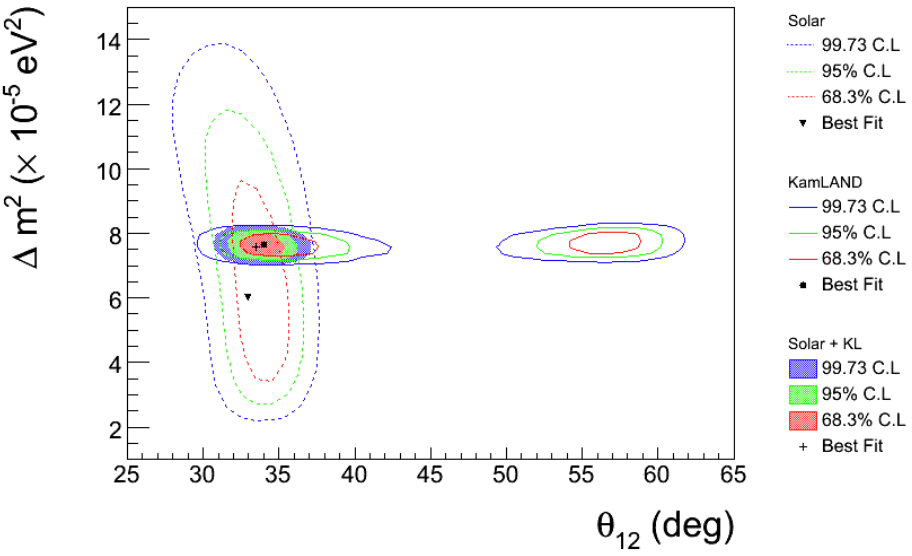

Figure 7.2: Allowed regions in Δm^2-θ_{12} space for a two-flavor analysis of (i) the KamLAND data, (ii) solar neutrino data and (iii) the KamLAND and solar data combined.

disfavored. The best-fit value is $\sin^2\theta_{13} = 0.025^{+0.035}_{-0.035}$; the 95% confidence level upper limit is $\sin^2\theta_{13} < 0.083$.

Figure 7.5 shows the binned energy spectrum of the candidates together with the best-fit background components and oscillated reactor-flux from the unbinned analysis. The Pearson-χ^2 per degree of freedom of the data and model is 16.4/17. Figure 7.5 also shows the expected spectrum assuming the best-fit backgrounds and an unoscillated reactor flux.

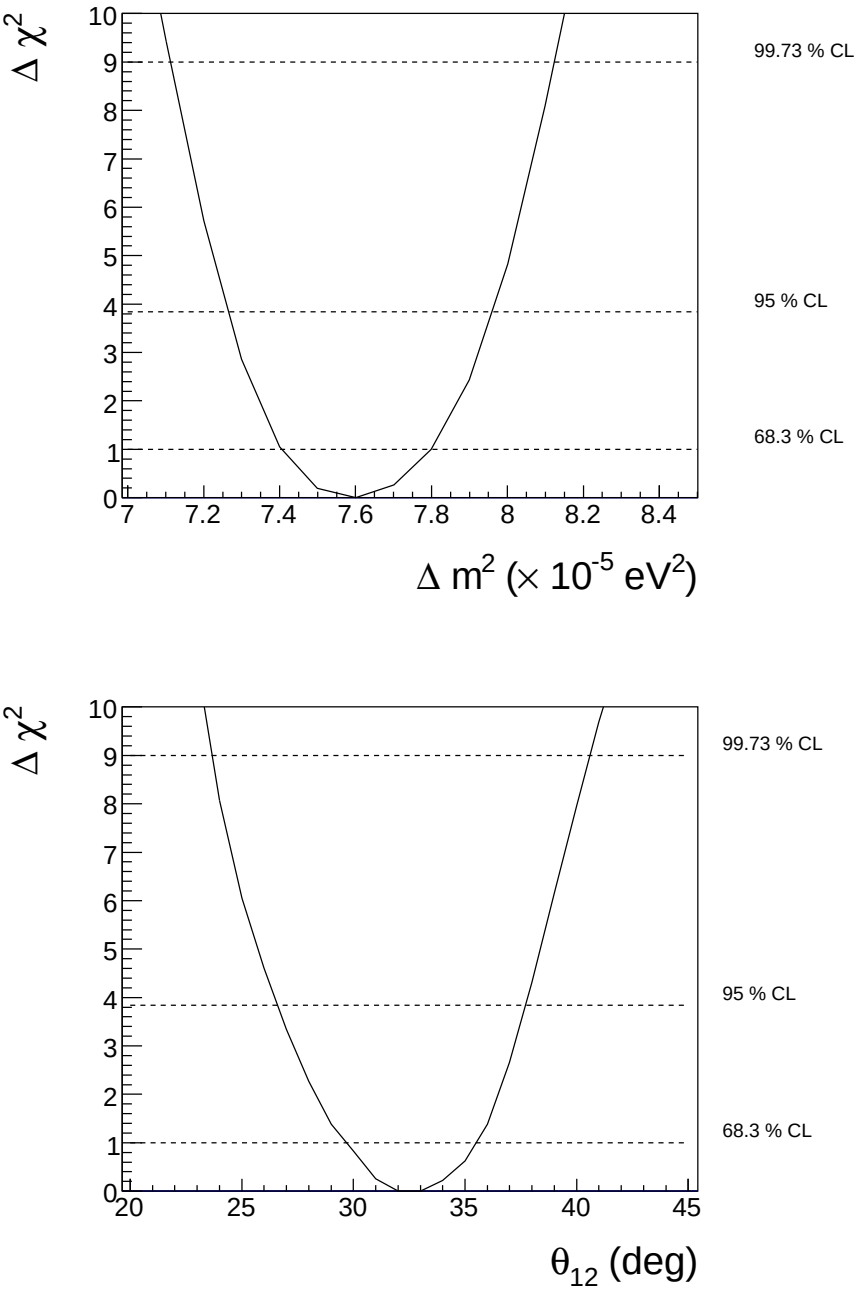

Figure 7.3: Projection of the profile likelihood onto the Δm^2_{21} axis (top) and θ_{12} axis (bottom) for a three-flavor analysis of the KamLAND data.

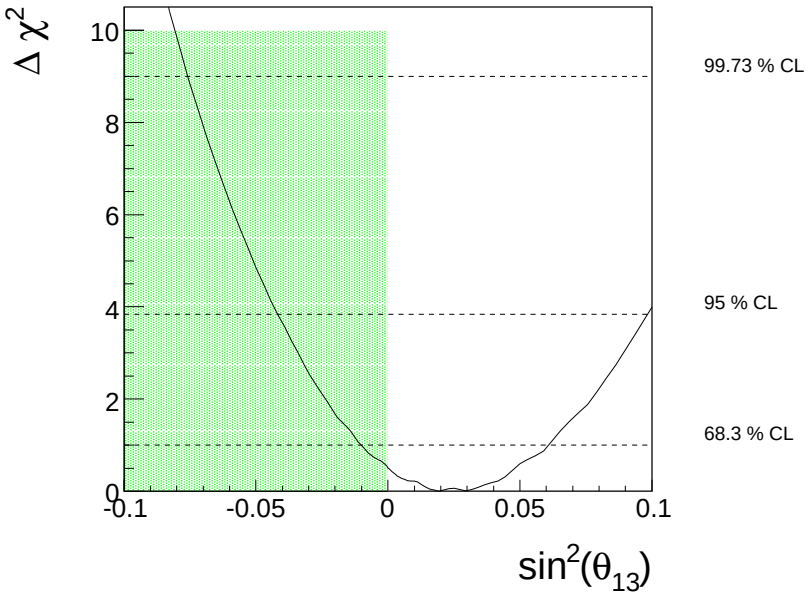

Figure 7.4: Projection of the profile likelihood onto the $\sin^2\theta_{13}$ axis for a three-flavor analysis of the KamLAND data. The unphysical region ($\sin^2\theta_{13} < 0$) is shaded green.

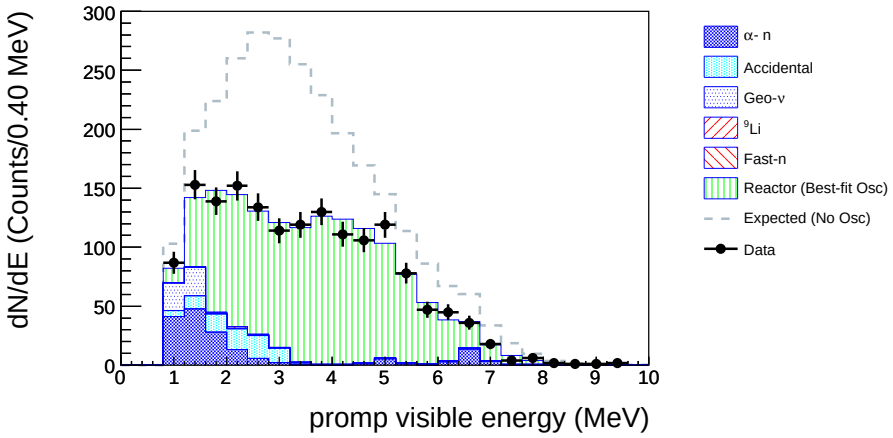

Figure 7.5: The data is the prompt visible energy spectrum of the selected $\bar{\nu}_e$ candidates. The shaded histograms are the expected component spectra given the best-fit background and oscillation parameters. These histograms are stacked. The line histogram is the expected candidate spectrum given the best-fit background spectra and an unoscillated reactor-flux.

7.5 Combined analysis of KamLAND and solar neutrino data

Assuming CPT invariance, solar neutrino experiments offer independent measurements of the oscillation parameters Δm^2_{21}, θ_{12} and θ_{13}. Solar experiments have weaker sensitivity to Δm^2_{21} than KamLAND but are more sensitive to θ_{12}. In this section we outline a likelihood model used to estimate the oscillation parameters from data published by solar neutrino experiments. The parameters of the model are listed in Table 7.3. The likelihood is defined as

$$\mathcal{L}_{Solar} = \frac{1}{N} e^{-\frac{1}{2}\chi^2_{solar}}\,, \tag{7.39}$$

where N is a normalization constant and

$$\chi^2_{Solar} = \sum_i \frac{(x_i(\vec{\rho}) - \mu_i)^2}{\sigma_i^2} + \chi^2_{penalty}\,. \tag{7.40}$$

The index i labels a measurement from one of the solar neutrino experiments, $x_i(\vec{\rho})$ is the expected value for this measurement given the model parameters $\vec{\rho}$, μ_i and σ_i are the best-fit value and uncertainty reported by the experiment, and $\chi^2_{penalty}$ is a term to constrain nuisance parameters and include correlations between the different measurements. The solar neutrino measurements included in $\mathcal{L}_{Solar}$ are listed in the next section.

7.5.1 Solar neutrino data

7.5.1.1 SNO

The electron neutrino survival probability, P_{ee}, and day-night asymmetry of the survival probability, A_{ee}, from a combined analysis of the three phases of the SNO experiment have recently been reported by the SNO collaboration [89]. They parametrize both quantities as polynomials in neutrino energy,

$$P^{SNO}_{ee}(E) = c_0 + c_1 \cdot (\frac{E}{1MeV} - 10) + c_2 \cdot (\frac{E}{1MeV} - 10)^2\,, \tag{7.41}$$

$$A^{SNO}_{ee}(E) = a_0 + a_1 \cdot (\frac{E}{1MeV} - 10)\,, \tag{7.42}$$

and report the best-fit values and covariance matrix of the coefficients c_0, c_1, c_2, a_0, a_1, $\phi_{^8B}$ — where $\phi_{^8B}$ is the estimator for the ^8B flux found from the neutral current measurements. The day-night asymmetry is defined as

$$A_{ee} = 2 \cdot \frac{P^N_{ee} - P^D_{ee}}{P^N_{ee} + P^D_{ee}}\,, \tag{7.43}$$

Free parameters		
Oscillation	1	Δm^2_{21}
	2	θ_{12}
	3	$\sin^2\theta_{13}$
Nuisance parameters		
^8B flux	4	$\phi_{^8B}$
^7Be flux	5	$\phi_{^7Be}$
Combined CNO flux	6	ϕ_{CNO}
SNO (see main text)	7	c_0
	8	c_1
	9	c_2
	10	a_0
	11	a_1

Table 7.3: Parameters of the likelihood model used to analyse the solar neutrino data.

where P^D_{ee} is the electron-neutrino survival probability expected during the day and P^N_{ee} is the survival probability expected during the night. The reason the survival probability might differ from day to night is because of matter effects experienced by neutrinos as the propagate to the detector through the Earth at night. To calculate the expected value of P^D_{ee} and P^N_{ee} in a three flavor scenario the approximate expressions derived in [90] and the standard solar model BS05OP [7] were used.

Let $\mathbf{X} = (\phi_{^8B}, c_0, c_1, c_2, a_0, a_1)$ be the subset of parameters in the model associated with SNO and let $\hat{\mathbf{X}}$ and V be the best-fit values and covariance matrix reported by SNO, the χ^2 contribution used in the analysis is

$$\begin{aligned}\chi^2_{SNO} = &\sum_i \frac{(P^{exp}_{ee}(E_i) - P^{SNO}_{ee}(E_i, \mathbf{X}))}{\delta P^{SNO}_{ee}(E_i, \mathbf{X})} \\ &+ \sum_i \frac{(A^{exp}_{ee}(E_i) - A^{SNO}_{ee}(E_i, \mathbf{X}))}{\delta A^{SNO}_{ee}(E_i, \mathbf{X})} \\ &+ \sum_{j,k=1}^{6} (X_j - \hat{X}_j) V^{-1}_{j,k} (X_k - \hat{X}_k)\,. \end{aligned} \tag{7.44}$$

The quantities P^{exp}_{ee} and A^{exp}_{ee} are the survival probability and day-night asymmetry expected from the MSW oscillation model; P^{SNO}_{ee}, A^{SNO}_{ee}, δP^{SNO}_{ee}, and δA^{SNO}_{ee}

are the survival probability, asymmetry and their uncertainties based on the SNO parametrization. The index i runs over 10 energy bins — equal bins between 5 MeV and 15 MeV were used. The parameters $\mathbf{X} = (\phi_{^8B}, c_0, c_1, c_2, a_0, a_1)$ float freely in the fit but are constrained to the values measured by SNO by the last term in Equation 7.44.

7.5.1.2 SuperKamiokande

The flux of ^8B solar neutrinos measured through neutrino-electron elastic scattering has been reported by the SuperKamiokande experiment, $\phi^{ES}_{SK}(^8B) = 2.32 \pm 0.04\ (\text{stat}) \pm 0.05\ (\text{syst})\ \text{cm}^{-2}\text{s}^{-1}$ [12]. The expected flux is

$$\phi^{ES}_{exp}(^8B) = \phi_{^8B} \int_{E_{min}}^{E_{max}} dE\ S_{^8B}(E)\ [P_{ee}(E) + (1 - P_{ee})\frac{\sigma_{\mu\tau}(E)}{\sigma_e(E)}]\,, \tag{7.45}$$

where $S_{^8B}$ is the ^8B solar neutrino spectrum [**?**] normalized to unity, P_{ee} is the electron neutrino survival probability described above, and σ_e and $\sigma_{\mu\tau}$ are the neutrino-electron elastic scattering cross sections for each flavor. The range of the integral is from $E_{min} = 5\,\text{MeV}$ to $E_{max} = 20$ MeV.

7.5.1.3 Borexino

The flux of mono-energetic, $E_\nu = 0.862\,\text{MeV}$, solar neutrinos, from ^{7}Be measured through neutrino-electron elastic scattering at Borexino was reported in [91], $\phi^{ES}_{Bor}(^7Be) = 3.10 \pm 0.15\ \text{cm}^{-2}\text{s}^{-1}$. The expected flux is

$$\phi^{ES}_{exp}(^7Be) = \phi_{^7Be} \cdot [P_{ee} + (1 - P_{ee}) \cdot \frac{\sigma_{\mu\tau}}{\sigma_e}]\,, \tag{7.46}$$

where P_{ee}, $\sigma_{\mu\tau}$ and σ_e are as defined above.

7.5.1.4 Chlorine experiment

We used the final result from the Homestake Chlorine detector. The production rate per target reported in [8] is

$$R_{Cl} = 2.56 \pm 0.16(\text{stat}) \pm 0.016(\text{syst})\,. \tag{7.47}$$

The expected rate is

$$R_{exp} = \sum_i \phi_i \int_{E_{Th}}^{E_{max}} S_i(E)\sigma_i\, dE \equiv \sum_i \phi_i \langle\sigma_i\rangle_{Eff}\,. \tag{7.48}$$

The sum is over the three fluxes that contribute to Ar production: $\phi_{^7Be}$, ϕ_{CNO} and $\phi_{^8B}$. The standard solar model, BP05OP [7], and the spectrum averaged cross sections reported in [8] were used.

7.5.1.5 Constraints from Standard Solar Model

The parameter associated with the ^8B flux is constrained to the value measured by SNO by Equation 7.44. We constrain the $\phi_{^7Be}$ and ϕ_{CNO} fluxes to the SSM values with the following term in the penalty χ^2:

$$\chi^2_{SSM} = \sum_i \frac{(\phi_i - \phi_{i,SSM})^2}{\sigma^2_{\phi_{i,SSM}}}\,, \tag{7.49}$$

where the index i labels the flux source (^7Be and CNO), and $\phi_{i,SSM}$ and $\sigma_{i,SSM}$ are the flux and its uncertainty predicted by the standard solar model. This expression does not account for correlations between the different flux sources.

As was done for the KamLAND-only analysis, a profile likelihood function for the solar data was built up by scanning a grid of points in the $\Delta m^2_{21}\,, \theta_{12}\,, \theta_{13}$ parameter space, at each point the values of the nuisance parameters that maximize the likelihood ratio were found using the Minuit minimizer.

7.5.2 Results

Since the nuisance parameters in the KamLAND and solar analyses are uncorrelated the profile likelihoods from both analyses can be combined

$$\chi^2_{Tot}(\Delta m^2_{21}, \theta_{12}, \theta_{13}) = \chi^2_{KL}(\Delta m^2_{21}, \theta_{12}, \theta_{13}) + \chi^2_{Solar}(\Delta m^2_{21}, \theta_{12}, \theta_{13})\,, \tag{7.50}$$

where χ^2_{KL} is the χ^2 associated with the KamLAND likelihood profile. The top panel of Figure 7.6 shows the likelihood profile projected onto the Δm^2_{21} axis for the KamLAND-only, solar-only and the KamLAND + solar combined analysis. The best-fit value for the combined analysis is $\Delta m^2_{21} = 7.60^{+0.20}_{-0.20} \times 10^{-5}\text{eV}^2$. The bottom panel shows the likelihood profiles projected onto the θ_{12} axis, the best-fit value for the combined χ^2 is $\theta_{12} = 33.5^{+1.0}_{-1.1}$ degrees. Figure 7.8 shows the projections onto the $\Delta m^2_{21} - \theta_{12}$ subspace. The projection onto the $\sin^2\theta_{13}$ axis is shown in Figure 7.7. The best-fit value for the combined analysis is $\sin^2\theta_{13} = 0.013 \pm 0.028$, the upper limit at the 95% confidence level is $\sin^2\theta_{13} < 0.06$. Figure 7.9 shows the projection onto the $\sin^2\theta_{13} - \tan^2\theta_{12}$ subspace.

7.6 Summary

The results presented in this chapter are summarized in Table 7.4. From the combined analysis Δm^2_{21} is measured to $\sim 2.6\%$ and θ_{12} is measured to $\sim 3\%$, with KamLAND dominating the Δm^2_{21} measurement and the solar data dominating the θ_{12} measurement. The parameter θ_{13} is the least known mixing angle, KamLAND and solar data place an upper bound of $\sin^2\theta_{13} < 0.06$ at the 95% confidence level but do not provide any significant lower bound. Accelerator-neutrino experiments

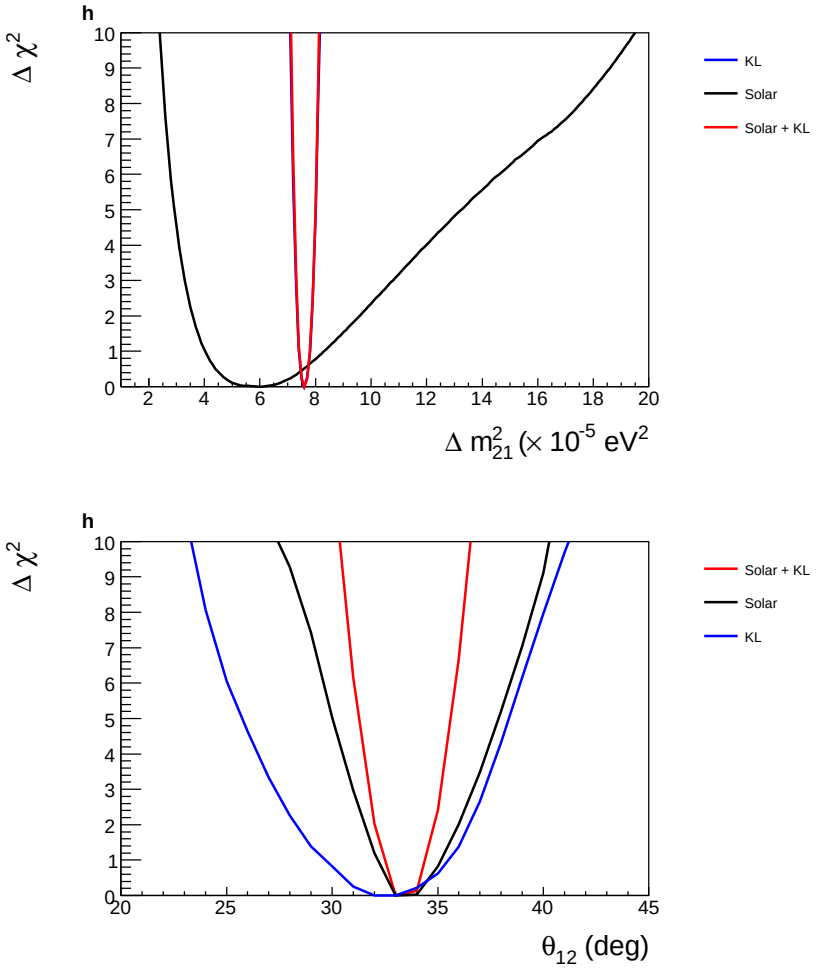

Figure 7.6: Projection of the profile likelihood onto the Δm^2_{21} axis (top) and θ_{12} axis (bottom) for a three-flavor analysis of (i) the KamLAND data, (ii) the solar neutrino data, and (iii) the KamLAND and solar data combined.

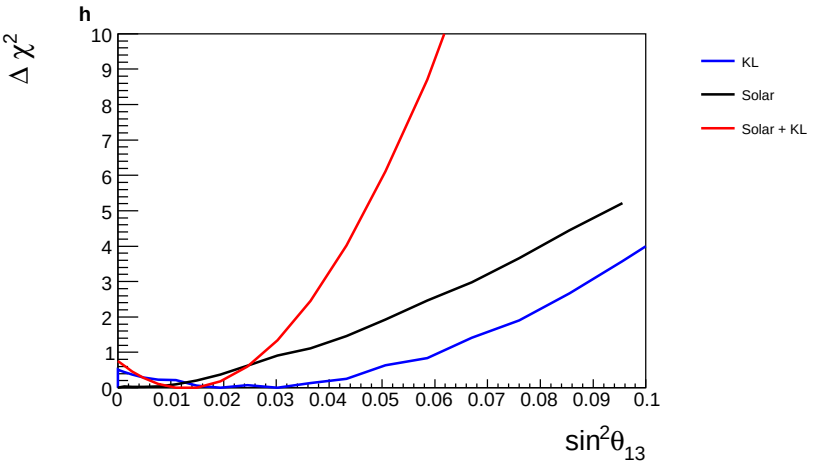

Figure 7.7: Projection of the profile likelihood onto the $\sin^2\theta_{13}$ (bottom) for a three-flavor analysis of (i) the KamLAND data, (ii) the solar neutrino data, and (iii) the KamLAND and solar data combined.

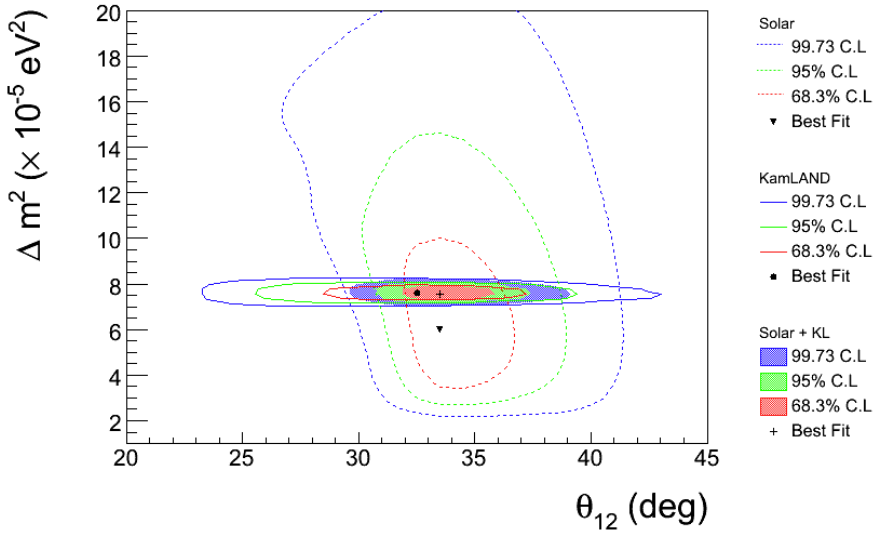

Figure 7.8: Allowed regions in Δm^2_{21}-θ_{12} space for a three-flavor analysis of (i) the KamLAND data, (ii) solar neutrino data and (iii) the KamLAND and solar data combined.

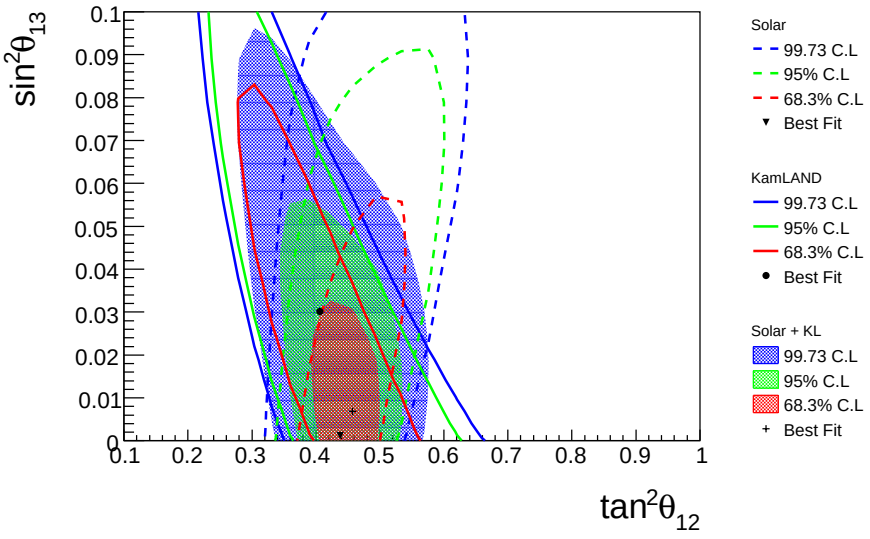

Figure 7.9: Allowed regions in $\sin^2\theta_{13}$-$\tan^2\theta_{12}$ space for a three-flavor analysis of (i) the KamLAND data, (ii) solar neutrino data and (iii) the KamLAND and solar data combined.

and short baseline reactor-neutrino experiments [**?**,38] which have just started or will soon begin taking data are expected to probe $\sin^2 2\theta_{13}$ down to the value of ~ 0.01 at 90% confidence level.

Table 7.4: Summary of oscillation parameter results for each analysis.

Analysis	$\Delta m^2_{21}(\times 10^{-5}$ eV$^2)$	θ_{12} (degrees)	$\sin^2\theta_{13}$
2-ν KL	$7.63^{+0.18}_{-0.19}$	$34.5^{+1.7}_{-1.8}$	—
3-ν KL	$7.60^{+0.20}_{-0.19}$	$32.5^{+2.9}_{-2.9}$	$0.025^{+0.035}_{-0.035}$ < 0.083 (95% CL)
3-ν KL + solar	$7.60^{+0.20}_{-0.20}$	$33.5^{+1.0}_{-1.1}$	0.013 ± 0.028 < 0.06 (95% CL)

Bibliography

[1] Particle Data Group, K. Nakamura et al., *Particle Data Book*, J. Phys. G **37** (2010).

[2] P. P. Rabindra Mohapatra, *Massive Neutrinos in Physics and Astrophysics*, World Scientific Lecture Notes in Physics Vol. 72 (World Scientific, 2004).

[3] T. K. Kuo and J. Pantaleone, *Neutrino oscillations in matter*, Reviews of Modern Physics **61**, 937 (1989).

[4] B. Kayser, *On the quantum mechanics of neutrino oscillation*, Phys. Rev. D **24**, 110 (1981).

[5] A. Balantekin and H. Yuksel, *Global analysis of solar neutrino and KamLAND data*, Journal of Physics G: Nuclear and Particle Physics **29** (2003).

[6] L. Wolfenstein, *Neutrino oscillations in matter*, Phys. Rev. D **17**, 2369 (1978).

[7] J. N. Bahcall, A. M. Serenelli and S. Basu, *New Solar Opacities, Abundances, Helioseismology, and Neutrino Fluxes*, The Astrophysical Journal Letters **621**, L85 (2005).

[8] B. T. Cleveland et al., *Measurement of the Solar Electron Neutrino Flux with the Homestake Chlorine Detector*, The Astrophysical Journal **496**, 505 (1998).

[9] SAGE Collaboration, J. N. Abdurashitov et al., *Measurement of the solar neutrino capture rate with gallium metal. III. Results for the 2002–2007 data-taking period*, Phys. Rev. C **80**, 015807 (2009).

[10] GALLEX Collaboration, W. Hampel et al., *GALLEX solar neutrino observations: results for GALLEX IV*, Physics Letters B **447**, 127 (1999).

[11] GNO Collaboration, M. Altmann et al., *Complete results for five years of GNO solar neutrino observations*, Physics Letters B **616**, 174 (2005).

[12] Super-Kamiokande Collaboration, K. Abe et al., *Solar neutrino results in Super-Kamiokande-III*, Phys. Rev. D **83**, 052010 (2011).

[13] Kamiokande Collaboration, Y. Fukuda et al., *Solar Neutrino Data Covering Solar Cycle 22*, Phys. Rev. Lett. **77**, 1683 (1996).

[14] SNO Collaboration, B. Aharmim et al., *Determination of the ν_e and total ^{8}B solar neutrino fluxes using the Sudbury Neutrino Observatory Phase I data set*, Phys. Rev. C **75**, 045502 (2007).

[15] SNO Collaboration, B. Aharmim et al., *Electron energy spectra, fluxes, and day-night asymmetries of ^8B solar neutrinos from measurements with NaCl dissolved in the heavy-water detector at the Sudbury Neutrino Observatory*, Phys. Rev. C **72**, 055502 (2005).

[16] SNO Collaboration, B. Aharmim et al., *Independent Measurement of the Total Active ^{8}B Solar Neutrino Flux Using an Array of ^{3}He Proportional Counters at the Sudbury Neutrino Observatory*, Phys. Rev. Lett. **101**, 111301 (2008).

[17] Kamiokande Collaboration, K. Hirata et al., *Experimental study of the atmospheric neutrino flux*, Physics Letters B **205**, 416 (1988).

[18] IMB Collaboration, D. Casper et al., *Measurement of atmospheric neutrino composition with the IMB-3 detector*, Phys. Rev. Lett. **66**, 2561 (1991).

[19] Yoshinari and Hayato, *Super-Kamiokande: status and perspectives*, Nuclear Instruments and Methods in Physics Research Section A: Accelerators, Spectrometers, Detectors and Associated Equipment **451**, 86 (2000).

[20] MINOS Collaboration, P. Adamson et al., *Measurement of the Neutrino Mass Splitting and Flavor Mixing by MINOS*, Phys. Rev. Lett. **106**, 181801 (2011).

[21] K2K Collaboration, M. H. Ahn et al., *Measurement of neutrino oscillation by the K2K experiment*, Phys. Rev. D **74**, 072003 (2006).

[22] MINOS Collaboration, P. Adamson, *Measurement of Neutrino Oscillations with the MINOS Detectors in the NuMI Beam*, Phys. Rev. Lett. **101**, 131802 (2008).

[23] KamLAND Collaboration, K. Eguchi et al., *First Results from KamLAND: Evidence for Reactor Antineutrino Disappearance*, Phys. Rev. Lett. **90**, 021802 (2003).

[24] H. Kwon et al., *Search for neutrino oscillations at a fission reactor*, Phys. Rev. D **24**, 1097 (1981).

[25] G. Zacek and F. v. Feilitzsch, *Neutrino-oscillation experiments at the Gosgen nuclear power reactor*, Phys. Rev. D **34**, 2621 (1986).

[26] Z. D. Greenwood et al., *Results of a two-position reactor neutrino-oscillation experiment*, Phys. Rev. D **53**, 6054 (1996).

[27] B. Achkar et al., *Comparison of anti-neutrino reactor spectrum models with the Bugey 3 measurements*, Physics Letters B **374**, 243 (1996).

[28] A. I. Afonin et al., *Anti-electron-neutrino spectra at two distances from the reactor of the Rovno nuclear power plant: Search for oscillations.*, JETP Lett **45**, 247 (1987).

[29] Y. V. Kozlov et al., *Antineutrino deuteron experiment at Krasnoyarsk reactor*, Phys. Atom. Nucl. **63**, 1016 (2000).

[30] CHOOZ Collaboration, M. Apollonio et al., *Limits on neutrino oscillations from the CHOOZ experiment*, Physics Letters B **466**, 415 (1999).

[31] F. Boehm et al., *Final results from the Palo Verde neutrino oscillation experiment*, Phys. Rev. D **64**, 112001 (2001).

[32] The Super-Kamiokande Collaboration, Y. Ashie et al., *Evidence for an Oscillatory Signature in Atmospheric Neutrino Oscillations*, Phys. Rev. Lett. **93**, 101801 (2004).

[33] V. Barger, J. G. Learned, S. Pakvasa and T. J. Weiler, *Neutrino Decay as an Explanation of Atmospheric Neutrino Observations*, Phys. Rev. Lett. **82**, 2640 (1999).

[34] E. Lisi, A. Marrone and D. Montanino, *Probing Possible Decoherence Effects in Atmospheric Neutrino Oscillations*, Phys. Rev. Lett. **85**, 1166 (2000).

[35] KamLAND Collaboration, T. Araki et al., *Measurement of Neutrino Oscillation with KamLAND: Evidence of Spectral Distortion*, Phys. Rev. Lett. **94**, 081801 (2005).

[36] The KamLAND Collaboration, S. Abe et al., *Precision Measurement of Neutrino Oscillation Parameters with KamLAND*, Phys. Rev. Lett. **100**, 221803 (2008).

[37] The MINOS Collaboration, P. Adamson et al., *New constraints on muon-neutrino to electron-neutrino transitions in MINOS*, Phys. Rev. D **82**, 051102 (2010).

[38] T2K Collaboration, K. Abe et al., *Indication of Electron Neutrino Appearance from an Accelerator-Produced Off-Axis Muon Neutrino Beam*, Phys. Rev. Lett. **107**, 041801 (2011).

[39] O. Tajima, Development of liquid scintillator for a large size neutrino detector, Master's thesis, Tohoku University, 2000.

[40] O. Tajima, *Measurement of Electron Anti-Neutrino Oscillation Parameters with a Large Volume Liquid Scintillator Detector, KamLAND*, Ph.D. thesis, Tohoku University, 2003.

[41] N. R. Tolich, *Experimental study of terrestrial electron anti-neutrinos with KamLAND*, Ph.D. thesis, Stanford University, 2005, UMI-31-62346.

[42] S. Enomoto, *Neutrino Geophysics and Observation of Geo-Neutrinos at KamLAND*, Ph.D. thesis, Tohoku University, 2005.

[43] F. Suekane, *An Overview of the KamLAND 1-kiloton Liquid Scintillator*, http://arxiv.org/abs/physics/0404071.

[44] L. Hsu, Noted in KamLAND simulation software (KLG4sim-materials.dat).

[45] H. Kume et al., *20 inch diameter photomultiplier*, Nuclear Instruments and Methods in Physics Research **205**, 443 (1983).

[46] Hamamatsu Photonics, www.hamamatsu.com, *Large Photocathode area photomultiplier tubes*.

[47] S. Enomoto, http://www.awa.tohoku.ac.jp/ sanshiro/kinoko-e/index.html.

[48] B. E. Berger, Kamfee data primer, kamland internal documentation. http://kamland.physics.colostate.edu/fee/docs.html.

[49] S. A. Kleinfelder, *A Multi-Gigahertz Analog Transient Recorder Integrated Circuit*, Ph.D. thesis, University of California Berkeley, 1992.

[50] D. A. Dwyer, *Precision Measurement of Neutrino Oscillation Parameters with KamLAND*, Ph.D. thesis, University of California, Berkeley, 2007.

[51] A. Savitzky and M. J. E. Golay, *Smoothing and Differentiation of Data by Simplified Least Squares Procedures.*, Analytical Chemistry **36**, 1627 (1964), [http://pubs.acs.org/doi/pdf/10.1021/ac60214a047].

[52] R. Brun et al., *ROOT http://root.cern.ch/drupal/.*

[53] F. James, *MINUIT Function Minimization and Error Analysis*, http://wwwasdoc.web.cern.ch/wwwasdoc/minuit/minmain.html , CERN.

[54] KamLAND Collaboration, S. Abe et al., *Production of radioactive isotopes through cosmic muon spallation in KamLAND*, Phys. Rev. C **81**, 025807 (2010).

[55] B. E. Berger et al., *The KamLAND full-volume calibration system*, Journal of Instrumentation **4**, P04017 (2009).

[56] T. I. Banks, Minical status report, Fall 2008, Internal report presented at the KamLAND Collaboration Meeting (unpublished).

[57] National nuclear data base (www.nndc.bnl.gov).

[58] D. W. McKee, J. K. Busenitz and I. Ostrovskiy, *A 13C([alpha],n)16O calibration source for KamLAND*, Nuclear Instruments and Methods in Physics Research Section A: Accelerators, Spectrometers, Detectors and Associated Equipment **587**, 272 (2008).

[59] B. K. Fujikawa, Quenching and cerenkov corrections to the kamland energy scale, KamLAND Internal Note, 2003.

[60] I. Kawrakow and D. W. O. Rogers, The egsnrc code system: Monte carlo simulation of electron and photon transport.

[61] J. Ziegler, http://www.srim.org/, the stopping power tables were kindly prepared using srim by b.k. fujikawa.

[62] KamLAND, S. Abe et al., *Production of Radioactive Isotopes through Cosmic Muon Spallation in KamLAND*, Phys. Rev. **C81**, 025807 (2010), [0907.0066].

[63] P. Vogel, *Analysis of the antineutrino capture on protons*, Phys. Rev. D **29**, 1918 (1984).

[64] P. Vogel and J. F. Beacom, *Angular distribution of neutron inverse beta decay,* $\bar{\nu}_e + p \to e^+ + n$, Phys. Rev. D **60**, 053003 (1999).

[65] Website of INSC, the International Nuclear Safety Center, http://www.insc.anl.gov.

[66] V. Kopeikin, L. Mikaelyan and V. Sinev, *Components of antineutrino emission in nuclear reactor*, Physics of Atomic Nuclei **67**, 1963 (2004), 10.1134/1.1825513.

[67] C. Bemporad, G. Gratta and P. Vogel, *Reactor-based neutrino oscillation experiments*, Rev. Mod. Phys. **74**, 297 (2002).

[68] K. Nakajima et al., *A simple model of reactor cores for reactor neutrino flux calculations for the KamLAND experiment*, Nuclear Instruments and Methods in Physics Research Section A: Accelerators, Spectrometers, Detectors and Associated Equipment **569**, 837 (2006).

[69] Z. Djurcic et al., *Uncertainties in the anti-neutrino production at nuclear reactors*, Journal of Physics G: Nuclear and Particle Physics **36**, 045002 (2009).

[70] P. Vogel, G. K. Schenter, F. M. Mann and R. E. Schenter, *Reactor antineutrino spectra and their application to antineutrino-induced reactions. II*, Phys. Rev. C **24**, 1543 (1981).

[71] K. Schreckenbach, G. Colvin, W. Gelletly and F. V. Feilitzsch, *Determination of the antineutrino spectrum from 235U thermal neutron fission products up to 9.5 MeV*, Physics Letters B **160**, 325 (1985).

[72] A. A. Hahn et al., *Antineutrino spectra from 241Pu and 239Pu thermal neutron fission products*, Physics Letters B **218**, 365 (1989).

[73] P. Vogel, *Conversion of electron spectrum associated with fission into the antineutrino spectrum*, Phys. Rev. C **76**, 025504 (2007).

[74] N. H. Haag, *Bestimmung des Antineutrinospektrums der Spaltprodukte von 238-U*, Ph.D. thesis, Technische Universitat Munchen., 2010.

[75] H. V. Klapdor and J. Metzinger, *Calculation of the antineutrino spectrum from thermal fission of 235U*, Physics Letters B **112**, 22 (1982).

[76] O. Tengblad et al., *Integral γn-spectra derived from experimental beta-spectra of individual fission products*, Nuclear Physics A **503**, 136 (1989).

[77] V. Kopeikin, L. Mikaelyan and V. Sinev, *Inverse beta decay in a nonequilibrium antineutrino flux from a nuclear reactor*, Physics of Atomic Nuclei **64**, 849 (2001), 10.1134/1.1378874.

[78] T. A. Mueller et al., *Improved predictions of reactor antineutrino spectra*, Phys. Rev. C **83**, 054615 (2011).

[79] B. Fujikawa, *Estimation of the mean neutron capture time in the KamLAND scintillator*, 2003, KamLAND Internal Note.

[80] S. Agostinelli et al., *Geant4âĂŽA simulation toolkit*, Nuclear Instruments and Methods in Physics Research Section A: Accelerators, Spectrometers, Detectors and Associated Equipment **506**, 250 (2003).

[81] http://wwwndc.jaea.go.jp/jendl/jendl.html.

[82] K. Ichimura, *Precise Measurement of neutrino oscillation parameters with KamLAND*, Ph.D. thesis, Tohoku University, 2008.

[83] S. Harissopulos et al., *Cross section of the $^{13}C(\alpha,n)^{16}O$ reaction: A background for the measurement of geo-neutrinos*, Phys. Rev. C **72**, 062801 (2005).

[84] G. W. Kerr, J. M. Morris and J. R. Risser, *Energy levels of ^{17}O from $^{13}C(\alpha,\alpha)^{13}C$ and $^{13}C(\alpha,n)^{16}O$*, Nuclear Physics A **110**, 637 (1968).

[85] R. B. Walton, J. D. Clement and F. Boreli, *Interaction of Neutrons with Oxygen and a Study of the $C^{13}(\alpha,\ n)O^{16}$ Reaction*, Phys. Rev. **107**, 1065 (1957).

[86] TUNL Nuclear Data Evaluation Group, *Energy levels of light nuclei, A =3-20*, http://www.tunl.duke.edu/nucldata/.

[87] W. A. Rolke, A. M. Lopez and J. Conrad, *Limits and confidence intervals in the presence of nuisance parameters*, Nuclear Instruments and Methods in Physics Research Section A: Accelerators, Spectrometers, Detectors and Associated Equipment **551**, 493 (2005).

[88] Particle Data Group, C. Amslet et al., *Particle Data Book*, Physics Letters B **667** (2008).

[89] SNO Collaboration, B. Aharmim et al., *Combined Analysis of all Three Phases of Solar Neutrino Data from the Sudbury Neutrino Observatory*, http://arxiv.org/abs/1109.0763.

[90] A. B. Balantekin and A. Malkus, *Solar Neutrino Matter Effects Redux*, http://arxiv.org/abs/1109.5216.

[91] Borexino Collaboration, G. Bellini et al., *Precision Measurement of the* ^{7}Be *Solar Neutrino Interaction Rate in Borexino*, Phys. Rev. Lett. **107**, 141302 (2011).

Appendix A

Analysis with new reactor spectra

The analysis was repeated with the expected reactor antineutrino flux and spectrum calculated using the new reactor-spectra described in Chapter 5. The results are summarized in Table A.1.

Table A.1: Summary of the best-fit oscillation parameter values for a two- and three-flavor analysis using the new reactor-spectra.

Parameter	Two flavor	Three flavor
$\Delta m^2\,(\mathrm{eV}^2)$	$7.63^{+0.20}_{-0.19} \times 10^{-5}$	$7.62^{+0.20}_{-0.20} \times 10^{-5}$
	Figure A.1 (top)	Figure A.2 (top)
$\theta_{12}\,(^\circ)$	$36.0^{+1.9}_{-1.7}$	$32.5^{+3.2}_{-2.8}$
	Figure A.1 (bottom)	Figure A.2 (bottom)
$\sin^2\theta_{13}$	$\equiv 0$	$0.045^{+0.035}_{-0.030}$; < 0.103 (95% C.L)
		Figure A.3

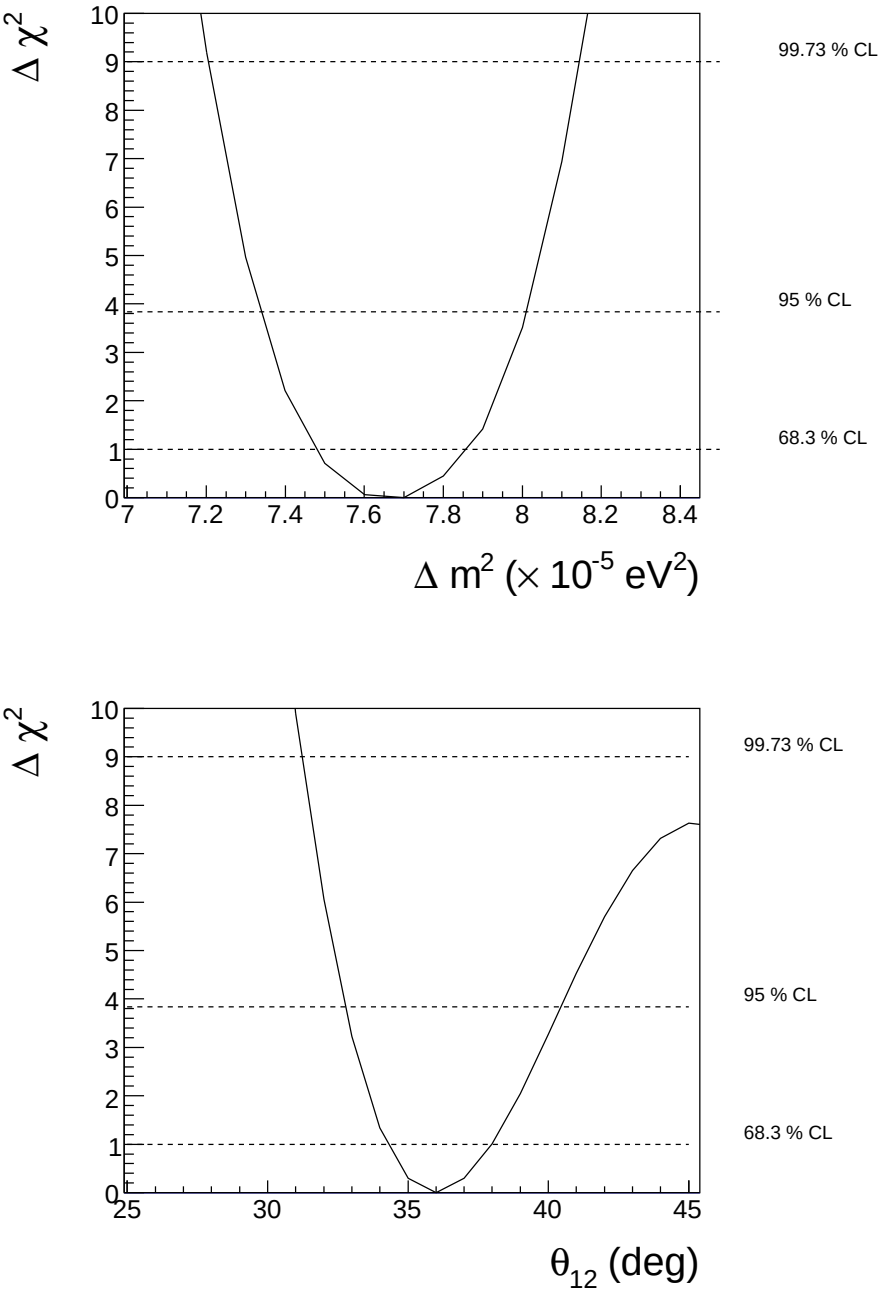

Figure A.1: Projection of the profile likelihood onto the Δm^2 axis (top) and θ_{12} axis (bottom) for a two-flavor analysis using the new reactor-spectra.

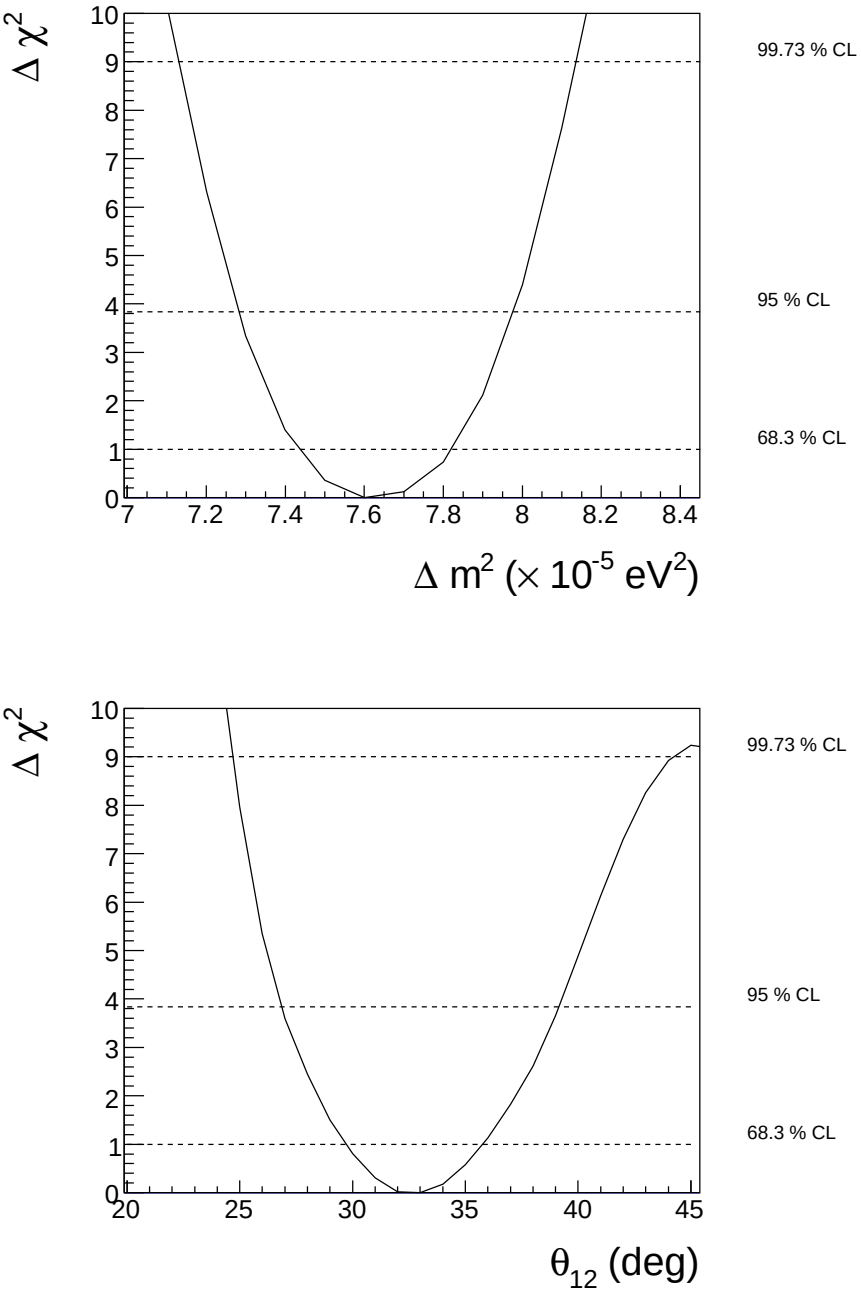

Figure A.2: Projection of the profile likelihood onto the Δm^2 axis (top) and θ_{12} axis (bottom) for a three-flavor analysis using the new reactor-spectra.

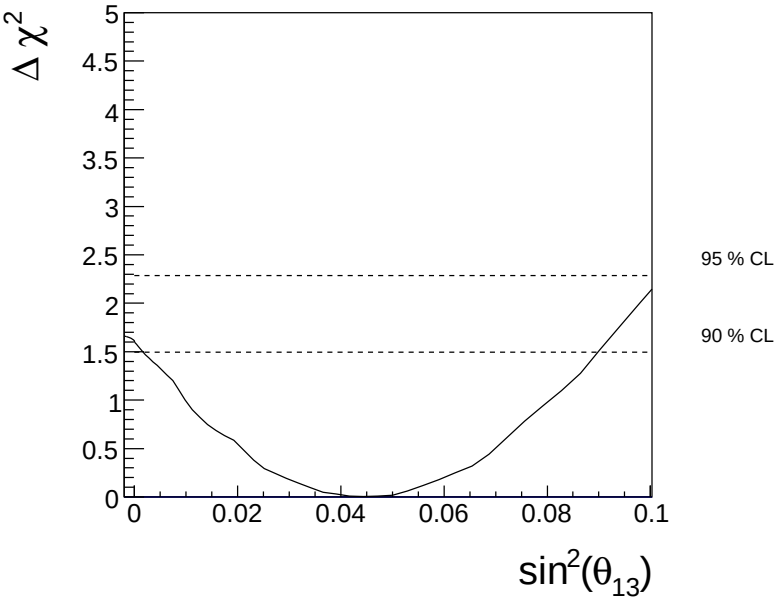

Figure A.3: Projection of the profile likelihood onto the $\sin^2\theta_{13}$ axis for a three-flavor analysis using the new reactor-spectra. The horizontal lines show the 90% and 95% one-sided (upper-limit) confidence regions.

Appendix B

Event classification

Events are classified using low level data such as trigger type, the value of NSum in the ID or OD regions, and the amount and distribution of charge collected in the ID. We introduce two additional variables to characterize the ID charge distribution:

1. Total number of photoelectrons collected in the ID-17-inch PMTs

$$N_{p.e-ID17} = \sum_i \hat{q}_i \,, \tag{B.1}$$

   where the sum is over all pulses collected on all ID-17-inch PMTs and $\hat{q}$ is the charge of each pulse in units of the spe charge of the associated channel.

2. The RMS of the pulse charges

$$\sigma_{p.e-ID} = \sqrt{\frac{\sum_i (\hat{q}_i - \bar{N}_{p.e})^2}{N_{\text{pulses}}}} \,, \tag{B.2}$$

   where $\bar{N}_{p.e}$ is the average pulse charge in units of single photoelectron charge $\bar{N}_{p.e} = \sum_i \hat{q}_i / N_{\text{pulses}}$ and N_{pulses} is the total number of pulses in the sum.

Table B.1 defines a number of event types. In broad terms there are 3 event categories (i) muon events, which are identified their large photoelectron yield in the ID or by OD triggers,(ii) noise events which occur after very energetic muons or some forced-acquisition triggers, and (iii) all other events.

Table B.1: Event types

Type Name	Definition
OD Muon	OD NSumMax > 10
Oil Muon	$N_{p.e-ID}$>1×10^3 and $\sigma_{p.e-ID}$>0.015
LS Muon	$N_{p.e-ID}$>1×10$^{4.8}$ or OD-To-ID trigger and ID NSumMax>1250
Post Muon Noise	Time since last LS muon < 50 μs and $N_{p.e-ID}$< $N_{p.e-ID}$ of that muon
ID NSum Muon	ID NSumMax>1250
Post ID NSum Muon Noise	Time since last ID NSum Muon < 50 μs
Shower Muon	$N_{p.e-ID}$>7×10^5
Neck	Trigger due to neck PMTs
Flasher	$N_{p.e-ID}$>1×10^3 and $\sigma^2_{p.e-ID}/N_{p.e-ID}$> 2
OD Noise	OD-To-ID trigger and only one of the 4 OD regions caused the trigger
Gap	Time since last trigger record > 100 ms or trigger type is a Disable Trigger
PostGap	Time since last pap event < 2 ms
PreGap	Time to next gap event < 2 ms
PPS	Global acquisition trigger launched on PPS pulse from GPS receiver
GPS	Forced acquisition trigger launched once every 32 PPS pulses